INTERGRANULAR WATER AND PERMEABILITY OF THE LAKE VOSTOK ACCRETION ICE, EASTERN ANTARCTICA

by

Steven Michael Jepsen

A dissertation submitted in partial fulfillment
of the requirements for the degree

of

Doctor of Philosophy

in

Engineering

MONTANA STATE UNIVERSITY
Bozeman, Montana

September 2005

APPROVAL

of a dissertation submitted by

Steven Michael Jepsen

This dissertation has been read by each member of the dissertation committee and has been found to be satisfactory regarding content, English usage, format, citations, bibliographic style, and consistency, and is ready for submission to the College of Graduate Studies.

Edward E. Adams

Approved for the Department of Civil Engineering

Brett W. Gunnink

Approved for the College of Graduate Studies

Joseph J. Fedock

STATEMENT OF PERMISSION TO USE

In presenting this dissertation in partial fulfillment of the requirements for a doctoral degree at Montana State University, I agree that the Library shall make it available to borrowers under rules of the Library. I further agree that copying of this dissertation is allowable only for scholarly purposes, consistent with "fair use" as prescribed in the U.S. Copyright Law. Requests for extensive copying or reproduction of this dissertation should be referred to ProQuest Information and Learning, 300 North Zeeb Road, Ann Arbor, Michigan 48106, to whom I have granted "the exclusive right to reproduce and distribute my dissertation in and from microform along with the non-exclusive right to reproduce and distribute my abstract in any format in whole or in part."

Steven Michael Jepsen

September 2005

ACKNOWLEDGEMENTS

I would like to extend my gratitude to the graduate committee for the many helpful discussions on topics in mechanics, thermodynamics, finite element analysis and the use of ANSYS software. I wish to thank the College of Engineering at Montana State University-Bozeman for the resources that allowed me to pursue the doctoral program in engineering. This study was made possible by financial support from the National Science Foundation Office of Polar Programs (OPP-0085400 and OPP-0346272).

TABLE OF CONTENTS

TABLE OF CONTENTS–CONTINUED

LIST OF TABLES

LIST OF FIGURES

LIST OF FIGURES–CONTINUED

LIST OF FIGURES–CONTINUED

NOMENCLATURE

List of Symbols

A_i	Various proportionality constants in creep equations (i = 1, 2, 3,...)
A_{DF}	Dimensionless constant in equation for diffusional creep
A_v	Water vein cross-sectional area
a_p	Dimensionless constant in equation for dislocation creep
a_v	Activity of H_2O solvent in solution
α	Coordinate describing c-axis orientation
α_m	Proportionality constant in Johnston's equation relating dislocation density to plastic strain
α_s	Linear coefficient of thermal expansion of ice in reference state
B_1	Proportionality constant in creep equation
b	Length of Burger's vector (4.52×10^{-10} m)
β_l	Volume coefficient of thermal expansion of water in reference state
C_i	Parameters in Norton creep equation (i = 1 to 3)
c^q_{ij}	Components of adiabatic engineering stiffness matrix in material frame (i, j = 1 to 6)
c_{eff}	Effective specific heat capacity of ice
c_l	Specific heat capacity of water
c_{0l}	Specific heat capacity of water in reference state
c_s	Specific hear capacity of ice
c_{0s}	Specific hear capacity of ice in reference state
χ_s	Moles solute per mole of solution (solute mole fraction)
χ_v	Moles H_2O solvent per mole of solution (solvent mole fraction)
D	Reference shear stress parameter in Johnston's equation
D_i	Taylor series expansion coefficients in fuel-tunneling criterion (i = 1 to 6)
D_b	Grain boundary diffusion coefficient
D_{0b}	Pre-exponential for boundary diffusion
D_v	Lattice diffusion coefficient
D_{0v}	Pre-exponential for lattice diffusion
d_g	Grain size
d^e_g	Grain size of ice used in Fuel-Ice Experiments
d^v_g	Grain size in Vostok accretion ice
d_{g1}	Width and depth of crystals in coarse mesh FE models (= 0.5 m in Vostok simulation)

d_{g2} Depth of crystals in FE submodel

d_v Water vein diameter

δ_b Width of grain boundary diffusion path

δ_{sb} Width of sliding boundary in grain boundary sliding constitutive law

E Stiffness in axial direction

$\mathbf{e}'_\mathbf{i}$ Unit vectors of global frame (i = 1 to 3)

$\mathbf{e}_\mathbf{i}$ Unit vectors of material frame (i = 1 to 3)

ϵ'_{ij} Components of tensorial strain in global frame (i, j = 1 to 3)

ϵ'_{ac} Axial component of creep strain in global frame

ϵ^{el}_{ij} Components of tensorial elastic strain in material frame (i, j = 1 to 3)

ϵ_{ij} Components of tensorial strain in material frame (i, j = 1 to 3)

ϵ_p Plastic strain in Johnston's equation

$\dot{\epsilon}'_a$ Axial strain rate in global frame

$\dot{\epsilon}'_{ac}$ Axial component of creep strain rate in global frame

$\dot{\epsilon}'_{ae}$ Elastic component of axial strain rate in global frame

$\dot{\epsilon}^c_{ij}$ Components of engineering creep strain rate in global frame (i, j = 1 to 3)

$\dot{\epsilon}^c_b$ Component of engineering creep strain rate resolved along crystallographic basal plane

$\dot{\epsilon}^c_e$ Effective creep rate for Hill anisotropy

$\dot{\epsilon}_p$ Plastic strain rate in Johnston's equation

$\dot{\epsilon}_q$ Equivalent strain rate of an isotropic material

η_b Grain boundary intrinsic viscosity

F Parameter in Hill creep potential

F_{bd} Activation energy for grain boundary diffusion

FM1 Setting for mesh density in x′y′ plane of FE submodel

FM2 Setting for mesh density in z′ direction of FE submodel

F_{PR} Activation energy for proton-rearrangement controlled glide

F_v Activation energy for lattice diffusion

G Parameter in Hill creep potential

γ_{bc} Component of engineering creep strain resolved along basal plane

γ_{GB} Solid-solid H_2O free surface energy [$65(\pm3)\times10^{-3}$ J m^{-2}]

γ_{SL} Solid-liquid H_2O free surface energy [$33(\pm3)\times10^{-3}$ J m^{-2}]

γ_v Mole-fraction-scale activity coefficient

$\dot{\gamma}_b$ Component of engineering strain rate resolved along crystallographic basal plane

$\dot{\gamma}_{bc}$	Component of engineering creep rate resolved along crystallographic basal plane
$\dot{\gamma}_d$	Shear strain rate (engineering) from diffusional creep
$\dot{\gamma}_s$	Shear strain rate (engineering) from proton-rearrangement controlled glide
H	Parameter in Hill creep potential
h_i	Depth in ice sheet
h_k	Height of kink in dislocation
J	Diffusion rate of aqueous hydrocarbons
J_c	Critical diffusion rate of aqueous hydrocarbons at onset of fuel-tunneling
K_f	Freezing point depression constant
K_l	Bulk modulus of water in reference state
K_s	Bulk modulus of ice in reference state
k_B	Boltzmann's constant (1.3807×10^{-23} J K^{-1})
k_t	Temperature dependent pre-factor of creep equation for basal glide
L	Parameter in Hill creep potential
L_d	Length of a line for counting intersections with dislocations
L_e	Length of a line in finite element mesh
$\delta L_{e,\min}$	Minimum element length along a line
Λ	Dislocation length per unit volume ice
λ_v	Water vein length per unit volume ice
M	Parameter in Hill creep potential
M_a	Moles impurities per L ice (bulk molarity of impurities)
M_a^e	Moles impurities per L ice in Fuel-Ice Experiments
M_a^v	Moles impurities per L ice in Vostok accretion ice
M_f	Moles hydrocarbons per L solution (hydrocarbon molarity)
M_f^e	Moles hydrocarbons per L solution in Fuel-Ice Experiments (fuel solubility)
M_f^v	Moles hydrocarbons per L solution in Vostok accretion ice (fuel solubility)
M_s	Moles solute per L solution (solute molarity)
M_u	Kg solution per mole solution (solution molar mass)
M_w	Molar mass of H_2O solvent (0.0180152 kg mol^{-1})
m_s	Moles solute per kg H_2O solvent (solute molality)
μ_e	Elastic shear modulus of ice
μ_l	Chemical potential of liquid H_2O solvent (J kg^{-1})
μ_{0l}	Chemical potential of liquid H_2O solvent when no solutes are in solution (J kg^{-1})

μ_n Elastic strain energy contribution to chemical potential of ice

μ_r Free surface energy contribution to chemical potential of ice

μ_s Chemical potential of solid H_2O (J kg^{-1})

μ_{0s} Chemical potential of solid H_2O when no solutes are in solid solution (J kg^{-1})

N Parameter in Hill creep potential

N_d Number of dislocation intersections with a line

N_e Number of element divisions along a line

$\mathbf{n}$ unit vector normal to ice-water interface

ni Different stress exponents in creep equations (i.e., $n1$, $n2$, $n3$,...)

ns Stress exponent in Johnston's equation

n_s Moles solute per m^3 of ice

ν_l Specific volume of water

ν_{0l} Specific volume of water in reference state

ν_s Specific volume of ice

ν_{0s} Specific volume of ice in reference state

ν_p Mean proton rearrangement frequency at temperature 0 K

Ω_v Volume per H_2O molecule in ice (3.27×10^{-29} m^3)

P Hydrostatic pressure in ice

P_l Hydrostatic pressure in liquid water

P_s Magnitude of stress component in solid ice acting normal to ice-water interface, equal to $|\mathbf{n} \cdot \mathbf{Tn}|$

Ψ_l Helmholtz free energy of liquid H_2O solvent (J kg^{-1})

Ψ_{0l} Helmholtz free energy of liquid H_2O solvent in reference state

Ψ_s Helmholtz free energy of solid H_2O (J kg^{-1})

Ψ_{0s} Helmholtz free energy of solid H_2O in reference state

ϕ Spherical coordinate describing c-axis orientation

ϕ_i Spherical coordinate describing c-axis orientation of crystal i (i = 1, 2,...)

$\hat{\phi}$ Spherical unit vector

Q Activation energy

Q_c Rate of heat dissipation from creep

Q_h Hill creep potential

$\mathbf{R}$ Rotation tensor

R_{ij} Components of rotation tensor (i, j = 1 to 3)

R_b Setting of parameters R_{xz} and R_{yz} in Hill creep potential

R_g Universal Gas constant (8.3145 J mol^{-1} K^{-1})

R_n Setting of parameters R_{xx}, R_{yy}, R_{zz} and R_{xy} in Hill creep potential

R_{xx} Parameter in Hill creep potential

R_{yy} Parameter in Hill creep potential

R_{zz} Parameter in Hill creep potential

R_{xy} Parameter in Hill creep potential

R_{yz} Parameter in Hill creep potential

R_{xz} Parameter in Hill creep potential

R_α Rotation angle of material basis that determines value of α

r_1 Principal radius of water vein curvature

r_2 Principal radius of water vein curvature

r_v Water vein radius of curvature

$\hat{r}$ Spherical unit vector

ρ_m Mobile dislocation density in Johnston's equation

ρ_u Kg solution per m^3 of solution (solution density)

S Entropy

S_e Spacing ratio setting along a line

S^q_{ijkl} Components of adiabatic linear elastic compliance tensor in material frame (i, j, k, l = 1 to 3)

S^t_{ijkl} Components of isothermal linear elastic compliance tensor in material frame (i, j, k, l = 1 to 3)

S'^t_{ijkl} Components of isothermal linear elastic compliance tensor in global frame (i, j, k, l = 1 to 3)

s_3 Third principal stress in solid (most compressive)

s_{ij} Components of deviatoric stress tensor with respect to material frame (i, j = 1 to 3)

s^q_{ij} Components of adiabatic engineering compliance matrix in material frame (i, j = 1 to 6)

s_l Specific entropy of liquid water

s_{0l} Specific entropy of liquid water in reference state

s_s Specific entropy of ice

s_{0s} Specific entropy of ice in reference state

σ_{ij} Components of stress tensor with respect to material frame

σ'_{ij} Components of stress tensor with respect to global frame

σ'^b_{ij} Components of stress tensor, at boundary of finite element model, with respect to global frame

σ_0 Yield stress in Hill creep potential

σ'_a Axial stress measured in global frame

σ_b Component of shear stress resolved along the crystallographic basal plane

σ_{b0} Component of shear stress resolved along the crystallographic basal plane at time t= t_0

$\sigma_{b,\max}$ Maximum magnitude of basal plane shear stress in model

σ_b^y Maximum recorded value of basal plane shear stress in constant strain rate test

σ_e Effective stress defined in terms of Hill creep potential

σ_h Local hydrostatic stress in solid (i.e., negative of the average principal stress)

$\sigma_h'^b$ Hydrostatic stress in solid at boundary of finite element model

$\sigma_{h,\max}$ Maximum hydrostatic stress in model

σ_q Equivalent stress

σ_q^t Transition equivalent stress between 3 and 5 MPa

σ_s^c Theoretical shear stress when diffusional and proton-rearrangement controlled creep rates in polycrystalline ice are equal

σ_s Shear stress in deformation mechanism map and creep laws for polycrystalline ice

$\sigma_s'^b$ Deviatoric stress in solid at boundary of finite element model

σ_ξ C-axis misalignment parameter

T Temperature

$\mathbf{T}$ Cauchy stress tensor in the ice

$\mathbf{T^b}$ Cauchy stress tensor representing boundary conditions in the ITJ Model simulation of the Vostok accretion ice

T_m Melting temperature (phase equilibrium temperature)

T_r Reference freezing temperature of pure liquid water

$T_{m,\min}^s$ Minimum melting temperature calculated in model, assuming pressures P_s and s_3 in the solid are equal

$T_{m,\min}^\sigma$ Minimum melting temperature calculated in model, assuming pressures P_s and σ_h in the solid are equal

ΔT Difference between actual temperature and freezing temperature of pure liquid water ($= T - T_r$)

ΔT^c Difference between temperature calculated from thermal ITJ Model and the macroscopic temperature, positive ΔT^c corresponds to "high spot temperature."

ΔT^e Value of ΔT at onset of fuel-tunneling in Fuel-Ice Experiments

$\Delta \overline{T}_{m,\min}^s$ Average minimum melting temperature calculated by ITJ Model assuming macroscopic hydrostatic stress minus the calculated value assuming macroscopic deviatoric stress

ΔT^v Value of ΔT at onset of fuel-tunneling in Vostok accretion ice

δT Difference between steady state temperature and the melting temperature of solid ice ($= T + \Delta T^c - T_m$)

t_i Thickness of ice sample

τ_d Shear stress causing dislocation glide in Johnston's equation

τ_{sb}	Component of shear stress resolved along grain boundary
θ	Spherical coordinate describing c-axis orientation
θ_a	Angle between crystal c-axis and direction of tension
θ_i	Spherical coordinate describing c-axis orientation angle of crystal i (i = 1, 2,...)
θ_v	Dihedral angle of water vein or lens
$\hat{\theta}$	Spherical unit vector
$\dot{U}$	Sliding velocity of grain boundary
u_e	Elastic strain energy density
V	Volume
V_c	Volume of one crystal plus water veins partitioned to it
V_v	Volume of water veins partitioned to one crystal
v_s	Velocity of screw dislocations
x	Coordinate axis of material frame
x′	Coordinate axis of global frame
ξ_{ij}	Angle between c-axis of crystal i and grain boundary j, used in definition of σ_ξ (i = 1 to 3, j = 1 to 2)
$\overline{\xi}$	Average value of ξ_{ij}
y	Coordinate axis of material frame
y′	Coordinate axis of global frame
z	Coordinate axis of material frame
z′	Coordinate axis of global frame

List of Abbreviations

CRL	Cold Regions Laboratory (Montana State University-Bozeman)
DM map	Deformation mechanism map
ETB Model	Elastic Two Blocks Model
ETJ Model	Elastic Triple Junction Model
FE	Finite element
FI Experiments	Fuel-Ice Experiments
GB	Grain boundary
GBS	Grain boundary sliding
IC instrument	Ion chromatography instrument
ITJ Model	Inelastic Triple Junction Model
LH	Liquid hydrocarbon
LNAPL	Light Non-Aqueous Phase Liquid
PRC glide	Proton-rearrangement controlled glide
RAE	Russian Antarctic Expedition
Tube FIA-1	First fuel tube observed in Fuel-Ice Experiment 1
Tube FIB-1	First fuel tube observed in Fuel-Ice Experiment 2
Tube FIB-2	Second fuel tube observed in Fuel-Ice Experiment 2

ABSTRACT

The relative importance of nonhydrostatic stress and lattice-rejected impurities on the phase equilibrium of intergranular liquid water in the Vostok accretion ice, Eastern Antarctica, was examined in this study. In addition, experiments were conducted to examine the influence of intergranular water in ice on the permeability of a Light Non-Aqueous Phase Liquid (LNAPL) hydrocarbon.

Sub-grain scale stresses in the Vostok accretion ice were simulated with anisotropic elastic and elasto-creep finite element (FE) models and compared to X-ray dislocation topographs. The phase equilibrium conditions were solved separately using stresses simulated by the FE models and ice chemistry data obtained from literature. The permeability of ice to JP-8 aviation fuel, the primary component of drilling fluid used in the Vostok borehole, was tested in three Fuel-Ice (FI) Experiments on unfractured ice in dark conditions near the melting point.

The shear stresses simulated by the elastic FE model indicated plastic deformation, via basal glide, in the Vostok accretion ice. This finding was supported by observed dislocation densities exceeding 10^7 m^{-2}, with higher values reported in literature. The elasto-creep FE model indicated onset of intergranular melt, at scales $\approx 1\%$ the crystal size, in the lower few meters of the westernmost accretion ice. Model predictions of strain rate and internal melt were in reasonable agreement with literature data on polycrystalline ice. Based on an impurity model, which assumed hydrostatic stress, millimeter-size intergranular water veins were predicted in the lower few dekameters of accretion ice. The FI Experiments indicated that these water veins in ice provide conduits for rapid (> 16 cm hr^{-1}) infiltration of JP-8 fuel in dark conditions near the melting point. This transport mechanism, referred to as fuel-tunneling, involved the formation of intergranular tubes, 1-2 mm in diameter, that were absent from experiments using ice grown from distilled water.

It was concluded that intergranular water veins in ice near the melting point provide tunneling conduits for LNAPL hydrocarbons. This fuel-tunneling may be accelerated in the basal-most part of the accretion ice due to intergranular melting from both deviatoric stress and mechanical anisotropy. These results have implications for environmentally-clean penetration methods of subglacial lake exploration.

CHAPTER 1

INTRODUCTION

Background Information

Many physical properties of polycrystallince ice are dependent on the quantity of internal liquid water. This liquid water tends to occur in the crystal interstices of ice for the following four reasons: impurities generally have low solubility in the ice lattice, non-planar freezing fronts can trap solutions, both intergranular solutes and surface energies of ice-water interfaces depress the phase equilibrium temperatures, and stress concentrations associated with melting temperature depressions are localized near grain boundaries. All of these mechanisms are synchronous with relative significance depending on the specific environment. Intergranular water affects the rheological properties of glaciers and ice sheets (Renaud, 1949), the effective specific heat of ice (Schwerdtfeger, 1963; Harrison, 1972; Nye, 1991), the permeability of contaminants, gases and solutes in ice (Lliboutry, 1971; Nye and Frank, 1973; Colbeck, 1976; Rempel et al., 2002), and the potential for ice to support microorganisms (Karl et al., 1999; Priscu et al., 1999; Price, 2000). These properties are of interest to various fields of study including climatology, engineering, environmental work and biology.

Research on climate change is concerned with impurities in ice because they provide snap-shots of past climatic conditions. Since many of these impurities are concentrated in intergranular solutions of varying concentration, they are susceptible to redistribution through diffusion (Rempel et al., 2002). This process is a consideration when comparing the ages of ice cores and the climate proxies they provide. Climate change studies utilize paleo-ice sheet reconstructions as sensitive indicators of past meteorologic conditions. Numerical reconstructions of ice sheets rely on flow models that assume a certain ice rheology, which in turn is significantly influenced by the presence of liquid water films along grain boundaries.

Important engineering applications of ice rheology include the interactions between ice and man-made structures. A few example structures are hulls of ice-breaking ships and ice drilling platforms. Barrette and Jordaan (2003) found that polycrystalline ice becomes more compliant at hydrostatic pressures greater than about 65 MPa. This peculiar finding may have been associated with pressure melting along grain boundaries in association with mechanical anisotropy. In a different study, McKittrick and Brown (1996) showed that freezing around brine pockets can nucleate dislocations in sea ice and increase its compliance.

Studies dealing with the transient thermal behavior of temperate ice or snow would consider the latent heat effects of intergranular water. As ice approaches the macroscopic melting point, water volume fractions increase, driving the effective specific heat to much greater values (Schwerdtfeger, 1963; Harrison,

1972; Nye, 1991). In fact, Harrison (1972) has defined temperate ice based on its effective specific heat relative to that of solid ice. Some applications possibly concerned with effective specific heats in ice are the closure rates of drilling bore-holes and the energy balance of temperate snow or ice packs.

Environmental studies on contaminant transport processes in ice may also consider the internal stress state and abundance of intergranular liquid water. However, the permeability of ice via the intergranular network has been the topic of a longstanding debate (Lliboutry, 1971; Nye and Frank, 1973; Colbeck, 1976; Lliboutry, 1993). Based on X-ray diffraction measurements of Vostok accretion ice samples indicating low lattice distortions, the Russian Federation (2001) has concluded that the ice permeability to hydrocarbon drilling fluids would be low. Yet, the mobility of hydrocarbon fluids in ice via the crystal interstices has never been carefully investigated. Past field reports on JP-5 and JP-8 fuel spills on Antarctic ice indicated average infiltration rates of almost 1 m day^{-1} (Tumeo and Larson, 1994; Alexander and Stockton, 2003). It is possible that the mechanisms of this fuel movement are associated with the granular structure of ice.

Microbiologists have become very interested in the ability of microbes to live in deep, icy environments following the discoveries of bacterial cells in the 4 km-deep ice overlying Lake Vostok, Eastern Antarctica (Priscu et al., 1999; Karl et al., 1999). Price (2000) has championed the notion that intergranular liquid solutions in ice could possibly nourish and support psychrophilic bacteria. These developments have invigorated the inquiries about extraterrestrial life below the icy surfaces of the planet Mars and Jupiter's moon Europa. They have also made apparent the need for biological decontamination protocols for ice core studies (Christner et al., 2005).

The presence of liquid water in ice has been explained and formulated in terms of phase equilibrium concepts in thermodynamics. Such treatments have taken the pressures in ice and liquid water to be homogeneous and, aside from capillarity effects, equal to the hydrostatic pressure. Use of the Clausius-Clapeyron equation is amenable to these approaches, with additional mathematical terms to account for surface tension (Steinemann, 1958; Ketcham and Hobbs, 1969; Nye and Mae, 1972) and dissolved solutes (Schwerdtfeger, 1963; Harrison, 1972; Nye, 1991). A more rigorous phase equilibrium approach for anisotropic solids would consider the nonhydrostatic stress contributions (Gibbs, 1948; Kamb, 1961b; Paterson, 1973). Such stresses could occur around the freezing of brine cells in sea ice (McKittrick and Brown, 1996) and in aggregates of anisotropic ice crystals. Therefore, the approximation of uniform, homogeneous pressure is only applicable at the macroscale (i.e., observation scale $>$ crystal size). The general solution of the phase equilibrium problem, which involves the coupling of solute colligative effects, nonhydrostatic stress, temperature and free surface energy, is extremely complex and not achieved in this study.

The anisotropic mechanical properties of single ice crystals have been thoroughly studied. However,

the state of knowledge about how mechanical anisotropy affects internal liquid water formation and ice recrystallization remains incomplete. Numerical methods in solid mechanics have the ability to simulate stress distributions in an aggregate of anisotropic ice crystals with the proper use of momentum balance, material constitutive equations, and boundary conditions. These stress results could in turn be used to address the effect of anisotropy on internal melting at sub-grain, or *microscopic*, scales. The term *microscopic* is used to refer to scales significantly smaller than the dimensions of crystals.

Purpose of Study

The goals of this study are to asses the relative importance of nonhydrostatic stress and impurities on the phase equilibrium of intergranular liquid water in the Lake Vostok accretion ice, Eastern Antarctica. This accretion ice consists of frozen water from underlying Lake Vostok, a body of water comparable in size to Lake Ontario and existing at the base of the $\sim$ 4 km-deep Antarctic ice sheet. This study also examines the influence of intergranular liquid water on the permeability of a liquid hydrocarbon fuel in ice. The fuel type chosen, JP-8 aviation fuel, is the main component of the drilling fluid used in the Vostok borehole. The purpose of the drilling fluid is to compensate for the overburden pressure from the ice and thereby prevent plastic borehole closure. The Vostok accretion ice is the subject of this study largely because of recent interests regarding the potential for intergranular solutions in ice to support *in situ* microbial life, as well as concerns about the possibility of lake contamination with drilling fluid.

The objectives of this study are three-fold: (1) an investigation on the effects of mechanical anisotropy on microscopic stress distributions in the Vostok accretion ice, (2) an assessment of the relative importance of nonhydrostatic stress and impurities on the presence of intergranular liquid water in the ice, and (3) the implications of items (1) and (2) on the permeability of ice to JP-8 fuel. The model will simulate deep, temperate environments in ice sheets where deviatoric stresses are relatively low. These conditions exist near the base of the Antarctic ice sheet, which is currently known to cover at least 70 subglacial lakes (Siegert et al., 2003; Dowdeswell and Siegert, 2003).

Previous Work

Renaud (1949) conducted a simple but brilliant experiment using electrical conductivity and preferential melting along grain boundaries to examine the spatial distribution of impurities in ice. The conclusion was that impurities were concentrated in "saline skins" surrounding grain boundaries, and that such coatings would probably influence the rheology of glacial ice. Later, Harrison and Raymond (1976) also used electrical conductivity measurements, in conjunction with ice textures and thermodynamic contraints, to

estimate proportions of impurities in grain boundaries, triple junctions and grain cores. Techniques in Raman spectroscopy (Fukazawa et al., 1998) and energy dispersive x-ray microanalysis (Mulvaney et al., 1988; Cullen and Baker, 2001a,b; Baker et al., 2003) have been used to show that acids and impurities tend to concentrate along grain boundaries in polar ice. This was shown to be true for sulfate salts in triple junctions of the Vostok accretion ice (Cullen and Baker, 2002). Additional studies have looked at the influence of growth conditions (e.g., freezing rates, temperature gradients, fluid convection) on segregation coefficients (Gross et al., 1975; Killawee et al., 1998) and crystal growth habits (Tiller, 1964) in ice.

The term *water veins* has been used to reference liquid water in concave outward volumes that follow grain boundary junctions in ice (Nye and Frank, 1973; Mader, 1992). Grain boundary junctions refer to the line of intersection between three or more crystals. The term *water lenses* has been used to refer to concave inward liquid water volumes located along grain boundaries in ice (Nye and Mae, 1972; Nye and Frank, 1973; Walford and Nye, 1991). In the present study, the term *intergranular water* is used to refer to water veins and lenses in a collective sense. Techniques in optical microscopy have been used to study the geometry and formation of intergranular water in ice (Nye and Mae, 1972; Raymond and Harrison, 1975; Walford and Nye, 1991; Mader, 1992). Mader (1992) recorded detailed measurements on water vein widths and dihedral angles (i.e., angles at the liquid corners) in temperate ice grown from distilled water. Another experimental technique for measuring the liquid water content in ice has been proton magnetic resonance. Using this, Clifford (1967) has detected liquid water signals in ice at temperatures as low as -12°C.

Internal melting in ice subjected to nonhydrostatic stresses was experimentally observed by Nye and Mae (1972). The ice samples underwent indentation, three- and four-point bending tests while being monitored under a microscope. It was concluded that normal stresses acting on grain boundaries tended to induce melting, and that internal melting was accompanied by heat exchange between water veins and lenses. Another study on internal melting in ice was conducted by Wilson et al. (1996) using plane strain experiments and an anisotropic numerical model. The conclusion was that heat dissipated from zones of localized deformation was a more important cause of melting than pressure concentrations. This interpretation seemed consistent with the contention of Lliboutry (1993), in a report on internal melting and ice accretion of temperate glaciers, that "microscopic stress equals more or less the macroscopic one". These conclusions were examined in the present study.

Numerous experiments have been conducted on single ice crystals to better understand their mechanical properties. McConnel (1891) carried out one of the first documented experiments on single ice crystals in a Swiss hotel room. A bar of ice was supported at its ends in a wooden box and weighted at its center using a mass tied to a string. He reported the deformation as resembling viscous sliding along an infinite

number of planes oriented normal to the optical axis (i.e., c-axis). Many decades later, numerous tests were carried out on the mechanical behavior of single ice crystals at temperatures near the melting point (Glen and Perutz, 1954; Griggs and Coles, 1954; Steinemann, 1954; Nakaya, 1958; Higashi et al., 1964; Higashi, 1967; Wakahama, 1967). The experiments in the 1950's measured the creep properties of crystals, while those in the following decade included the imposition of constant strain rates. The experimental interpretations during the 1960's had the benefit of insight from recently-developed theories in dislocation mechanisms (Johnston and Gilman, 1959; Van Bueren, 1959; Johnston, 1962).

An exhaustive set of bending experiments by Nakaya (1958) eloquently demonstrated that single ice crystals readily deform by gliding along their basal planes (Figure 1.1). Griggs and Coles (1954) carried out creep tests on single ice crystals between temperatures of -1 and -18°C. They found that ice crystals exhibited creep behavior when a shear stress was resolved along the basal (0001) plane, and noted a rather anomalous strain softening behavior. Steinemann (1954) also conducted creep tests on single ice crystals oriented for basal glide at a temperature of -2.3°C. The descriptor "oriented for basal glide" has been used to refer to the crystal orientation which maximizes shear stress in the basal plane. Steinemann related steady state strain rates to shear stresses using a power law relation. In a later study, single ice crystals were subjected to bending and constant-strain rate tension tests over a temperature range of -15 to -40°C (Higashi et al., 1964; Higashi, 1967). The peak stresses in the tension tests were shown to be related to strain rates by an Arrhenius power law. This finding was considered confirmation that Johnston's theory (Johnston and Gilman, 1959) of dislocation-driven deformation was applicable. In yet another study, Wakahama (1967) conducted constant strain rate and stress relaxation experiments on single ice crystals. An insightful description was presented on the relationship between mobile dislocation generation and stresses within the deforming ice. The experimental stress relaxation curves were shown to have the same form as theoretical ones based on dislocation theory.

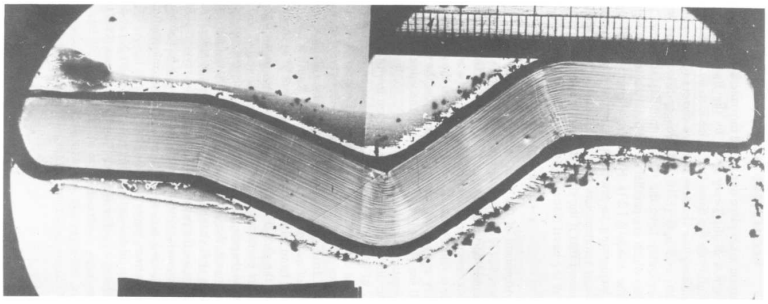

Figure 1.1: Single ice crystal deforming along gliding layers parallel to the basal plane in experiments by Nakaya (1958). Shadow photography was used in this photo by A. Fukuda (taken from Hobbs, 1974).

Nonhydrostatic internal stresses associated with mechanical anisotropy have been studied in numerical models aiming to better understand active slip systems and fabric development. Castelnau et al. (1997) applied the Viscoplastic Self-consistent (VPSC) Model (Hutchinson, 1976) to polycrystalline ice in order to study the relationship between fabric development and anisotropic behavior. Using an inverse-approach to optimize the agreement between experimental data and numerical results, the activities of the basal, prismatic and pyramidal slip systems in ice were calculated. The shear stresses along non-basal slip systems in ice were predicted to be about two orders of magnitude greater than those along the basal plane. These results provided constraints on the relative strain rates along different slip systems and, in addition, an indication about magnitudes of deviatoric stresses in polycrystalline ice. (As a side note, it was interesting to compare these predicted shear stress variations to the notion of Lliboutry (1993) that internal microscopic stresses were everywhere close to the macroscopic stress.) In another study, Wilson and Zhang (1994) carried out simple shear experiments on ice, in conjunction with numerical modeling, to investigate the effects of microscopic stress inhomogeneities on structural developments like kinking, lattice distortion and recrystallization. These structures were reported to be consistent with results from the numerical model at temperatures below -10°C. However, at warmer temperatures, the experimental observations were found to increasingly depart from results of the numerical simulations due to grain-boundary migration.

CHAPTER 2

ICE-WATER EQUILIBRIUM

Theoretical Development

Ice Ih has a hexagonal crystal structure with oxygen atoms in tetrahedral coordination. This form of ice is stable at the moderate pressure-temperature conditions existing near the earth's surface (Hobbs, 1974, Fig. 1.18). The pressure-temperature environment of the Lake Vostok accretion ice falls within these conditions; therefore, this study considers only the hexagonal Ih form of ice. The pressure-temperature state when pure liquid water and ice are in phase equilibrium is described by the Clausius-Clapeyron equation:

$$\frac{dP}{dT} = \frac{\Delta s}{\Delta \nu}$$

where P is the pressure, T the temperature, Δs the phase change entropy, and $\Delta \nu$ the phase change volume. dP/dT represents the slope of the boundaries separating the equilibrium fields for pure ice and water on a P-T phase diagram. Liquid water has greater mass density and specific entropy than ice, therefore the value of dP/dT is negative. This thermodynamic property is rather anomalous among geologic minerals and explains the melting of ice upon application of pressure. Let Δs be the specific entropy (J kg^{-1}K^{-1}) of water minus that of ice near a reference pressure P_0 and temperature T_0 of 101.3×10^3 N m^{-2} and 0°C, respectively. Also, let $\Delta \nu$ be the specific volume of liquid water, ν_{0l}, minus that of ice, ν_{0s}, at a pressure and temperature of P_0 and T_0. Using values for Δs and $\Delta \nu$ from Table 2.1, the Clausius-Clapeyron equation is integrated to obtain the following linear approximation at pressures and temperatures near P_0 and T_0:

$$T - T_0 \approx (-7.6 \times 10^{-8})(P - P_0) \tag{2.1}$$

This equation, valid for small excursions from the reference state, expresses the pressure-dependent temperature at which pure liquid water and ice exist in phase equilibrium. Using this relation, the equilibrium temperature along the ice-water interface above southern Lake Vostok can be estimated. Under an assumed hydrostatic pressure of 33.7 MPa, corresponding to 3750 m of ice, the lake ceiling equilibrium temperature would be about -2.6°C. This temperature is about 0.5°C lower than that estimated by Souchez et al. (2000) based on the downward extrapolation of a known 0.02°C m^{-1} gradient at a borehole depth of 3600 m. The discrepancy between the observed and predicted lake ceiling temperature has been attributed to water salinity which would further depress the ice-water equilibrium temperature. Based

Parameter	Description	Value	Source
T_0	Reference state equilibrium temperature	273.158 K	Calculated
Δs_0	Specific entropy of water minus specific entropy of ice at $P =$ 600 N m^{-2} and $T = 273.16$ K.	1199 J (kg K)$^{-1}$	Hobbs (1974), p. 65
ν_{0l}	Specific volume of water at $P =$ 1.013×10^5 N m^{-2}, $T = 273.15$ K	1.000×10^{-3} m^3 kg^{-1}	Lide (2001), Tbl. 6-5
ν_{0s}	Specific volume of ice at $T =$ 273.15 K (P not listed)	1.091×10^{-3} m^3 kg^{-1}	Lide (2001), Tbl. 6-6
$c_{0l} - c_{0s}$	Specific heat capacity of water minus that of ice at $T = 273.15$ K, $P = 1.00\times10^5$ N m^{-2} for water (P for ice N.L.)	2108 J (kg K)$^{-1}$	Lide (2001), Tbls. 6-3 & 6-7
α_s	Linear thermal expansion coefficient of ice at $T = 273.15$ K, P N.L.	53.0×10^{-6} K^{-1}	Lide (2001), Tbl. 6-7
β_l	Volume thermal expansion coefficient of water at $P = 1.013$ $\times10^5$ N m^{-2}, $T = 273.15$ K.	-58.9$\times10^{-6}$ K^{-1}	Derived using Lide (2001), Tbl. 6-5
K_l	Bulk modulus of water at $P \approx$ 6×10^5 N m^{-2}, $T = 273.16$ K	19.6×10^8 N m^{-2}	Derived using Lide (2001), Tbl. 6-13
K_s	Bulk modulus of ice at $P = 0$ N m^{-2}, $T = 270.15$ K	85.3×10^8 N m^{-2}	Gagnon et al. (1987)
R_g	Universal Gas constant	8.315 J (K mol)$^{-1}$	
M_w	Molar mass of H_2O	0.01802 kg mol^{-1}	
γ_{SL}	Solid-liquid free surface energy of H_2O	(33$\pm$3)$\times10^{-3}$ J m^{-2}	Ketcham and Hobbs (1969)

Table 2.1: Definitions and values of parameters in ice-water phase equilibrium relation (2.25), N.L. = not listed, P = pressure, T = temperature. The values listed are for pressures and temperatures as close as possible to the reference values of 0 N m^{-2} and 273.158 K, respectively.

on sea ice data from Assur(1960) and presented in Schwerdtfeger (1963), the salinity of the lake water would need to be about 9 ‰ (i.e., 9 g dissolved salt per kg solution) to shift the melting temperature of ice downward by 0.5°C. This figure appears to be an order of magnitude too high based on past considerations of Vostok accretion ice chemistry and typical ice-water partitioning coefficients (Souchez et al., 2000; Siegert et al., 2003).

There are additional factors to consider in the microscopic phase equilibrium condition between ice and liquid water. One is the small elastic anisotropy (compliance variations on the order of 10%) and large plastic anisotropy (several orders of magnitude) of single ice crystals. The term *plastic* has been used quite loosely in the literature, and in this report is synonymous with the term *inelastic*. Thus, the term *plastic* is not meant to imply rate-independent inelastic behavior which differs from creep and viscoplasticity.

Because the stress-strain properties of a single ice crystal depend largely on its crystallographic orientation, stresses in a polycrystalline aggregate of non-crystallographically aligned ice crystals will in general be inhomogeneous. Another factor involved in ice-water phase equilibrium is the solid-liquid free surface energy, γ_{SL}, also known as *surface tension* (McLean, 1957, p. 44). Ketcham and Hobbs (1969) defined the free surface energy as the amount of energy required to create unit area of surface between ice and water, and experimentally found it to be $(33\pm3)\times10^{-3}$ J m^{-2}. This quantity has a vital impact on nearly all processes involving crystal nucleation and growth (Jones, 1974). Two competing forces determine the strength of the free surface energy (Zumdahl, 1993, p. 444): 1) the cohesive forces between polar liquid water molecules, and 2) the adhesive forces exerted *by* the liquid water *on* the solid ice. In ice, γ_{SL} is smallest along the basal (0001) plane (Lliboutry, 1971), but this difference is relatively small and within the experimental errors of Ketcham and Hobbs (1969). This lower free surface energy is known to be a reason why inclusions and *Tyndall Figures*, internal melt figures commonly associated with heat absorption, tend to be oriented nearly parallel to the basal plane (Lliboutry, 1971; Hobbs, 1974, p. 589). Nye and Mae (1972) discussed the influence of free surface energies on equilibrium temperature variations and the implications for heat conduction from water lenses to water veins in ice.

Salinity is one of the more important factors governing phase equilibria between ice and liquid water. Many of the dissolved impurities in freezing water are rejected by the ice lattice and concentrated as interstitial fluid along grain boundaries. The concentration of dissolved solutes alters the colligative properties of water, causing a depression in the freezing temperature. For ideally dilute solutions, the freezing temperature depression, ΔT, is linearly related to the *molality* of solutes in solution, m_s, by the following relation:

$$\Delta T = K_f m_s \tag{2.2}$$

where the units of molality are moles solute per kg solvent. If the solute is dissociated, the colligative law (equation 2.2) should include the van't Hoff pre-factor which converts moles of solute to moles of ions in solution. The constant K_f is the known as the *freezing point depression constant*, and for water is typically taken to be -1.86°C kg mol^{-1} at temperatures near 0°C.

To address the effects of mechanical anisotropy on intergranular water in ice, a phase equilibrium relation is needed that considers not only temperature and pressure, but also the general stress state, salinity and free surface energy. The general stress state can be nonhydrostatic as a result of both the overall deformation regime (e.g., pure shear, longitudinal compression, etc.) and the anisotropy of single ice crystals. When phases of liquid water and ice are in equilibrium, their chemical potentials are equal

(Chandler, 1987):

$$\mu_l = \mu_s \tag{2.3}$$

where μ_l and μ_s are the chemical potentials of H_2O species in the liquid and solid phases, respectively, in units of J kg^{-1}. The term *H_2O solvent* is used to refer to H_2O species in the liquid phase. Equation (2.3) reduces from a more general treatment of stressed solids involving jump conditions in the *Eshelby energy-momentum tensor* (Liu, 2002, p. 150), or equivalently, the *chemical potential tensor* (Kondaurov, 2002). In the present study, shear surface tractions are considered negligible along all ice-water interfaces. In this limit, continuity in normal components of the Eshelby energy-momentum tensor across the phase interface reduces to continuity in chemical potentials (equation 2.3). The chemical potential of H_2O in a particular phase (i.e., μ_l or μ_s) is defined as the change in energy of that phase per change in mass of H_2O, with all other state variables held fixed.

The chemical potential, μ_l, of H_2O solvent is decreased upon mixing with a solute to form a solution. When solutes are dissolved in water, the chemical potential of H_2O solvent in the solution becomes (Levine and Levine, 1988, p. 318):

$$\mu_l = \mu_{0l} + (R_g T / M_w) \ln a_v \tag{2.4}$$

where μ_{0l} is the chemical potential of pure H_2O solvent, M_w is the molar mass of pure water ($0.018\,\mathrm{kg\,mol^{-1}}$), R_g the Universal Gas constant, T the absolute temperature, and a_v the H_2O solvent *activity in the solution*. The activity a_v is a dimensionless quantity expressed as the product of the solvent mole fraction, χ_v (moles H_2O per mole solution), and the *mole-fraction-scale activity coefficient*, γ_v, as follows:

$$a_v = \gamma_v \chi_v \tag{2.5}$$

The convenience of equation (2.5) is that the complicated nonlinearities have been pulled inside the term γ_v. This term describes how far the solution deviates from an *ideal solution* as a result of electrostatic interactions between molecules of different species. The ideal solution, analogous to an ideal gas, is one for which these interactions are negligible. The activity coefficient, γ_v, is sometimes approximated as unity for very dilute solutions.

This study will make the first order approximation that the ice lattice rejects all solutes. In this limit, the chemical potential of the solid H_2O species, μ_s, is equal to that of pure ice, μ_{0s}. Restating this relationship for reference:

$$\mu_s = \mu_{0s} \tag{2.6}$$

Substituting equations (2.4), (2.5) and (2.6) into (2.3), the phase equilibrium relation between liquid water

and ice becomes:

$$\mu_{0l} + (R_g T/M_w)\ln(\gamma_v \chi_v) = \mu_{0s} \tag{2.7}$$

In a review on the thermodynamic theory of nonhydrostatically-stressed solids, Kamb (1961b) expounded on the theory previously set forth by Gibbs (1948, p. 364). Based on considerations of this theory, at thermodynamic equilibrium the chemical potential of solid H_2O, μ_{0s}, is found to be:

$$\mu_{0s} = \Psi_s + \nu_s P_s \tag{2.8}$$

where Ψ_s is the Helmholtz free energy (J kg^{-1}) of the ice, ν_s the specific ice volume (m^3 kg^{-1}) and P_s the magnitude of the normal component of stress on the ice-water interface. P_s can be expressed as the absolute value of the quantity $\mathbf{n} \cdot \mathbf{Tn}$, where $\mathbf{T}$ is the Cauchy stress tensor in the solid at the interface and $\mathbf{n}$ is the unit vector normal to the interface. Generalizing from equation (2.8), and verifying the result with the *Gibbs free energy jump condition* between a solid and fluid (Liu, 2002, p. 151), the chemical potential of pure H_2O solvent, μ_{0l}, is as follows:

$$\mu_{0l} = \Psi_l + \nu_l P_l \tag{2.9}$$

where Ψ_l is the Helmholtz free energy (J kg^{-1}) of pure H_2O solvent, ν_l the specific volume of H_2O solvent and P_l the pressure in the liquid. Note that, because of surface tension along the ice-water interface, the fluid pressure P_l does not necessarily equal the pressure P_s on the solid side of the interface. This difference in pressure is addressed later. The phase equilibrium relation for H_2O species in pure ice and liquid water solution is obtained by substituting equations (2.8) and (2.9) into (2.7):

$$\Psi_l + \nu_l P_l + (R_g T/M_w)\ln(\gamma_v \chi_v) = \Psi_s + \nu_s P_s \tag{2.10}$$

Equation (2.10) is the sought after equilibrium condition. It essentially expresses continuity in chemical potentials of H_2O in the solid and liquid phases, but with an additional colligative term $(R_g T/M_w)\ln(\gamma_v \chi_v)$ that acts to lower the free energy of H_2O solvent from its maximum, pure-form value of Ψ_l. Also, note that in the limit of hydrostatic stress and zero solutes in solution, $\chi_v \to 1$ and equation (2.10) becomes the phase equilibrium condition that expresses the continuity in Gibbs free energy.

Approximations will now be derived for the specific Helmholtz free energies Ψ_l and Ψ_s of pure liquid water and pure ice, respectively. The Helmholtz free energy of ice is taken to be a function of temperature, T, and components of the infinitesimal elastic strain tensor, ϵ_{ij}^{el}. The importance of elastic deformations

on phase equilibrium are much greater than the inelastic ones (Steinemann, 1958, p. 255). The inelastic strains may indirectly effect phase equilibrium through local temperature changes associated with sources of heat dissipation. This effect is later considered in the finite element Inelastic Triple Junction Model of Chapter 5. A Taylor series expansion of the Helmholtz free energy of ice to quadratic terms, about the reference states $T = T_0$ and $\epsilon_{ij}^{el} = 0$, yields the following relation:

$$\Psi_s(T, \epsilon_{ij}^{el}) = \Psi_{0s} - A(T - T_0) + B_{ij}\epsilon_{ij}^{el} - \frac{1}{2}C(T - T_0)^2 + \frac{1}{2}D_{ij}(T - T_0)\epsilon_{ij}^{el} + \frac{1}{2}E_{ijkl}\epsilon_{ij}^{el}\epsilon_{kl}^{el} \tag{2.11}$$

Unless stated otherwise, repeated indices imply a summation from 1 to 3. The term Ψ_{0s} is the Helmholtz free energy of ice in the reference state, $\Psi_s(T = T_0, \epsilon_{ij}^{el} = 0)$; A is recognized as the specific entropy, s_{0s}, of ice in the reference state; and C the ratio of heat capacity, c_{0s}, to temperature, T_0, in the reference state. At equilibrium, Ψ_s is a minimum with respect to variations in elastic strain, therefore the coefficients B_{ij} must vanish. We next shift our attention to the terms D_{ij} and E_{ijkl} in equation (2.11). The assumption has been made that ice is a hyperelastic material with internal energy a function of the infinitesimal elastic strains. Therefore, the stress-strain constitutive law for ice is expressed as follows (Liu, 2002, p. 136):

$$\sigma_{mn} = \frac{1}{\nu_{0s}}\frac{\partial \Psi_s}{\partial \epsilon_{mn}^{el}} \tag{2.12}$$

where σ_{mn} are the stress components and ν_{0s} the specific volume of ice in the reference state. Inserting the Helmholtz free energy expansion for ice (equation 2.11) into relation (2.12), the following equation for stress is obtained:

$$\sigma_{ij} = \frac{1}{2\nu_{0s}}(T - T_0)D_{ij} + \frac{1}{\nu_{0s}}E_{ijkl}\epsilon_{kl}^{el} \tag{2.13}$$

Equation (2.13) represents the stress-strain law for a linear thermoelastic material. In order to more clearly associate the D_{ij} terms with the expansion coefficient of ice, it is convenient to consider the inverted form of the stress-strain constitutive relation for a linear thermoelastic material:

$$\epsilon_{ij}^{el} = S_{ijkl}\sigma_{kl} + \delta_{ij}\alpha_s(T - T_0) \tag{2.14}$$

where δ_{ij} is the Kronecker delta, S_{ijkl} the linear elastic compliance tensor, T_0 the reference temperature for zero thermal strain and α_s the coefficient of linear thermal expansion. The reasonable approximation has been made that ice is isotropic with respect to thermal expansion (Hobbs, 1974, p. 347). Next, the stress-strain law (2.14) is inverted to yield the following:

$$\sigma_{ij} = C_{ijkl}\epsilon_{kl}^{el} - \alpha_s(T - T_0)\delta_{kl}C_{ijkl} \tag{2.15}$$

where C_{ijkl} is the linear elastic stiffness tensor. A comparison of equations (2.13) and (2.15) yields the following relations for coefficients D_{ij} and E_{ijkl} in the Helmholtz free energy of ice:

$$\begin{aligned} E_{ijkl} &= \nu_{0s} C_{ijkl} \\ D_{ij} &= -2\alpha_s \nu_{0s} \delta_{kl} C_{ijkl} \end{aligned} \tag{2.16}$$

The terms C_{ijkl} are proportional to the second derivative of the Helmholtz free energy with respect to elastic strain at a fixed temperature (equation 2.11). Therefore, the terms C_{ijkl} represent the isothermal components of the linear elastic stiffness tensor.

Substitution of relations (2.16) into the Helmholtz free energy expansion (2.11) for ice yields the following:

$$\Psi_s = \Psi_{0s} - s_{0s}(T - T_0) - \frac{c_{0s}}{2T_0}(T - T_0)^2 - \alpha \nu_{0s} \sigma_{ii}(T - T_0) + \frac{\nu_{0s}}{2} C_{ijkl} \epsilon_{ij}^{el} \epsilon_{kl}^{el} \tag{2.17}$$

The term σ_{ii} is the trace of the stress tensor and equal to negative of thrice the hydrostatic pressure in the ice. The quantities s_{0s}, c_{0s} and ν_{0s} are the specific entropy, specific heat capacity and specific volume, respectively, of ice in the reference state. Expressing the strain energy density term in equation (2.17) in terms of stress rather than strain, the final form of the Helmholtz free energy of ice is obtained:

$$\Psi_s = \Psi_{0s} - s_{0s}(T - T_0) - \frac{c_{0s}}{2T_0}(T - T_0)^2 - \alpha_s \nu_{0s} \sigma_{ii}(T - T_0) + \frac{\nu_{0s}}{2} S_{ijkl} \sigma_{ij} \sigma_{kl} \tag{2.18}$$

Next, consider the Helmholtz free energy of liquid water. It is assumed that the liquid water contains no shear stresses, a valid approximation because of low viscosity of water. The free energy expansion for pure liquid water follows from equation (2.18), but with σ_{ij} replaced by the fluid pressure $-\delta_{ij} P_l$:

$$\Psi_l = \Psi_{0l} - s_{0l}(T - T_0) - \frac{c_{0l}}{2T_0}(T - T_0)^2 + \beta_l \nu_{0l} P_l (T - T_0) + \frac{\nu_{0l} P_l^2}{2K_l} \tag{2.19}$$

where the quantities P_l, s_{0l}, c_{0l}, β_l, ν_{0l}, K_l are the pressure, specific entropy, specific heat capacity, volume thermal expansion coefficient, specific volume and bulk modulus, respectively, of water in the reference state (i.e., $P_l = 0$ and $T = T_0$).

The specific volumes of ice and water, ν_s and ν_l, (equation 2.10) reference the *current* state, and are different from the reference state values due to pressure and temperature:

$$\begin{aligned} \nu_s &= \nu_{0s} \left[1 + \epsilon_{ii} + 3\alpha_s (T - T_0)\right] \\ \nu_l &= \nu_{0l} \left[1 - \frac{P_l}{K_l} + \beta_l (T - T_0)\right] \end{aligned} \tag{2.20}$$

Substitution of equations (2.20), (2.18) and (2.19) into phase equilibrium relation (2.10) yields the following equilibrium condition for pure ice and liquid water solution:

$$\begin{aligned}
&\Psi_{0l} - s_{0l}(T-T_0) - \frac{c_{0l}}{2T_0}(T-T_0)^2 + \nu_{0l}\beta_l P_l(T-T_0) + \frac{\nu_{0l}P_l^2}{2K_l} + \nu_{0l}P_l - \frac{\nu_{0l}P_l^2}{K_l} \\
&\quad + \beta_l\nu_l P_l(T-T_0) + (R_gT/M_w)\ln(\gamma_v\chi_v) \\
=&\Psi_{0s} - s_{0s}(T-T_0) - \frac{c_{0s}}{2T_0}(T-T_0)^2 - \alpha_s\nu_{0s}\sigma_{ii}(T-T_0) + \frac{\nu_{0s}}{2}S_{ijkl}\sigma_{ij}\sigma_{kl} \\
&\quad + \nu_{0s}P_s + \nu_{0s}\epsilon_{ii}P_s + 3\alpha_s\nu_{0s}P_s(T-T_0)
\end{aligned} \tag{2.21}$$

In general, the pressure in the fluid, P_l, is different than the component of stress in the ice acting normal to the phase interface, P_s, as a result of surface tension (Defay et al., 1966, p. 7). This pressure difference depends on the interface radius of curvature, r_m, and free surface energy, γ_{SL}, as follows:

$$P_l - P_s = \frac{2\gamma_{SL}}{r_m} \tag{2.22}$$

where r_m is the *mean curvature* of the phase interface defined as follows:

$$\frac{1}{r_m} = \frac{1}{2}\left(\frac{1}{r_1} + \frac{1}{r_2}\right) \tag{2.23}$$

with r_1 and r_2 being the two principal radii of curvatures of the surface separating the solid and liquid phases. The sign convention for r_m follows that used in past literature on ice. Liquid water volumes having concave outward (Figure 2.1a) boundaries are referred to as *veins* and have a negative radius of curvature, while water volumes with concave inward boundaries are termed *lenses* and have a positive radius of curvature. Ketcham and Hobbs (1969) found the anisotropy in free surface energy between ice

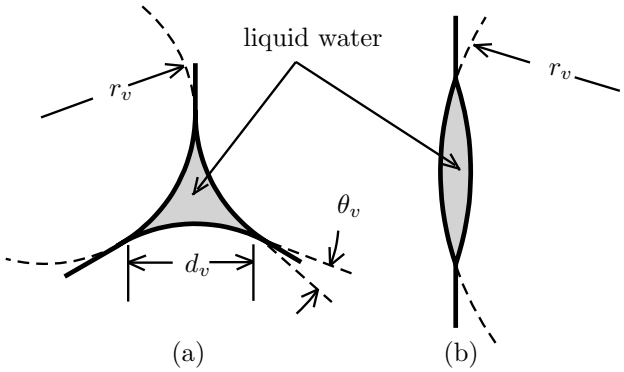

Figure 2.1: Cross sections and geometric parameters of (a) concave-outward water vein and (b) concave-inward water lens. r_v is the radius of curvature, d_v the vein diameter and θ_v the dihedral angle.

and water to be small and within experimental error. Therefore, γ_{SL} is approximated as isotropic in the present study.

At the temperatures and pressures near Lake Vostok, the linear terms $\nu_{0l}P_l$ and $\nu_{0s}P_s$ in equation (2.21) are an order of magnitude greater than the quadratic terms in stress, strain and temperature. In this analysis, only the first order effects of free surface energy on equilibrium are considered. Therefore, equation (2.22) is substituted into the linear term $\nu_{0l}P_l$ in equation (2.21). For all of the other quadratic terms, the approximation is made that $P_l \approx P_s$. Next, the terms Ψ_{0s} and Ψ_{0l} are considered. In the limits that $P_s \to 0$, $\sigma_{ij} \to 0$, $\chi_v \to 1$ (i.e., zero solutes) and $r_m \to \infty$, the equilibrium temperature must approach the reference state value T_0. Enforcing this condition in equation (2.21), the difference $\Psi_{0s} - \Psi_{0l}$ is found to vanish.

In order to adopt shorter notation, the quadratic terms in the phase equilibrium have been labeled as Q_i, with i ranging from 1 to 5. In addition, the differences $s_{0l} - s_{0s}$ and $\nu_{0l} - \nu_{0s}$ have been labeled as Δs_0 and $\Delta\nu_0$, respectively. These notation changes are summarized below:

$$
\begin{aligned}
&\Delta s_0 = s_{0l} - s_{0s} && \Delta\nu_0 = \nu_{0l} - \nu_{0s} \\
&Q_1 = \frac{c_{0l} - c_{0s}}{2T_0}(T - T_0)^2 && Q_2 = (3\alpha_s\nu_{0s} - \beta_l\nu_{0l})(T - T_0)P_s \\
&Q_3 = -(\alpha_s\nu_{0s}\sigma_{ii} + \beta_l\nu_{0l}P_s)(T - T_0) && Q_4 = \nu_{0s}\epsilon_{ii}P_s + \frac{\nu_{0l}P_s^2}{K_l} \\
&Q_5 = \frac{\nu_{0s}}{2}S_{ijkl}\sigma_{ij}\sigma_{kl} - \frac{\nu_{0l}P_s^2}{2K_l}
\end{aligned}
\tag{2.24}
$$

The final form of the phase equilibrium condition between pure ice and liquid water solution is expressed as follows:

$$\Delta s_0(T - T_0) - \Delta\nu_0 P_s + \sum_{i=1}^{5} Q_i - (R_g T/M_w)\ln(\gamma_v\chi_v) - \frac{2\nu_{0l}\gamma_{SL}}{r_m} = 0 \tag{2.25}$$

In equation (2.25), T is the absolute temperature and P_s is the magnitude of the pressure in the ice acting normal to the ice-water interface. The parameter definitions and numerical values in equations (2.25) and (2.24) are listed in Table 2.1. The reference temperature T_0 value of 273.158 K was calculated by substituting $\sigma_{ij} = -P_s$, $P_s = 1.013 \times 10^5$ N m^{-2}, T = 273.150 K, and $\chi_v = 1$ (i.e., zero solutes) into equation (2.25) while taking the limit that $r_m \to \infty$. In solving for T_0, the stresses in the ice were assumed to be hydrostatic with the following replacements being made in equation (2.25): $\frac{1}{2}S_{ijkl}\sigma_{ij}\sigma_{kl} \to P_s^2/(2K_s)$ and $\epsilon_{ii} \to -P_s/K_s$, where K_s is the bulk modulus of ice.

At relatively low stresses, the quadratic stress terms Q_i are much smaller than the linear pressure term $\Delta\nu_0 P_s$ in equation (2.25). For example, at a hydrostatic stress of 1.013×10^5 N m^{-2} and temperature of 273.15 K, the sum $\sum_{i=2}^{5} Q_i$ is four orders of magnitude smaller than the linear pressure term. However,

at higher stresses the quadratic terms in the phase equilibrium relation become increasingly important. For example, the pressure and temperature near the ceiling of southern Lake Vostok, located 3750 m beneath the Vostok station, are about 3.37×10^7 N m^{-2} and 270.6 K, respectively. Inserting this pressure and temperature into equation (2.25), the sum $\sum_{i=2}^{5} Q_i$ is 6% of the linear pressure term. Next, consider the limiting case of no solutes in solution, relatively low stresses and low temperature excursions from 0°C. In this limit, the colligative term $\chi_v \rightarrow 1$ and the quadratic Q_i terms become negligible. The phase equilibrium relation (2.25) then reduces to the approximation used by Nye and Mae (1972) in their analysis on the effect of nonhydrostatic stress on melting in ice.

Next, it will be shown that under certain conditions, phase equilibrium relation (2.25) reduces to the familiar *colligative law* for freezing point depression. First, all stresses are assumed to be hydrostatic and small enough (e.g., atmospheric pressure) that the quadratic Q_i terms can be neglected. Let T_r denote the freezing temperature for *pure* water in the limit that $r_m \rightarrow \infty$ (i.e., planar ice-water interface), and let T denote the freezing temperature of an ideally dilute solution adjacent to pure ice along a planar interface. The mole fractions of total dissolved solute, χ_s, and H_2O solvent, χ_v, must sum to one as follows:

$$\chi_s + \chi_v = 1 \tag{2.26}$$

The units of χ_s and χ_v are moles solute per mole solution and moles solvent per mole solution, respectively. A first order Taylor series expansion of the colligative term in equation (2.25), with the use of equation (2.26), yields the following relation for an ideally dilute solution:

$$\ln(\gamma_v \chi_v) \approx \ln(1-\chi_s) \approx -\chi_s \tag{2.27}$$

Solving for temperatures T and T_r by substituting equation (2.27) into equation (2.25) yields:

$$\begin{aligned} T_r &= T_0 + \frac{\Delta\nu_0 P_s}{\Delta s_0} \\ T &= \left(T_0 + \frac{\Delta\nu_0 P_s}{\Delta s_0}\right)\left(1 + \frac{R_g \chi_s}{\Delta s_0 M_w}\right)^{-1} \end{aligned} \tag{2.28}$$

The freezing point depression ΔT, defined as the difference $T - T_r$, follows from equations (2.28). Expanding T to first order in χ_s, and making the additional approximation that one mole of solution contains one mole of H_2O solvent, valid for an ideally dilute solution, the following is obtained:

$$\Delta T = -\frac{R_g}{\Delta s_0}\left(T_0 + \frac{\Delta\nu_0}{\Delta s_0} P_s\right) m_s \tag{2.29}$$

where m_s is the molality (moles solute per kg solvent) of the liquid water solution. The relation for the freezing point constant, K_f, is found by associating equation (2.29) with the familiar colligative law (2.2) often used to calculate freezing point depression:

$$K_f = -\frac{R_g}{\Delta s_0}\left(T_0 + \frac{\Delta \nu_0}{\Delta s_0} P_s\right) \tag{2.30}$$

The K_f-value calculated from equation (2.30) is -1.89 kg °C mol^{-1} at a pressure P_s of 1.013×10^5 N m^{-2}. This result is very close to the commonly used value of -1.86 kg °C mol^{-1}.

Effect of Solutes and Free Surface Energy on Water Veins in Ice

In the previous section, a phase equilibrium relation (2.25) was derived for pure ice and a liquid water solution under the assumption that all impurities were rejected from the ice lattice. This simplification was not necessary, but was deemed suitable for first order approximations in this study. The variables in the equilibrium condition are stress, temperature, H_2O solvent activity in solution, and the phase interface curvature.

In order to asses the importance of mechanical anisotropy on water veins in the Vostok accretion ice, a logical first step is to analyze the influence of dissolved solutes and surface tension on water vein sizes without the influence of mechanical anisotropy. This is the goal of the remainder of Chapter 2 and seems particularly relevant to the Vostok accretion ice, which is thought to be under very low deviatoric stress based on numerical modeling (Mayer and Siegert, 2000) and X-ray diffraction studies (Montagnat et al., 2001). In the next step, implemented later in Chapter 5, the effects of solutes and free surface energy on phase equilibrium are excluded, and the importance of deviatoric stress and mechanical anisotropy on internal melting in the accretion ice is considered. This approach thus examines and compares the separate effects of dissolved solutes/free surface energy and mechanical anisotropy on the equilibrium of intergranular water in the accretion ice. The study does not solve the full phase equilibrium problem which involves coupling among phase changes, stresses and temperatures.

For the remainder of this chapter, stresses in the ice are approximated as being hydrostatic. As a result of surface tension, the fluid pressure in a water vein is lower than that in the surrounding ice. This pressure difference is described by equation (2.22), where the radii of curvature for a water vein is negative. Based on phase equilibrium theory, a water vein should have a lower melting temperature than a water lens if stresses are hydrostatic, the former therefore being more thermodynamically stable (Lliboutry, 1971; Nye and Mae, 1972; Nye and Frank, 1973). This generalization is supported by experiments by Nye and Mae (1972) and Walford and Nye (1991), which indicated that water lenses (Figure 2.1b) tend to form in ice

that is subjected to deviatoric stress, particularly along grain boundaries oriented normal to the direction of compression. Since stresses are approximated as hydrostatic, the intergranular water is modeled as concave-outward veins extending along all grain boundary (GB) junctions. This same approach was taken by Nye (1991) in a study on the heat capacity of temperate ice.

One formation mechanism of water veins is the entrapment of fluid solutions between crystals during dendritic growth of ice. The onset of dendritic growth depends on the relative magnitudes of the temperature gradient and solute concentration near the freezing front (Tiller, 1964; Pfann, 1966; Gross et al., 1975). Further freezing around trapped fluids, and continued rejection of solutes, would drive the fluid salinity higher. Freezing would eventually stop once the pressure, temperature and solute concentrations reach the conditions for phase equilibrium. Another possible formation mechanism of water veins in accretion ice is the gathering of soluble impurities along migrating grain boundaries (Price, 2000) during *abnormal grain growth*, a type of recrystallization driven by the reduction in free surface energy (Montagnat et al., 2001). A third possible mechanism is the incorporation of impurities into the accretion ice by the accretion and growth of frazil ice crystals from supercooled water (Souchez et al., 2000).

The degree to which dissolved solutes are rejected from ice during growth depends on solute concentrations, solute solubility in ice, freezing rates and interface structure (Gross et al., 1975). When growth rates are slow enough that the ice and adjacent liquid are very near equilibrium, the concentration of solute incorporated into the ice can be described by the *equilibrium segregation coefficient* k_i:

$$k_i = C_{s(i)}/C_{l(i)} \tag{2.31}$$

where k_i is the equilibrium segregation coefficient of solute i, $C_{s(i)}$ is the concentration of solute i in the ice near the interface, and $C_{l(i)}$ is the concentration of solute i in the water near the interface. Killawee et al. (1998) estimated k_i-values for various solute ions in ice, ranging from 0.0004 to 0.003, from a set of experiments involving freezing rates not less than 3 mm hr^{-1}. They found that once solute concentrations in water reached about 20 mmol L^{-1}, the *effective segregation coefficients* rose dramatically due to trapping of solid and liquid inclusions.

Past studies have shown that sulfate anion has a particular tendency to collect in triple junctions in ice. X-ray microanalysis studies by Cullen and Baker (2002) have indicated that sulfate salts are concentrated in triple junctions in the Vostok accretion ice. In an earlier study, Fukazawa et al. (1998) used Raman scattering to show that aqueous solutions of nitric and sulfuric acid have concentrated in triple junctions of the Nansen and South Yamato ice from Antarctica. Mulvaney et al. (1988) also detected sulfuric acid in triple junctions of ice from the Antarctic Peninsula using energy-dispersive X-ray microanalysis. The

sulfate anion seems to have a particularly low ability to substitute into the ice lattice. This would result in a very low equilibrium segregation coefficient. Based on these considerations, the approximation is made that all sulfate anion present in the accretion ice is concentrated in aqueous water vein solutions along triple junctions. This approximation is similar to that used in an earlier study by Price (2000), where all impurities were assumed to concentrate in triple junctions of the Vostok accretion ice. It should be noted that several studies on the Vostok accretion ice have shown that sulfate occurs in solid inclusions and is therefore not entirely concentrated in water vein solutions (Montagnat et al., 2001; De Angelis et al., 2004). Therefore, the assumption of the present study likely overestimates the fraction of sulfate concentrated in triple junctions. However, this overestimate should be partly offset by the presence of other solutes that are not being considered.

The mole fraction (moles solute per mole solution) of sulfate, χ_s, is given by difference $1-\chi_v$ (equation 2.26), where χ_v is the mole fraction of H_2O solvent in solution. Using this relation and a first order Taylor series expansion of the term $\ln(\gamma_v\chi_s)$ in the equilibrium condition, we get:

$$\begin{aligned} \ln(\gamma_v\chi_v) &= \ln\left[\gamma_v(1-\chi_s)\right] \\ &= \ln\gamma_v + \ln(1-\chi_s) \\ &\approx \ln\gamma_v - \chi_s \end{aligned} \tag{2.32}$$

This approximation is valid for $\chi_s \ll 1$. The activity coefficient, γ_v, is a complex function of pressure, temperature, solute type and solute concentration whose treatment is beyond the scope of this study. Therefore, the ideally dilute solution approximation is made that $\ln\gamma_v \approx 0$, which is valid in the limit that $\chi_s \to 0$. This approximation is reasonable for a first order analysis on the effects of impurities and free surface energy on the quantity of intergranular water in ice. Therefore, the following ideally dilute solution approximation is substituted into phase equilibrium condition (2.25):

$$\ln(\gamma_v\chi_v) \approx -\chi_s \tag{2.33}$$

where χ_s is the mole fraction of sulfate in the water vein solution. The approximation is also made that water veins follow all triple junctions between crystals having identical geometry. This rather crude simplification allows χ_s to be related to the overall, or *bulk*, concentration of sulfate in the ice, n_s, using the following relation expressing conservation of moles:

$$\chi_s\rho_u V_v/M_u = n_s V_c \tag{2.34}$$

where χ_s is the sulfate mole fraction in the vein solution (moles sulfate per mole solution), ρ_u the density of the vein solution (kg per m^3 of solution), V_v the volume of veins partitioned to one crystal, M_u the molar mass of the vein solution (kg per mole solution), n_s the bulk molar concentration of sulfate in the ice (moles sulfate per m^3 ice) and V_c the volume of one crystal plus the water veins partitioned to it. In the limit that $\chi_s \ll 1$, the solution density, ρ_u, is approximately equal to $1/\nu_{0l}$, the density of pure water in the reference state. Also in this limit, the molar mass of the vein solution, M_u, is approximately equal to M_w, the molar mass of pure H_2O. Using these simplifications, equation (2.34) becomes:

$$\chi_s = \nu_{0l} M_w n_s \frac{V_c}{V_v} \tag{2.35}$$

Next, the ratio V_v/V_c, the *water vein volume fraction*, is related to idealized water vein and crystal geometry. The cross sectional area, A_v, of a water vein is related to its radius of curvature, r_v, which is typically taken to be a constant. This relationship is expressed as follows (Mader, 1992):

$$A_v = \alpha_v r_v^2 \tag{2.36}$$

where α_v is a function of the dihedral angle, θ_v (Figure 2.1). Past microscopic studies on water veins measured typical dihedral angles ranging from 25 to 40° (Nye and Mae, 1972; Mader, 1992). A value of 32° was quite typical with an associated α_v-value of 0.0725 (Mader, 1992). In this study, the approximation is made that $\alpha_v \approx 0.0725$. Nye (1991) used an α_v-value about 40% larger than this in their model on the effective specific heat of ice. For a θ_v-value of 32°, the relationship between radius of vein curvature r_v and vein diameter d_v (see Figure 2.1a) is (Mader, 1992):

$$d_v \approx 0.48 r_v \tag{2.37}$$

The above relation is later used to convert calculated water vein radii-of-curvatures to diameters.

Water veins are approximately prismatic, with the prism axes aligned along the triple junction. Therefore, water veins are approximated as having a radius of curvature r_v in the plane normal to the triple junction, and an infinite radius of curvature in the direction of the triple junction. Following this approximation, the radius of vein curvature, r_v, and mean radius of curvature, r_m, differ by a factor of 2 (see equation 2.23):

$$r_v = \frac{r_m}{2} \tag{2.38}$$

In a model by Price (2000) on water veins in the Vostok accretion ice, the assumption was made that ice

crystals had the geometry of identical truncated octahedra (Frank, 1968), space-filling polyhedra having 36 edges, each of which form a triple junction with the nearest neighbors (Figure 2.2). This idealized crystal geometry, established by Frank (1968), is also used in the present study. However, several other idealized shapes are also considered in order to explore the sensitivity of the V_v/V_c ratio (equation 2.35) to crystal geometry. Following the example set by Nye (1991), a new parameter λ_v, herein referred to as the *crystal geometry parameter*, is defined as follows:

$$\lambda_v \alpha_v r_v^2 = V_v/V_c \tag{2.39}$$

λ_v is the *water vein length per unit volume of ice*, and when multiplied by the vein cross sectional area, $\alpha_v r_v^2$, gives the water vein volume fraction in ice. The value of λ_v depends only on the size and shape of the crystal. A truncated octahedron of diameter d_g (Figure 2.2) has 36 edges each of length $\sqrt{2}d_g/4$, each shared equally by three crystals. Therefore, each crystal has a water vein volume as follows:

$$V_v = \left(\frac{1}{3}\right) 36 \left(\frac{\sqrt{2}d_g}{4}\right) A_v = 3\sqrt{2}d_g \alpha_v r_v^2 \tag{2.40}$$

where the factor of $1/3$ in equation (2.40) arises from the sharing of each polyhedron edge by three crystals. The volume of one truncated octahedron of diameter d_g is:

$$V_c = d_g^3/2 \qquad \text{(truncated octahedron)} \tag{2.41}$$

Substituting equations (2.40) and (2.41) into equation (2.39), the value of λ_v for the truncated octahedron is:

$$\lambda_v = 6\sqrt{2}d_g^{-2} \qquad \text{(truncated octahedron)} \tag{2.42}$$

Several other simple, idealized crystal shapes are shown in Figure 2.3 for the consideration of different

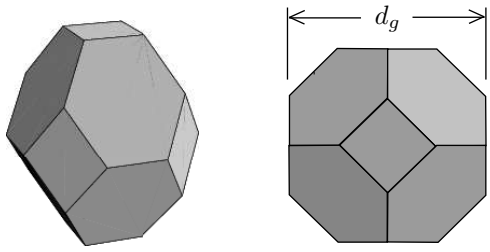

Figure 2.2: Geometry of a truncated octahedron, a space-filling polyhedron originally used by Frank (1968) for an idealized representation of crystals (Image from Weisstein).

plausible λ_v-values. The hexagonal prism (Figure 2.3a) of height and depth d_g has a λ_v-value of $(7/\sqrt{3})d_g^{-2}$ $\approx 4d_g^{-2}$. For a square prism (Figure 2.3b) of aspect ratio d_{g2}/d_{g1}, the value of λ_v is:

$$\lambda_v = \frac{d_{g1}}{d_{g2}} \left[\frac{2 + (d_{g2}/d_{g1})}{d_{g1}^2} \right] \qquad \text{(square prism)} \tag{2.43}$$

For an aspect ratio d_{g2}/d_{g1} ranging from 5 to 1/5, the square prism has a λ_v-value ranging from about $1.4d_{g1}^{-2}$ to $11d_{g1}^{-2}$. The low end of this range is a factor of six less than that for a truncated octahedron ($\approx 8.5d_g^{-2}$). Therefore, if crystals in the Vostok accretion ice are elongated, λ_v could be significantly smaller. Unfortunately, detailed information about crystal geometries in the accretion ice is not available.

Substituting the definition of λ_v from equation (2.39) into equation (2.35), the sulfate mole fraction in the water vein becomes:

$$\chi_s = \frac{\nu_{0l} M_w n_s}{\lambda_v \alpha_v r_v^2} \tag{2.44}$$

The above relation is substituted into the phase equilibrium relation (2.25) to yield a condition involving temperature, pressure, bulk solute concentration, water vein radius and crystal geometry. As previously stated, this part of the study assumes that stresses are hydrostatic with a magnitude of P. Using this assumption, the stress and strain terms in the phase equilibrium equation (2.25) simplify to the following:

$$\begin{aligned} P_s &= P & \sigma_{ii} &= -3P \\ \frac{1}{2} S_{ijkl} \sigma_{ij} \sigma_{kl} &= \frac{P^2}{K_s} & \epsilon_{ii} &= \frac{-P}{K_s} \end{aligned} \tag{2.45}$$

where σ_{ii} and ϵ_{ii} are the traces of the stress and strain tensors, respectively, S_{ijkl} is the isothermal linear elastic compliance tensor of ice, and K_s is the isothermal bulk modulus of ice. Substituting equations (2.33) and (2.44) into phase equilibrium relation (2.25), the following equilibrium relation is obtained for

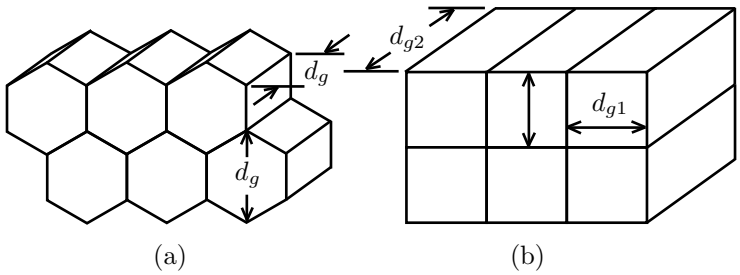

Figure 2.3: Geometry of (a) hexagonal and (b) square prisms for use as idealized crystal shapes. The crystal geometry parameter λ_v for these simple shapes is compared to that for the truncated octahedron.

use in this part of the study:

$$\Delta s_0(T - T_0) - \Delta\nu_0 P + \sum_{i=1}^{5} Q_i + \frac{R_g T \nu_{0l} n_s}{\lambda_v \alpha_v r_v^2} - \frac{\nu_{0l}\gamma_{SL}}{r_v} = 0 \tag{2.46}$$

in conjunction with the following definitions:

$$\Delta s_0 = s_{0l} - s_{0s} \qquad \Delta\nu_0 = \nu_{0l} - \nu_{0s}$$

$$Q_1 = \frac{c_{0l} - c_{0s}}{2T_0}(T - T_0)^2 \qquad Q_2 = (3\alpha\nu_{0s} - \beta\nu_{0l})(T - T_0)P$$

$$Q_3 = (3\alpha\nu_{0s} - \beta\nu_{0l})(T - T_0)P \qquad Q_4 = \left(\frac{\nu_{0l}}{K_l} - \frac{\nu_{0s}}{K_s}\right)P^2$$

$$Q_5 = \left(-\frac{\nu_{0l}}{2K_l} + \frac{\nu_{0s}}{2K_s}\right)P^2$$

Phase equilibrium equation (2.46) is used to predict water vein sizes in the Lake Vostok accretion ice resulting from sulfate concentrated in water veins and free surface energy. The variables in the phase equilibrium relation are as follows: temperature T, hydrostatic pressure P, crystal geometry λ_v, water vein radius r_v, and bulk sulfate concentration n_s. The parameter definitions and values in equation (2.46) are listed in Table 2.1.

Before applying this model to the Lake Vostok accretion ice, it is used to predict water vein sizes that were reported in experiments by Mader (1992). In these experiments, a microscope was used to observe water veins in ice held very close to the macroscopic melting point. The ice was sufficiently close to the melting point that the water vein sizes were very large and relatively stable with time. Thermodynamic arguments involving increasing specific heat with temperature suggested that the ice temperature was somewhere between -0.001 and 0°C. The ice crystal dimensions were 1 to 10 mm in horizontal direction, and 1 to 400 mm in the vertical growth direction. The ice was grown from distilled water with a bulk impurity content of about 10^{-3} mol m^{-3}.

In the numerical simulation of the Mader experiments, the crystal geometry parameter, λ_v, is set equal to that of a square prism (Figure 2.3b, equation 2.43) in order to capture the elongated nature of the laboratory ice crystals. The crystal size parameters d_{g1} and d_{g2} are set to 0.005 and 0.2 m, yielding an aspect ratio of 40 and a λ_v-value of $1.1d_g^{-2} = 4.4\times10^4$ m^{-2}. The bulk solute concentration, n_s, is set to 10^{-3} mol m^{-3}. The pressure, P, is held fixed at 1.013×10^5 N m^{-2} while the temperature, T, is varied between -1 and 0°C. The water vein radii of curvature are calculated by solving phase equilibrium equation (2.46) as a quadratic in r_v. The diameters of the veins are then calculated from the radii of curvature and equation (2.37).

The numerically predicted water vein diameters, d_v, are plotted in Figure 2.4. The calculated water vein

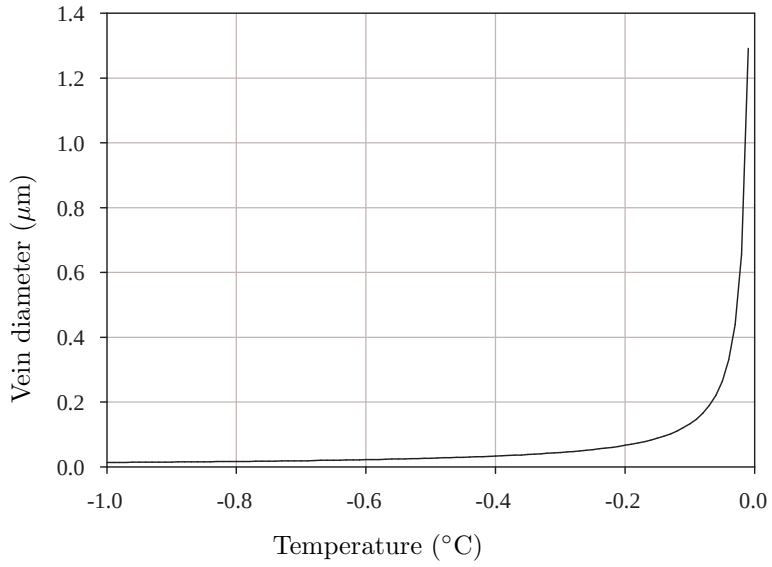

(a)

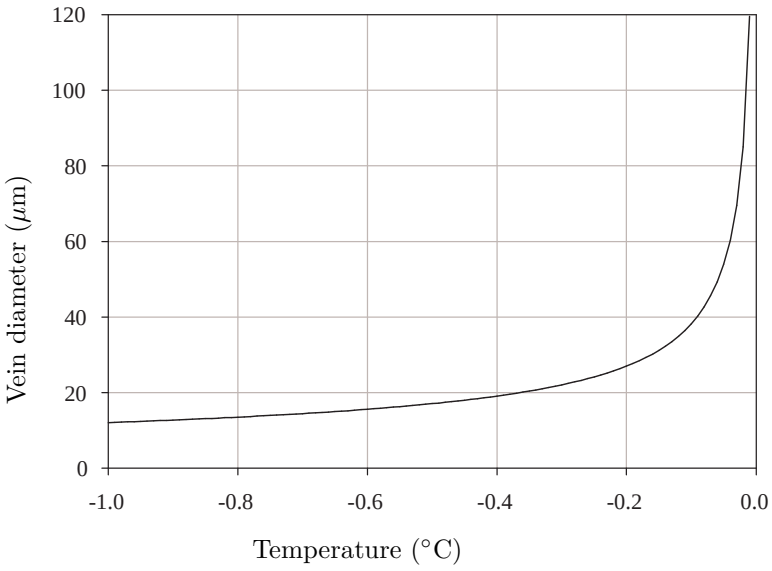

(b)

Figure 2.4: Results of the water vein size simulation of the Mader (1992) experiments, (a) without impurities and (b) with impurities. The predicted water vein diameters in ice with impurities are 119 μm and 339 μm at temperatures of -0.01 and -0.001°C, respectively.

sizes increase as the macroscopic melting point (i.e., 0°C) is approached. Their diameters increase from 119 to 339 μm as the temperature increases from -0.01 to -0.001°C, respectively. In comparison, Mader reported water vein diameters ranging from about 100 to 120 μm at temperatures probably between -0.001 and 0°C. Thus, the model results appear to be within a factor of three of experimental values. Several possible reasons for the model's overestimate in water veins sizes is the incorporation of some solutes into

the ice lattice and their occurrence as solid inclusions. Different studies using X-ray microanalysis have found sulfur-rich inclusions in the Greenland GISP2 ice (Cullen and Baker, 2001a) and Vostok accretion ice (Montagnat et al., 2001; De Angelis et al., 2004), with sodium chloride homogeneously distributed in the latter. Mechanical softening has been observed in HCl-doped ice, suggesting that hydrogen chloride can enter the ice lattice through ionic substitution (Nakamura and Jones, 1970). If it is assumed that 10% of the bulk impurities are concentrated in triple junctions (i.e., $n_s = 10^{-4}$), the calculated water vein diameters are 110 μm at -0.001°C. This result appears to be in excellent agreement with experimental observations by Mader (1992).

The effect of free surface energy on water vein sizes is negligible compared to that of dissolved solutes (Figure 2.4). The calculated water vein sizes in ice with impurities (Figure 2.4b) are two orders of magnitude larger than in ice without impurities (Figure 2.4a). Over the simulated temperature range of -0.1 to -0.001°C, the numerically calculated χ_s-values range from about 10^{-3} to 10^{-5}, validating the ideally dilute solution approximation. The calculated molarities are about 1 to 50 mmol L^{-1} over a temperature range of -0.001 to -0.1°C, the upper end slightly greater than the 20 mmol L^{-1} value noted by Killawee et al. (1998) when inclusions and solute trapping rapidly accelerate in ice.

The large crystal sizes, ranging from 0.2 to 1 m (Jouzel et al., 1999), and warm temperatures in the Vostok accretion ice provide conditions amenable to relatively large water veins. This is illustrated by the $1/(\lambda_v r_v^2)$ term in phase equilibrium relation (2.46), indicating that water vein radii, r_v, tend to scale with grain size, d_g, when all other variables are fixed. Major uncertainties related to water vein formation in the accretion ice are the degree of solution trapping during ice accretion, the quantity of sulfate in the form of solid inclusions, and the partitioning of impurities between grain boundaries, triple junctions and grain interiors. Nevertheless, the numerical model provides an order of magnitude prediction about vein sizes and solute concentrations in the Lake Vostok accretion ice. A critical assumption of the model is that all sulfate anion is concentrated in triple junctions.

The model is now used to predict water vein sizes in the southern Lake Vostok accretion ice (3540-3750 m) below the Vostok drilling station. The pressure, P, is set equal to gh_i/ν_{0s}, where the gravitational constant $g = 9.8$ m s^{-2}, h_i is the depth in the ice (3540-3750 m), and ν_{0s} is the specific ice volume (Table 2.1). The temperatures are approximated from an assumed linear function of depth, h_i, ranging from an average surface value of -55°C (Petit et al., 1999) to an inferred value of -2.7°C at $h_i = 3750$ m based on pressure-temperature equilibrium. The model parameter n_s, the bulk solute mole fraction in the ice, is assigned a value based on sulfate concentrations measured in samples from the Vostok accretion ice (Table 2.2). As shown in Table 2.2, large variations in sulfate concentration exist in the accretion ice. Though not illustrated in the table, impurity concentrations are significantly lower in *accretion ice-2*,

SO_4^{2-} range (ppb)	Average (ppb)	Standard deviation	Source	Notes
7-3412	878	1290	Royston-Bishop, unpublished data	Four samples, each repeated, depths 3548-3622 m.
315-1165	643	373	Souchez et al. 2000	Three samples, depths 3549-3601 m.
1-6224	617	1154	De Angelis et al. 2004	36 samples, depths 3538-3619 m.

Table 2.2: Sulfate anion concentrations measured in Lake Vostok accretion ice samples. Note the large standard deviation in concentrations. 1 ppb = 1 mass unit anion per 10^9 mass units ice.

located below a depth of 3609 m (De Angelis et al., 2004). This spatial variation in impurities is not included in this order of magnitude analysis, but is an important consideration. Based on an average sulfate mass fraction of 700 ppb from Table 2.2, the numerical model takes the bulk solute mole fraction n_s to be 6.7×10^{-3} mol m^{-3}. The ice crystals are approximated as truncated octahedra (Figure 2.2) of diameter $d_g = 0.5$ m, with a λ_v-value of $6\sqrt{2}d_g^{-2} \approx 33.9$ m^{-2}. This crystal size reflects an intermediate size of the 0.2-1 m range reported in literature (Jouzel et al., 1999).

The numerically predicted water vein diameters range from about 0.6 mm near the top of the accretion ice to 3 mm near the lake water at 3740 m (Figure 2.5). The predicted water vein diameters over the majority of the Vostok accretion column are between 1 and 2 mm for an assumed bulk solute concentration, n_s, of 6.7×10^{-3} mol m^{-3}. Water vein sizes in ice without impurities (Figure 2.5a) are three orders of magnitude smaller than ice with impurities. The calculated solute mole fractions, χ_s, based on equation (2.44), range from 2.8×10^{-2} to 1.4×10^{-3} between depths of 3550 and 3740 m, respectively. These values are quite high, corresponding to molarities of 0.08 to 1.6. These molarities are 1 to 2 orders of magnitude greater than the value of 0.02 noted by Killawee et al. (1998) when segregation coefficients increase dramatically and ion incorporation occurs "indiscriminately." These high solute concentrations indicate that the ideally dilute solution approximation $\gamma_v \approx 1$ could be a significant source of error. Therefore, the results of this analysis are considered less reliable than those from the simulation of the Mader experiments. A more rigorous treatment of phase equilibrium in the accretion ice should further consider segregation coefficients and the importance of the solvent activity coefficient, γ_v.

In a similar estimate on water vein sizes in the Vostok accretion ice, Price (2000) calculated vein diameters of equivalent cylinders ranging from about 0.2 to 1 mm, increasing with proximity to the lake. The calculated vein cross sectional areas and molarities were very similar to those predicted in the present study. Price assumed a bulk sulfate concentration of 38 ppb, compared to 700 ppb in the present study, but also included the effects of all other ions. When the numerical model in the present study was repeated

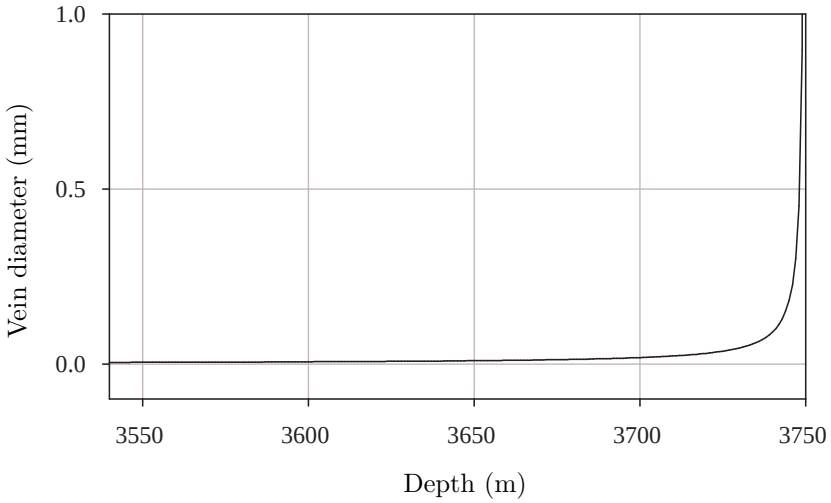

(a)

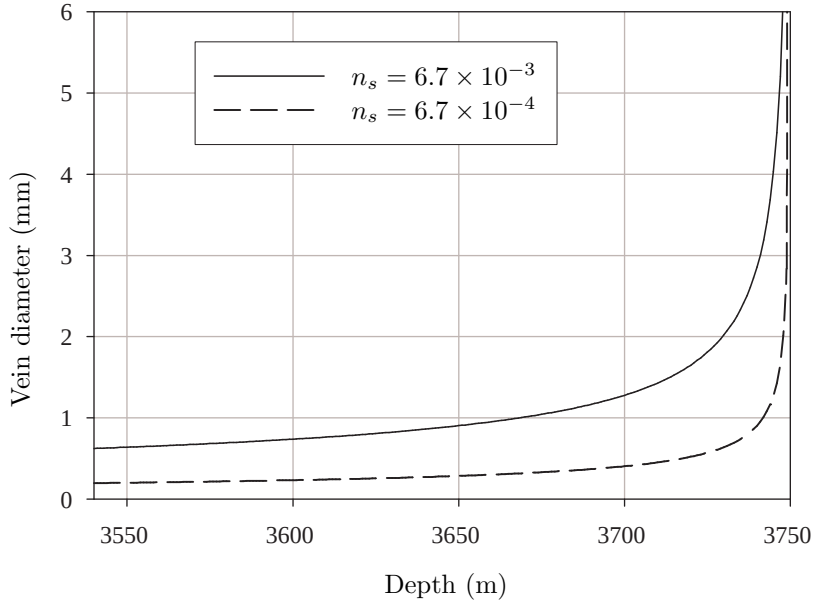

(b)

Figure 2.5: Numerical model prediction of water vein sizes in the southern Lake Vostok accretion ice, (a) without impurities and (b) with impurities. The assumed bulk solute mole concentrations in (b) were 6.7×10^{-3} and 6.7×10^{-4} mol m^{-3}.

using an order of magnitude smaller bulk solute concentration, n_s, of 6.7×10^{-4} mol m^{-3} (70 ppb), the calculated vein diameters decreased by about a factor of three (Figure 2.5b).

From this chapter of the study, it was concluded that typical solute concentrations rejected to triple junctions in ice result in water vein sizes orders of magnitude larger than those attributed to free surface energy alone. Numerical calculations in this study and by Price (2000) suggest mm-size water veins

in the lower few dekameters of the Vostok accretion ice under the critical assumption that solutes are concentrating in triple junctions. Price has argued that nutrients in water veins could sustain numerous microbe cells per cm^3 of accretion ice. Water veins may also influence the permeability of the accretion ice to hydrocarbon drilling fluids. This topic is revisited in the last chapter of this study.

The natural question arises as to why mm-size water veins have not been reported from cursory examinations of ice cores from the Lake Vostok accretion ice. All first-hand observations of the accretion ice in the Cold Regions Laboratory, Montana State University, Bozeman, have been in a cold chamber maintained at temperatures of -10 to -20°C. It seems likely that most other observations, including those at the Vostok drilling station, are made in fairly cool temperatures. However, the temperatures in the lower few dekameters of the accretion ice are very close to the macroscopic melting point, probably within 0.3 or 0.4°C. This temperature difference is considered to be a likely reason why mm-size water veins have not been reported from laboratory examinations of the accretion ice.

This section explored the effects of solutes and free surface energy on the equilibrium of water veins in ice. The focus will now shift to mechanical anisotropy of ice and its effect on internal melting. It is hoped that, in doing this, the relative importance of mechanical anisotropy, solutes and free surface energy on intergranular water in ice will be further understood. In the next chapter, the anisotropy of single crystals is discussed with implications for stress inhomogeneities in polycrystalline ice.

CHAPTER 3

ELASTIC PROPERTIES OF SINGLE ICE CRYSTALS

Compliance in a Hydrostatic Environment

As a starting point, the elastic properties of ice crystals are considered under the rationale that strains are recoverable up to yielding. Ice Ih crystals have a hexagonal crystal structure described by crystallographic axes a_1, a_2, a_3 and c (Figure 3.1). The three a-axes lie in the crystallographic basal plane and subtend angles of 120° to one another. The crystallographic c-axis, which is along the optic axis, is normal to the basal plane. Four Miller-Bravais indices are typically used to describe the orientation of different planes and directions in the hexagonal crystal lattice. These indices reference the non-orthogonal crystallographic axes of the crystal. However, the elastic properties of ice are usually described using an orthogonal reference frame with one axis fixed along the c-axis. This is the practice used in this study to develop the elastic properties of ice crystals. Nevertheless, since Miller-Bravais symbols are mentioned in this study, the symbols are briefly described. The reader is referred to texts on crystallography and Hobbs (1974, p. 725) for more detailed information about their use. The directions of the three a-axes in ice are given by the vectors $[2\bar{1}\bar{1}0]$, $[\bar{1}2\bar{1}0]$, and $[\bar{1}\bar{1}20]$ (Figure 3.1). The family of directions along the three a-axes is denoted as $<2\bar{1}\bar{1}0>$. A Burger's vector is the length and direction (i.e., a vector) along which a *dislocation* allows partial slip to take place in a crystal lattice. The three shortest, and thus energetically favorable, Burger's vectors in ice are $(b/3)[11\bar{2}0]$, $(b/3)[\bar{2}110]$ and $(b/3)[1\bar{2}10]$, where b is a unit cell parameter with a value of about 4.52×10^{-10} m near 0°C (Hobbs, 1974, p. 22, 249). These Burger's vectors have a length of b and are parallel to the three a-axes. There are six crystallographic *prism* planes

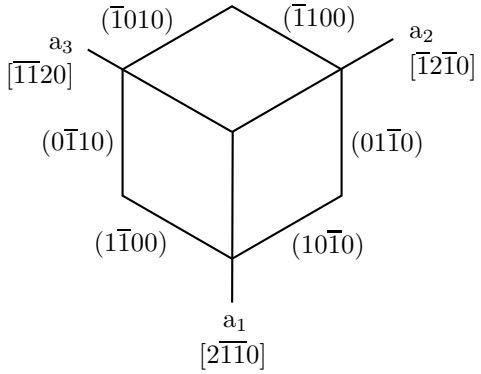

Figure 3.1: Three crystallographic a-axes of Ice Ih shown with planes and directions in the crystal lattice described by Miller-Bravais indices. The crystallographic c-axis, denoted by [0001], is normal to both the basal plane and the plane of the figure. The six sides of the hexagon represent the projection of the prism planes onto the basal plane.

that are each oriented normal to the basal plane. These six planes are described by indices $(10\overline{1}0)$, $(01\overline{1}0)$, $(\overline{1}100)$, $(\overline{1}010)$, $(0\overline{1}10)$ and $(1\overline{1}00)$ (Figure 3.1). The family of the six prism planes is denoted as $\{1\overline{1}00\}$. There are additional planes of symmetry in the Ice Ih lattice (e.g., pyramidal planes), but Miller-Bravais indices for these are not further mentioned in this study.

The elastic properties of Ice Ih crystals are transversely isotropic about the c-axis. In other words, the elastic stress-strain properties of the crystal do not change when the crystal is rotated about the c-axis. Because of anisotropy, the elastic strains depend not only on the applied stresses, but also on the orientation of the c-axis. Ice crystals within a polycrystalline aggregate are constrained by the deformation of neighboring grains which may have differently aligned c-axes. This phenomena leads to stress inhomogeneities, particularly near grain boundaries where strain interference tends to be greatest. These inhomogeneities in stress influence inelastic processes including creep, melting, recrystallization and fracture.

Consider the linear elastic deformation of an ice crystal in a hydrostatic stress environment, the limiting case of low deviatoric stress conditions. First, a *global frame* is defined with unit vectors $\mathbf{e'_i}$ (i = 1 to 3) oriented along an orthogonal set of axes (Figure 3.2). The global frame represents the frame in which strains are "observed." Next, a local *material frame* is introduced with an orthogonal set of unit vectors $\mathbf{e_i}$ (i = 1 to 3). The material frame is fixed along the crystallographic directions of the ice crystal, with $\mathbf{e_1}$ along the a_1 axis (i.e., direction $[2\overline{1}\overline{1}0]$) and $\mathbf{e_3}$ along the c-axis (i.e., direction [0001]). The direction of $\mathbf{e_2}$ follows from $\mathbf{e_1}$, $\mathbf{e_3}$ and the right-hand-rule. Fixing $\mathbf{e_1}$ along the a_1 axis is a logical choice; however, it is quite arbitrary since Ice Ih is transversely isotropic about the c-axis. The orientations of the crystallographic directions are specified by the directions in space of the material frame unit vectors. Let us determine how the normal strain of the ice crystal in the global $\mathbf{e'_3}$ direction, ϵ'_{33}, varies with crystallographic orientation. This is done by specifying the orientation of the material frame and then calculating ϵ'_{33}.

At a fixed temperature, the infinitesimal elastic strain ϵ'_{33} of the ice crystal resulting from the compo-

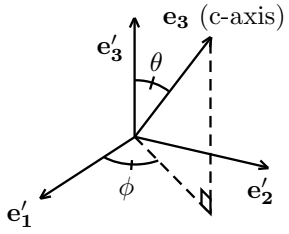

Figure 3.2: Orientation of an ice crystal c-axis relative to an orthogonal global frame. The $\mathbf{e_3}$ unit vector is fixed along the c-axis, and unit vectors $\mathbf{e'_1}$, $\mathbf{e'_2}$ and $\mathbf{e'_3}$ are along the axes of the global frame. The orientation of the $\mathbf{e_3}$ unit vector, relative to the global frame, is described by spherical coordinates θ and ϕ.

nents of stress in the global frame, σ'_{ij}, is as follows:

$$\epsilon'_{33} = S'^{t}_{33ij}\sigma'_{ij} \tag{3.1}$$

where S'^{t}_{ijkl} are the isothermal (superscript 't') components of the linear elastic compliance tensor with respect to the global frame and σ'_{ij} are components of the Cauchy stress tensor with respect to the global frame. The stresses are taken to be hydrostatic and of magnitude P. Thus, σ'_{ij} is replaced by $-\delta'_{ij}P$, where δ'_{ij} is the Kronecker delta, and equation (3.1) simplifies to the following:

$$\epsilon'_{33} = -PS'^{t}_{33ii} \tag{3.2}$$

Repeated indices imply a summation from 1 to 3 unless stated otherwise. Equation (3.2) involves the compliance tensor components in the global frame, which are obtained from a coordinate transformation of the tensor components in the material frame. The compliance tensor components in the material frame exhibit the transversely isotropic properties of the crystal and are obtained from literature. The coordinate transformation of the compliance tensor uses the tensor components S^{t}_{ijkl}, which are with respect to the material frame, and the angles between the global and material unit vectors $\mathbf{e'_i}$ and $\mathbf{e_j}$, respectively. The material unit vectors $\mathbf{e_j}$ are resolved into the global unit vectors by the following linear transformation:

$$\begin{aligned} &\mathbf{e_j} = R_{ij}\mathbf{e'_i} \\ &\text{or equivalently,} \\ &\mathbf{e} = \mathbf{R}\mathbf{e}' \end{aligned} \tag{3.3}$$

where $\mathbf{R}$ is the rotation tensor of components R_{ij} that are equal to $\mathbf{e'_i} \cdot \mathbf{e_j}$. The components R_{ij} are sometimes referred to as the components of the direction-cosines matrix. The linear transformation of the compliance tensor components from the material frame to the global frame follows the transformation rule for fourth-order tensors:

$$S'^{t}_{ijkl} = R_{im}R_{jn}R_{ko}R_{lp}S^{t}_{mnop} \tag{3.4}$$

where S^{t}_{mnop} are the components of the isothermal compliance tensor in the material frame and R_{ij} are components of the rotation tensor as defined above. In order to carry out transformation (3.4), the rotation tensor components, R_{ij}, must be calculated. This requires specification of the orientation of the material unit vectors relative to the global frame.

A convenient way to orient the crystallographic directions is to express the material unit vectors as

combinations of spherical unit vectors $\hat{r}$, $\hat{\theta}$ and $\hat{\phi}$ (Figure 3.3), which in turn are expressed as combinations of the global frame unit vectors. The relationships between the spherical and global unit vectors are as follows (Wangsness, 1986):

$$\begin{aligned}
\hat{r} &= \mathbf{e_1'} \sin\theta\cos\phi + \mathbf{e_2'} \sin\theta\sin\phi + \mathbf{e_3'} \cos\theta \\
\hat{\theta} &= \mathbf{e_1'} \cos\theta\cos\phi + \mathbf{e_2'} \cos\theta\sin\phi - \mathbf{e_3'} \sin\theta \\
\hat{\phi} &= -\mathbf{e_1'} \sin\phi + \mathbf{e_2'} \cos\phi
\end{aligned} \tag{3.5}$$

The $\mathbf{e_3}$ unit vector is defined to be along the $\hat{r}$ vector. The spherical coordinates θ and ϕ specify the orientation of the $\hat{r}$ vector relative to the global frame, and thus the orientation of the c-axis which is fixed along $\hat{r}$. The spherical vectors $\hat{\theta}$ and $\hat{\phi}$ are orthogonal to $\hat{r}$ and therefore lie in the basal plane of the crystal. The material unit vectors are defined to be the following combinations of spherical unit vectors:

$$\begin{aligned}
\mathbf{e_1} &= \hat{\phi}\cos\alpha - \hat{\theta}\sin\alpha \\
\mathbf{e_2} &= -\hat{\phi}\sin\alpha - \hat{\theta}\cos\alpha \\
\mathbf{e_3} &= \hat{r} \quad \text{(c-axis)}
\end{aligned} \tag{3.6}$$

The angle α specifies the orientation of the material $\mathbf{e_1}$ and $\mathbf{e_2}$ unit vectors in the basal plane of the crystal (Figure 3.3b). Because the elastic properties of the crystal are transversely isotropic about the c-axis, the compliance tensor transformation (equation 3.4) is independent of the value of α. Thus, an arbitrary value

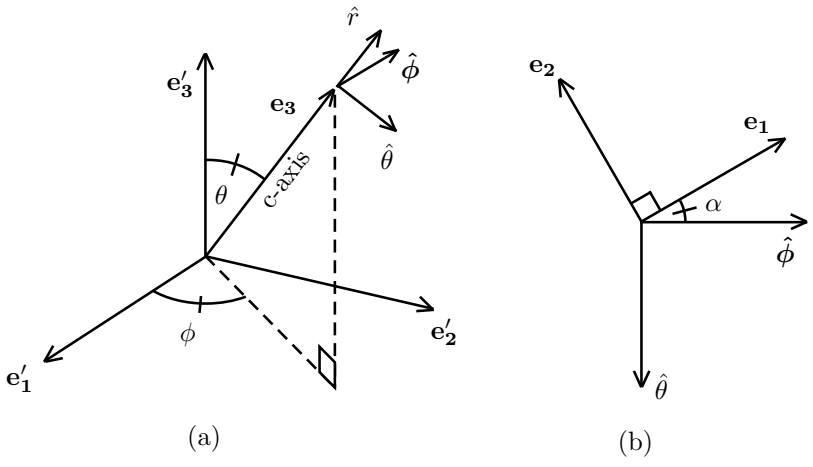

Figure 3.3: Spherical unit vectors used for coordinate transformation of the elastic compliance tensor for an ice crystal. The material unit vectors $\mathbf{e_i}$ are expressed in terms of the spherical unit vectors $\hat{r}$, $\hat{\theta}$ and $\hat{\phi}$, with $\hat{r}$ defined to be parallel to $\mathbf{e_3}$. (a) Orientation of $\mathbf{e_3}$ relative to global unit vectors $\mathbf{e_i'}$ and spherical unit vectors; (b) view looking down material unit vector $\mathbf{e_3}$, where angle α describes the orientation of material unit vectors $\mathbf{e_1}$ and $\mathbf{e_2}$ relative to the $\hat{\phi}$ direction.

of α is used for purposes of carrying out the transformations. The components of the rotation tensor, R_{ij}, are calculated by substituting equations (3.5) into (3.6) and then using equation (3.3).

The coordinate transformation between the material and global unit vectors (equation 3.3) represents three successive rotations, by euler angles ϕ, θ and R_α, of the material unit vectors from an initial configuration coincident with the global frame. The angle R_α is defined below. The first rotation, the sense of which follows the right-hand-rule, is by angle ϕ about the material $\mathbf{e_3}$ direction. The second rotation is by angle θ about the *new* material $\mathbf{e_2}$ direction. The last rotation is by angle R_α about the new material $\mathbf{e_3}$ direction, where R_α is defined as $\alpha + \pi/2$. For no third rotation, R_α is zero and the value of α is $-\pi/2$. The exact relationship between R_α and α is arbitrary because the third rotation has no effect on the transformation of the elastic compliance tensor (transverse isotropy).

The ice crystal is assumed to have the minimum displacement constraints that prevent rigid body translation and rotation. The geometry of the problem is symmetrical with respect to spherical coordinate ϕ. Therefore, the strain ϵ'_{33} in the global frame is independent of ϕ. The independent variables of the strain ϵ'_{33} are pressure P, isothermal compliance components S^t_{ijkl} in the material frame, and spherical coordinate θ.

The isothermal stress-strain law for the ice crystal follows from the development of a hyperelastic material (equation 2.15) in Chapter 2. The matrix form of this constitutive law, after incorporating transversely isotropic symmetry about the c-axis (3-direction), is:

$$\begin{Bmatrix} \sigma_{11} \\ \sigma_{22} \\ \sigma_{33} \\ \sigma_{23} \\ \sigma_{13} \\ \sigma_{12} \end{Bmatrix} = \begin{bmatrix} c^t_{11} & c^t_{12} & c^t_{13} & 0 & 0 & 0 \\ c^t_{12} & c^t_{11} & c^t_{13} & 0 & 0 & 0 \\ c^t_{13} & c^t_{13} & c^t_{33} & 0 & 0 & 0 \\ 0 & 0 & 0 & c^t_{44} & 0 & 0 \\ 0 & 0 & 0 & 0 & c^t_{44} & 0 \\ 0 & 0 & 0 & 0 & 0 & \frac{c^t_{11}-c^t_{12}}{2} \end{bmatrix} \begin{Bmatrix} \epsilon_{11} \\ \epsilon_{22} \\ \epsilon_{33} \\ 2\epsilon_{23} \\ 2\epsilon_{13} \\ 2\epsilon_{12} \end{Bmatrix} \tag{3.7}$$

where c^t_{ij} are components of the 6x6 isothermal (superscript 't') stiffness matrix in the material frame. The index 3 corresponds to the c-axis direction in ice, and indices 1 and 2 correspond to mutually orthogonal but otherwise arbitrary directions in the basal plane. The stress-strain relation inverse to equation (3.7)

is as follows:

$$\begin{Bmatrix} \epsilon_{11} \\ \epsilon_{22} \\ \epsilon_{33} \\ 2\epsilon_{23} \\ 2\epsilon_{13} \\ 2\epsilon_{12} \end{Bmatrix} = \begin{bmatrix} s^t_{11} & s^t_{12} & s^t_{13} & 0 & 0 & 0 \\ s^t_{12} & s^t_{11} & s^t_{13} & 0 & 0 & 0 \\ s^t_{13} & s^t_{13} & s^t_{33} & 0 & 0 & 0 \\ 0 & 0 & 0 & s^t_{44} & 0 & 0 \\ 0 & 0 & 0 & 0 & s^t_{44} & 0 \\ 0 & 0 & 0 & 0 & 0 & 2(s^t_{11} - s^t_{12}) \end{bmatrix} \begin{Bmatrix} \sigma_{11} \\ \sigma_{22} \\ \sigma_{33} \\ \sigma_{23} \\ \sigma_{13} \\ \sigma_{12} \end{Bmatrix} \tag{3.8}$$

where s^t_{ij} are components of the 6x6 isothermal compliance matrix in the material frame.

This study uses the *adiabatic* elastic stiffnesses measured by Gagnon et al. (1987) using Brillouin spectroscopy over a pressure and temperature range of 0 to 2.8 kbar and -4 to -35°C, respectively. The ice samples were obtained from monocrystals of the Mendenhall Glacier in Alaska. Their results were within 1% of values measured by Gammon et al. (1980), using the same technique, at a temperature and pressure of -3°C and 1 atm ($\approx 10^{-3}$ kbar). The adiabatic stiffnesses measured by Gagnon et al. were linearized in pressure P and temperature T to form the following relations:

$$\begin{aligned} c^q_{11}(P,T) &= 137.67 - (27.871 \times 10^{-2})(T+3) + 4.6648P \\ c^q_{12}(P,T) &= 69.852 - (14.131 \times 10^{-2})(T+3) + 5.0743P \\ c^q_{13}(P,T) &= 56.692 - (11.477 \times 10^{-2})(T+3) + 6.4189P \\ c^q_{33}(P,T) &= 148.52 - (29.992 \times 10^{-2})(T+3) + 4.7546P \\ c^q_{44}(P,T) &= 29.911 - (60.537 \times 10^{-3})(T+3) - 0.5662P \end{aligned} \tag{3.9}$$

The superscripts 'q' indicate that the stiffnesses are adiabatic values. The units of c^q_{ij}, P and T in equation (3.9) are kbars, kbars and °C, respectively. The units of kbar have been retained in order to facilitate cross-referencing with Gagnon et al. (1987). The adiabatic elastic stiffness matrix is the 6x6 matrix in equation (3.7), but with c^t_{ij} replaced by c^q_{ij}. In this analysis, the pressure and temperature are set to 0.328 kbar and -4.1°C, respectively, to approximate conditions near the vertical center (3650 m) of the southern Vostok accretion ice. For these conditions, the adiabatic elastic stiffnesses are (in kbar):

$$\begin{aligned} c^q_{11} &= 139.51 & c^q_{12} &= 71.673 & c^q_{13} &= 58.924 \\ c^q_{33} &= 150.41 & c^q_{44} &= 29.793 \end{aligned} \tag{3.10}$$

The components of the isothermal compliance tensor S^t_{ijkl}, with respect to the material frame, are sought in order to apply transformation equation (3.4). Toward this end, three steps are followed, beginning with the known c^q_{ij}-values in equation (3.10). First, the adiabatic stiffness matrix in the material frame, consisting of components c^q_{ij}, is inverted to form the adiabatic compliance matrix, consisting of the adiabatic compliances s^q_{ij}. Next, the s^q_{ij}-values are used to form the components S^q_{ijkl} of the adiabatic compliance tensor in the material frame. Lastly, the components of the adiabatic compliance tensor are converted to corresponding isothermal values S^t_{ijkl} at a temperature of -4.1°C. The reason that isothermal compliances are sought is that the Helmholtz free energy Ψ_s of ice is a function of temperature (see page 13). The elastic stiffness values, inversely related to the compliances, are defined in terms of the second derivative of Ψ_s with respect to elastic strain at a fixed temperature.

Components of the adiabatic compliance matrix, s^q_{ij}, at pressure and temperature of 0.328 kbar and -4.1°C, respectively, are found by substituting the c^q_{ij} terms of equation (3.10) into the stiffness matrix in equation (3.7) and then inverting to obtain the adiabatic compliance matrix. The results are as follows (in kbar^{-1}):

$$\begin{aligned} &s^q_{11} = 1.0401 \times 10^{-2} && s^q_{12} = -4.3406 \times 10^{-3} && s^q_{13} = -2.3740 \times 10^{-3} \\ &s^q_{33} = 8.5084 \times 10^{-3} && s^q_{44} = 3.3565 \times 10^{-2} \end{aligned} \tag{3.11}$$

To obtain components of the fourth-order adiabatic compliance tensor in the material frame, the following linear elastic relation is recalled between stress and tensorial strain:

$$\epsilon_{ij} = S^q_{ijkl}\sigma_{kl} \tag{3.12}$$

Comparison of matrix equation (3.8) and tensor relation (3.12) elucidates the following relations between the components s^q_{ij} and S^q_{ijkl}:

$$\begin{aligned} &S^q_{1111} = s^q_{11} && S^q_{1122} = s^q_{12} && S^q_{1133} = s^q_{13} \\ &S^q_{2211} = s^q_{12} && S^q_{2222} = s^q_{11} && S^q_{2233} = s^q_{13} \\ &S^q_{3311} = s^q_{13} && S^q_{3322} = s^q_{13} && S^q_{3333} = s^q_{33} \\ &S^q_{3223} = \frac{s^q_{44}}{4} && S^q_{3232} = \frac{s^q_{44}}{4} && S^q_{2323} = \frac{s^q_{44}}{4} && S^q_{2332} = \frac{s^q_{44}}{4} \\ &S^q_{1313} = \frac{s^q_{44}}{4} && S^q_{1331} = \frac{s^q_{44}}{4} && S^q_{3113} = \frac{s^q_{44}}{4} && S^q_{3131} = \frac{s^q_{44}}{4} \\ &S^q_{1212} = \frac{s^q_{11} - s^q_{12}}{2} && S^q_{1221} = \frac{s^q_{11} - s^q_{12}}{2} && S^q_{2112} = \frac{s^q_{11} - s^q_{12}}{2} && S^q_{2121} = \frac{s^q_{11} - s^q_{12}}{2} \end{aligned} \tag{3.13}$$

All other S^q_{ijkl}-values in the material frame are zero. The reader is referred to Nye (1957, p. 134) for the general relations between matrix and tensorial elastic moduli in compact form. Equations (3.13) are used to convert the compliances s^q_{ij}, listed in equations (3.11), into components of the fourth-order compliance tensor, S^q_{ijkl}, in the material frame. The last step in this process is to apply the adiabatic-to-isothermal correction of the compliance tensor for a temperature of -4.1°C. To do this, the following correction is used (Nye, 1957, p. 178):

$$S^q_{ijkl} - S^t_{ijkl} = -\alpha_{ij}\alpha_{kl}T/c_{0s} \tag{3.14}$$

where S^q_{ijkl} are components of the adiabatic compliance, S^t_{ijkl} are components of the isothermal compliance, T the absolute temperature, c_{0s} the specific heat capacity and α_{ij} the linear thermal expansion coefficient in the ij-direction. As stated on page 12, the thermal expansion properties of ice are approximated as isotropic. Therefore, the assignment $\alpha_{ij} \rightarrow \delta_{ij}\alpha_s$ is made. The value of α_s in the reference state is 53.0×10^{-6} K^{-1} (Table 2.1). The specific heat capacity c_{0s}, at the reference temperature 273.158 K, is 1.934×10^6 J m^{-3} K^{-1} (Lide, 2002). From this point on in the study, the stress units of elastic moduli are N m^{-2}. The components of the isothermal compliance tensor in the material frame, at a pressure and temperature of 3.28×10^8 N m^{-2} and -4.1°C, respectively, follow from equations (3.11), (3.13) and (3.14) in units of m^2 N^{-1}:

$$\begin{aligned}
&S^t_{1111} = S^t_{2222} = 1.0440 \times 10^{-10} \\
&S^t_{1122} = S^t_{2211} = -4.3016 \times 10^{-11} \\
&S^t_{1133} = S^t_{3311} = S^t_{2233} = S^t_{3322} = -2.3350 \times 10^{-11} \\
&S^t_{3333} = 8.5475 \times 10^{-11} \\
&S^t_{1313} = S^t_{1331} = S^t_{3113} = S^t_{3131} = 8.3913 \times 10^{-11} \\
&S^t_{1212} = S^t_{1221} = S^t_{2112} = S^t_{2121} = 7.3707 \times 10^{-11}
\end{aligned} \tag{3.15}$$

The strain ϵ'_{33} of the ice crystal is computed using equations (3.2), (3.4), (3.5), (3.6), (3.15) with the spherical coordinate θ varying from 0 to 90°. As stated earlier, the normal strain ϵ'_{33} is independent of spherical coordinates ϕ and α. These coordinates were therefore assigned arbitrary values which did not affect the results. The results are shown in Figure 3.4 for a pressure of unit magnitude. These results indicate that the ice crystal is 2% more compliant in a direction parallel to the c-axis (i.e., $\theta = 0°$) than directions normal to it (i.e., $\theta = 90°$). These results seem ironic considering that the compliance parallel to the c-axis, s_{33}, is 18% less than that orthogonal to it, s_{11} (see equation 3.11). However, because the magnitude of s^q_{12} is greater than that of s^q_{13}, the Poissonic effects acting orthogonal to the c-axis are larger

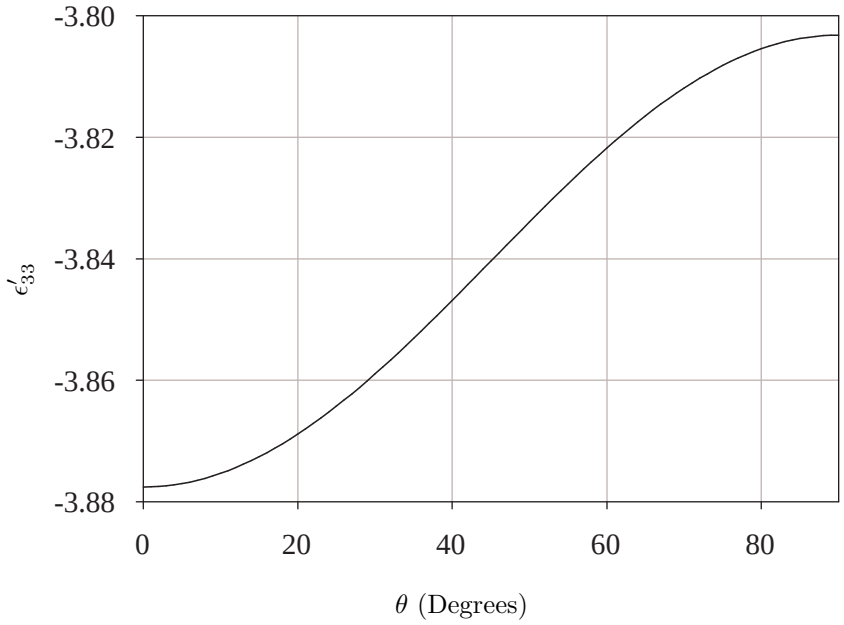

Figure 3.4: Computed strain ϵ'_{33} of an ice crystal, in units of 10^{-11}, as a function of c-axis angle θ under a hydrostatic stress of unit magnitude.

than those parallel to it. As a result, in hydrostatic stress conditions the strain parallel to the c-axis exceeds that orthogonal to it.

The maximum compliance of an ice crystal along the c-axis when stresses are hydrostatic has implications for stress inhomogeneities in high pressure, low deviatoric stress environments. These conditions tend to exist at great depths within ice sheets, where the pressures are much greater than shear stresses. These conditions also likely exist in the Lake Vostok accretion ice furthest removed from the grounded ice. If macroscopic stresses in polycrystalline ice are hydrostatic, then a crystal with a c-axis parallel to a grain boundary will be more compliant along the boundary than an adjacent crystal having a differently aligned c-axis. The resulting interference in strain would be accompanied by stress inhomogeneities, particularly near grain boundaries where interference tends to be localized. As the stress environment becomes increasingly deviatoric, this situation changes. Due to the relative ease with which ice crystals deform along the basal plane (McConnel, 1891; Glen and Perutz, 1954; Nakaya, 1958), crystals with a c-axis 45° to the maximum principle stress will be most compliant. This orientation places a crystal in an "easy glide" orientation which maximizes the shear stress resolved in the basal plane. Conversely, crystals having c-axes parallel to the principal stresses are said to be in "hard glide" orientations. The stresses and dynamic structural changes between ice crystals in easy and hard glide orientations have been simulated by Wilson and Marmo (1999) using numerical finite differencing techniques. In the next section, stress

concentrations between *bonded* ice crystals, having anisotropic elastic properties, is explored with use of the finite element method. Based on the results of the present section, stress concentrations are expected occur between ice crystals even when macroscopic stresses are hydrostatic.

Finite Element Elastic Two Blocks (ETB) Model

The previous section illustrated how the elastic compliance of a hydrostatically-loaded ice crystal varied with crystallographic orientation. Assuming linear elastic behavior in a hydrostatic environment at -4.1°C, the crystal was 2% more compliant parallel to the c-axis than orthogonal to it. In this section, a finite element (FE) model, implemented with ANSYS commercial software, is used to investigate the stress concentrations between two bonded, elastic ice crystals having misaligned c-axes. As no closed-form solutions are known to exist for this problem, the FE method is well suited. The Elastic Two Blocks (ETB) Model consists of a simple geometry in order to emphasize the effects of anisotropic material properties on stress concentrations in ice. The two ice crystals are modeled as bonded cubes of side length 0.5 m with linear elastic material properties (Figure 3.5).

Each crystal has its own set of material unit vectors $\mathbf{e_1}$, $\mathbf{e_2}$ and $\mathbf{e_3}$ defined along the local x, y and z axes, respectively. As in the last section, $\mathbf{e_3}$ is defined to be along the c-axis of the crystal. The *local frame* is fixed to the x, y, and z axes and is synonymous with the term *material frame* used in the last section. The global unit vectors $\mathbf{e_1'}$, $\mathbf{e_2'}$ and $\mathbf{e_3'}$ are fixed along the x′, y′ and z′ axes of the global frame. The c-axis of each crystal is oriented by determining suitable values of spherical coordinates θ and ϕ (Figure 3.3). The local frame orientations in ANSYS are specified by the three euler angles $THXY$, $THYZ$ and $THZX$.

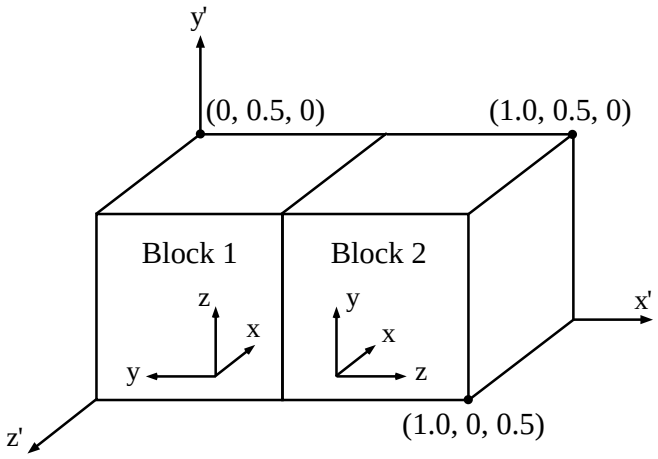

Figure 3.5: Crystal geometry of the finite element Elastic Two Blocks (ETB) Model. Each crystal cube has side length 0.5 m and anisotropic elastic properties of an ice crystal. The local and global axes are x, y, z, and x', y', z', respectively.

Before any rotations, the local and global frames are coincident. The local frame is first rotated by angle $THXY$ about the z axis. The sense of rotation follows the right hand rule, with thumb pointing along the positive (or negative) axis for a positive (or negative) rotation. The second rotation of the local frame is by angle $THYZ$ about the new x axis. The last rotation is by angle $THZX$ about the new y axis. Rotations are cumulative and order dependent. The relationships between spherical coordinates θ and ϕ and ANSYS parameters $THXY$, $THYZ$ and $THZX$ are as follows:

$$THXY = \phi - 270^\circ \qquad THYZ = \theta \qquad THZX = 0^\circ \tag{3.16}$$

The specification of spherical coordinates θ and ϕ to orient the crystal c-axis is considered to be more convenient and easier to visualize than that of ANSYS euler angles $THXY$, $THYZ$ and $THZX$. Therefore, the method used is to first determine a suitable value of θ and ϕ for the c-axis orientation of each crystal, and then use relations (3.16) to calculate the input parameters for ANSYS. Henceforth, the local frame of crystal i will be specified by spherical coordinates θ_i and ϕ_i. For example, the c-axis orientation of Block 1 in the ETB Model is described by spherical coordinates θ_1 and ϕ_1, and that for Block 2 is described by coordinates θ_2 and ϕ_2. For the ETB Model, the following c-axis spherical coordinates are used: $\theta_1 = 90^\circ$, $\phi_1 = 90^\circ$, $\theta_2 = 90^\circ$ and $\phi_2 = 0^\circ$. The resulting c-axis orientations are illustrated in Figure 3.5 and are defined to be along the local z directions.

The model uses 3D brick elements (SOLID95) having quadratic displacement freedom and orthotropic elastic properties specified with respect to the local frame. The orthotropic compliance matrix in ANSYS is defined in the following context (ANSYS Theory Reference, equation 2.4):

$$\begin{Bmatrix} \epsilon_{11} \\ \epsilon_{22} \\ \epsilon_{33} \\ 2\epsilon_{23} \\ 2\epsilon_{13} \\ 2\epsilon_{12} \end{Bmatrix} = \begin{bmatrix} 1/E_x & -\nu_{xy}/E_x & -\nu_{xz}/E_x & 0 & 0 & 0 \\ -\nu_{yx}/E_y & 1/E_y & -\nu_{yz}/E_y & 0 & 0 & 0 \\ -\nu_{zx}/E_z & -\nu_{zy}/E_z & 1/E_z & 0 & 0 & 0 \\ 0 & 0 & 0 & 1/G_{yz} & 0 & 0 \\ 0 & 0 & 0 & 0 & 1/G_{xz} & 0 \\ 0 & 0 & 0 & 0 & 0 & 1/G_{xy} \end{bmatrix} \begin{Bmatrix} \sigma_{11} \\ \sigma_{22} \\ \sigma_{33} \\ \sigma_{23} \\ \sigma_{13} \\ \sigma_{12} \end{Bmatrix} \tag{3.17}$$

Indices 1, 2, 3 correspond to the x, y, and z directions, respectively, of the local frame. The isothermal

orthotropic moduli are determined by comparing the compliance matrices in equations (3.8) and (3.17):

$$\begin{aligned} E_x &= \frac{1}{s_{11}^t} & E_y &= \frac{1}{s_{11}^t} & E_z &= \frac{1}{s_{33}^t} \\ \nu_{xy} &= -\frac{s_{12}^t}{s_{11}^t} & \nu_{yz} &= -\frac{s_{13}^t}{s_{11}^t} & \nu_{xz} &= -\frac{s_{13}^t}{s_{11}^t} \\ G_{xy} &= \frac{1}{2(s_{11}^t - s_{12}^t)} & G_{yz} &= \frac{1}{s_{44}^t} & G_{yz} &= \frac{1}{s_{44}^t} \end{aligned} \tag{3.18}$$

The parameters ν_{xy}, ν_{yz} and ν_{xz} are known as the *major Poisson's ratios* and are labelled as $PRXY$, $PRYZ$ and $PRXZ$, respectively, in ANSYS.

The edge of each cube-shaped crystal is divided into 16 elements. The model boundary conditions consist of a uniform pressure of 32.8 MPa on all external surfaces and minimum displacement constraints to prevent rigid body translation and rotation. These displacement constraints amount to holding fixed a material point in the model and preventing rigid body rotations about that point. The compliance values have been corrected for a temperature and pressure of -4.1°C and 32.8 MPa, respectively, using the method demonstrated on pages 33-36. This pressure and temperature approximates conditions near the vertical center of the southern Lake Vostok accretion ice at a depth of 3650 m.

Consider the compliance of each block along its boundary (i.e., x′ = 0.25 m plane of model), referred to as the crystal boundary. Based on the analysis in the last section, Block 1 should be more compliant than Block 2 along the y′ direction, and both blocks should be equally compliant along the z′ direction. Therefore, one may suspect that the resulting differences in strain along the crystal boundary would induce localized sinistral (i.e., left-handed) $\sigma_{1'2'}$ shear stress (primed stresses reference global frame) near the top (i.e., y′ = 0.5 m) of the crystal boundary, and dextral $\sigma_{1'2'}$ shear stress near the bottom of the crystal boundary. This suspicion is confirmed by the FE model results of σ_{23} shear stress (Figure 3.6). The calculated $\sigma_{1'3'}$ shear stress is about zero, which is consistent with both blocks being equally compliant along the global z′ direction under hydrostatic stress.

The shear stress σ_{23} represents that resolved along the basal plane of each crystal. The maximum calculated σ_{23}-value is almost 0.1 MPa, at least 5 times greater than the yield stress of single ice crystals (Steinemann, 1954; Wakahama, 1967). These results suggest that the hydrostatic stress in the Vostok accretion ice is great enough to cause plastic deformation in ice crystals as a result of elastic anisotropy. However, the ETB Model's geometry was a bit too simplistic to draw firmer conclusions. In the next section, a more elaborate FE model, consisting of numerous crystals and triple junctions, will further explore the possible stress concentrations between bonded elastic ice crystals in the Vostok accretion ice.

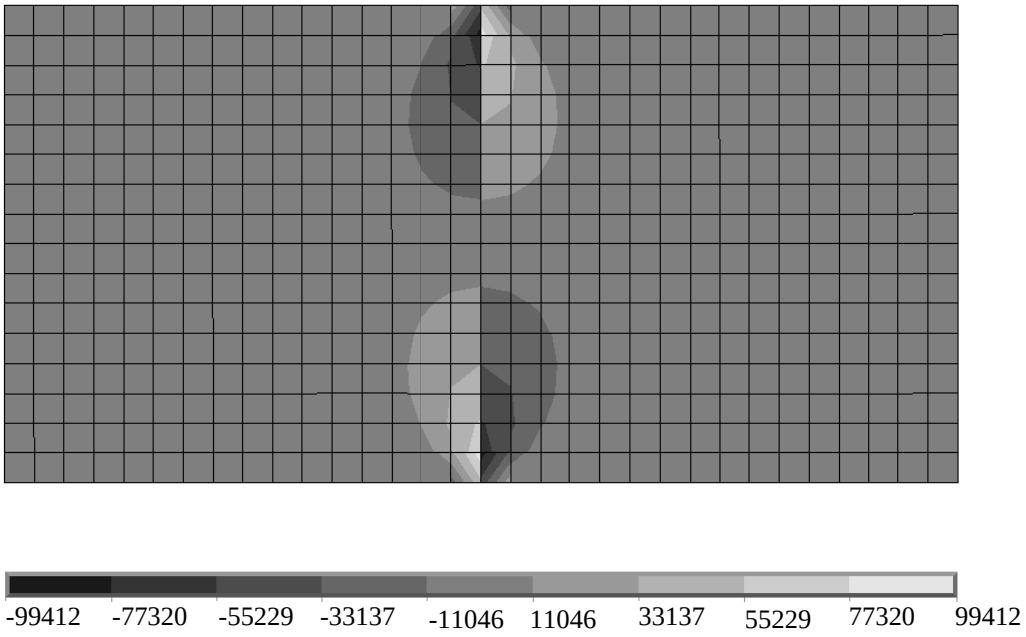

Figure 3.6: ANSYS contour plot of local element σ_{23} shear stress (N m^{-2}) calculated from the finite element ETB Model. This shear stress represents that resolved along the basal plane of each crystal. The section is along the global z$'$ = 0.25 m plane.

Finite Element Elastic Triple Junction (ETJ) Model

To investigate more rigorously the microscopic (defined on page 3) stresses in crystals of the Vostok accretion ice, the Elastic Triple Junction (ETJ) Model has been developed using ANSYS software. The baseline material assumption is that crystals are well bonded (no sliding allowed) and have linear elastic material properties. A submodeling procedure is used to essentially *focus in* on stresses in a network of numerous crystals. In this routine, the nodal displacements from a coarse mesh model (Figure 3.7a), consisting of crystals having idealized geometries of hexagonal prisms, are interpolated onto the boundaries of a fine mesh submodel (Figure 3.7b). Following Saint-Venant's principle, the accuracy of the submodel increases as the outer *cut boundaries* become increasingly distant from the region of scrutiny. Therefore, the primary region of interest in the submodel is the central triple junction and grain boundary vicinity.

Four different alternating local frames are used to represent the different crystallographic c-axis orientations. As in the ETB Model, the orientation of local frame i, where i ranges from 1 to 4 (Figure 3.7), is specified by spherical coordinates θ_i and ϕ_i. The local frames are randomly oriented, with θ_i and ϕ_i taking on random values of 0 to 90° and 0 to 360°, respectively. These random values are generated by ANSYS, implemented in the model, and exported to a data file. The geometry of each crystal is represented by a hexagonal prism of diameter and depth d_g (Figure 3.7). A d_g-value of 0.5 m is used to represent an ap-

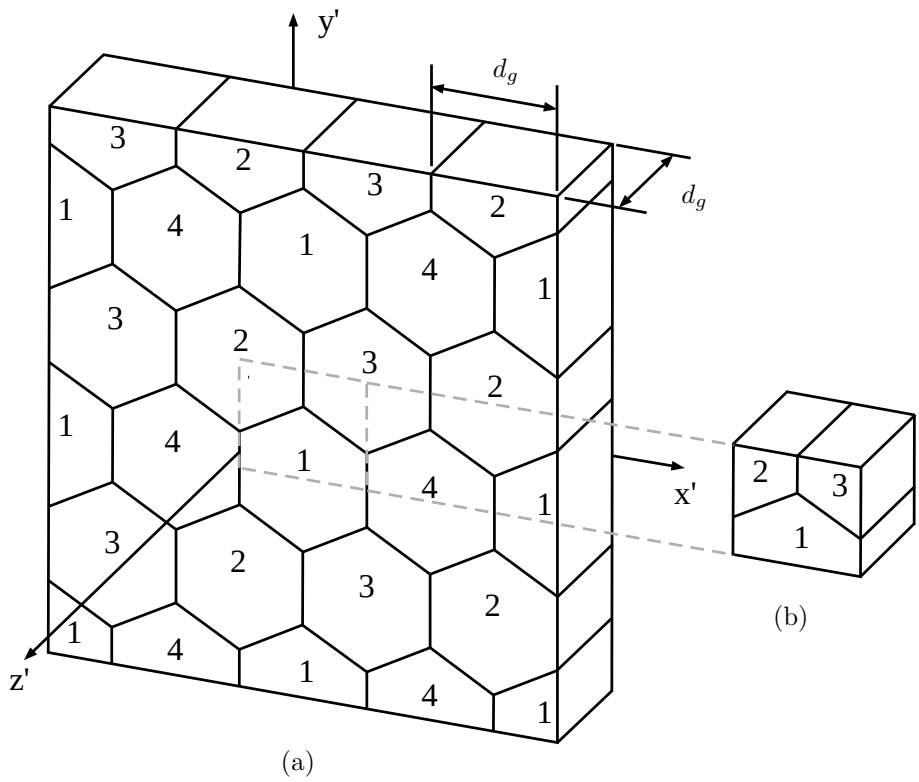

Figure 3.7: Volumes, dimensions and local frames of the (a) coarse mesh model and (b) fine mesh submodel of the finite element Elastic Triple Junction (ETJ) Model. Each of the four alternating local frames are identified by the number i, ranging from 1 to 4. Spherical coordinates θ_i and ϕ_i describe the c-axis orientation of local frame i ($i = 1$ to 4). A crystal dimension d_g of 0.5 m is chosen to reflect typical crystal sizes in the Vostok accretion ice. The hexagon pattern shown represents geometries of grain boundaries and not crystallographic a-axes.

proximate median crystal size in the Vostok accretion ice (Jouzel et al., 1999). More detailed information on crystal shapes and aspect ratios in the accretion ice are not available for use in this study.

A $x'y'$ section view of the submodel geometry is shown in Figure 3.8. The triple junction of the submodel is located at $x' = 0.25$ m, $y' = 0.25$ m. The stress results of the ETJ Model are selected from the centroids of elements having nodes between $x' = 0.125$ and 0.375 m in the $z' = 0.25$ m plane, away from the cut boundaries of the submodel (Figure 3.8).

The advantage of the ETJ Model over the previous ETB Model is that the interfering effects of crystals surrounding the submodel are captured. The boundary displacements of the ETB Model were not constrained by the deformation of neighboring crystals. It is unclear what role these unconstrained displacements had on the localization of shear stresses near the boundary (Figure 3.6). The crystals of the ETJ Model have the least interference from neighbors along the external $z' = 0$ and 0.5 m surfaces because only one layer of crystals in the z' direction is included. In order to examine the effects of increased constraints along these two surfaces, additional analyses are carried out that couple the nodal

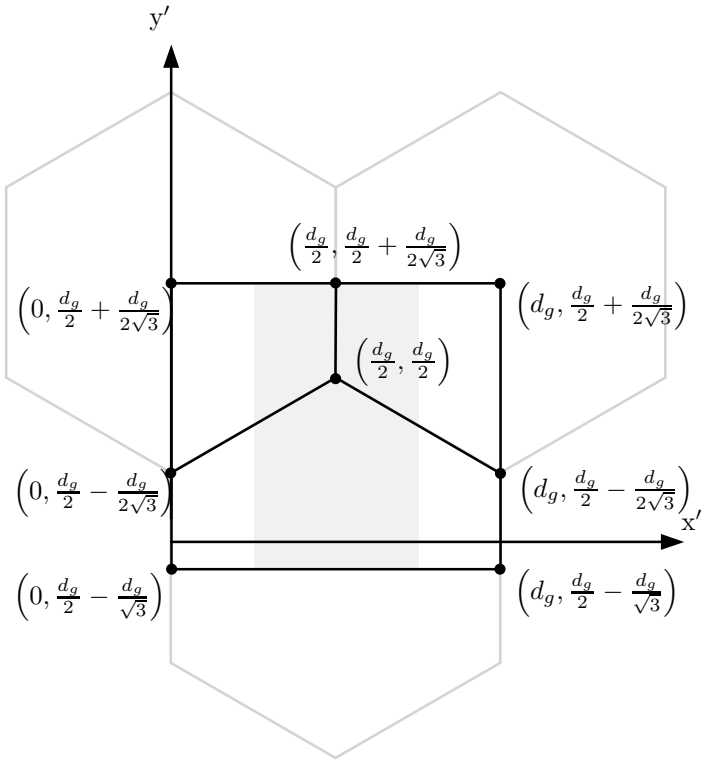

Figure 3.8: Section view of the ETJ submodel geometry along the x′y′ plane. Crystal dimension d_g= 0.5 m. Stress results are selected from centroids of elements having nodes inside the shaded region, between x′= 0.125 and 0.375 m.

z′ displacements on the z′ = 0 and 0.5 m surfaces. These analyses are referred to as *coupled node* to distinguish them from the *non-coupled node* analyses which do not enforce nodal coupling. Restated, the coupled node analyses set equal the nodal z-displacements on the z = 0 m face of the model, as well as the nodal z-displacements on the z = 0.5 m face of the model. These analyses are carried out in an attempt to qualitatively capture the greater constraining effects of more crystals in the model z′ direction.

Each ice crystal in the coarse model is divided into six elements across the width and three elements along the depth (Figure 3.9a). The element density of the submodel is scaled with parameters FM1 (Fine Mesh 1) and FM2. Parameter FM1 scales the mesh density in the x′ and y′ directions, and parameter FM2 specifies the number of element divisions in the z′ direction. For illustration purposes, FM1 and FM2 settings of 6 and 5, respectively, correspond to the mesh density shown in Figure 3.9. The number of elements along the segment marked "2FM1" in Figure 3.9 is equal to twice the value of FM1 (e.g., 12 for a FM1 setting of 6). The ETJ Model uses FM1- and FM2-values of 6 and 7, respectively. Thus, the mesh of the ETJ Model looks like that shown in Figure 3.9, but with two more element divisions along the depth (z′ direction). Geometric lines in the x′y′ plane are meshed using a *spacing ratio* of two. This accounts for the variations in element dimensions along the x′y′ plane shown in Figure 3.9. Later, a mesh

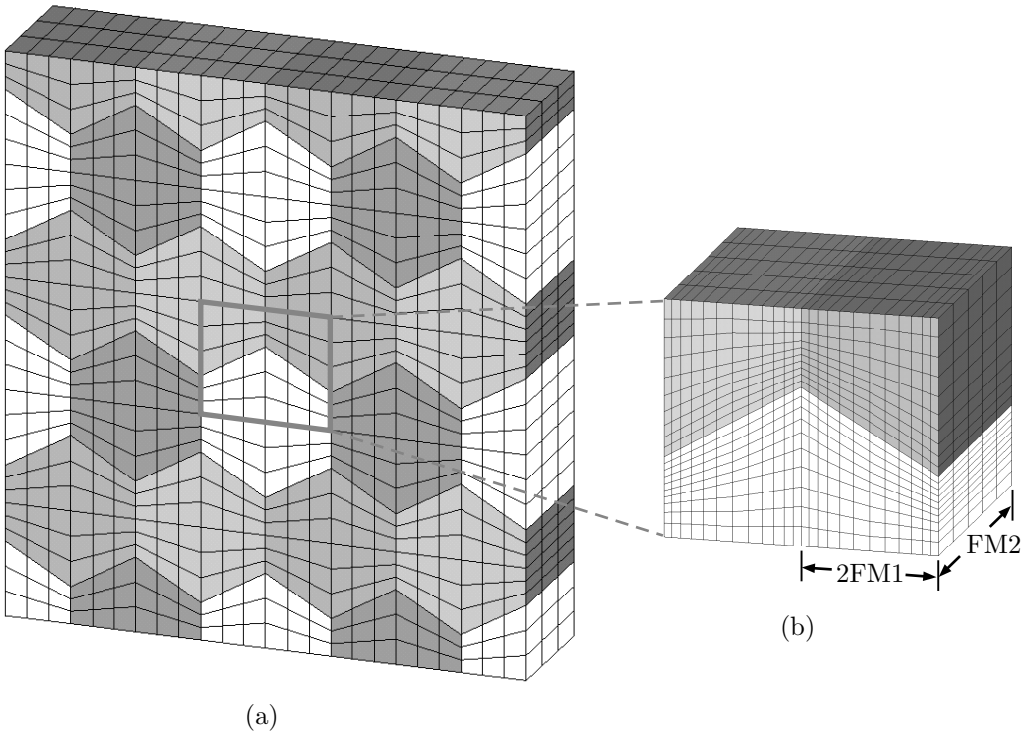

Figure 3.9: Element mesh for the (a) coarse model and (b) fine mesh submodel of the ETJ Model. The submodel mesh density is scaled with parameters FM1 and FM2, having values 6 and 5, respectively, for the mesh shown. FM2 is the number of elements along the depth of the model. The number of elements along the segment labeled "2FM1" above is twice the value of FM1.

convergence study is carried out in order to compare the sensitivity of stress results to the settings of parameters FM1 and FM2.

The boundary conditions of the coarse model consist of a uniform pressure on all external surfaces and displacement constraints to prevent rigid body rotation and translation. These displacements essentially consist of pinning a node and preventing rigid body rotations about that node. The pressure and temperature are set to 32.8 MPa and -4.1°C, respectively, to simulate conditions near the vertical center of the southern Vostok accretion ice at a depth of 3650 m. The orthotropic elastic constants are adjusted to isothermal values following the procedure demonstrated on pages 34-36. The model uses 20-node quadratic brick elements (SOLID186).

In this application of the ETJ Model, 100 coupled node and 100 non-coupled node analyses are carried out. Each of the 100 analyses use a different set of c-axis orientations. The hydrostatic stresses, σ_h, and shear stresses resolved in the basal plane, σ_b, are computed as follows:

$$\begin{aligned} \sigma_h &= -(\sigma_{11} + \sigma_{22} + \sigma_{33})/3 \\ \sigma_b &= \sqrt{\sigma_{13}^2 + \sigma_{23}^2} \end{aligned} \tag{3.19}$$

Post-processing after each model execution consists of recording the randomly generated spherical coordinates θ_i and ϕ_i ($i = 1$ to 4), which describe the c-axis orientations for each local frame (Figure 3.7), and the maximum value of σ_h and σ_b at the centroids of elements with nodes in the z′= 0.25 m plane of the submodel, located between x′ = 0.125 and 0.375 m. Rather than use model execution numbers 1 to 100, each representing a different set of c-axis orientations, for the abscissae of data plots, a more physically significant parameter, σ_ξ, is introduced. This parameter is a measure of the overall degree of c-axis misalignment in the submodel, and is introduced to seek patterns between stress extrema and c-axis orientations. ξ_{ij} is defined as the angle, in degrees, between the c-axis of crystal i and adjacent grain boundary j in the submodel. Each of the three crystals in the shaded region of Figure 3.8 have two grain boundaries between x′= 0.125 and 0.375 m. The $j = 1$ grain boundary of crystal i is defined to be that encountered in a counterclockwise rotation as viewed from the positive z′ direction, and the $j = 2$ grain boundary of crystal i is defined to be that encountered in a counterclockwise rotation. The *c-axis misalignment parameter* σ_ξ is defined as the standard deviation of the six different ξ_{ij}-values of each model execution. σ_ξ is defined as follows:

$$\sigma_\xi = \sqrt{\frac{1}{5}\sum_{i=1}^{3}\sum_{j=1}^{2}\left(\xi_{ij} - \overline{\xi}\right)^2} \tag{3.20}$$

where $\overline{\xi}$ is the average of the six different ξ_{ij}-values. Local frame 4 is not considered in the calculation of the c-axis misalignment parameter since crystals oriented by this frame are removed from the region of scrutiny (i.e., x′ = 0.125 to 0.375 m). The 100 different σ_ξ-values in this analysis are used as the abscissae for plotting the maximum shear stresses and hydrostatic pressures. In the extreme case where all c-axes are parallel, $\sigma_\xi \to 0$. The other extreme case occurred in the ETB Model, where the c-axes of two adjacent crystals were parallel and normal to the boundary of separation. For this case, $\sigma_\xi \approx 64°$. The values of σ_ξ in the ETJ Model are expected to lie somewhere between 0 and 64°.

The maximum computed basal plane shear stress, $\sigma_{b,\max}$, from the 100 coupled node and 100 non-coupled node analyses are plotted against the parameter σ_ξ in Figure 3.10. The $\sigma_{b,\max}$-values in both the coupled node and non-coupled node analyses form very similar clusters, ranging from about 20 to 90 kPa. There is no obvious trend between the $\sigma_{b,\max}$- and σ_ξ-values. The average $\sigma_{b,\max}$-value in the coupled node and non-coupled node analyses are 49.5 and 52.3 kPa, respectively. Since the stresses are evaluated at the centroid locations of quadratic elements, the data plotted in Figure 3.10 represent the average value for the corresponding element. For illustrative purposes, a sample ANSYS contour plot of σ_b is shown in Figure 3.11 for the c-axis spherical coordinate set $\{\theta_1, \phi_1, \theta_2, \phi_2, \theta_3, \phi_3, \theta_4, \phi_4\} = \{90°, 0°, 90°, 120°, 90°, 60°, 90°, 0°\}$. For convenience, all θ_i-values were set to zero, resulting in c-axes all aligned in the

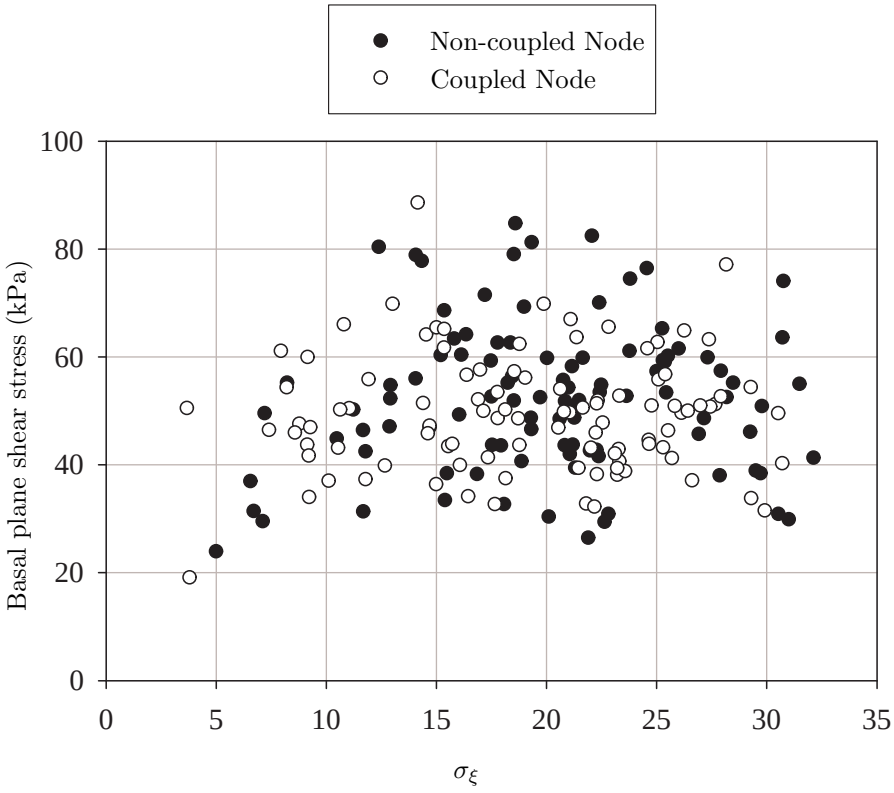

Figure 3.10: Plot of maximum calculated values in basal plane shear stress, σ_b (kPa), verses c-axis misalignment parameter, σ_ξ, from the ETJ Model. Stresses chosen from centroids of elements with nodes in the bisecting z′ = 0.25 m plane of the submodel, located between x′= 0.125 and 0.375 m. A uniform pressure of 32.8 MPa was applied to the boundary of the model. Elastic constants were corrected to a temperature of -4.1°C.

plane of Figure 3.11. As indicated by the results of the ETB Model, all crystals with c-axis orientations described by $\theta = 90°$ have equal compliance in the z′ direction. Because each crystal deforms equally in the z′ direction, the local shear stresses σ_{12} are negligible. Therefore, $\sigma_b \approx \sigma_{13}$, the latter of which was plotted in Figure 3.11.

The maximum computed hydrostatic pressures, $\sigma_{h,\max}$, range from 32.79 to 32.92 MPa, very small departures from the applied pressure of 32.80 MPa (Figure 3.12). The coupled node and the non-coupled node analyses produced very similar $\sigma_{h,\max}$-values. Interestingly, there appears to be a weak visual trend between $\sigma_{h,\max}$ and the c-axis misalignment parameter, σ_ξ, but not enough of one to justify a statistical analysis. The σ_ξ parameter will no longer be considered in this study, mainly because later inelastic models use boundary conditions that include deviatoric stress. The σ_ξ parameter, as originally defined, is not suitable when the macroscopic stress is deviatoric because it fails to take into account the principal stress orientations.

The maximum $\sigma_{h,\max}$-values are only about 0.4% greater than the applied pressure at the model

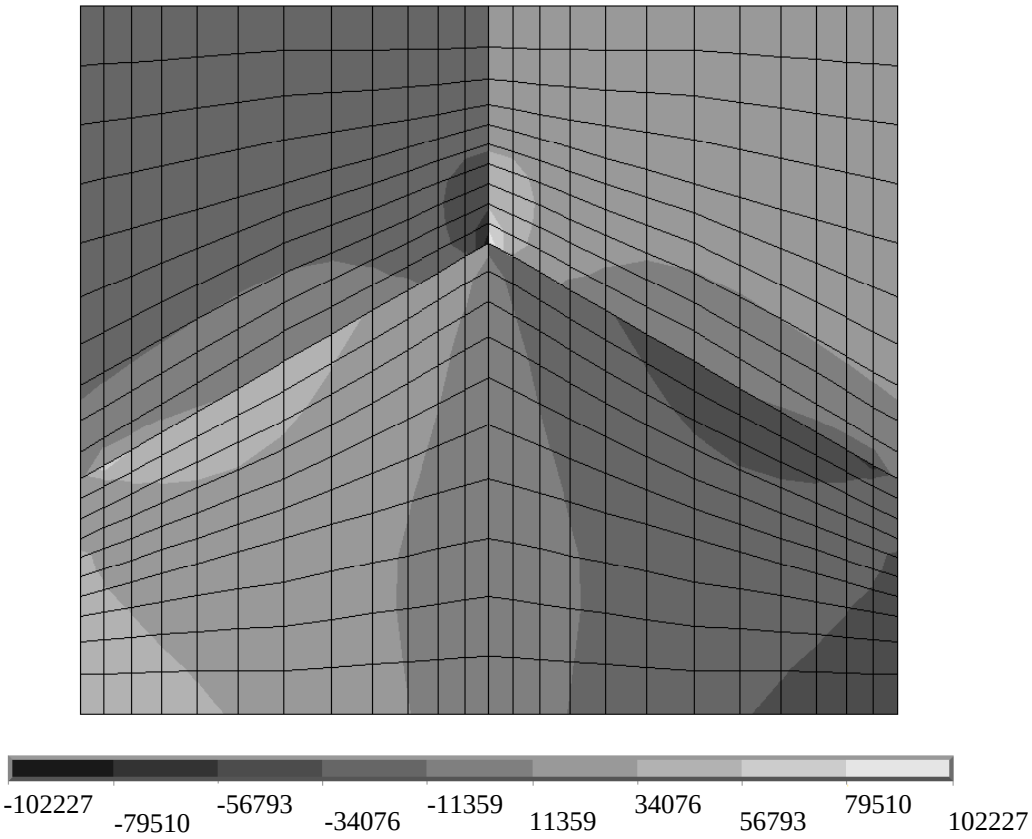

Figure 3.11: ANSYS contour plot of basal plane shear stress, σ_b (N m^{-2}), calculated in the x$'$ = 0.25 m plane of ETJ submodel. The c-axis coordinates were $\{\theta_1, \phi_1, \theta_2, \phi_2, \theta_3, \phi_3, \theta_4, \phi_4\}$= {90°, 0°, 90°, 120°, 90°, 60°, 90°, 0°}. A uniform pressure of 32.8 MPa was applied to the boundary of the model. Elastic constants were corrected to a temperature of -4.1°C.

boundaries. Based on an approximation from the Clausius-Clapeyron equation (equation 2.1), this slight pressure concentration would result in a melting temperature depression of only about 0.01°C. However, it should be noted that the smallest element sizes in the model are considerably larger than the proposed dimensions of liquid water habitats in the Vostok accretion ice (Price, 2000). More on this in the following paragraph. Smaller element sizes would better resolve pressure concentrations at the small scales of potential liquid water habitats in the accretion ice. However, element sizes at these scales in a three-dimensional model seem computationally impractical.

The meshing process of the FE models involve specification of element divisions along different geometrical lines. A useful relationship for element lengths along any meshed line is the following:

$$\delta L_{e,\min} = \frac{L_e \left[1 - S_e^{\frac{1}{Ne-1}}\right]}{1 - S_e^{\frac{Ne}{Ne-1}}} \tag{3.21}$$

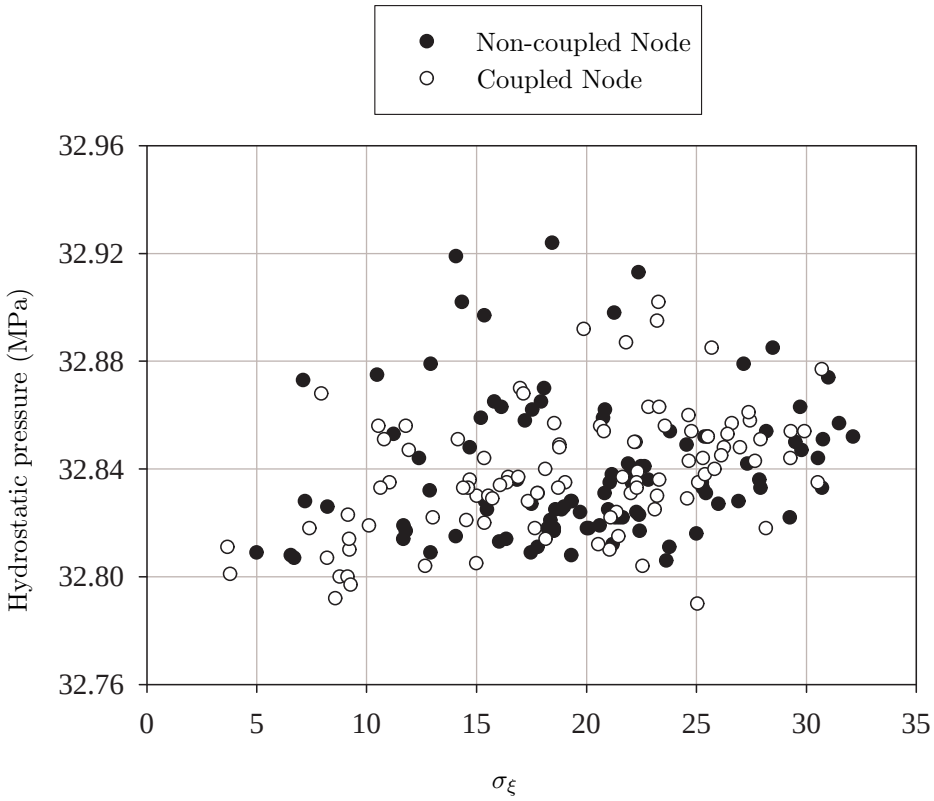

Figure 3.12: Plot of maximum calculated hydrostatic pressure, $\sigma_{h,\max}$ (MPa), verses c-axis misalignment parameter, σ_ξ, from the ETJ submodel. Stresses were evaluated at element centroids in the $z' =$ 0.25 m plane of the submodel, between $x' = 0.125$ and 0.375 m. A uniform pressure of 32.8 MPa was applied to the boundary of the model. Elastic constants were corrected to a temperature of -4.1°C.

where L_e is the length of the meshed line, $\delta L_{e,\min}$ is the minimum element length along the meshed line, S_e the spacing ratio (taken to be greater than 1), and N_e the number of element divisions along the meshed line. Equation (3.21) is valid only for $S_e > 1$; for $S_e = 1$, the minimum element length $\delta L_{e,\min}$ is simply L_e/N_e. The mesh of the ETJ Model uses a S_e-value of 2 with element dimensions becoming finer toward the triple junction. From equation (3.21), the smallest element edge length, $\delta L_{e,\min}$, was about 1 cm and adjacent to the triple junction. This dimension is an order of magnitude larger than water vein sizes predicted earlier in this study and by Price (2000), and is thus clearly not adequate. It should be noted that preliminary model analyses indicated that pressure concentrations (i.e., $\sigma_{h,\max}$) generally increase with mesh density.

The greatest σ_b stress calculated by the ETJ Model is about 0.1 MPa (Figures 3.10 and 3.11). This basal plane shear stress is five times greater than values experimentally shown to cause plastic deformation in single ice crystals (Steinemann, 1954; Wakahama, 1967). These findings indicate that ice crystals in the Vostok accretion ice have undergone at least some plastic deformation due to elastic anisotropy. If

deviatoric stresses were included in the boundary conditions of the ETJ Model, the calculated shear stresses would be even greater. Such macroscopic deviatoric stresses may occur near the bedrock margins of Lake Vostok, where the transition from grounded to ungrounded ice is associated with abrupt changes in flow patterns (e.g., thinning of ice layers, ice flow divergence). Therefore, an inelastic material model is necessary to further explore the possible microscopic stresses in the Vostok accretion ice. The inelasticity of ice crystals is the subject of the next chapter, with a goal of developing a suitable inelastic material model.

X-ray dislocation data on samples from the Vostok accretion ice corroborate findings of the ETJ Model. Accretion ice samples from varying depths, between 3540 and 3610 m, were irradiated with white-beam X-rays at beamline X-19 of the National Synchroton Light Source at Brookhaven Laboratory (Adams and Brown, unpublished data). The scattered X-rays provided data about the spatial distribution of dislocations in the ice samples. The samples were scanned over their the basal (0001) planes with diffraction vectors of either $< 10\bar{1}0 >$ or $< 11\bar{2}0 >$ (see Figure 3.1). The crystallographic $< 10\bar{1}0 >$ directions are normal to the prism planes. The dislocations are delineated by the numerous fine dark lines in the topographs (Figure 3.13). To investigate the degree of plastic deformation in the Vostok accretion ice samples, the dislocation densities were estimated using the counting technique of Smith and Guttman (1953), as described in Ham (1961) and Hirsch et al. (1965, p. 422). The method consists of drawing measured, randomly-oriented lines on the X-ray topos and counting their intersections with dislocations. The dislocation length per unit volume, Λ, is then given by the following relation:

$$\Lambda = \frac{2N_d}{L_d} t_i \tag{3.22}$$

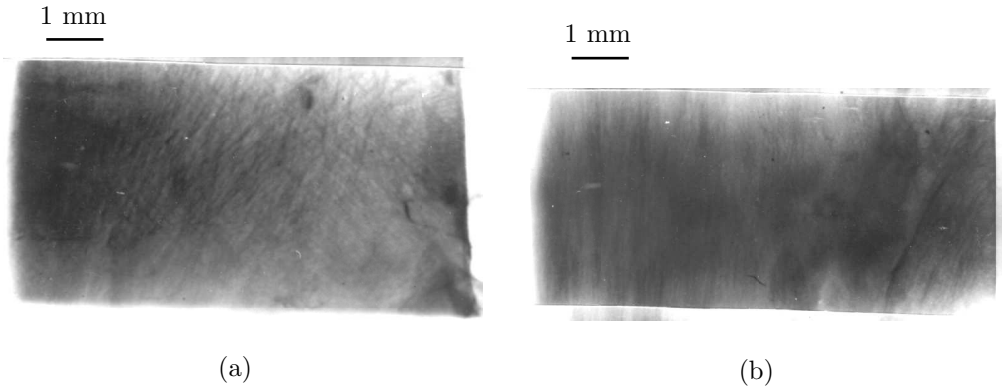

Figure 3.13: Laue patterns from X-ray dislocation topographs of Vostok accretion ice, depths (a) 3566 m and (b) 3575 m. Samples scanned over the basal (0001) planes with diffraction vectors of $<10\bar{1}0>$ in the plane of the images shown.

Where N_d is the number of dislocations intersecting the line of length L_d, and t_i is the sample thickness. Schoeck (1962) has pointed out that, for practical purposes, a factor of two difference exists between *the number of dislocations intersecting a unit area* and the value of Λ. However, this discrepancy will not be further considered for two reasons: the literature on ice tends not to describe dislocation counting techniques, and order of magnitude estimates are sought in this study. The dislocation counting in the Vostok X-ray topos was limited to depths 3566 and 3575 m, in accretion ice-1, due to limitations in optical resolution. The estimated minimum Λ-values were $1(\pm 0.2) \times 10^7$ m^{-2}. The typical occurrences of dark, patchy regions in the Laue patterns likely contained unresolvable, and therefore uncounted, dislocation traces. Cullen and Baker (2002) reported dislocation densities in a Vostok accretion ice sample from depth 3550 m, containing three grain boundaries and a triple junction, of between 10^7 m^{-2} and an unresolvably high value ($> 10^{10}$ m^{-2}). This dislocation density is greater than those estimated in the present study for possibly two reasons: (1) the ice sample analyzed by Cullen and Baker contained a triple junction, where stress concentrations associated with anisotropy would likely be relatively high (e.g., Figure 3.11), and (2) the limited resolution of the X-ray topos in this study precluded the observation of the higher actual dislocation densities.

The estimated dislocation densities in Vostok accretion ice samples 3566 and 3575 m are higher than those reported in literature for ice crystals grown in quiescent laboratory conditions. According to Cullen and Baker (2002), Liu (2002) has grown laboratory ice with dislocation densities less than 10^5 m^{-2}. The Improved Bridgman method has been used to grow high quality single ice crystals with dislocation densities of about 10^6 m^{-2} (Oguro, 1988). Based on reports from Cullen and Baker (2002) and interpretations of X-ray topos in the present study, samples of the Vostok accretion ice have dislocation densities ranging from 10^7 to 10^{10} m^{-2}, two orders of magnitude higher than some reported values for laboratory grown ice (10^5-10^6 m^{-2}). The Vostok accretion ice is freezing at rates of centimeters per year (Kwok et al., 2000; Bell et al., 2002), much slower than typical laboratory growth rates. Therefore, the Vostok accretion ice would seemingly contain fewer grown-in dislocations than laboratory ice. These findings suggest that the Vostok accretion ice samples have undergone some degree of plastic deformation. This conclusion is consistent with results of the finite element ETJ Model, which simulated basal plane shear stresses as high as 0.1 MPa, a value five times greater than shear stresses known to cause plastic deformation in single ice crystals. On the other hand, Montagnat et al. (2001) concluded from diffraction widths of X-ray patterns that the Vostok accretion ice was "non-plastically deforming." A plausible scenario consistent with all of these findings is that stress relaxation, via inelastic processes, has occurred in crystals of the accretion ice, but that large-scale plastic deformation leading to highly distorted lattices has not occurred. Or, if large-scale plastic deformation has occurred, it has been overprinted by the annealing effects of

diffusional creep. Terms "non-plastically deforming" and "large-scale" are not quantitative and therefore leave considerable room for interpretation.

Mesh Convergence Study of Finite Element ETJ Model

Because of the FE numerical method of the ETJ model, a certain amount of error is attributed to mesh discretization. Convergence theorems of the FE method are global in nature. The *energy error*, a scalar measure of the total error in the model, converges to zero only as the maximum element size approaches zero (Burnett, 1987, p. 321). The discretization error of the ETJ model is estimated by comparing the differences in element stress results for three different submodel meshes. Each mesh is identified by the number 'n' ranging from 1 to 3. The calculated basal plane shear stresses, σ_b, for each mesh are interpolated onto predefined paths passing the interior of the ETJ submodel for four different, randomly-generated spherical coordinate sets of θ_i and ϕ_i describing the c-axis orientations (Table 3.1). The predefined paths follow the x′ axis, between x′= 0.125 and 0.375 m (i.e., Figure 3.8), at central location z′ = 0.25 m. The y′ position of each path is determined from the results of the model with the n = 2 mesh. The n = 1, 2 and 3 meshes use (FM1, FM2) settings of (3, 3), (6, 7) and (12, 15), respectively (see page 43). Based on equation (3.21), and the spacing ratio, S_e, of 2 in the x′y′ plane and 1 in the z′ direction, the ratios of *maximum* element sizes for the n = 1, 2, 3 meshes are 5:2:1, respectively, and ratios of the *minimum* element sizes are 4:2:1. Therefore, each successive mesh refinement represents a factor of two reduction in element sizes. The mesh of the coarse model is held fixed as shown in Figure 3.9. The path plots of calculated σ_b-values are shown in Figure 3.14.

The path y′-positions are close to the central triple junction at y′= 0.25 m and away from the cut boundary y′-faces of the submodel. The FE stress results converged rapidly with mesh refinement, as indicated by the small differences in calculated σ_b-values (Figure 3.14). This is partly due to the use of quadratic elements, which are known to converge faster than linear elements with mesh refinement. For the four c-axis spherical coordinate sets (a)-(d), the σ_b-values increase toward the central triple junction.

Set	θ_1	ϕ_1	θ_2	ϕ_2	θ_3	ϕ_3	θ_4	ϕ_4	y′
(a)	32°	265°	86°	275°	78°	18°	17°	198°	0.252 m
(b)	82°	302°	17°	225°	42°	327°	50°	134°	0.238 m
(c)	13°	337°	35°	326°	7°	252°	55°	195°	0.252 m
(d)	32°	239°	30°	132°	62°	352°	34°	3°	0.252 m

Table 3.1: Crystal c-axis spherical coordinates and path y′ locations for the mesh convergence study of the ETJ model. Sets (a)-(d) above correspond to σ_b plots (a)-(d) in Figure 3.14. Paths follow the indicated y′-values, each corresponding to the occurrence of $\sigma_{b,\max}$ calculated from the n = 2 intermediate mesh model.

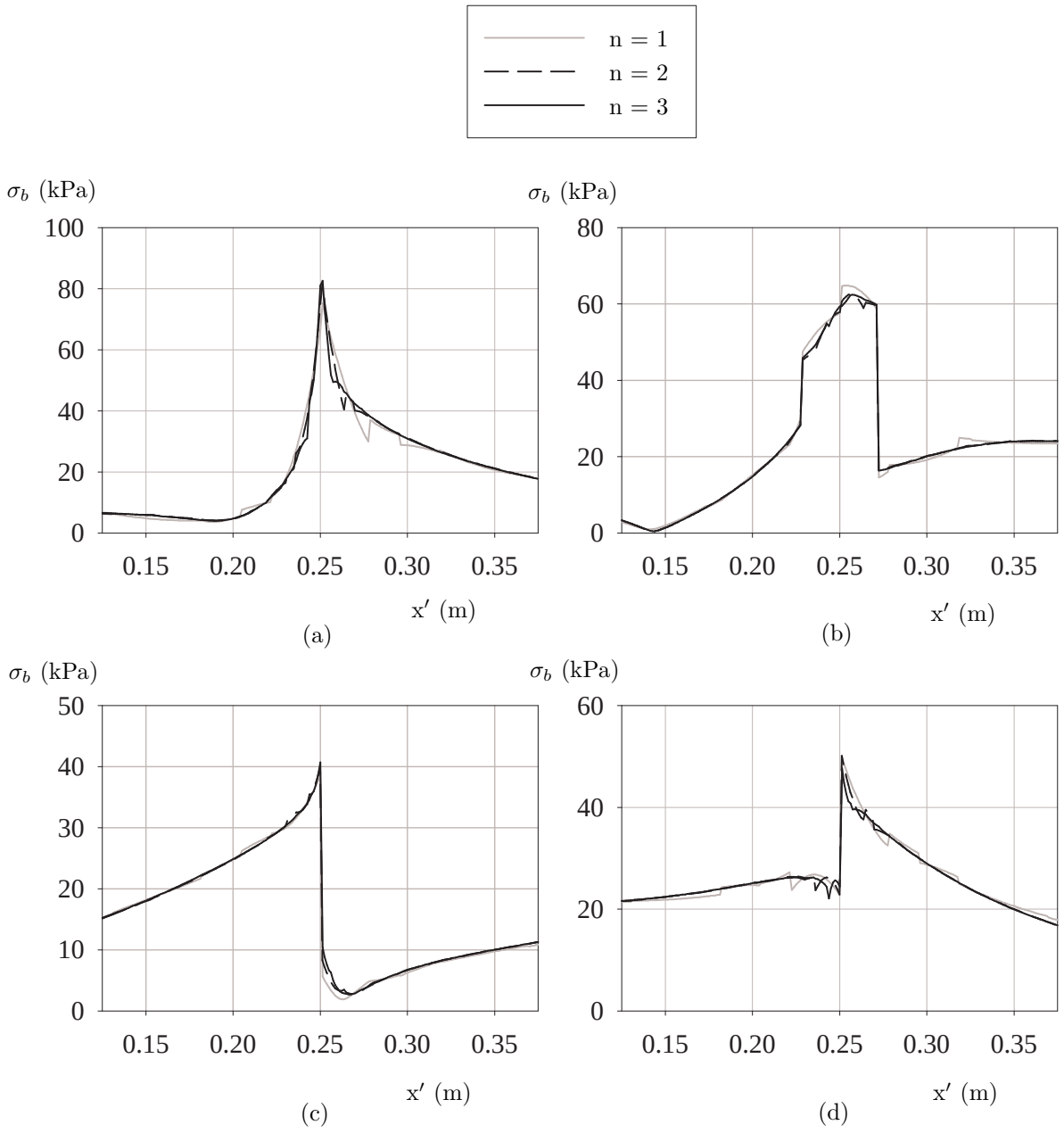

Figure 3.14: Path plots of calculated σ_b-values for three meshes (n = 1 to 3), and four randomly-generated c-axis coordinate sets (a)-(d), from the mesh convergence study of the ETJ Model. Paths are between x′ = 0.125 and 0.375 m, in the bisecting z′ = 0.25 m plane of the ITJ submodel. The spherical coordinates for sets (a)-(d) are listed in Table 3.1. The submodel mesh parameters (FM1, FM2) for the n = 1, 2 and 3 meshes are (3, 3), (6, 7) and (12, 15), respectively.

The physical interpretation of this is that the triple junction is the region of greatest strain interference and therefore contains the largest stress concentration. This result supports reason 1, page 50, hypothesized to explain the relatively high dislocation densities reported by Cullen and Baker (2002). The greatest differences in stress between the three meshes occur very close to the central triple junction, where a

material discontinuity occurs due to the abrupt change in c-axis alignment across crystal boundaries. However, short distances away from the triple junction, the differences in mesh results are much smaller than their margin over 20 kPa, a shear stress that is known to cause plastic deformation in single ice crystals (Steinemann, 1954; Wakahama, 1967). This leads to the following conclusion of the mesh convergence study: the discretization error of the ETJ model is minor and does not change the interpretation that crystals in the Vostok accretion ice have likely undergone some plastic deformation as a result of the large pressures and elastic anisotropy of single ice crystals.

CHAPTER 4

INELASTIC BEHAVIOR OF ICE CRYSTALS

A suitable inelastic material model must be established in order to further investigate the effects of mechanical anisotropy on stress distributions and internal melting in the Vostok accretion ice. A reasonable model should have a physical basis rooted in known deformation mechanisms and be supported by experimental data. The first step in this process is an examination of past experiments on single ice crystals. This is followed by a consideration of important deformation mechanisms at the temperature and pressure conditions in the Vostok accretion ice. Lastly, an inelastic material model is developed using the standard material options in ANSYS finite element software.

Review of Past Work on Single Ice Crystals

The ease with which single ice crystals deform along their crystallographic basal planes was demonstrated in early experiments by McConnel (1891). In a hotel room in Davos, Switzerland, McConnel hung a weight from the center of a simply supported, thin slip of ice cut from a single crystal. After several hours, McConnel discovered the crystal bent and laying intact in the box below. He recalled the following:

> In fact, as I noted at the time, the crystal behaved as if it consisted of an infinite number of indefinitely thin sheets of paper, normal to the optic axis, attached to each other by some viscous substance which allowed one to slide over the next with great difficulty.

Thus it was shown that ice crystals readily deform in shear along their basal planes. As noted by Hobbs (1974, p. 275), Mügge (1895) confirmed this observation four years later.

A resurgence in research work on single ice crystals occurred during the 1950's (Glen and Perutz, 1954; Griggs and Coles, 1954; Steinemann, 1954; Nakaya, 1958). Experiments by Glen and Perutz (1954) confirmed that the gliding layers in plastically deforming ice crystals were parallel to the basal (0001) plane. X-ray diffraction patterns were analyzed to determine whether glide along the basal plane followed the $< 11\bar{2}0 >$ directions (see page 29), but results were inconclusive. These directions are parallel to the shortest Burger's vectors and would thus be energetically favorable directions for slip in the crystal lattice. In another study by Steinemann (1954), simple shear creep tests were conducted on single ice crystals to measure rates of plastic shear strain for different applied stresses (Figure 4.1). The stress-strain rate data for different a-axis alignments, with c-axis direction fixed, showed too much scatter to deduce a glide direction along the basal plane. Steinemann therefore concluded that the glide direction was approximately that of the shear stress resolved along the basal plane. In general, the ice crystals

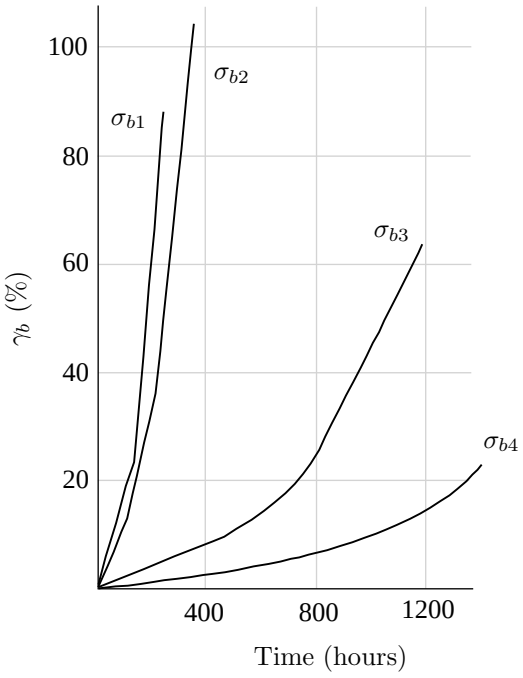

Figure 4.1: Plots of shear strain, γ_b, along basal plane of single ice crystals as a function of time from experiments by Steinemann (1954). The results shown are for different applied shear stresses along the basal plane. Shear stresses σ_{b1}, σ_{b2}, σ_{b3} and σ_{b4} = 216, 186, 64 and 44 kPa, respectively (after Steinemann, 1954).

were observed to work soften during a transition shear strain of about 10 to 20%, during which time shear strain rates increased under a constant stress. The ice crystals were said to shift from *hard crystals*, before the transition, to *soft crystals*, after the transition. This transition was noted as being irreversible. The following power law was deemed suitable for relating shear stresses to shear strain rates in both hard and soft crystals:

$$\dot{\gamma_b} = A_1 \sigma_b^{n1} \tag{4.1}$$

where $\dot{\gamma_b}$ was the engineering shear strain rate along the basal plane, σ_b the shear stress resolved along the basal plane and A_1 and $n1$ free parameters. The smallest applied σ_b-value was 20 kPa, for which case the power law (4.1) still applied. It was duly noted that if a yield stress exists for basal shear in single crystals, it must be below 20 kPa. Hard crystals were found to have $n1$-values between 2.3 and 4, with a mean of 3.2. Soft crystals were reported to have $n1$-values between 1.3 and 1.8, with a mean of 1.6. Recrystallization occurred in single crystals in regions where strains were sufficiently great and inhomogeneous, usually in association with growth defects. This took the form of small, newly-formed grains enclosed by the original crystal. An interesting comment was that in areas of recrystallization, soft crystals underwent a reverse transition back into hard crystals. Recrystallization is known to be a cause

for the transition from secondary to tertiary creep in polycrystalline ice.

Constant load compression tests on single ice crystals, grown both artificially and naturally, were counducted by Griggs and Coles (1954). The ice samples were cut into cylinders with crystallographic c-axes oriented either 90 or 45° to the load direction. Crystals of the former orientation displayed the slowest creep rates. This, and the occurrence of basal plane surface markings, indicated to Griggs and Coles that deformations occurred as translations along the basal plane. They also found that the crystals work softened with increasing strain and time. They expressed curiosity about this anomalous work softening behavior, having heard of similar findings only from Andrade and Jollife (1952) on experiments involving warm lead. Griggs and Coles fit their transient creep data to concave upward plots expressed by quadratic functions of temperature and time.

During the 1960's, many experiments, including creep, stress-strain and stress relaxation, were conducted on single ice crystals with analyses utilizing recently developed dislocation theories (Johnston and Gilman, 1959; Van Bueren, 1959; Johnston, 1962). Wakahama (1967) conducted compression tests on thin rectangular samples cut from ice monocrystals. Both artificial and natural crystals were used, grown using Griggs-Coles' method and collected from the Mendenhall Glacier, Alaska. Experiments were conducted in a cold room at temperatures between -3 and -10°C. The crystal c-axes were in the plane of the plates, at angles between 20 and 45° to the load axis. A schematic representation of the stress verses time data for constant applied strain rates is shown in Figure 4.2. Constant strain rates were applied up until times c, c′ and c″ in Figure 4.2. Starting at these times, strains were held fixed while the stresses were allowed to relax. In the higher strain rate experiments, either failure or strain softening occurred past the yield points (e.g., curves 3 and 4 in Figure 4.2). In contrast, the applied stresses in the slower strain rate

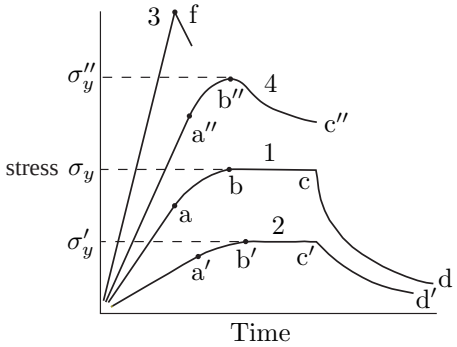

Figure 4.2: Schematic of compressive stress, in single ice crystals, verses time from constant strain rate experiments by Wakahama (1967). The actual stress depended on the angle between the c-axis and load direction. Curves 1 and 2 were typical for strain rates of 1.4×10^{-5} and 2.8×10^{-6} s^{-1}, respectively. The yield stresses, σ_y, are indicated at the stress peaks. Brittle failure occurred at point f, curve 3, for a strain rate $> 2.8 \times 10^{-6}$ s^{-1} (after Wakahama, 1967).

tests approached steady state values (e.g., curves 1 and 2). Stress magnitudes were significantly higher when the c-axes were either parallel or normal to the load direction. The maximum applied load in the experiments ranged from about 0.05 and 5 MPa, with particular values depending on strain rate, when the c-axes subtended angles of 38 to 44° to the load direction. The reader is referred to the appendix of Wakahama for plots of the actual stress vs. strain data.

Wakahama provided an insightful explanation of the observed stress verses time curves involving the multiplication of *active basal planes*. According to this explanation, shear stresses resolved along the basal planes were insufficient early in the tests to activate slip planes. Once the shear stress reached a threshold value, slip began to occur on certain basal planes having Frank-Read sources of sufficient length. Frank-Read sources provide a mechanism by which a dislocation can expand and regenerate from an initial segment that is sessile at both ends (Hull and Bacon, 1984, p. 169). A critical shear stress is required for the Frank-Read source to become unstable and regenerate. This critical stress is inversely related to the length of the initial dislocation segment. Wakahama explained that with progressive strain, the number of active basal planes multiplied and accommodated more of the applied deformation. At the yield points (e.g., points b, b' and b" in Figure 4.2), the component of strain rate due to slip on active basal planes equaled the total strain rate. At these points, the elastic strains and stresses became stationary. In the higher strain rate tests, the continued multiplication of active basal planes resulted in inelastic deformation rates large enough to relieve elastic strains, thus causing the crystal to strain soften (e.g., segment b″-c″ in Figure 4.2)

Wakahama (1967) used an equation of the following form to fit the stress relaxation data to time in the steady state stages of the experiments (e.g., segments b-c and b′-c′ in Figure 4.2):

$$\frac{1}{\sigma_b} = \frac{1}{\sigma_{b0}} + A_2(t - t_0) \tag{4.2}$$

where σ_b was the shear stress resolved in the basal plane, A_2 a constant, t the time, t_0 the starting time of stress relaxation, and σ_{b0} the reference value of σ_b at time $t = t_0$. The stress σ_b was observed to relax for σ_{0b}-values $>$ 20 kPa at a temperature of -10°C. Wakahama derived an expression in the form of equation (4.2) using concepts similar to those of Johnston's theory (Johnston and Gilman, 1959). This theory had been used to explain strain softening in single crystals of lithium flouride and is revisited in the next section of the present study. The transient stages of the stress curves observed by Wakahama are associated with the accelerating part of the creep curves recorded by Steinemann (1954) and Griggs and Coles (1954). The yield stresses in constant strain rate experiments (e.g., points b, b′ and b″ of Figure 4.2) are also associated with minimum strain rates observed in creep experiments.

A series of bending creep tests and constant strain rate tensile tests were carried out by Higashi et al. (1964, 1967) on single ice crystals collected from the Mendenhall Glacier, Alaska. The crystals were oriented with their c-axes 45° to the load direction. The tensile test data was presented in the form of plots showing shear stress resolved in the basal plane, σ_b, verses axial (i.e., parallel to load direction) strain, ϵ'_a, for different axial strain rates, $\dot{\epsilon}'_a$ (Figure 4.3). The initial slopes of the stress verses strain curves were found to be steeper in the higher strain rate experiments. Distinct stress peaks, σ_b^y, were observed in the higher strain rate tests at strains between 0.5 and 1%. Following these stress peaks, drops in stress occurred in association with strain softening of the crystals. Higashi et al. (1964) found that the maximum stresses, σ_b^y, were related to the constant strain rates, $\dot{\epsilon}'_a$, by the following Arrhenius power law:

$$\dot{\epsilon}'_a = A_3 \, (\sigma_b^y)^{n3} \exp(-Q/R_g T) \tag{4.3}$$

where R_g is the Universal Gas constant, T the absolute temperature and $n3$ the stress exponent. The values of $n3$ and Q were found to be 1.53 and 67 kJ mol^{-1}, respectively. Interestingly, this stress exponent was close to the mean value of 1.6 (see page 55) previously measured by Steinemann (1954) for "soft" crystals. Higashi et al. argued that the observed stress drops were a strong indication that Johnston's theory of dislocation motion was operative.

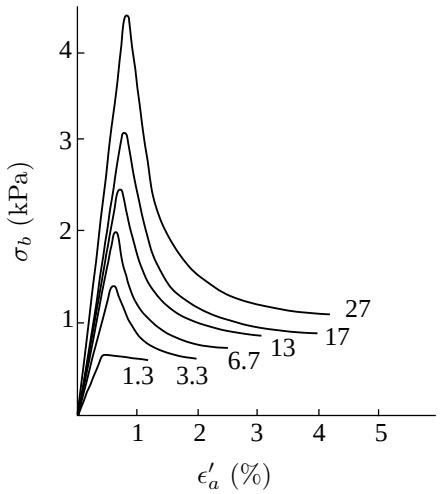

Figure 4.3: Curves showing basal plane shear stress, σ_b, verses axial strain, ϵ'_a, in single ice crystals at -10°C from tensile tests by Higashi et al. (1964). The constant axial strain rates, in units of 10^{-7} s^{-1}, are indicated near each curve.

According to Johnston's theory (Johnston and Gilman, 1959; Van Bueren, 1959), the plastic strain rate, $\dot{\epsilon}_p$, was a function of the mobile dislocation density, ρ_m, and the velocity of screw dislocation segments, v_s:

$$\dot{\epsilon}_p = 2b\rho_m v_s \tag{4.4}$$

The term b denoted the length of the Burger's vector. A possible factor of two error was noted involving the relative velocities of edge and screw dislocation segments. The velocity of screw dislocation segments, v_s, was expressed as a power function of the applied shear stress, τ_d, at a constant temperature:

$$v_s = (\tau_d/D)^{ns} \tag{4.5}$$

with D and ns being constants characteristic of a particular crystal type. Johnston noted that the mobile dislocation density in lithium flouride crystals increased linearly with plastic strain, so that the following relation held:

$$\rho_m = \alpha_m \epsilon_p \tag{4.6}$$

where ϵ_p was the plastic strain and α_m an experimentally measured proportionality constant. The plastic strain rate was expressed as a function of plastic strain and shear stress by substituting equations (4.5) and (4.6) into (4.4):

$$\dot{\epsilon}_p = 2b\alpha_m \epsilon_p (\tau_d/D)^{ns} \tag{4.7}$$

In both ice Ih and metals with a hexagonal close-packed crystal lattice, the primary plane of slip for dislocations is the basal (0001) plane. In single crystals of these materials, most of the plastic strain, ϵ_p, occurs in the form of translations along the basal plane under a resolved shear stress, σ_b. Using equation (4.7) to relate shear stress, σ_b, along the basal plane to plastic shear strain rate, $\dot{\gamma}_{bc}$, along the basal plane:

$$\dot{\gamma}_{bc} = 2b\alpha_m \gamma_{bc} (\sigma_b/D)^{ns} \tag{4.8}$$

Suppose that a single ice crystal is subjected to a uniaxial load, σ'_a, with the c-axis oriented at angle θ_a to the load direction. The magnitude of shear stress, σ_b, resolved along the basal plane is then given by $\sigma'_a \cos\theta_a \sin\theta_a$. The axial component of the plastic strain, ϵ'_{ac}, would be equal to $\gamma_{bc} \cos\theta_a \sin\theta_a$. Substituting these values into equation (4.8), the axial plastic strain rate is expressed by the following relation:

$$\dot{\epsilon}'_{ac} = 2b\alpha_m \epsilon'_{ac} \left(\frac{\sigma'_a}{D}\right)^{ns} (\cos\theta_a \sin\theta_a)^{ns} \tag{4.9}$$

Suppose that the total axial strain rate, $\dot{\epsilon}'_a$, is the sum of the elastic and plastic components. With the use of equation (4.9), the total axial strain rate is then as follows:

$$\dot{\epsilon}'_a = \frac{\dot{\sigma}'_a}{E(\theta_a)} + 2b\alpha_m \epsilon'_{ac} \left(\frac{\sigma'_a}{D}\right)^{ns} (\cos\theta_a \sin\theta_a)^{ns} \tag{4.10}$$

where, as a result of elastic anisotropy, the axial stiffness $E(\theta_a)$ is a function the angle θ_a between the c-axis and load direction. This anisotropy was addressed in Chapter 3 for the case of hydrostatic stress. Equation (4.10) represents the mechanical analog of an anisotropic spring in series with a nonlinear dashpot.

The strain rate equation (4.10) is used to illustrate the argument of Higashi et al. (1964) that Johnston's theory accounted for their stress verses strain data for single ice crystals. A distinct characteristic of Johnston's theory was the prediction of a stress peak, or "yield stress," with a magnitude that depended on the applied strain rate. Higashi et al. (1964) recognized this distinction in their data, and from analytical considerations concluded that Johnston's theory was applicable. At the peak stresses of the tensile tests (Figure 4.3), the time derivative of axial stress, $\dot{\sigma}'_a$, vanishes. For this condition, rearrangement of equation (4.10) to solve for the peak stress, σ'^{y}_a, produces the following:

$$\begin{aligned} \sigma'^{y}_a &= A_4 \left(\dot{\epsilon}'_a\right)^{1/ns} \\ A_4 &= D \left[1/\left(2b\alpha_m \epsilon'^{y}_{ac}\right)\right]^{1/ns} (\cos\theta_a \sin\theta_a)^{-1} \end{aligned} \tag{4.11}$$

where σ'^{y}_a and ϵ'^{y}_{ac} are the axial stress and plastic strain rate at the yield point, respectively. Higashi et al. (1964, Figure 8) showed that equation (4.11) represented their data of σ'^{y}_a verses $\dot{\epsilon}'_a$ when ns took on a value of 1.53. Thus, their findings seemed to be consistent with Johnston's theory. This was perhaps the most significant conclusion of their study. It appears that Higashi et al. approximated A_4 to be a constant. This seems reasonable considering that the measured axial strains, ϵ'^{y}_a, at peak stresses had similar values between about 0.5 and 1%. If it is assumed that $\epsilon'^{y}_{ac} \approx \epsilon'^{y}_a \approx$ constant, and $\theta_a \approx$ constant since rotational deformations were similar at peak stresses, then A_4 is also approximately constant. On a different but interesting note, their measured ns-value of 1.53 from tensile tests closely matched that of 1.58 obtained from separate measurements of steady state creep in bending (Higashi, 1967).

Higashi (1967) also conducted constant strain rate tensile tests on single ice crystals oriented for non-basal glide. The c-axes were oriented orthogonal to the tensile axis so that the magnitude of shear stress resolved along the basal plane was about zero. This orientation would tend to suppress slip along the basal plane and facilitate slip along the prism $\{10\bar{1}0\}$ planes. The crystals oriented for non-basal glide yielded at stresses about 20 times greater than those in basal glide. In addition, the crystals exhibited strain hardening, rather than softening, behavior.

It is interesting to note that strain rate equation (4.10), which is based on Johnston's theory, reduces to equation (4.2), used by Wakahama (1967) to fit stress relaxation data, when the mobile dislocation density is stationary and the exponent ns equals 2. In the steady state stage of deformation, the plastic strain rate is a function of stress, but not of strain and time. For this type of deformation, the mobile dislocation density, ρ_m, would approach the steady state value, ρ_{mf}. Enforcing this assumption, and holding the strain fixed at time $t = t_0$, equation (4.10) becomes:

$$\frac{\dot{\sigma}'_a}{E(\theta_a)} + A_5(\theta_a)\sigma'^2_a = 0 \tag{4.12}$$

where $A_5(\theta_a) = 2b\rho_{mf}\left(\cos\theta_a \sin\theta_a\right)^2 D^{-2}$. Integrating the above equation from time t_0 to t, the stress relaxation function becomes simply:

$$\frac{1}{\sigma_b(t)} = \frac{1}{\sigma_b(t_0)} + \left[A_5(\theta_a)E(\theta_a)\cos\theta_a \sin\theta_a\right](t - t_0) \tag{4.13}$$

This result has the same form as equation (4.2) used by Wakahama (1967) to fit stress relaxation data for ice crystals during steady state stress conditions (e.g., segments c-d and c′-d′ in Figure 4.2).

Review of Deformation Mechanisms in Polycrystalline Ice

Maps showing deformation mechanism fields for polycrystalline ice were assembled by Goodman et al. (1981). These display the fastest deformation mechanisms in ice in a given setting of shear stress, temperature, strain rate and grain size. The maps are based on numerous experimental data and theoretical models of steady state deformation mechanisms including dislocation creep, diffusional creep and the theoretical strength of the crystal lattice. Each deformation mechanism (DM) map for polycrystalline ice is three dimensional for a fixed grain size, with variables of strain rate, normalized shear stress and homologous temperature. The hydrostatic pressure is not included because of its lesser role in inelastic processes; however, pressures are assumed great enough to suppress crack formation. The normalized shear stress is defined as σ_s/μ_e, where σ_s is the shear stress and μ_e the elastic shear modulus. The *ideal strength* is defined as the theoretical upper limit of a crystal lattice's shear strength. According to Goodman et al. (1981), Kelly (1966) predicted the ideal strength to be between $\mu_e/5$ and $\mu_e/30$. However, ice is known to deform plastically under shear stresses orders of magnitude less than this. Goodman et al. attributed this plastic behavior to the ability of *kink segments* in dislocations to advance through a crystal. Under low normalized shear stresses ($\lesssim 2 \times 10^{-4}$), the velocities of kink segments in dislocations are controlled by the rearrangement rates of protons associated with the diffusion of ionic and Bjerrum defects through the

lattice (Goodman et al., 1981, p. 669). These stresses are known to exist in the basal regions of glaciers, which typically have normalized shear stresses in the range of 2×10^{-5} to 5×10^{-5} (i.e., 0.05 to 0.15 MPa) (Hobbs, 1974, p. 338). Steady state creep in these conditions is represented by the following equation for *proton-rearrangement controlled glide* (Goodman et al., 1981, p. 670)]:

$$\dot{\gamma}_s = a_p \nu_p \frac{\mu_e h_k b^2}{k_B T} \left(\frac{\sigma_s}{\mu_e} \right)^3 \exp\left(-\frac{F_{PR}}{R_g T} \right) \tag{4.14}$$

In the above equation for proton-rearrangement controlled (PRC) glide, σ_s is the shear stress and other parameters are listed in Table 4.1. A creep power law with an exponent of 3 was also derived by Weertman (1957, 1963) using Eshelby's (1961) treatment of steady state dislocation drift through a viscoelastic medium. Arrhenius power laws, similar in form to equation (4.14), have also been used to describe steady state creep in single ice crystals oriented for easy glide at temperatures greater than -15°C, with exponents ranging from 1.3 to 4 (Steinemann, 1954; Higashi et al., 1964; Higashi, 1967).

At greater normalized shear stresses ($\gtrsim 2 \times 10^{-4}$), proton rearrangement plays a lesser role in the velocity of dislocation kinks in ice (Goodman et al., 1981). As a result, the PRC glide equation (4.14) becomes less applicable. Constitutive creep laws for this higher shear stress regime are not further discussed

Parameter	Description	Value
a_p	Constant in PRC glide equation	1.2×10^3
ν_p	Mean proton rearrangment frequency at 0 K	1.57×10^{15} s^{-1}
μ_e	Elastic shear modulus of ice at 273.15 K	3.0×10^9 N m^{-2}
b	Burger's vector length	4.52×10^{-10} m
h_k	Kink height	$\sqrt{3}b/2$
F_{PR}	Activation energy for PRC glide	78.1 kJ mol^{-1}
d_g	Crystal grain size in Vostok accretion ice	0.5 m
k_B	Boltzmann's constant	1.3807×10^{-23} J K^{-1}
R_g	Universal Gas constant	8.3145 J (K mol)$^{-1}$
Ω_v	Volume per H_2O molecule in ice	3.27×10^{-29} m^3
D_v	Lattice diffusion coefficient	
D_{0v}	Pre-exponential for lattice diffusion	9.13×10^{-4} m^2 s^{-1}
D_b	Grain boundary diffusion coefficient	
D_{0b}	Pre-exponential for boundary diffusion	9.13×10^{-4} m^2 s^{-1}
δ_b	Width of grain boundary diffusion path	2b
A_{DF}	Constant in diffusional creep equation	42
F_v	Activation energy for lattice diffusion	59.4 kJ mol^{-1}
F_{bd}	Activation energy for boundary diffusion	38.3 kJ mol^{-1}

Table 4.1: Parameter definitions and values in proton-rearrangement controlled (PRC) glide and diffusional creep equations (from Goodman et al., 1981)

.

because they are outside the scope of this study.

At high homologous temperatures, conditions quite typical for ice, shear stress can induce the diffusion of material through a solid. Diffusion is generally driven by gradients in chemical potential (Ashby, 1972), the latter of which is partly a function of the stress and strain energy density. The accepted expression for diffusional creep strain rate, $\dot{\gamma}_d$, in polycrystalline ice is (Goodman et al., 1981):

$$\dot{\gamma}_d = A_{DF} \frac{\sigma_s \Omega_v}{kT d_g^2} D_v \left[1 + \frac{\pi \delta_b}{d_g} \frac{D_b}{D_v} \right] \tag{4.15}$$

where σ_s is the shear stress and other parameters are listed in Table 4.1. The diffusional creep equation (4.15) matches that developed by Raj and Ashby (1971) when the grain boundary wavelength was set equal to the grain size, d_g. This equation contains contributions from a d_g^{-2} term, representing the diffusion of material *through* grains (i.e., Nabarro-Herring creep), and a d_g^{-3} term, representing diffusion of material along grains (i.e., Coble creep) (Raj and Ashby, 1971; Ashby, 1972). The diffusion coefficients D_v and D_b have an Arrhenius temperature dependence expressed by the following relations (Hobbs, 1974, p. 378):

$$\begin{aligned} D_v &= D_{0v} \exp\left(\frac{-F_v}{R_g T} \right) \\ D_b &= D_{0b} \exp\left(\frac{-F_{bd}}{R_g T} \right) \end{aligned} \tag{4.16}$$

The terms F_v and F_{bd} represent the activation energies for lattice and grain boundary diffusion, respectively, and are listed in Table 4.1. Raj and Ashby (1971) note that grain boundary sliding (GBS) and diffusional flow must be coupled when lattice glide is not involved in the accommodation process arising from incompatibilities in deformation. In these conditions, they are aptly described as either *diffusional creep* or *grain boundary sliding with diffusional accommodation*. Because of the nonlinear inverse dependency of diffusional creep rates, $\dot{\gamma}_d$ on grain size, d_g, diffusional creep becomes a larger portion of the total creep as grain sizes decrease. In addition, because the stress exponent of diffusional creep (equation 4.15) is less than that for PRC glide (equation 4.14), $\dot{\gamma}_d$ becomes increasingly more significant than $\dot{\gamma}_s$ as shear stresses become smaller. It is also known that diffusional creep tends to overprint (i.e., remove) c-axis fabrics in ice, whereas dislocation glide tends to develop such fabrics. There are no reports of c-axis orientation patterns in the Vostok accretion ice, but there are reports of low overall lattice distortion (Montagnat et al., 2001). This could be an indication that diffusional creep is occurring rapidly enough in the Vostok accretion ice to remove any c-axis alignments associated with lattice dislocation glide.

A deformation mechanism (DM) map, from Goodman et al. (1981), for low normalized shear stress and high homologous temperature is shown in Figure 4.4. The fields in this map indicate the fastest

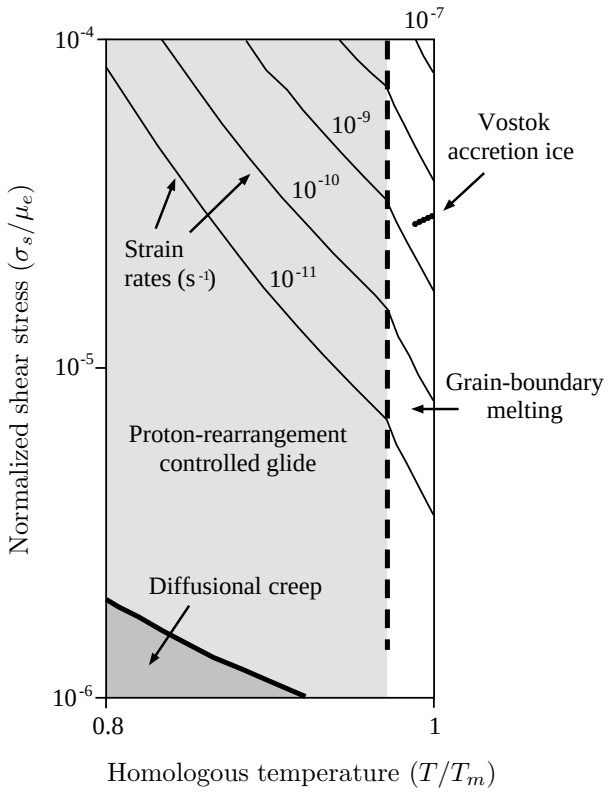

Figure 4.4: Deformation mechanism (DM) map for polycrystalline ice of 1 cm grain size, fields indicate fastest deformation mechanism. Points for Vostok accretion ice based on a maximum basal plane shear stress (σ_b) of 0.1 MPa from the finite element Elastic Triple Junction (ETJ) Model.

deformation mechanism for a given normalized shear stress and homologous temperature. The homologous temperature is defined as the ratio of the absolute temperature to the melting temperature. Numerically calculated stress-temperature points for the southern Vostok accretion ice, depths 3540 to 3750 m, are plotted on the DM map. These points are based on the maximum calculated σ_b-value of 0.1 MPa from the ETJ Model (Chapter 3), which used a hydrostatic stress boundary condition of 32.8 MPa (3650 m) and a temperature of -4.1°C. The points for different depths are calculated by scaling the ETJ Model results, a practice valid for a linear elastic material, to different depths between 3540 and 3740 m. The temperatures in the Vostok accretion ice are approximated as a linear function of depth, from an average surface temperature of -55°C (Petit et al., 1999) to -2.7°C at the ice-water interface. As a starting point, the stresses from an elastic model seem to be a reasonable criteria for exploring the potentially important deformation mechanisms. The shear stress σ_b-value of 0.1 MPa, simulated by the ETJ Model for a depth of 3650 m, is also representative of the typical shear stress range (0.05 to 0.15 MPa) for the basal ice of many glaciers. More accurate predictions would require impossible knowledge about the "true" inelastic material model, and thus the deformation mechanisms *a priori*. Moreover, the elastic anisotropy partly

drives the stress concentrations between ice crystals which, in turn, influence inelastic processes.

The stress-temperature points plotted on the DM map for the Vostok accretion ice indicate creep strain rates of 10^{-9} to 10^{-8} s^{-1}. It should be noted that the DM map is based on a grain size of 1 cm, an order of magnitude less than typical crystal sizes in the accretion ice. Based on the nonlinear inverse relation between diffusion creep rate, $\dot{\gamma}_d$, and grain size, d_g, larger grain sizes would shift the boundary separating the diffusional creep and PRC glide fields towards lower normalized shear stresses, thus farther from the stress-temperature points for the Vostok accretion ice. Other features of the DM map, such as strain rate contours and the grain boundary melting field, would change very little in the vicinity of the plotted stress-temperature points for the accretion ice.

The points plotted for the Vostok accretion ice lie within the grain boundary melting regime, but also lie close to the PRC glide dominated field. Because, as Goodman et al. (1981) pointed out, analytical models quantifying the relative significance of grain boundary melting and PRC glide have not been developed, the relative importance of dislocation glide and grain boundary melting cannot be ascertained. Based on the DM map, the dominant deformation mechanisms in the Vostok accretion ice are PRC glide and grain boundary melting, with relative significance that is unclear.

The critical shear stress, σ_s^c, defined as that which causes equal rates of PRC glide and diffusional creep, is found by equating $\dot{\gamma}_s$ and $\dot{\gamma}_d$ from equations (4.14) and (4.15), and then solving for σ_s. Using the parameters listed in Table 4.1, the normalized shear stress, σ_{sc}/μ_e, when PRC glide and diffusional creep rates are equal in the Vostok accretion ice is about 10^{-8}. This stress is three orders of magnitude less than those indicated on the DM map for the accretion ice. One reason for this low σ_{sc}/μ_e-value is the nonlinear inverse dependence of diffusional creep rates on grain size, which are very large in the accretion ice. In conclusion, based on temperature, grain size and shear stress calculated from the ETJ model, the PRC glide mechanism would be much faster than diffusional creep. This would also be true for the typical maximum shear stresses in glaciers.

Goldsby and Kohlstedt (1997, 2001) studied the grain size-sensitive processes of diffusional creep and grain boundary sliding (GBS) in very fine-grained polycrystalline ice. The transition from creep dominated by dislocation glide, to that dominated by diffusional flow, tends to occur at exceedingly slow strain rates in laboratory ice of typical grain size. This is illustrated in equation (4.15) by the linear dependence of creep strain rate on stress and nonlinear inverse dependence on grain size. This is consistent with the observation that overall deformation in coarse-grained materials tends to be dominated by dislocation glide in the grain cores (Gifkins, 1976). Goldsby and Kohlstedt conducted mechanical tests on very fine-grained (3-90 μm) ice with the goal of observing diffusional creep at practical strain rates. They found

three different deformation regimes, each described by the familiar Arrhenius power law:

$$\dot{\epsilon}_q = B_1 \sigma_q^n \exp(-Q/R_g T) \tag{4.17}$$

where $\dot{\epsilon}_q$ was the equivalent strain rate, σ_q the equivalent stress, Q the activation energy and B_1 a parameter that depended on grain size. A transition equivalent stress, σ_q^t, was observed between 3 and 5 MPa. When $\sigma_q > \sigma_q^t$, strain rates were characterized by $n = 4$ and $Q = 64$ kJ mol^{-1}, with a weak B_1-dependence on grain size. These results were associated with dislocation creep in polycrystalline ice, where glide along the basal (0001) and prism $\{10\overline{1}0\}$ planes could provide the four minimum slip systems for the general deformation hexagonal polycrystals (Taylor, 1938; Hutchinson, 1977). Fewer slip systems require non-slip mechanisms for deformation to proceed in general, like diffusional flow and void growth.

For $\sigma_q < \sigma_q^t$, two different deformation regimes were observed with n-values of 1.8 and 2.4. These regimes were different in that $\dot{\epsilon}_q$ became markedly dependent on grain size. This suggested that diffusional creep and GBS were involved. This was further supported by the observation of numerous, newly-formed four-grain junctions under an environmental electron scanning microscope. They concluded that GBS and basal glide were the dominant deformation mechanisms in the $n = 1.8$ and 2.4 regimes. It was hypothesized that GBS, acting in concert with basal glide, could provide the four minimum slip systems for hexagonal polycrystals. Their hypothesis was as follows. As equivalent stress decreased, GBS would play an ever increasing role relative to dislocation glide. In the intermediate stress range of 1 MPa $< \sigma_q < \sigma_q^t$, corresponding to the $n = 1.8$ regime, GBS would be slower than basal slip, the former thus limiting the overall rate of deformation. At the lowest experimental stress of $\sigma_q < 1$ MPa, corresponding to the $n = 2.4$ regime, GBS would become faster than basal glide, the latter thus becoming the "rate-limiting" deformation mechanism. The difference between the rate-limiting and fastest deformation mechanisms have a significant influence on the degree of strain interference and microscopic stress concentrations in a deforming polycrystalline material.

Evidence for GBS in ice has been found in additional studies. Kuroiwa (1964) measured internal friction in ice crystals containing different impurities. In these experiments, ice blocks were driven into a resonant frequency, then allowed to freely oscillate. The internal friction was determined by measuring the decrement in free oscillations. The positions of internal friction peaks, and the associated relaxation times, between temperatures of -10 and -40°C were consistent with energy dissipation processes associated with proton rearrangement. However, separate and distinct internal friction peaks were also observed near the melting point (> -10°C). These were attributed to *grain boundary internal friction* in association with the viscosity of grain boundaries (Kuroiwa, 1964, p. 20). The experiments were repeated on both

single crystals and artificially bonded bicrystals. The resulting grain boundary internal friction was either absent or much less pronounced (Kuroiwa, 1964, p. 32), indicating minor energy dissipation along grain boundaries. These interesting findings indicated that grain boundaries in polycrystalline ice near the melting point exhibit viscous characteristics that were closely associated with the presence of impurities. In another study by Weiss and Schulson (2000), the development of *decohesions*, or discontinuous openings, along grain boundaries in polycrystalline ice were observed. The conclusion was that viscous GBS was associated with the formation of these structures. In a different study, the attenuation of acoustic waves in clean ice of the Athabasca glacier, Alberta, Canada was measured by Clee et al. (1969). The conclusion was that the source of energy dissipation from the acoustic waves was grain boundary relaxation via grain boundary slip. It was believed that the same mechanism of internal friction was involved in the Kuroiwa (1964) experiments.

Inelastic Material Model for the Vostok Accretion Ice

Based on temperature, grain size and plausible shear stress in the Vostok accretion ice, the DM map indicates that PRC glide and GBS would be the fastest deformation mechanisms. The creep equation for PRC glide has the same form as Johnston's theory in the limit of stationary mobile dislocation density, ρ_m (equations 4.6 and 4.6). Johnstons's theory has been shown to account for single crystal creep via basal glide (Higashi et al., 1964; Higashi, 1967). In the limit of stationary ρ_m-values, this theory leads to the same creep law as those applied in previous studies on single ice crystals oriented for basal glide (Steinemann, 1954; Wakahama, 1967). Therefore, the inelastic material model of this study adopts a constitutive law of the same form as the PRC glide equation (4.14), but applicable only to shear stress and strain rate resolved along the crystallographic basal plane. The model thus includes the assumption that the steady state form of Johnston's theory is applicable for shear strains along the basal planes of ice crystals. Previous experiments (Higashi, 1967) have shown that, for the shear stresses considered in this study, slip along the prism $\{10\bar{1}0\}$ planes (i.e., "prismatic glide") would be much slower than that along the basal (0001) plane. As implemented later in Chapter 5, the material model has the capability to allow creep on non-basal planes. However, these planes are not the prism $\{10\bar{1}0\}$ planes of the hexagonal crystal, but rather a set of orthogonal planes of a local reference frame. Inclusion of minor slip along these orthogonal planes can semi-quantitatively simulate the effect of minor prismatic glide on stress results of the numerical model. The examination of deformation mechanisms in the last section indicated that GBS and GB melting are also important deformation mechanisms to consider. These two processes are likely coupled near the melting point since liquid water along grain boundaries would drastically lower their resistance to sliding.

Dislocation glide along the basal plane provides two independent slip directions. Previous studies have established that four independent slip directions are necessary for the general deformation of hexagonal polycrystals without void growth (Taylor, 1938; Hutchinson, 1977). Prismatic glide could provide the two additional directions of slip (Hutchinson, 1977). As mentioned earlier, this mechanism would be much slower than basal glide for the low values of shear stress likely present in the Vostok accretion ice. However, it is possible that GBS and diffusional creep together provide the accommodation mechanism for general deformation in the ice (Goldsby and Kohlstedt, 1997). The mechanisms of prismatic glide and diffusional creep would operate slower than basal glide and GBS in the conditions of the accretion ice. Thus, the former two mechanisms would be *rate-limiting* in the sense that they limit the overall rate of deformation. The inelastic material model will first-and-foremost include the fastest deformation mechanism, PRC basal glide and GBS, but will also address the possible rate-limiting mechanism of prismatic glide. The latter is semi-quantitatively addressed in the model by referencing the orthogonal axes of the local material frame. As mentioned earlier, this does not accurately represent the six prism planes, but does provide a sense for the effect of minor non-basal glide on the stress results of the inelastic model.

The inelastic material model of this study simulates PRC glide, acting primarily along the basal (0001) plane, and GBS between crystals. A constitutive relation is adopted in the form of Johnston's theory (equation 4.7) applied to slip along the basal plane, with the added assumption that the mobile dislocation density, ρ_m, has reached a stationary value. The model is thus steady state, with time acting as essentially a dummy variable and not necessarily reflecting time scales in the Vostok accretion ice. The temperature dependence of the model assumes the Arrhenius form based on the PRC glide equation (4.14). The following steady state equation is used to describe creep shear strain rate, $\dot{\gamma}_{bc}$, along the basal plane:

$$\dot{\gamma}_{bc} = \frac{A}{T}\sigma_b^{C_2} \exp\left(\frac{-Q}{R_g T}\right) \tag{4.18}$$

where C_2 is a dimensionless parameter, T the absolute temperature, A a parameter with units of K s^{-1}(N $m^{-2})^{-C_2}$, Q the activation energy in units of kJ mol^{-1}, and R_g the Universal Gas constant. Note that equation (4.18) has the same form as previous relations used to describe the creep rate of single ice crystals oriented for basal glide (equations 4.1 and 4.3).

A standard material option in ANSYS for modeling anisotropic creep behavior uses the Hill orthotropic yield function, Q_h, in conjunction with Norton creep. The creep flow rule for this material option is as follows:

$$\dot{\epsilon}_{ij}^c = \frac{3}{2}\frac{\dot{\epsilon}_e^c(\sigma_e)}{\sigma_e}\frac{\partial Q_h}{\partial \sigma_{ij}} \tag{4.19}$$

where $\dot{\epsilon}^c_{ij}$ are the *engineering* components of creep strain rate in the material frame, σ_e the "effective stress" with respect to the material frame, $\dot{\epsilon}^c_e$ the effective creep rate as a function of σ_e, and Q_h the Hill orthotropic yield function. The index 3 is defined to be along the c-axis of the crystal. It is emphasized that the shear strain rate components of equation (4.19) are actually the engineering values (e.g., $\dot{\epsilon}_{12} = \dot{\gamma}_{12}$). Restated, the strain rate $\dot{\epsilon}_{12}$ in ANSYS is equivalent to the engineering strain rate $\dot{\gamma}_{12}$, a notation that is somewhat unorthodox. Flow rule (4.19) yields zero dilatational creep strain, a result consistent with a lattice-slip deformation mechanism of the model. This property is a consequence of the independence of the Hill orthotropic yield function on hydrostatic stress. Both hand solutions and isotropic limiting cases were examined in order to verify equation (4.19).

The total engineering strain rate is the sum of the contributions from creep and linear elastic deformation:

$$\dot{\epsilon}_{ij} = (2 - \delta_{ij}) S^t_{ijkl} \dot{\sigma}_{kl} + \frac{3}{2} \frac{\dot{\epsilon}^c_e(\sigma_e)}{\sigma_e} \frac{\partial Q_h}{\partial \sigma_{ij}} \tag{4.20}$$

(no sum on indices i and j), where δ_{ij} is the Kronecker delta. The prefactor $(2 - \delta_{ij})$ in equation (4.20) is necessary in order to convert from tensorial to engineering strain values. The elastic strains are infinitesimal in nature and valid in the linear elastic regime of ice. This regime is generally valid for strains less than about 1%, which hold true for the results of this study.

The effective stress, σ_e, and Hill orthotropic yield function, Q_h, are defined as follows:

$$\begin{aligned} Q_h &= \frac{1}{3}\left[F(\sigma_y - \sigma_z)^2 + G(\sigma_z - \sigma_x)^2 + H(\sigma_x - \sigma_y)^2 + 2L\sigma^2_{yz} + 2M\sigma^2_{xz} + 2N\sigma^2_{xy}\right] - \frac{\sigma_0^2}{3} \\ \sigma_e &= \sqrt{F(\sigma_y - \sigma_z)^2 + G(\sigma_z - \sigma_x)^2 + H(\sigma_x - \sigma_y)^2 + 2L\sigma^2_{yz} + 2M\sigma^2_{xz} + 2N\sigma^2_{xy}} \end{aligned} \tag{4.21}$$

where the stresses and directions x, y and z are with respect to the material (local) frame. The x, y and z directions correspond to indices 1, 2 and 3, respectively, in equation (4.19). The parameter σ_0 is the "yield stress" in an anisotropic, rate-independent plastic model. This term drops out of the creep flow rule due to the stress gradient operation. The yield criteria for a non-hardening plasticity model is $Q_h = 0$ (Hill, 1950, p. 318). This criteria is slightly modified from that in Hill (1950) due to the multiplication by a factor of $(2/3)\sigma_0^2$. This change only redefines the values of R_{ij}, mentioned below, but does not otherwise change the yield criteria.

The effective creep rate, $\dot{\epsilon}^c_e$, is defined as a function of effective stress, σ_e, by the *implicit* creep constitutive laws in ANSYS. In this study, the following *Norton* implicit creep relation is used in order to attain a constitutive law of the same form as equation (4.18):

$$\dot{\epsilon}^c_e = C_1 \sigma_e^{C_2} \exp\left(-\frac{C_3}{T}\right) \tag{4.22}$$

The terms C_1, C_2 and C_3 are free model parameters. C_3 has units of temperature (K), C_2 is dimensionless, and C_1 has units of $\mathrm{s}^{-1}(\mathrm{N\ m}^{-2})^{-\mathrm{C}_2}$. The values of these parameters are determined using data from literature on single ice crystals.

The Hill parameters F, G, H, L, M and N in equation (4.21) are used to specify the ratios in creep strain rates in the material frame directions for a given deviatoric stress. They are defined as follows (ANSYS Theory Reference):

$$\begin{aligned} F &= \frac{1}{2}\left(\frac{1}{R_{yy}^2}+\frac{1}{R_{zz}^2}-\frac{1}{R_{xx}^2}\right) & G &= \frac{1}{2}\left(\frac{1}{R_{zz}^2}+\frac{1}{R_{xx}^2}-\frac{1}{R_{yy}^2}\right) \\ H &= \frac{1}{2}\left(\frac{1}{R_{xx}^2}+\frac{1}{R_{yy}^2}-\frac{1}{R_{zz}^2}\right) & L &= \frac{3}{2R_{yz}^2} \\ M &= \frac{3}{2R_{xz}^2} & N &= \frac{3}{2R_{xy}^2} \end{aligned} \tag{4.23}$$

The Hill parameters R_{xx}, R_{yy}, R_{zz}, R_{xy}, R_{yz} and R_{xz} define the ratios of the different $\dot{\epsilon}_{ij}^c$-values in the material frame for a given deviatoric stress state. In the isotropic limiting case that the Hill parameters are an equal value, flow rule (4.19) reduces to the *Mises type flow rule for isotropic materials* (Skrzypek, 1993, p. 12,410). The Hill parameter values are chosen with the goal of suppressing all creep strains except the basal 12- and 13-components.

By resolving the glide components along the Burger's vectors $<11\overline{2}0>$, Kamb (1961a) predicted that resolved glide and shear stresses would be parallel if the power law exponent C_2 equaled 1 or 3. Previous mechanical experiments on single ice crystals have been unable to definitively establish a preferred glide direction along the basal plane (Glen and Perutz, 1954; Steinemann, 1954). It is therefore reasonable to model the creep behavior of an ice crystal as being transversely isotropic about the material 3-direction (i.e., c-axis). Using relations (4.23), and conditions for transversely isotropic symmetry about the 3-direction (Hill, 1950, p. 318-320), the following assignments are made: $R_{xz} = R_{yz} \rightarrow R_b$, and $R_{xx} = R_{yy} = R_{zz} = R_{xy} \rightarrow R_n$. The creep strain rate ratios, with respect to the material frame, are then formed using equations (4.19), (4.21) and (4.23):

$$\begin{aligned} \frac{\dot{\epsilon}_b^c}{\dot{\epsilon}_{xx}^c} &= 2\left(\frac{R_n}{R_b}\right)^2\frac{\sigma_b}{s_{xx}} & \frac{\dot{\epsilon}_b^c}{\dot{\epsilon}_{yy}^c} &= 2\left(\frac{R_n}{R_b}\right)^2\frac{\sigma_b}{s_{yy}} \\ \frac{\dot{\epsilon}_b^c}{\dot{\epsilon}_{zz}^c} &= 2\left(\frac{R_n}{R_b}\right)^2\frac{\sigma_b}{s_{zz}} & \frac{\dot{\epsilon}_b^c}{\dot{\epsilon}_{xy}^c} &= \left(\frac{R_n}{R_b}\right)^2\frac{\sigma_b}{\sigma_{xy}} \end{aligned} \tag{4.24}$$

The subscript 'b' denotes a shear stress or strain rate along the basal plane (i.e., 13- and 23- components) and s_{ij} are the deviatoric stress components evaluated in the material frame. Creep along all non-basal directions is suppressed in the limit that $R_b/R_n \rightarrow 0$. Letting $R_b = 3^{1/2}$ and $R_n = (3/2)^{1/2} \times 10^6$, the

creep strain rate along the basal plane is 12 orders of magnitude greater than that along other material directions *for a given deviatoric stress*. This accomplishes the goal of suppressing all creep strains other than the basal shear components.

The inelastic model also uses R_b and R_n settings of $3^{1/2}$ and $(3/2)^{1/2} \times 10^2$, respectively, in order to allow for slow creep strain rates along the material xy plane. This is intended to semi-quantitatively represent the effect of increased non-basal glide on the model results. The R_n-value of $(3/2)^{1/2} \times 10^2$ was determined using equations (4.24), non-basal glide creep data from Higashi (1967), a stress ratio σ_{12}/σ_b of 70 based on Castelnau et al. (1997), and a shear stress σ_b-value of 0.01 MPa. This shear stress was fairly typical in the steady state part of the numerical model results. Based on these values for R_b and R_n, the creep rate, $\dot{\epsilon}^c_b$, along the basal plane is about 4 orders of magnitude greater than that along the material xy plane (i.e., $\dot{\epsilon}^c_{xy}$). If the latter creep component is associated with prismatic glide, then this creep rate difference is in excellent agreement with previous experimentally-observed values (Duval et al., 1983).

By expressing the creep flow rule (equation 4.19) in a more recognizable form, the Norton creep parameters C_1, C_2 and C_3 can be readily associated with past experimental data on single ice crystals. Substituting the Norton equation (4.22) into the creep flow rule, the constitutive relation for creep becomes:

$$\dot{\epsilon}^c_{ij} = \frac{3C_1}{2}\sigma_e^{C_2-1}\frac{\partial Q_h}{\partial \sigma_{ij}}\exp\left(\frac{-C_3}{T}\right) \tag{4.25}$$

When $R_b/R_n \approx 0$ and $R_b = 3^{1/2}$, the terms Q_h and σ_e are approximated as follows:

$$\begin{aligned} Q_h &\approx \frac{1}{3}\left(\sigma^2_{xz} + \sigma^2_{yz}\right) \\ \sigma_e &\approx \sqrt{\sigma^2_{xz} + \sigma^2_{yz}} \end{aligned} \tag{4.26}$$

Thus, in this limit, the effective stress, σ_e, becomes the resolved shear stress along the basal plane. When Q_h and σ_e are approximated by the limiting cases of equations (4.26), the creep equation (4.25) reduces to the following recognizable Arrhenius power law:

$$\dot{\gamma}_{bc} = C_1\sigma_b^{C_2}\exp\left(\frac{-C_3}{T}\right) \tag{4.27}$$

where $\dot{\gamma}_{bc}$ and σ_b are the resolved creep strain rate and stress, respectively, in the basal plane of the modeled ice crystal. Creep equation (4.27) has the same form as that with which the inelastic model began (equation 4.18). It also has the form of equations used in previous studies (Steinemann, 1954; Higashi et al., 1964) to fit experimental creep data for single ice crystals oriented for basal glide. Thus, parameters C_1, C_2 and C_3 are readily determined by associating equation (4.27) with the results of these

past studies.

Steinemann (1954) measured a stress exponent (equation 4.1) between 1.3 and 1.8, with a mean of 1.6, for soft crystals optimally oriented for basal glide. This is considered to represent the stress exponent for steady state creep after the mobile dislocation density, ρ_m, has reached a stationary value. Hard crystals were observed during the early stage of the experiments, when ρ_m was presumably increasing with strain and time. The stress exponent for hard crystals was found to be between 2.3 and 4, with a mean of 3.2. Higashi et al. (1964) considered stress peaks in tensile tests on ice crystals, along with consideration of Johnston's theory, to calculate a stress exponent of 1.5 in equation (4.3). The inelastic material model in this study uses stress exponents, C_2, of both 1.5 and 3.1. The C_2-value of 3.1 is very close to the mean exponent measured by Steinemann for hard crystals, and allows the direct use of the log-log plot in their Figure 7. The C_2-value of 1.5 simulates the behavior of soft crystals observed by Steinemann (1954).

Based on a comparison of equations (4.18) and (4.27), the Norton creep parameter C_3 equals Q/R_g, where Q is the activation energy of PRC glide and R_g is the Universal Gas constant. Higashi et al. (1964) calculated a Q-value of 67 kJ mol^{-1} from their tensile test data on single crystals optimally oriented for basal glide. Past studies have reported Q-values for dislocation creep in polycrystalline ice ranging from 60 to 80 kJ mol^{-1} (Goldsby and Kohlstedt, 1997). Based on these considerations, the material model uses an intermediate Q-value of 70 kJ mol^{-1}, corresponding to a C_3-value of 8.4×10^3 K.

The temperature dependent parameter C_1 is calculated by associating the creep curves published by Griggs and Coles (1954), Steinemann (1954), and Higashi et al. (1964) to an equation of the following form with temperature-dependent parameter k_t:

$$\dot{\gamma}_{bc} = k_t \sigma_b^{C_2} \tag{4.28}$$

where $C_2 = 1.5$ for soft crystals and 3.1 for hard crystals. The parameters k_t, C_1 and A are all readily related by comparing equations (4.18), (4.27) and (4.28):

$$\begin{aligned} k_t &= C_1 \exp\left(\frac{-C_3}{T}\right) \\ &= \frac{A}{T} \exp\left(\frac{-Q}{R_g T}\right) \end{aligned} \tag{4.29}$$

Thus, the model parameters $C_1 = A/T$ and $C_3 = Q/R_g$, where T is the absolute temperature (K), R_g is the Universal Gas constant, and Q is the activation energy (70 kJ mol^{-1}). Table 4.2 lists the calculated values of k_t from past experiments along with the corresponding A-values based on equation (4.29). The soft crystal A-values based on Steinemann (1954) and Griggs and Coles (1954) are quite similar, with a

C_2	Average k_t	N	σ_k	A	Source
3.1	3.4×10^{-21}	n/a	n/a	2.9×10^{-5}	Steinemann, 1954, Fig. 7
1.5	1.1×10^{-12}	n/a	n/a	9.4×10^{3}	Steinemann, 1954, Fig. 7
1.5	8.8×10^{-15}	6	1.5×10^{-15}	3.3×10^{2}	Higashi et al., 1964, Fig. 2
1.5	3.4×10^{-13}	4	0.63×10^{-13}	7.4×10^{3}	Griggs and Coles, 1954, Fig. 14

Table 4.2: Values and sources of parameters used in inelastic material model. The units of k_t are $\mathrm{s}^{-1}(\mathrm{N\ m}^{-2})^{-\mathrm{C}_2}$ and that of A are $\mathrm{K\ s}^{-1}(\mathrm{N\ m}^{-2})^{-\mathrm{C}_2}$. N is the number of stress-strain rate points measured, and σ_k the square root of the variance in calculated k_t-values. The data from Steinemann (1954) was based on their log-log linear fit. Values in the A column are based on the average k_t-value and equation (4.29).

difference of only 24%. This agreement is considered excellent in light of the large uncertainties of the model. The soft crystal A-value based on Higashi et al. (1964) is an order of magnitude off from those based on Steinemann (1954) and Griggs and Coles (1954) (Table 4.2). This difference illustrates the large uncertainties of the parameters in this model.

The Norton creep parameter C_1 $(= A/T)$ for soft crystals is assigned the average A-value of 8.4×10^3 $\mathrm{K\ s}^{-1}(\mathrm{N\ m}^{-2})^{-1.5}$ based on the data in Table 4.2 from Steinemann (1954) and Griggs and Coles (1954). The C_1-value for hard crystals is assigned an A-value of 2.9×10^{-5} $\mathrm{K\ s}^{-1}(\mathrm{N\ m}^{-2})^{-3.1}$ based on the $n = 3.1$ creep curve in Steinemann (1954, Figure 7). The Norton creep parameters of the inelastic material model are summarized in Table 4.3.

The atomistic mechanism of GBS is the motion of dislocations along the boundary plane with Burger's vectors that are usually not lattice vectors (Ashby, 1972). The GBS process is made possible by the diffusional flow of defects across the grain boundary. The *intrinsic* mechanical properties of the boundary are in part a function of the discontinuity in c-axis alignments. The constitutive relation for GBS follows the *Stokes-Einstein* relation (Ashby, 1972; Raj and Ashby, 1971):

$$\tau_{sb} = \eta_b \frac{\dot{U}}{\delta_{sb}} \tag{4.30}$$

where τ_{sb} is the shear stress along the boundary plane, η_b the boundary viscosity, δ_{sb} the boundary

	Hard crystal	Soft crystal
C_1	$\lceil (2.9 \times 10^{-5})/T \rceil$ $\mathrm{K\ s}^{-1}(\mathrm{N\ m}^{-2})^{-3.1}$	$\lceil (8.4 \times 10^{3})/T \rceil$ $\mathrm{K\ s}^{-1}(\mathrm{N\ m}^{-2})^{-1.5}$
C_2	3.1	1.5
C_3	8.4×10^3 K	8.4×10^3 K

Table 4.3: Summarized values of Norton anisotropic creep parameters, for both soft and hard crystals, for input into ANSYS finite element model. T is the absolute temperature (K). The units of C_1 and C_3 are $(\mathrm{N\ m}^{-2})^{-C_2}$ s^{-1} and K, respectively.

thickness and $\dot{U}$ the sliding velocity. In general, incompatibilities exist along the grain boundary (e.g., asperities, constraints from neighboring grains) that require an accommodation process if GBS is to proceed. Accommodation is more difficult at triple junctions than grain boundaries, the former thus usually limiting the accommodation process (Gifkins, 1976). At low temperatures and stresses (i.e., below yielding), GBS is accommodated by elastic deformation of the crystal lattice (Ashby, 1972; Raj and Ashby, 1971). This process results in *anelastic* behavior. At higher temperatures, GBS is increasingly accommodated by the diffusive flow of matter across grain boundaries. Finally, at stresses past yielding, GBS is accommodated by plastic deformation of the crystal lattice. Experiments that measure internal friction, which is associated with anelastic behavior, are a method of measuring the intrinsic grain boundary viscosity, η_b (Raj and Ashby, 1971). According to Mosher and Raj (1974), Weinig and Machlin (1957) measured the relaxation time in pure copper, which could in turn be used to calculate the intrinsic viscosity ratio η_b/δ_{sb} in the GBS equation (4.30).

According to Vulliet and Hutter (1988), a number of sliding laws with forms similar to equation (4.30) have been proposed. A number of these were considered for their model involving the basal properties of landslides. Ghahremani (1980a,b) have used sliding relation (4.30) to numerically model the effect of GBS on anelasticity and steady state creep in polycrystals. Picu and Gupta (1995a,b) modeled crack nucleation in columnar ice with the use of material properties that included GBS and elastic anisotropy.

A sliding law in the form of Stokes-Einstein equation (4.30) is the preferred constitutive law for GBS between ice crystals in the present study. Instead, however, frictionless sliding is used in the inelastic material model for the following three reasons: (1) data for the grain boundary viscosity ratio η_b/δ_{sb} is not readily available, (2) conducting internal friction experiments to measure η_b/δ_{sb} is beyond the scope of this study, and (3) material *contact* properties in ANSYS do not include options for viscous behavior. Contact using frictionless sliding simulates viscous GBS in the limit that the intrinsic boundary viscosity approaches zero. This is a reasonable first approximation for GBS in warm ice, where intergranular water may significantly reduce the grain boundary viscosity. In frictionless sliding, shear stresses along contact planes (i.e., grain boundaries) are fully relaxed, while normal stresses are fully transmitted. This type of GBS was used in an elastic model by Picu and Gupta (1996) to model stress singularities at triple junctions in polycrystals. For future reference, thin-layer interface elements, discussed by Schweiger and Haas (1988) for geotechnical applications, may be suitable for modeling viscous GBS between ice crystals.

CHAPTER 5

INELASTIC TRIPLE JUNCTION (ITJ) MODEL

Model Description

An anisotropic elasto-creep model has been developed to examine the influence of mechanical anisotropy on microscopic melting in deep glacial ice. The model consists of an array of hexagonal prisms, each representing a crystal of dimensions d_{g1} and d_{g2} (Figure 5.1). The sides of the hexagons represent the idealized crystal boundaries and have no association with the crystallographic prism planes. A *submodeling* routine is used that approximates the displacement boundary conditions of the fine mesh submodel (Figure 5.1b) by an interpolation of results from the coarse mesh model (Figure 5.1a). The submodel geometry is cylindrical in order to maximize distance between the central triple junction of interest and the outer *cut boundaries*. The crystal dimension, d_{g1}, is set to 0.5 m to reflect a median crystal size in the Vostok accretion ice (Jouzel et al., 1999). The radius of the submodel is set to the value $0.44d_{g1}$. The central

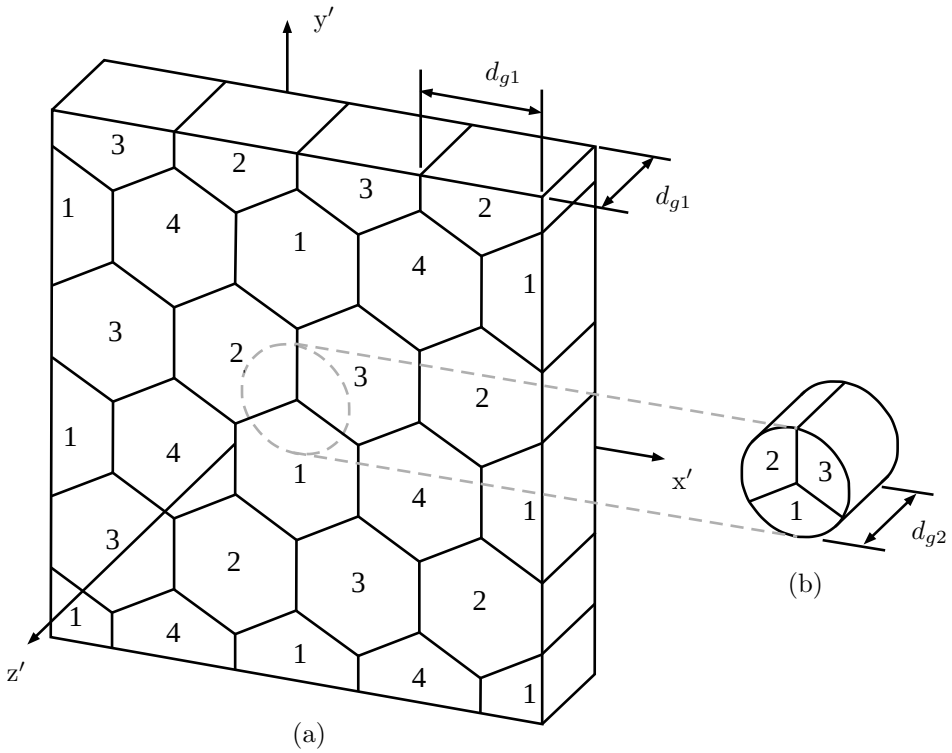

Figure 5.1: Geometry of the finite element Inelastic Triple Junction (ITJ) Model. A submodeling routine interpolates nodal displacements from (a) the coarse mesh model onto the boundaries of (b) the fine mesh submodel. Four different local frames are used to represent the different crystallographic c-axis orientations. These are indicated by numbers 1 to 4.

triple junction of the submodel is located at global coordinates $x' = d_{g1}/2$, $y' = d_{g1}/2$. The z' coordinate of the submodel ranges from $(1/2)(d_{g1} - d_{g2})$ to $(1/2)(d_{g1} + d_{g2})$, where $d_{g2} < d_{g1}$. This coordinate range centers the submodel with respect to the coarse model in the z' direction. Four different local (material) frames are used to represent an alternating pattern of crystallographic c-axis orientations. These frames are numbered 1 to 4 in Figure 5.1 and each represent a different crystallographic orientation. Limiting the total number of local frames to four eases specification of c-axis spherical coordinates while not changing the overall results of the model. Additional details about the local frames are described for the ETJ Model on page 41.

The ITJ Model consists of linear 8-node brick elements (SOLID185), with selective reduced integration, for two reasons: (1) a linear element yields constant stress results, which are convenient for data post-processing to infer locations of melting where fluid pressures would be uniform, and (2) linear elements have 8 nodes, rather than the 20 of quadratic brick elements, and thus allow for smaller element sizes. Crystals of the coarse model are always meshed with six elements across, along the $x'y'$ plane, and three elements in depth (Figure 5.2a). The mesh parameters FM1 and FM2 specify the number of element divisions along the radius and z' direction, respectively, of the submodel. The smallest elements of the submodel are located adjacent to the central triple junction. The smallest element dimensions along

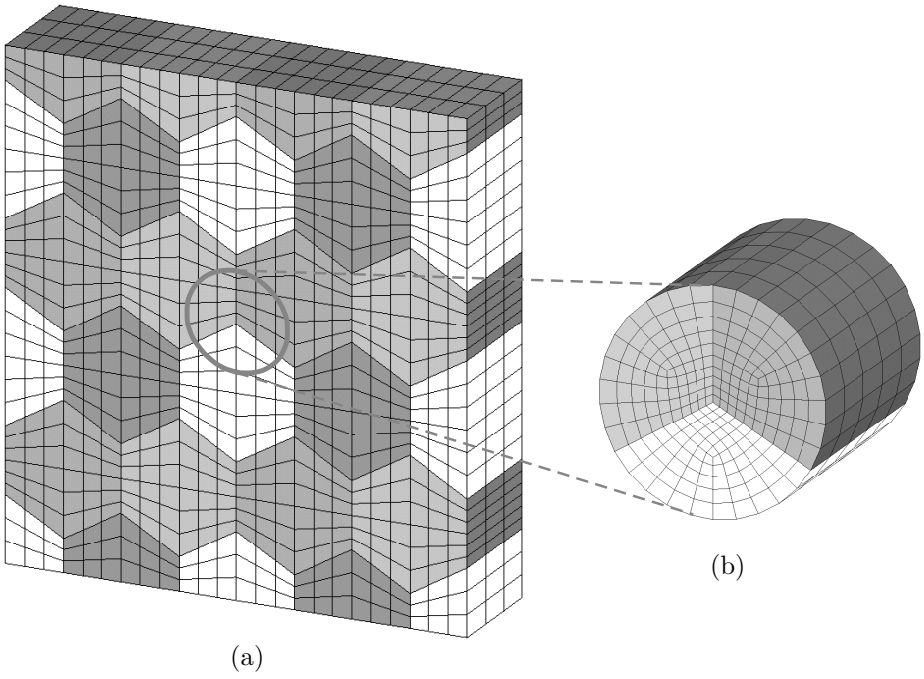

Figure 5.2: Element mesh of the (a) coarse model and (b) fine mesh submodel of the ITJ Model. Mesh parameters FM1 and FM2 specify the number of element divisions along the radius and z' direction (depth), respectively, of the submodel. The radial spacing ratio of the submodel is 2 as shown above.

crystal edges of the submodel can be approximated with equation (3.21) and either $L_e = 0.44d_{g1}$, $S_e = 2$, N_e = FM1 (in the x′y′ plane), or $L_e = d_{g2}$, $S_e = 1$, N_e = FM2 (in the z′ direction).

All executions of the ITJ Model use stress boundary conditions that are applied to the coarse model. Unfortunately, models using frictionless GBS did not yield convergent solutions when boundary conditions consisted of prescribed stress. To work around this problem, the following procedure has been developed for analyses that include frictionless GBS. First, a coarse mesh model solution is obtained using stress boundary conditions and excluding GBS. The nodal displacements from this solution are then applied as displacement boundary conditions in a subsequent coarse model analysis that includes GBS. Lastly, the nodal displacements from the intermediate coarse model, which included GBS, are interpolated onto the cut boundaries of the submodel, which also uses GBS. The intermediate submodeling step essentially allows the use of displacement controlled boundary conditions for the coarse model analysis. An alternative approach would have been to start with displacement boundary conditions for the coarse model and skip the intermediate submodeling step. However, the problem would then arise of estimating realistic strain rates for the calculation of boundary displacements. One approach is not considered to be clearly better than the other.

A steady state solution is sought where the transient stress changes become negligible. Stresses in the Vostok accretion ice most likely change very little over short time scales. Therefore, the steady state solution is deemed appropriate. Automatic time-stepping is used in ANSYS to increment the solution forward in time, where time acts as a dummy variable without correspondence to actual time scales in the ice. The final times were determined by visual inspection of the stress results. This method is considered adequate because of the following observation. When deviatoric stress boundary conditions were applied, the stress concentrations always *increased* with time to approach steady state values. On the other hand, when hydrostatic stress boundary conditions were applied, stress concentrations always diminished with time. As is clarified after an examination of the model results, stepping the solution further out in time only strengthens the conclusions drawn from the model.

The heat dissipation rate (J m^{-3} s^{-1}) from creep, Q_c, is calculated from the FE model results and the following relation:

$$Q_c = \sigma_{ij}\dot{\epsilon}^c_{ij} \tag{5.1}$$

This quantity represents the rate that irreversible work is converted into heat. In order to calculate the effects of heat dissipation on local temperatures in the Vostok accretion ice, Q_c-values are evaluated at element centroids in the ITJ submodel, then transferred as element loads to a separate, steady state thermal model having an identical mesh. The nodes on the outer faces of the thermal model are prescribed

temperature boundary conditions based on the overall, or *macroscopic*, temperature in the ice. The macroscopic temperature, T, is estimated from an assumed linear function of depth, h_i, below the Vostok drilling station above southern Lake Vostok as follows:

$$T(h_i) = -55°\text{C} + (0.01394°\text{C m}^{-1})h_i \tag{5.2}$$

The value of T is assumed to increase downward from a surface average of -55°C (Petit et al., 1999) to an equilibrium value of -2.7°C along the ice-water interface, where $h_i = 3750$ m. Zero conductive heat flux is assumed through the flat z′ faces of the thermal model. Thus, it is assumed that creep strain rates, which act as thermal body loads, have little variation in the z′ direction. This is a reasonable approximation for the *pure shear*-type of deformation imposed in the Vostok simulation (i.e., plane strain in the limit of mechanical isotropy). These boundary conditions assume zero macroscopic plastic strain in the z′ direction, hence plastic plane strain only along the x′y′ plane. The calculated, steady state temperatures are then given by $T + \Delta T^c$. The term ΔT^c represents the local temperature increase in the ice caused by heat dissipated from creep (equation 5.1).

Finally, the results from the mechanical and thermal FE models are together evaluated to infer regions of internal melting. The melting temperatures, T_m, are calculated by substituting the stress results, from element centroids in the ITJ submodel, into the phase equilibrium condition (2.25). The influence of impurities is not considered in the ITJ Model; therefore, the solute concentration, χ_s, and free surface energy, γ_{SL}, are set to zero. Two melting temperatures are calculated based on stresses in the solid ice: a melting temperature assuming that P_s equals the hydrostatic pressure, σ_h, and a melting temperature assuming that P_s equals the maximum compressive stress, s_3. The first regions in ice to melt would seemingly be oriented normal to the greatest compressive principal stress, s_3. Once the melt had formed, the pressure, P_s, in the adjacent solid could be as high as s_3, but probably not lower than σ_h. Therefore, both σ_h and s_3 are considered for predicting regions of melt, but the latter is used to indicate an *onset* of melt.

The temperature values $T + \Delta T^c$, calculated by the steady state thermal model, are combined with the calculated melting temperatures, T_m, using the following relation:

$$\delta T = T + \Delta T^c - T_m \tag{5.3}$$

δT is calculated at the centroid locations of elements in the ITJ submodel (Figure 5.2b). Elements having positive δT-values have temperatures above their respective stress-dependent melting points. For these cases, the liquid phase is interpreted to be thermodynamically more stable than the solid phase.

Conversely, elements having negative δT-values have temperatures below their respective stress-dependent melting points; the ice in these regions is interpreted to be more stable than the liquid phase. In other words, regions with positive δT-values are associated with an onset of melting.

The ITJ model is based on numerous assumptions regarding material properties and boundary conditions. These assumptions are best tested through comparisons of model results with experimental data. To this end, the ITJ Model is used to simulate three forms of experimental data: (1) previously reported strain rates in polycrystalline ice, (2) observations of localized melting in ice by Wilson et al. (1996), and (3) descriptions of internal melting in ice by Nye and Mae (1972). The anisotropic mechanical model used by Wilson et al. (1996) assumed elastic, perfectly plastic properties. The ITJ Model can therefore supplement their findings with an added perspective on how rate-dependent material properties could influence stress concentrations. No mechanical model was used to supplement the observations of Nye and Mae (1972); in this respect, the ITJ Model can also make a contribution. After simulation of these experimental data, the model is used to predict microscopic stresses and creep rates in the Vostok accretion ice. These data are used to predict onset of internal melting based on stresses and localized heating with the use of equation (5.3). The boundary conditions in this simulation include both zero and small deviatoric stress to represent plausible values for the base of the Antarctic ice sheet.

In order to resolve stresses of anywhere near millimeter-scale in the ITJ submodel, the depth and mesh parameters d_{g2} and FM2, respectively, are minimized without "overly" compromising accuracy. This minimization process is carried out with a mesh sensitivity analysis using different values of mesh parameters d_{g2} and FM2. In addition, model results with and without frictionless GBS are compared.

Mesh Sensitivity of ITJ Model

Numerical analyses of the finite element ITJ Model are carried out to determine the sensitivity of results to mesh parameters FM2 and d_{g2}. The components of the stress boundary conditions are denoted by σ'^{b}_{ij}, where superscript 'b' indicates "boundary" and the apostrophe indicates a value referencing the global frame. A fixed set of stress boundary conditions, temperatures and material properties are used in the mesh sensitivity model so that only the mesh densities vary. The boundary condition stresses consist only of normal components as follows: $\sigma'^{b}_{11} = \sigma'^{b}_{h} - \sigma'^{b}_{s}$, $\sigma'^{b}_{22} = \sigma'^{b}_{h} + \sigma'^{b}_{s}$, and $\sigma'^{b}_{33} = \sigma'^{b}_{h}$, where hydrostatic stress $\sigma'^{b}_{h} = 32.8$ MPa and deviatoric stress $\sigma'^{b}_{s} = 0.05$ MPa. These boundary conditions are justified later in the section "ITJ Model Simulation of Vostok Accretion Ice." Briefly stated, they represent macroscopic plane strain conditions in the x′y′ plane for the creep components of deformation. The applied hydrostatic stress corresponds to 3650 m of ice overburden, while the deviatoric stress represents a typical low value in the basal ice of glaciers (Hobbs, 1974, p. 338). The model temperature is set to -4.1°C to reflect conditions

near the vertical center of the southern Vostok accretion ice. The crystal size, d_{g1}, is set to 0.5 m to reflect a median crystal size in the accretion ice (Jouzel et al., 1999). The Norton creep parameters are assigned the soft crystal values (see page 73) for purposes of applying the mesh sensitivity model. These particular choices for stress, temperature and material properties are very close to those used in the final simulation of the Vostok accretion ice. However, for this mesh sensitivity analysis, it is more important that they are all held fixed so that the only parameters varying are those controlling mesh density.

The stress results had nearly reached steady state values by the final time of 5×10^3 s. All reported stress values are for this final time. Model executions were carried out using six different, randomly-generated, c-axis spherical coordinate sets (1)-(6) (Table 5.1). In each model execution, hydrostatic pressures, σ_h, are evaluated at element centroids in the submodel. These pressures are interpolated onto a path in the z′ = 0.25 m plane, between the central triple junction and the outer cylindrical surface of the submodel. The azimuthal orientation of the path is such that it intersects the centroid of the submodel element containing the maximum σ_h-value.

For each of the six c-axis spherical coordinate sets, analyses are carried out with and without frictionless GBS using four different meshes. Thus, a total of 48 model simulations are executed. The only mesh parameters varied in the mesh sensitivity study are FM2 and d_{g2} (defined on pages 75-76). All analyses use the same FM1-value of 18, and a coarse mesh as illustrated in Figure 5.2. The FM2-values of Meshes 1, 2, 3 and 4 are 13, 9, 5 and 1, respectively. The element z′ dimensions in the submodel for all four meshes are set equal to $d_{g1}/13$. This assignment is made so that the depth, d_{g2}, of the Mesh 1 submodel is equal to d_{g1}. Meshes 1 to 4 become progressively shallower in the z′ direction. The purpose of only varying FM2 in this analysis is to determine a suitable ratio of FM1:FM2 for use later in the Vostok simulation.

Several different stress parameters are defined for comparing the results from different meshes. The *pressure concentration* is defined as the calculated difference between the local hydrostatic stress and that at the model boundary, given by $\sigma_h - \sigma_h'^b$. This parameters emphasizes the effect of anisotropy on the

Set	θ_1	ϕ_1	θ_2	ϕ_2	θ_3	ϕ_3	θ_4	ϕ_4
(1)	34°	264°	18°	195°	57°	280°	19°	19°
(2)	65°	84°	63°	267°	35°	0°	72°	351°
(3)	66°	49°	55°	305°	25°	342°	57°	336°
(4)	68°	359°	264°	69°	40°	67°	45°	135°
(5)	87°	293°	88°	350°	75°	39°	70°	321°
(6)	13°	158°	11°	60°	5°	66°	28°	285°

Table 5.1: Values of randomly-generated c-axis spherical coordinates θ_i, ϕ_i used in the mesh sensitivity study of the Inelastic Triple Junction (ITJ) Model. Subscript i ranges from 1 to 4 and denotes a particular c-axis (local frame) orientation.

maximum calculated hydrostatic stress. The *pressure signal* is defined to be the pressure concentration calculated from Mesh 1. The *discretization error* for Mesh j, where $j \neq 1$, is defined as the difference between the pressure signal and the pressure concentration for Mesh j (i.e., $\sigma_{h,\text{Mesh 1}} - \sigma_{h,\text{Mesh j}}$). In other words, the discretization error in the result from a particular mesh is approximated as the difference between that result and the one from the finest mesh.

The calculated pressure concentrations for analyses without GBS are plotted in Figure 5.3, and those for analyses with GBS are plotted in Figure 5.4. Based on the non-GBS results of Figure 5.3, the Mesh 4 discretization error is far greater than the pressure signal. This is a clear indication of unacceptable results. On the other hand, the Mesh 2 and 3 discretization errors are, for the most part, significantly less than the pressure signals. The pressure signals of the non-GBS analyses range from -0.31 to +0.23 MPa, with extrema about 6 times greater than the applied shear stress of 0.05 MPa. The discretization errors of Meshes 2 and 3 in the non-GBS analyses range from -0.05 to +0.05 MPa, values that are smaller than the pressure signals. In contrast, the discretization errors of the analyses with GBS range from -0.07 to +1.2 MPa, values considerably larger than the pressure signals, which ranged from -0.12 to +0.14 MPa (Figure 5.4). In conclusion, the Mesh 3 results are considered acceptable with a FM1:FM2 ratio of 18:5. Using this same ratio, and taking practical computation times into account, *all* remaining meshes of this study use FM1 and FM2 settings of 26 and 7, respectively, and the d_{g2}-value of Mesh 3 in this sensitivity study, $5d_{g1}/13$.

The discretization errors of the analyses that included GBS are generally larger than the pressure signals, an indication of poor mesh convergence. This is not the case for the analyses that excluded GBS. Also, and importantly, the stresses calculated from the analyses with GBS exhibit dubious patterns of alternating positive and negative pressure signals from element to element in the z′ direction. Due to poor mesh convergence, and dubious alternation patterns in pressure signals, there is little confidence in the validity of results from models that include GBS. For these reasons, *GBS is excluded from all remaining analyses in this study.* For reasons that are unclear, frictionless contact and anisotropic creep do not appear to work well together. It is hoped that future models can explore the use of a viscous GBS mechanism, possibly involving user-developed interface elements, with more reasonable results.

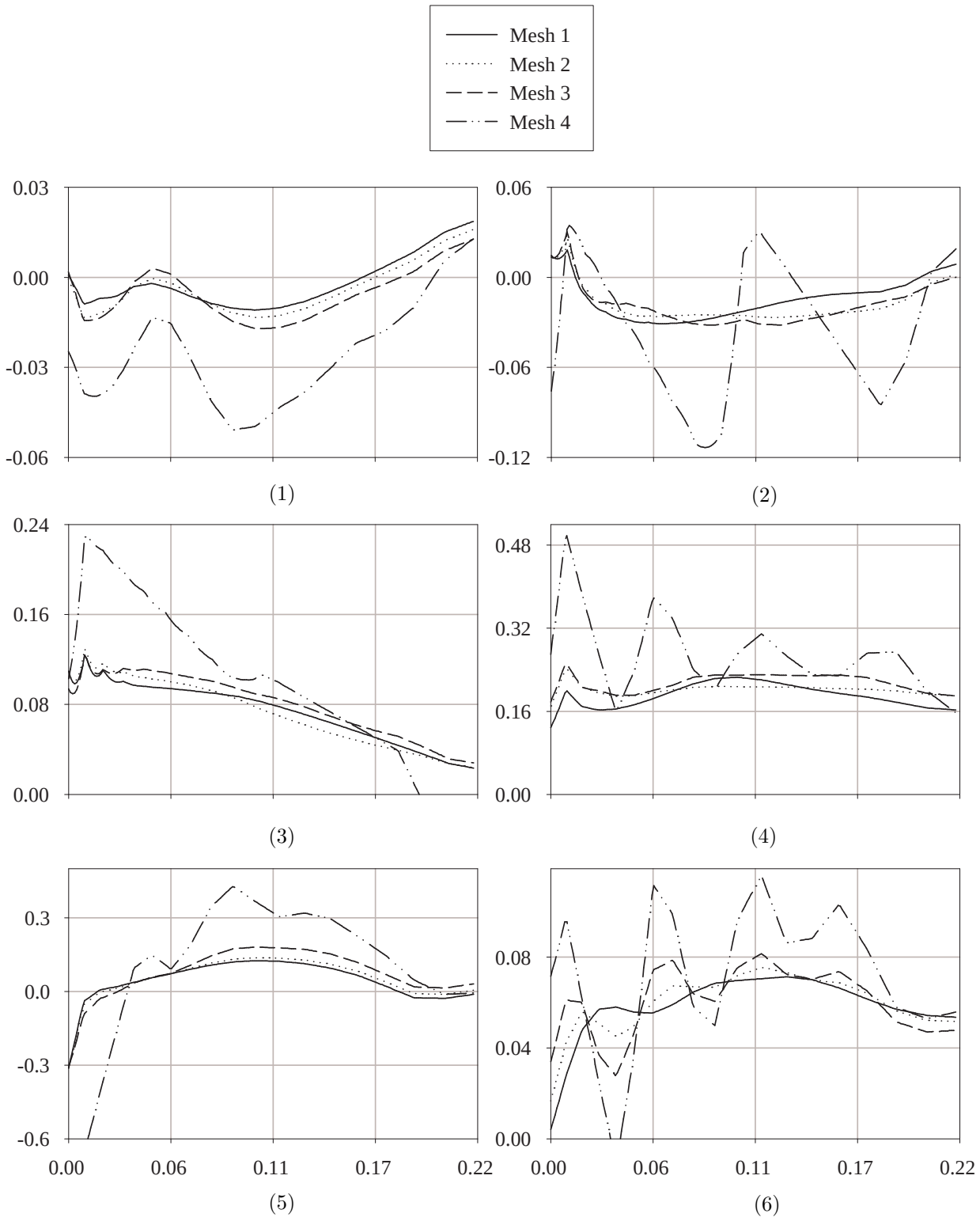

Figure 5.3: Path plots of calculated pressure concentrations (MPa) in central $z' = 0.25$ m plane of ITJ submodel for six c-axis spherical coordinate sets (1)-(6). Grain boundary sliding (GBS) is not included. Abscissae represent radial distances (m) from the central triple junction.

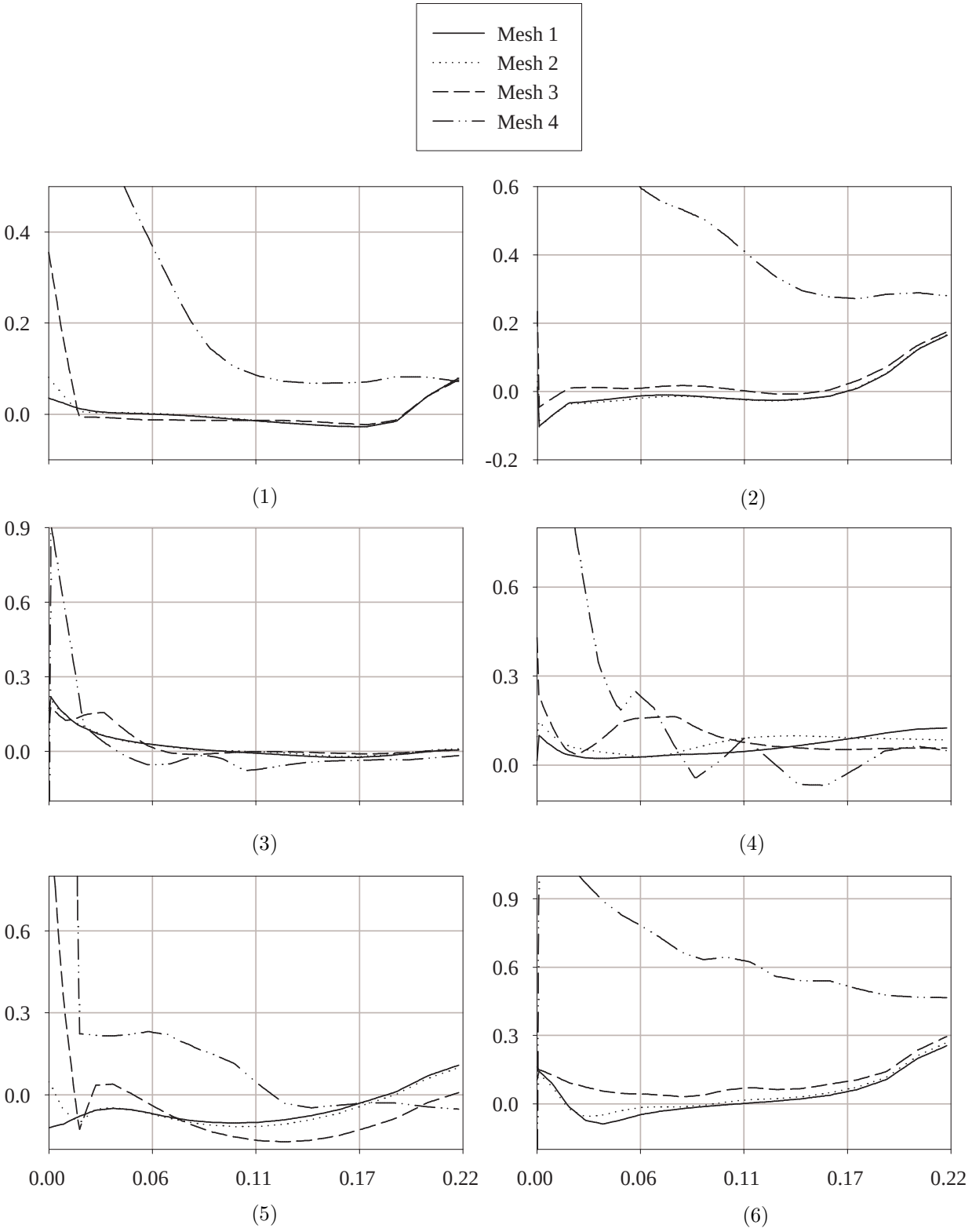

Figure 5.4: Path plots of calculated pressure concentrations (MPa) in central $z' = 0.25$ m plane of ITJ submodel for six c-axis spherical coordinate sets (1)-(6). Grain boundary sliding (GBS) is included. Abscissae represent radial distances (m) from the central triple junction.

ITJ Model Simulations of Experiments on Polycrystalline Ice

Strain Rates in Ice

In this section, the data from sixty ITJ Model executions were compared to past experimentally-measured strain rates in polycrystalline ice. The temperature in the model was set to -1°C and a uniaxial compressive stress, σ'^{b}_{y}, of 0.286 MPa was applied in the y′ direction. The compressive stress was ramped linearly between time t = 0 and 1 s, then held constant until the final time of 5×10^3 s when steady state conditions were apparent. Twenty c-axis spherical coordinate sets were randomly generated in the ANSYS routine and exported to data files. For brevity, the c-axis spherical coordinates have been omitted. Three different material combinations were used for each c-axis coordinate set, yielding a total of sixty executions.

In order to apply these numerical analyses to the experiments of Nye and Mae (1972) and Wilson et al. (1996), the crystal c-axes were oriented randomly in the x′y′ plane, thus bearing similarity to type S2 columnar ice (Michel, 1978, p. 69). This type of ice consists of grains elongated in the vertical direction, with c-axes randomly oriented in the horizontal plane. This type of ice tends to eventually form below the surface of lakes having surfaces that are too agitated to nucleate platelets with c-axes that were initially vertical (Petrenko and Whitworth, 1999, p. 287). Ice with these crystal orientations is considered to adequately represent isotropic polycrystalline ice.

Three different materials were used in this simulation. The *Soft 1* material used soft crystal Norton creep parameters (Table 4.3) with Hill parameters R_b and R_n of $3^{1/2}$ and $(3/2)^{1/2} \times 10^6$, respectively. For this material, the ratio of basal (i.e., 13- and 23-components) to non-basal creep strain rates were about 10^{12} for a given deviatoric stress (see equations 4.24). The *Soft 2* material also used soft crystal Norton creep parameters, but with Hill parameters R_b and R_n of $3^{1/2}$ and $(3/2)^{1/2} \times 10^2$, respectively (see page 71 for explanation). Use of the Soft 2 material was intended to examine the sensitivity of the ITJ Model results to faster non-basal components of creep, perhaps emulating the effects of minor dislocation glide along the crystallographic prism planes. Finally, the *Hard* material used the hard crystal Norton creep parameters with Hill parameters R_b and R_n of $3^{1/2}$ and $(3/2)^{1/2} \times 10^6$, respectively.

The crystal dimension, d_{g1}, was set to 5 mm; however, this setting would not effect model results since the material constitutive law is unaffected by grain size. In accordance with conclusions from the mesh sensitivity study (page 81), the submodel depth, d_{g2}, was set equal to $5d_{g1}/13 = 1.92$ mm, and mesh density parameters FM1 and FM2 were set equal to 26 and 7, respectively.

The sixty model executions required 16 hours of continuous computing time on a personal 2 GHz computer. The calculated strain rates in the y′ direction (see page 75) are plotted in Figure 5.5 along with

experimental values from Barnes et al. (1971) and values from the PRC glide equation of Goodman et al. (1981). The calculated y′ strain rates shown in Figure 5.5 represent values averaged from the centroids of elements in the submodel.

Barnes et al. (1971) carried out compression tests on cylinders of polycrystalline ice between temperatures of 0 and -48°C. For a uniaxial load of 0.29 MPa at -2°C, the secondary creep rate was about 1.7×10^{-8} s^{-1}. This rate was faster than predicted from their numerical fit using a sinh function of stress, which showed better experimental agreement at temperatures below -8°C where dislocation glide was thought to dominate creep. According to the sinh law of Barnes et al. (1971), an axial stress of 0.286 MPa, a

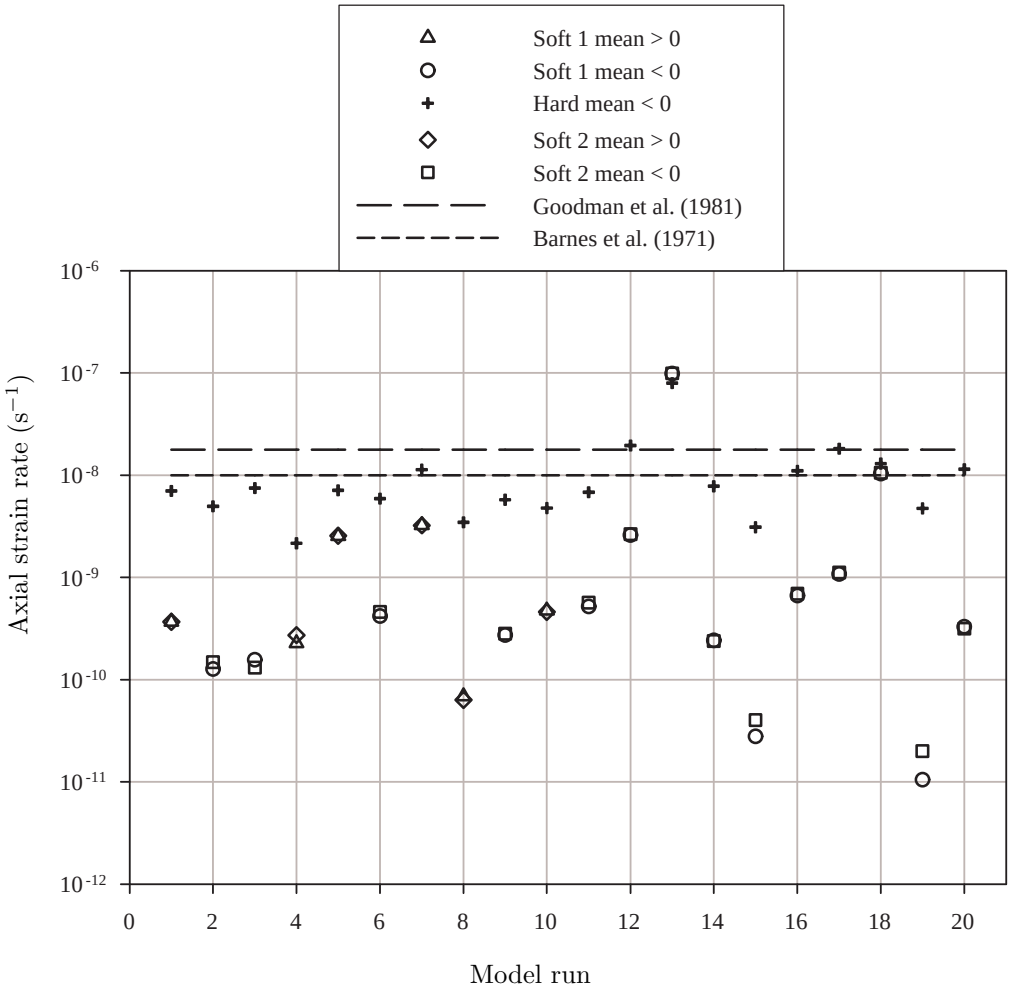

Figure 5.5: Plot of y′ strain rates calculated from ITJ Model for comparison with experimental values from Barnes et al. (1971) and dislocation creep equation of Goodman et al. (1981). The axial stress is 0.286 MPa. Plot based on Barnes et al. (1971) uses their sinh function of stress corrected to a temperature of -1°C with Arrhenius equation (4.18) and $Q = 78.1$ kJ mol^{-1}. Plot based on Goodman et al. (1981) uses PRC glide equation (4.14) generalized to 3D Glen's flow law. Mean strain rates > 0 indicated deformation in a direction *opposite* to applied stress.

temperature correction using creep equation (4.18), and an activation energy of 78.1 kJ mol^{-1} (Table 4.1), the axial secondary creep rate would be 10^{-8} s^{-1} (Figure 5.5). This is in excellent agreement with the average strain rate of 1.1×10^{-8} s^{-1} predicted by the ITJ Model using hard crystal properties. Based on the PRC glide equation (4.14) from Goodman et al. (1981) generalized to the 3D Glen's flow law for ice, the axial strain rate would be 1.8×10^{-8} s^{-1} (Figure 5.5). Thus, the results of the ITJ Model using hard crystal properties appear to be within a factor of two of experimentally-supported secondary creep rates dominated by dislocation creep. The actual, previously recorded strain rates at temperatures around -1°C are considerably higher than those predicted by dislocation creep models. For example, the strain rate measured by Barnes et al. (1971) was about twice as fast as their prediction using the sinh function of stress, which showed much better experimental agreement at temperatures below -8°C. Near 0°C and at a uniaxial load of 0.29 MPa, Mellor and Testa (1969) measured strain rates of about 6×10^{-7} s^{-1}, nearly two orders of magnitude greater than would be expected from creep dominated by dislocation glide. They attributed this high compliance to grain boundary melting or the presence liquid films between ice crystals.

The strain rates from the ITJ Model using Soft 1 and Soft 2 materials were in poor agreement with past experimental data (Figure 5.5). The mean calculated axial strain rates of the soft crystals were both positive and negative, and several orders of magnitude less than those of the hard crystals. The mean strain rates in some analyses were actually *opposite* (i.e., $\dot{\epsilon}'_y > 0$) to the direction of the applied load. While these results were non-physical, they did provide an interesting extreme case of an aggregate of compliant crystals each constrained to deform along their crystallographic basal planes. As deformation proceeded, creep near grain boundaries was strongly impeded due to differences in strain rates associated with anisotropy. These interferences resulted in localized accumulations of stresses and strain energy densities along grain boundaries (demonstrated later in the chapter). The average strain rates always decreased from their initial values as stress concentrations accumulated along grain boundaries. The Soft 1 and Soft 2 materials were compliant to the extent that the aggregate essentially "locked up," with associated stress concentrations taking on peak values (i.e., higher than less compliant hard crystals).

Calculations from the ITJ Model correctly indicated that polycrystalline ice is three orders of magnitude less compliant than single crystals oriented for basal glide. For a uniaxial stress and temperature of 0.286 MPa and -1°C, respectively, the axial strain rates of single soft and hard crystals were 3.3×10^{-5} and 2.0×10^{-5} s^{-1}, respectively (equation 4.27 and Table 4.3). These values were about three orders of magnitude greater than strain rates calculated by the ITJ Model. This finding was in excellent agreement with past experimental data on polycrystalline and monocrystalline ice (Weertman, 1973; Duval et al., 1983). Hexagonal polycrystals are much less compliant than individual crystals, optimally oriented for

basal glide, due to a limited number of slip directions. This has been attributed to the blocking effect of grain boundaries on gliding dislocations (Dudley et al., 1994; Liu and Baker, 1994; Baker et al., 2000). Interference at grain boundaries prevents the individual crystals from reaching true steady state creep. The soft crystal properties assumed that true steady state creep was reached, where the mobile dislocation density has reached a stationary value. The results from ITJ Model using soft crystals overestimated stress relaxation along the basal plane, causing larger "back stresses" along grain boundaries and "locking up" of the polycrystal.

In conclusion, the strain rates calculated by the ITJ Model, using hard crystal properties, were in satisfactory agreement (i.e., within factor of two) with previously observed secondary creep rates in polycrystalline ice at temperatures sufficiently low ($\lesssim -8°C$) that dislocation creep dominates. At warmer temperatures, the model results increasingly deviated from experimental data. The cause for this was probably GBS and liquid water films along grain boundaries, not included in the model, which would increase the compliance of ice (Mellor and Testa, 1969; Barnes et al., 1971). The deviation of the model from experimental data at warmer temperatures was consistent with the use of a deformation mechanism limited to basal slip. The strain rates calculated by the ITJ Model were also self-consistent in that they closely matched those predicted by the DM map, which was originally used to help decide on the significant deformation mechanisms involved.

Experiment of Wilson et al. (1996)

The ITJ Model next simulated the following from the Wilson et al. (1996) experiment: stress concentrations, melting temperatures, and spot temperatures associated with heat dissipation from creep. This test imposed a constant strain rate of 9×10^{-5} s^{-1} on polycrystalline ice in plane strain conditions at -1°C. The crystals had c-axes randomly oriented in the plane of strain. During the course of the experiment, the axial loads progressively decreased from about 0.5 to 0.1 MPa. Internal melting was localized near grain boundaries and first observed at an intermediate stress of about 0.26 MPa. They simulated the experiments with an anisotropic elastic, perfectly plastic model that used a yield stress of 2×10^5 N m^{-2} in shear along the basal plane. Based on their experimental observations, GBS provided a negligible contribution to deformation and was thus excluded from their model. They concluded that "high spot temperatures" and heat generation rates associated with regions of high shear strain were probably the main causes of internal melting. The comment was made that a rate-dependent model, perhaps addressing creep or viscoplasticity, may have provided an analytical contribution.

The ITJ Model simulation of the Wilson et al. (1996) experiment provided a different interpretation of the important mechanisms of internal melting. This simulation consisted of the same sixty model

executions that were applied in the simulation of strain rates in polycrystalline ice (see page 84). The applied axial stress of 0.286 MPa, in the ITJ Model, was similar to the value ($\approx$ 0.26 MPa) when melting was first observed in the Wilson et al. (1996) experiment. Although plane strain was enforced in the experiment, it was not applied in the numerical simulation. The results of preliminary analyses with and without plane strain were compared. Their differences with regard to internal melting were not sufficiently significant to merit a separate set of numerical analyses enforcing plane strain.

All reported results of the ITJ Model were evaluated at element centroid locations in the central z′ = 2.5 mm plane of the submodel. The following definitions were made to streamline presentation of the results: $\sigma_{h,\max}$ = maximum magnitude of hydrostatic stress (i.e., $-\sigma_{ii}/3$); $s_{3,\max}$ = maximum magnitude of most compressive principal stress, s_3; $\sigma_{b,\max}$ = maximum resolved shear stress along the basal plane; $T^{\sigma}_{m,\min}$ = minimum melting temperature assuming pressure P_s equals the hydrostatic stress in solid; $T^{s}_{m,\min}$ = minimum melting temperature assuming pressure P_s equals the magnitude of s_3 in the solid; and $\Delta T^{c}_{\max}$ = maximum temperature increase caused by heat dissipation from creep. The calculated values of these extrema are shown in Figure 5.6. The values of $\sigma_{h,\max}$, $s_{3,\max}$, $\sigma_{b,\max}$, $T^{\sigma}_{m,\min}$, and $T^{s}_{m,\min}$ averaged over the twenty model executions for Soft 1, Soft 2 and Hard materials are listed in Table 5.2.

The greatest calculated stress concentrations always occurred along grain boundaries and the triple junction. The values of $\overline{s}_{3,\max}$ were an order of magnitude larger than the applied stress of 0.286 MPa. It was immediately evident that these stress concentrations would cause noteworthy depressions in the melting point. The calculated stress concentrations and melting temperatures for the Soft 1 and Soft 2 materials were practically indistinguishable. This demonstrated that models including rate-limiting (slower) deformation mechanisms 12 and 4 orders of magnitude slower than the fastest mechanism, basal glide,

	Soft 1	Soft 2	Hard
$\overline{\sigma}_{h,\max}$	1.8 MPa	1.8 MPa	1.4 MPa
$\overline{s}_{3,\max}$	3.5 MPa	3.5 MPa	2.7 MPa
$\overline{\sigma}_{b,\max}$	1.3 kPa	1.4 kPa	22 kPa
$\overline{T}^{\sigma}_{m,\min}$	-0.14°C	-0.14°C	-0.11°C
$\overline{T}^{s}_{m,\min}$	-0.27°C	-0.27°C	-0.20°C

Table 5.2: Average calculated extrema in stress and melting temperature from the ITJ Model simulation of the Wilson et al. (1996) experiment. The calculated extrema were averaged over each of the twenty model executions for Soft 1, Soft 2 and Hard materials to yield the values listed. $\overline{\sigma}_{h,\max}$ = average of maximum of hydrostatic stress, $\overline{s}_{3,\max}$ = average of greatest magnitude in compressive principal stress s_3, $\overline{\sigma}_{b,\max}$ = average of maximum resolved shear stress along basal plane, $\overline{T}^{\sigma}_{m,\min}$ = average of minimum melting temperature assuming pressure P_s equals hydrostatic stress, and $\overline{T}^{s}_{m,\min}$ = average of minimum melting temperature assuming pressure P_s equals compressive principal stress s_3.

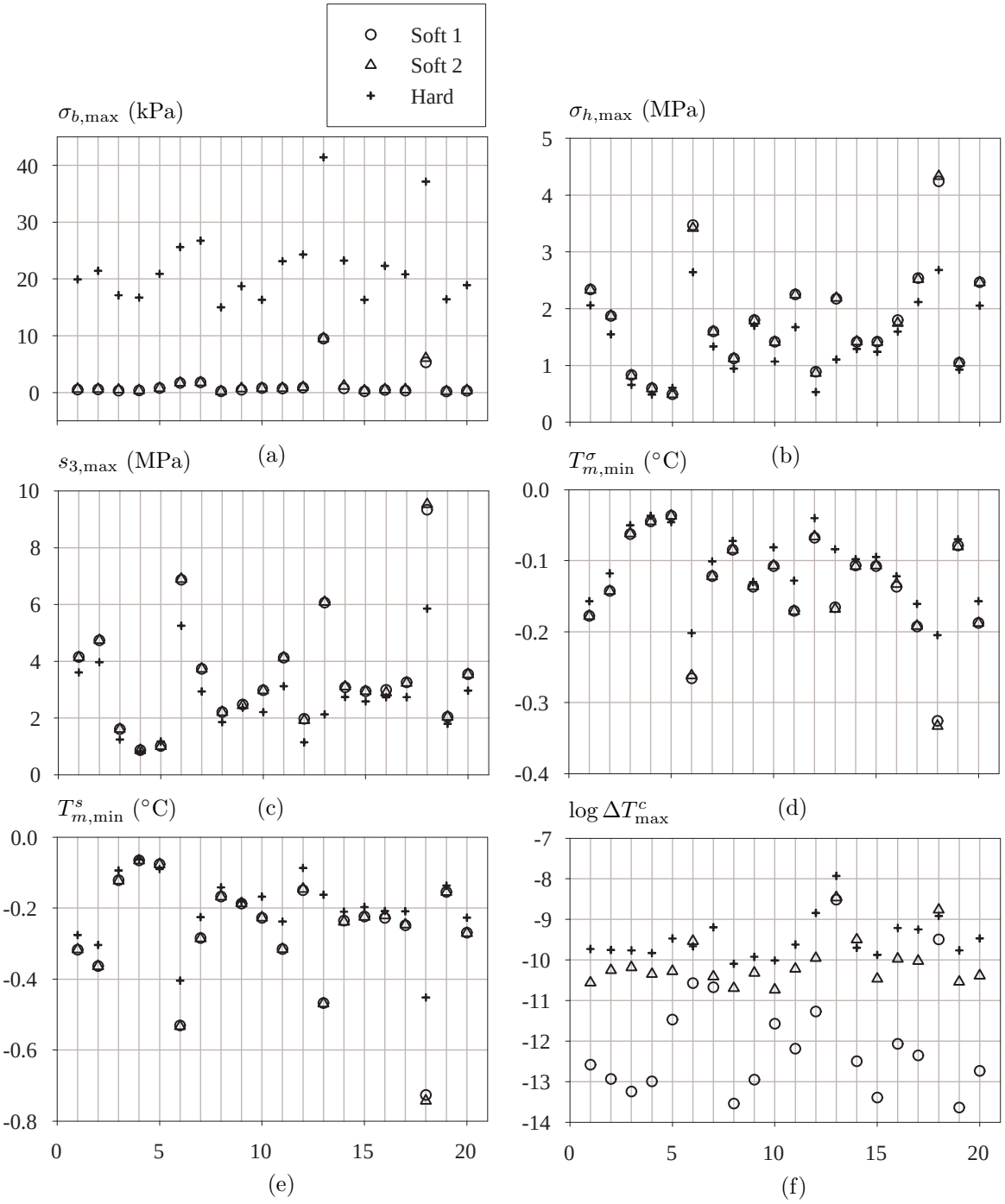

Figure 5.6: Calculated extrema in stresses, melting temperatures and spot temperatures from the ITJ Model simulation of the Wilson et al. (1996) experiment. Abscissae values index the different spherical coordinate set numbers that describe the c-axis orientations. The spherical coordinates themselves are not included. $\sigma_{b,\max}$ = maximum resolved shear stress along basal plane, $\sigma_{h,\max}$ = maximum magnitude of hydrostatic stress, $s_{3,\max}$ = maximum magnitude of most compressive principal stress, $T^{\sigma}_{m,\min}$ = minimum melting temperature assuming pressure P_s equals hydrostatic stress, $T^{s}_{m,\min}$ = minimum melting temperature assuming pressure P_s equals most compressive principal stress, and $\Delta T^{c}_{\max}$ = maximum temperature increase caused by heat dissipation from creep.

would not produce appreciably different stress results. In other words, the influence of minor slip along the crystallographic prism planes or grain boundaries would probably not change the stress results of the analyses in a significant way.

There was an interesting, inverse (not necessarily linear) relationship between $\sigma_{b,\max}$ and both $\sigma_{h,\max}$ and $s_{3,\max}$ of the hard and soft crystal analyses. The hard crystal results showed much greater $\sigma_{b,\max}$-values than those of the soft crystals. Conversely, soft crystal results showed greater pressures $\sigma_{h,\max}$ and $s_{3,\max}$ than those of the hard crystals. The explanation for this is as follows. The soft crystals were more compliant than hard crystals, and thus tended to undergo greater shear stress relaxation along the basal plane. This greater degree of localized relaxation was directly offset by the transfer of larger "back stresses" to grain boundaries. Hence, the numerical results using soft crystal properties had smaller values of $\sigma_{b,\max}$, and greater values of both $\sigma_{h,\max}$ and $s_{3,\max}$, than the results using hard crystal properties. On a different but related note, the calculated $\sigma_{b,\max}$-values for hard crystals were very close to the yield stress of the elastic, perfectly plastic model of Wilson et al. (1996). This indicated that, in all of the ITJ Model executions, basal plane shear stresses relaxed to a much greater degree than would be the case for an elastic, perfectly plastic model. Following the reasoning above, the ITJ Model should therefore predict larger pressure concentrations and associated melting point depressions.

A significant conclusion of this simulation involves the relative importance of pressures and heating on the onset of internal melting in polycrystalline ice. The calculated temperature changes, $\Delta T^c_{\max}$, associated with heat dissipation were many orders of magnitude smaller than the stress-induced depressions in melting temperature. This was evident from a comparison of Figure 5.6f and the last two rows of Table 5.2. This finding was different from that of Wilson et al. (1996) that high spot temperatures from heating were a main cause of internal melt, and that pressure concentrations were of less importance. One likely cause for this difference in conclusion was the use of a rate-dependent creep material in the present study, which allowed greater stress relaxation along the basal plane. This stress relaxation, and the associated reduction in macroscopic (i.e., mean) strain rate, was closely linked to the localized accumulation of pressure near grain boundaries.

Typical ANSYS contour plots of most compressive principal stress, s_3, and basal plane shear stress, σ_b, at times t = 1 and 5×10^3 s are displayed in Figure 5.7. The stresses calculated at time t = 5×10^3 s approximate the steady state solution. The results shown in Figure 5.7 were generated using hard crystal properties and c-axis alignments of the twentieth spherical coordinate set. This coordinate set was chosen because it yielded intermediate final stress extrema (see Figure 5.6). The c-axes were oriented in the x′y′ plane, with spherical coordinates ϕ_1, ϕ_2, ϕ_3, and ϕ_4 of 10°, 197°, 44°, and 252°, respectively. The stresses were evaluated at element centroids in the bisecting z′ = 2.5 mm plane of ITJ submodel.

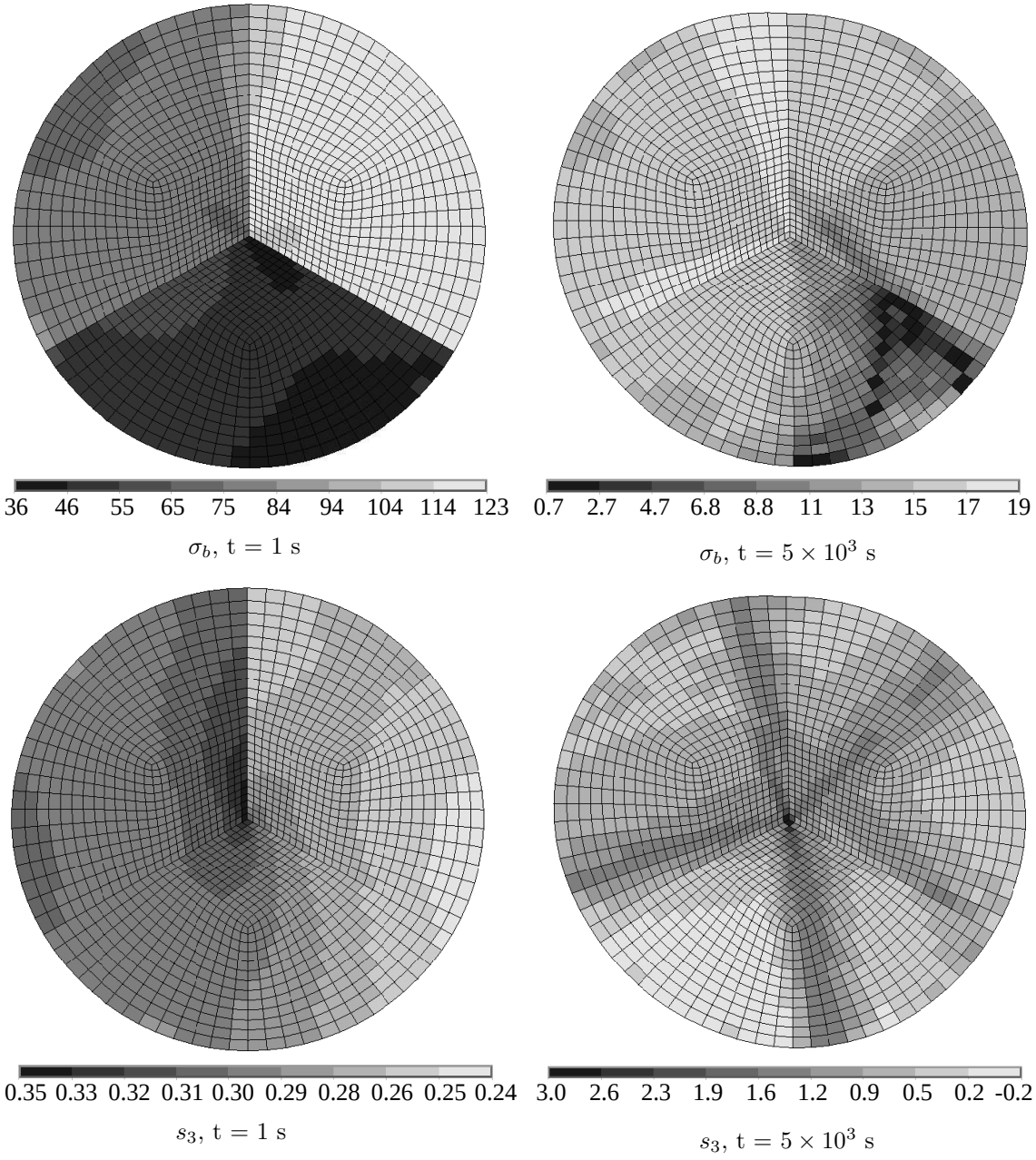

Figure 5.7: ANSYS contour plots of calculated most-compressive principal stress, s_3 (MPa), and basal plane shear stress, σ_b (kPa), from the ITJ Model simulation of the Wilson et al. (1996) experiment. Results shown are for times (t) of 1 and 5×10^3 s, the latter approximating the steady state solution. Compressive stresses are positive. The sections are along the bisecting $z' = 2.5$ mm plane of the ITJ submodel.

At the initial time of 1 s, the magnitude of shear stress σ_b in crystal i ($i = 1$ to 3) was approximately equal to the resolved value of $0.286 \sin\theta_i \cos\theta_i$ MPa. At this time, the maximum principal stress, $s_{3,\max}$, differed from the applied load of 0.286 MPa by about 20% as a result of the initial anisotropic elastic response. With increasing time, the σ_b-values relaxed to values much lower than 20 kPa. This relaxation process transferred localized pressure to grain boundaries and the triple junction, where strain interference

between neighboring crystals was greatest. By the final time, the principal stress, s_3, near the triple junction was an order of magnitude greater than the value of the applied load. This example typified results of the ITJ Model. The largest observed magnitude in s_3 from analyses using hard crystal properties was 5.8 MPa, calculated from the eighteenth c-axis spherical coordinate set. This value was twenty times greater than the applied load. It was also noted that the σ_{12} shear stress always increased with time at the sites where pressures were most concentrated. Thus, the relaxation process of shear stress along the basal plane was also accompanied by the localized accumulation of shear stress along non-basal planes (e.g., crystallographic prism planes in ice).

The ITJ Model simulation of the Wilson et al. (1996) experiment, using hard crystal properties, produced an average melting temperature $\overline{T}^{s}_{m,\min}$ of -0.20°C. The minimum value of -0.45°C was calculated using the eighteenth c-axis coordinate set (Figure 5.6). These temperature depressions were orders of magnitude greater than the calculated spot temperature variations associated with heat dissipation. However, they are still inadequate to account for the melting observed by Wilson et al. at a temperature of -1°C. One likely cause for this shortfall were the relatively coarse element sizes compared to the possible scales of internal melting. As mesh densities were refined in preliminary model studies, stress concentrations increased in magnitude while decreasing in size. Another possible cause for the shortfall in predicted melting temperatures was the lack of a viscous GBS mechanism in the model. In past studies, the observed increase in compliance of polycrystalline ice at temperatures warmer than about -8°C has been attributed to GBS and intergranular melting. Still another possible cause for the shortfall in calculated melting point depression was the continuum assumption that deformation is distributed over an infinite number of slip planes. In reality, slip bands have been observed in the deformation of ice (and metals) (Nakaya, 1958; Gold, 1963). Stress relaxation concentrated along slip bands may produce localized stress concentrations, possibly larger than those calculated by the ITJ Model.

Experiments of Nye and Mae (1972)

Nye and Mae (1972) carried out a series of bending and indentation experiments on polycrystalline ice to examine the effects of nonhydrostatic stress on microscopic melt processes. The ice consisted of clear, candle-shaped grains, 5-20 mm in size, that were elongated in the direction of growth. The crystal c-axes were roughly orthogonal to the growth direction, which tended to run parallel to the water veins. The triple junctions were monitored with a microscope from the top of an ice-water bath maintained at 0°C. A three-point bending apparatus was used to observe the melting effect of a shear stress on a grain boundary. No melting was observed in this case, their conclusion thus being that a shear stress as great as 0.07 MPa on a grain boundary produced no noticeable phase change.

In another set of experiments using of a four-point bending apparatus, observations were made of melting along grain boundaries subjected to normal stresses. The ice sample was bent in such a way as to produce either a tensile or compressive stress of 0.26 MPa in a given region of interest (Figure 5.8). After a tensile stress had been applied for 40 minutes, water lenses were apparent in the horizontal grain boundary oriented parallel to the direction of tension (Figure 5.8a). The direction of bending was reversed in order to apply an equal compressive stress in the same region. Water lenses were then seen freezing along the horizontal grain boundary and forming along the adjacent grain boundary oriented normal to the direction of compression. Figure 5.8b shows the sample ten minutes after the tensile stress had been replaced by a compressive one.

One of their conclusions was that water lenses in ice tended to first form along grain boundaries oriented normal to the maximum compressive stress. They explained melting in grain boundaries oriented parallel to tension by a GBS mechanism of plastic yielding along crystal interfaces (Nye and Mae, 1972, Fig. 9). This concept was illustrated with a free body diagram, which showed that ice containing weak crystal interfaces would be subjected to compressive stresses directed normal to the direction of applied

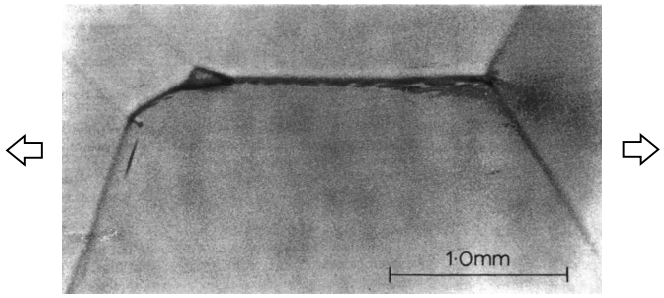

(a)

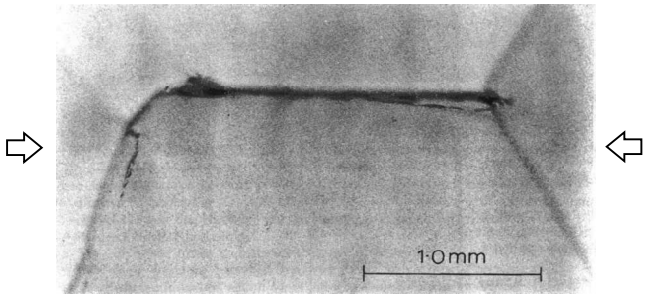

(b)

Figure 5.8: Image of melting along grain boundaries in four-point bending experiments by Nye and Mae (1972). (a) Water lenses forming along central grain boundary oriented parallel to tension. After tensile force was replaced with a compressive one, (b) lenses formed along adjacent grain boundary oriented normal to direction of compression.

tension. According to this mechanism, the application of a tensile load could cause melting along grain boundaries oriented normal to the load direction. They noted the complicating effects of creep and GBS on stress variations in ice, and addressed the thermal part of the problem involving heat exchange between evolving water veins and lenses.

The twenty ITJ Model executions using hard crystal material properties, which were also used to simulate strain rates in polycrystalline ice (page 84) and the Wilson et al. (1996) experiment (page 87), were compared with the observations of Nye and Mae (1972). The calculated stress concentrations (Figure 5.6) could account for the observed melting along grain boundaries. For a uniaxial compressive stress of 0.286 MPa, the average calculated *minimum* melting temperature $\overline{T}^{s}_{m,\min}$ was -0.20°C (Table 5.2). Although the applied stress exceeded that used in Nye and Mae (1972) by 10%, the results can still be generalized to their experiments, which maintained the ice temperature very close to 0°C with the use of a saline bath.

A separate ITJ Model analysis was carried out to compare the calculated melting temperatures for tension and compression. In this simulation, hard crystal material properties were used and the applied stress was set to 0.26 MPa to match that used by Nye and Mae (1972). All other model settings matched those of the sixty executions described on page 84. The crystal c-axes were oriented in the global $x'y'$ plane using the following, randomly-generated spherical coordinates: ϕ_1, ϕ_2, ϕ_3, ϕ_4 = 137.24°, 270.59°, 192.64°, 240.48°, respectively. The calculated melting temperature, T^s_m (°C), evaluated at element centroids in the $z' = 2.5$ mm plane of the ITJ submodel, are contoured in Figure 5.9. In this particular analysis, the lowest T^s_m-values were along the grain boundary oriented normal to the direction of compression. This suggested preferable melting along a grain boundary normal to the direction of compression, consistent with observations by Nye and Mae. However, low values of T^s_m did not occur along the grain boundary oriented parallel to the direction of tension. In this respect, the model did not reproduce observations by Nye and Mae. Additional numerical analyses of distributions in melting temperature, using different c-axis orientations, showed no obvious pattern between direction of applied stress and locations of melting.

The regions of internal melt predicted by the ITJ Model occurred near grain boundaries, with the most unstable areas coincident with the central triple junction. No patterns were evident between c-axis orientations and the distributions in stress concentrations and melting temperatures. Nor were predicted areas of melt found to be along grain boundaries oriented normal to an applied compression or parallel to an applied tension, as was observed by Nye and Mae (1972). This negative finding is considered to be a clue about the prevalent deformation mechanisms in ice near the macroscopic melting point. Nye and Mae explained the pattern between locations of intergranular melting and the direction of applied loads on the presence of grain boundaries intrinsically weak in shear. That the ITJ Model lacked a GBS mechanism,

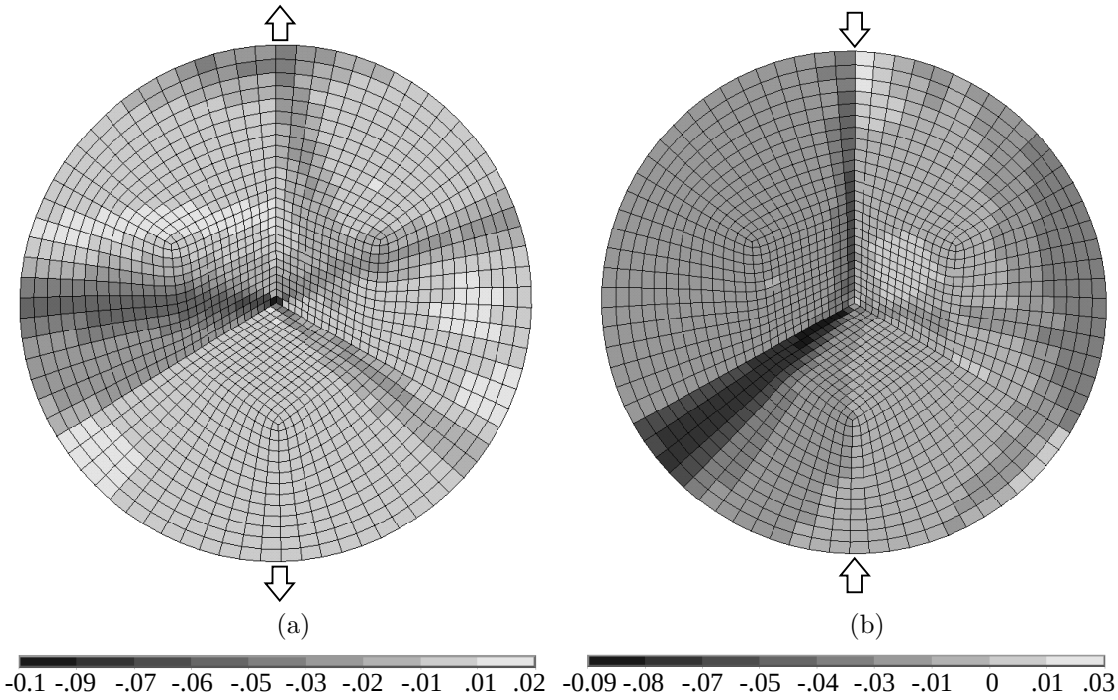

Figure 5.9: ANSYS countour plots of calculated melting temperature, T_m^s (°C), from the ITJ Model simulation of the experiments by Nye and Mae (1972). The results shown are for a time of 5×10^3 s and approximate the steady state solution. T_m^s is the melting temperature assuming that the pressure P_s equals the most compressive principal stress, s_3. The displayed section is along the central $z' = 2.5$ mm plane of the submodel. The magnitude of the applied (a) tensile and (b) compressive stress is 0.26 MPa.

and failed to show a dependence of incipient melt localities on grain boundary orientation, was interpreted to be further evidence that GBS processes have a significant effect on internal stress distributions in ice near the melting point.

The results of the ITJ Model indicated that stress concentrations in ice, under a compression of 0.286 MPa, could account for intergranular melting within several tenths of a degree, and as much as 0.45°C, of the macroscopic melting point. These results also conclusively showed that heat dissipated in ice from anisotropic creep would cause negligible temperature variations. The numerically calculated melting temperatures were not found to depend on the orientation of grain boundaries relative to the macroscopic stress direction, contrary to the findings of Nye and Mae (1972). This discrepancy was attributed to the exclusion of a GBS mechanism. The strain rates simulated by the model were very consistent (i.e., within a factor of two) with previously reported values for polycrystalline ice not so near the melting point (i.e., $\lesssim -8$°C), where overall deformation rates are dominated by dislocation creep and not GBS. This finding seemed quite natural considering that the ITJ Model lacked a GBS mechanism. The model underestimated melting temperature depressions by at least a factor of two considering the

experimental observations by Wilson et al. (1996) on internal melting in ice at -1°C. This discrepancy was attributed to insufficient finite element mesh densities, lack of a viscous GBS mechanism, and the continuum assumption of an infinite number of slip planes in creep, when in reality basal glide tends to concentrate along discrete planes (Nakaya, 1958; Gold, 1963).

ITJ Model Simulation of Vostok Accretion Ice

In the last section, the ITJ Model was shown to produce axial strain rates that compared reasonably well with results from past studies on polycrystalline ice (Barnes et al., 1971; Goodman et al., 1981). The simulated stress concentrations associated with anisotropic elasto-creep could account for observations of melt between deforming ice crystals (Nye and Mae, 1972), although the predicted melting point depressions fell short of observed values (Wilson et al., 1996) by at least a factor of two. The model was next used to simulate the microscopic stresses and melting temperatures in the Vostok accretion ice of Eastern Antarctica. This pursuit could have implications for the prediction of intergranular liquid water habitats (Price, 2000; Siegert et al., 2003), permeability of ice to contaminants and gases (Nye and Frank, 1973; Lliboutry, 1993; Knight, 1997), and the curious manner by which sediment particles become entombed in the accretion ice (Royston-Bishop, in press).

Lake Vostok is located about 4 km beneath the ice sheet of Eastern Antarctica. It is one of the largest lakes on earth, with a north-northwest oriented long axis (Studinger et al., 2003) of 230 km (length) and shorter axis of up to 50 km (Kwok et al., 2000). The deep ice core drilling project at the Russian Vostok station (78°28'S, 106°48'E) commenced in 1990 during the 35^{th} Soviet Antarctic Expedition (Russian Federation, 2001; Victor, 2003). The drilling stopped in 1998 at a borehole depth of 3623 m, about 120 m above the ceiling of Lake Vostok. Samples from the deep ice cores have extended the paleoclimate records back to include the last four glacial-interglacial cycles over the last 420,000 years (Petit et al., 1999). In addition, the discoveries of microorganisms in Vostok accretion ice samples (depths > 3539 m) have suggested that frozen, high pressure environments can sustain microbial life (Priscu et al., 1999; Karl et al., 1999).

Analyses of airborne radar data by Siegert et al. (2000) indicate that the base of the ice sheet entering northern Lake Vostok is melting. This has been attributed to lower melting temperatures induced by greater pressures in the deeper part of the ice sheet. Interpretations of radar and GPS data by Bell et al. (2002) indicate that the base of the ice sheet flowing into southern Lake Vostok is accreting at rates of 0.7 to 3.8 cm yr^{-1}, with the fastest rates near the lake margins. This pattern of accretion pertains to the ice along the flowline passing southern Lake Vostok beneath the drilling station.

The thickness of the ice sheet over Lake Vostok decreases in a north to south direction from about

4300 to 3700 m (Studinger et al., 2003). The surface of the ice sheet above the lake is smooth, with a gradual southward dip of ∼60 m over the length of the lake. These numbers indicate a ratio of surface dip to lake ceiling dip of about 1:10 in opposite directions. This ratio is close to the value of 1:11 expected for isostastic equilibrium, where vertical forces are balanced by fluid pressures.

The regional ice flow around Lake Vostok is in an eastward direction from the Ridge B divide, which is located several hundred kilometers west of the lake. The ice sheet west and east of Lake Vostok flows normal to the surface elevation contours (Kapitsa et al., 1996; Kwok et al., 2000). The flow direction of the ice surface diverts slightly south over the lake, an observation attributed to the southward dip of the ice sheet surface over the lake. The surface ice flow velocities range from 2.0 to 4.5 m yr^{-1} over southern Lake Vostok, reaching a maximum value near the drilling station. Thus, the flow of the ice sheet surface over the lake varies in both direction and magnitude. This, by definition, indicates shear strain rates in the ice.

Lake Vostok occupies a subglacial topographic trough characteristic of a rift basin (Kapitsa et al., 1996), with a steep linear eastern margin (Studinger et al., 2003), that is infilled with hundreds of meters of sediment (Masolov et al., 2001). Recent microseismicity, along with contrasts in local gravity and magnetic fields across the lake, are further indications of a tectonic origin for the Vostok basin (Studinger et al., 2003). The persistence of water in the Vostok basin is attributed to the combined effects of geothermal heat flow and catchment topography. Because water has a low viscosity, and the circulation rates in Lake Vostok are very low, the shear stress along the lake ceiling would be vanishingly small. Therefore, it is believed that ice flow over the lake may involve horizontal extension or compression, similar to that occurring in ice shelves, rather than the base-parallel shear found in grounded ice sheets and glaciers (Kwok et al., 2000).

Based on a 60-MHz airborne radar study by Siegert et al. (2000), the thickness of the ice changes very little in an east to west direction across Lake Vostok. This was interpreted to indicate an absence in deformation of the ice layers *away* from the lake margins. In another study by Bell et al. (2002), radar data were analyzed showing ice layer thicknesses along a vertical section following the "Vostok core trajectory." This trajectory followed the ice flow line passing beneath the Vostok drilling station, where it pointed 131° relative to true north, with a velocity of about 3 m yr^{-1}. As previously mentioned, this flow line diverted slightly south over the lake (Kwok et al., 2000). Bell et al. (2002) found that the ice thickness decreased from 3900 m near the western lake margin to 3750 m below Vostok station. At the same time, the thickness of the accretion ice was found to increase with distance from the western lake margin, reaching a value of 180 m below Vostok station. These findings indicated that the ice layers undergo hundreds of meters of thinning during transit across the lake. According to Bell et al., the accretion ice becomes thicker in a

southeastward direction along the Vostok core trajectory, reaching a value of 250 m near the eastern lake margin. Some of this thickening may have resulted from compressive stresses. Along the eastern margin of the lake, the lower layers in the ice sheet (3300-2800 m) have undergone 7% thickening, possibly due to compressive stresses where the floating ice becomes grounded.

A numerical flow model was implemented by Mayer and Siegert (2000) to simulate the ice flow dynamics along a two-dimensional east-west profile over the north-south center of Lake Vostok. Solutions for velocity, stress and temperature were obtained using the coupled equations for mass, energy and momentum balance. Their published stress results were not of adequate spatial resolution for detailed inferences in the present study. Nevertheless, Figure 6 in Mayer and Siegert (2000) was used to help make estimates in plausible deviatoric stress magnitudes in the accretion ice. The calculated deviatoric stress was effectively zero in ice near the east-west center of the lake. However, this stress was shown to abruptly increase near the western lake margin, reaching values of at least 40 kPa. Their numerical model was two-dimensional and thus did not include the north-south flow gradients clearly prevalent in InSAR data (Kwok et al., 2000). This indicated that the deviatoric stress in the ice over southern Lake Vostok could be greater than those predicted in the model of Mayer and Siegert.

For the ITJ Model simulation of the Vostok accretion ice, it is assumed that there is a tensile deviatoric stress of 50 kPa, directed along the horizontal flow line, in the accretion ice within several km of the western lake margin. This deviatoric stress is close to numerically calculated values in the accretion ice near the west margin of Lake Vostok (Mayer and Siegert, 2000), and is in the low range of basal shear stresses in most glaciers (Hobbs, 1974, p. 338). It is also assumed that stresses in the accretion ice are hydrostatic near the east-west center of the lake. The marginal distance of several kilometers is assumed for the sake of interpreting model results; however, it is also a reasonable value considering spatial scales in numerically predicted stresses by Mayer and Siegert. Based on these assumptions, an ice flow velocity of 3 m yr^{-1} (Bell et al., 2002), and an accretion rate of 3.8 cm yr^{-1}, the upper several dekameters (e.g., 20-30 m) of the accretion ice, sampled in the Vostok ice core, would have formed where the deviatoric stress was 50 kPa.

Since the shear stress along the floating ice ceiling is effectively zero, it is reasonable to assume that the plane of maximum shear stress, $\sigma_s'^b$, is inclined 45° to the lake ceiling. The assumed *macroscopic* stress state is illustrated in Figure 5.10a. It is emphasized that elements (a) and (b) in Figure 5.10 represent equivalent stress states. This macroscopic stress state is equivalent to *pure shear* superimposed on hydrostatic stress (Dieter, 1986, p. 92-95). It represents plastic flow of an isotropic solid constrained to the $x'y'$ plane, as described by the Prandtl-Reuss equations for an elasto-plastic material. The directions of maximum finite stretch and shortening do not rotate during pure shear deformation (Davis and Reynolds,

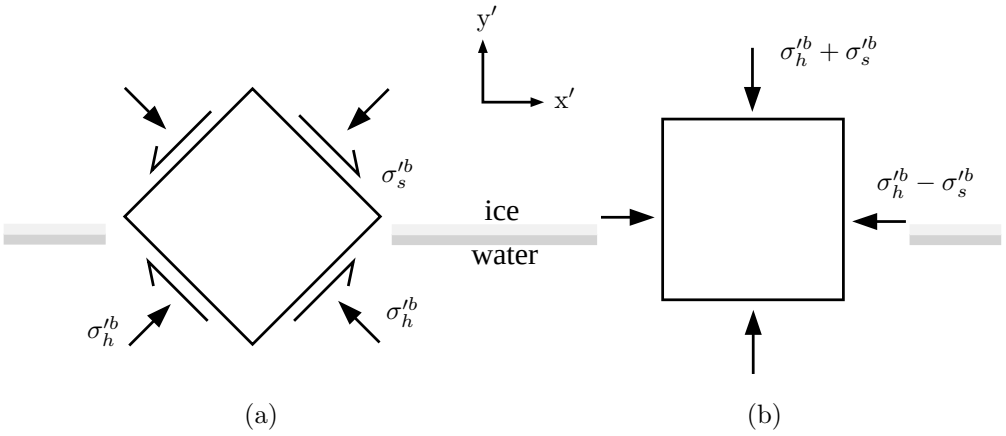

Figure 5.10: Stress elements representing assumed boundary conditions for the ITJ Model simulation of the Vostok accretion ice. The z′ element faces are subjected only to normal stress $\sigma_h'^b$. Elements (a) and (b) represent equivalent stress states. The axes of the global reference frame are shown.

1996, p. 85). This type of deformation is consistent with the observed thinning (Bell et al., 2002) in ice layers of the western Vostok accretion ice. The boundary condition stress of the model, $\mathbf{T^b}$, in matrix form with respect to the global frame is:

$$\mathbf{T^b} = -\sigma_h'^b \mathbf{I} + \begin{bmatrix} +\sigma_s'^b & 0 & 0 \\ 0 & -\sigma_s'^b & 0 \\ 0 & 0 & 0 \end{bmatrix} \tag{5.4}$$

where $\mathbf{I}$ is the identity matrix, $\sigma_h'^b$ the hydrostatic stress (positive), and $\sigma_s'^b$ the deviatoric stress. A positive $\sigma_s'^b$-value represents an tensile deviatoric stress directed along the ice-water interface (i.e., x′ direction). Models using a non-zero value of $\sigma_s'^b$ are said to include a macroscopic deviatoric stress.

The hydrostatic stress, $\sigma_h'^b$, was set to 32.8 MPa to represent the pressure near the vertical center of the southern Vostok accretion ice at depth 3650 m. This pressure is probably 2 to 6% less than the value at the ice-water interface along the Vostok core trajectory (defined on page 97). Based on preliminary model analyses, this small pressure difference would have a negligible effect on the calculated melting temperature depressions. The numerical simulations used a macroscopic deviatoric stress, $\sigma_s'^b$, of both zero and 50 kPa. The temperature was estimated from an assumed linear function of temperature (equation 5.2). The elastic and creep material parameters were temperature-corrected to -4.1°C based on a reference ice depth of 3650 m.

A total of twenty model executions were carried out, each with a different, randomly-generated c-axis spherical coordinate set. These coordinates were generated in ANSYS and exported to data files, the

values of which have been omitted for brevity. The Norton creep material properties were set to hard crystal values listed in Table 4.3. The Hill parameters R_b and R_n were set to $3^{1/2}$ and $(3/2)^{1/2} \times 10^6$, respectively. It was shown earlier that use of a smaller R_n-value, emulating the effects of increased slip along non-basal crystallographic planes, had no significant effect on calculated melting temperatures and stress concentrations (Figure 5.6). The crystal size, d_{g1}, was set to 0.5 m to reflect a median value for the accretion ice (Jouzel et al., 1999). Other mesh settings were as determined from the mesh sensitivity study (see page 81). Based on equation (3.21), the element dimensions in the x′y′ plane ranged from 6 to 12 mm, and in the z′ direction were 27 mm. These dimensions yielded acceptable maximum aspect ratios of 5:1. Smaller element sizes were desired, but not practical due to excessive computing times. The smallest element dimensions near the triple junction were roughly 1% of the crystal size.

The applied loads were linearly ramped during the first second of the solution and were thereafter held constant. The solution was incremented out to a final time of 5×10^3 s with automatic time-stepping in ANSYS. By this final time, stresses had effectively reached steady state values. Time acted as essentially a dummy variable in the model and did not necessarily correspond to physical time scales in the accretion ice. The following symbols continue to be in use: σ_b = shear stress resolved along crystallographic basal plane, s_3 = magnitude of most compressive principal stress, T_m^s = melting temperature assuming pressure P_s in solid equals s_3, and ΔT^c = temperature increase caused by heat dissipation from creep. All model results were evaluated at centroid locations, in the z′ = 0.25 m plane, of elements in the ITJ submodel. The numerically calculated extrema in σ_b, s_3, T_m^s, and ΔT^c are plotted in Figure 5.11 for deviatoric stresses of both zero and 50 kPa.

Localized concentrations in most compressive principal stress, s_3, always occurred along the grain boundaries and near the triple junction. When the macroscopic stress was deviatoric (i.e., boundary condition $\sigma_s'^b = 50$ kPa), the concentrations in s_3 always increased toward the steady state solution. On the other hand, when the macroscopic stress was hydrostatic, concentrations in s_3 always diminished as steady state conditions were approached. The concentrations in s_3 were coincident with localizations in both strain energy density and minimum melting temperature $T^s_{m,\min}$. Therefore, the differences between the calculated $T^s_{m,\min}$-values from analyses with and without macroscopic deviatoric stress represented minimum quantities. Restated, stepping the solution to larger times would have resulted in lower $T^s_{m,\min}$-values for models with macroscopic deviatoric stress, and higher $T^s_{m,\min}$-values for models with macroscopic hydrostatic stress. It appeared that the calculated values of $T^s_{m,\min}$ in models with macroscopic hydrostatic stress approached the melting temperature corresponding to a hydrostatic stress.

The average calculated values of $s_{3,\max}$, $\sigma_{b,\max}$, and $T^s_{m,\min}$ (defined on page 88) are listed in Table 5.3. The calculated minimum melting temperatures, $T^s_{m,\min}$, in analyses using a macroscopic deviatoric stress

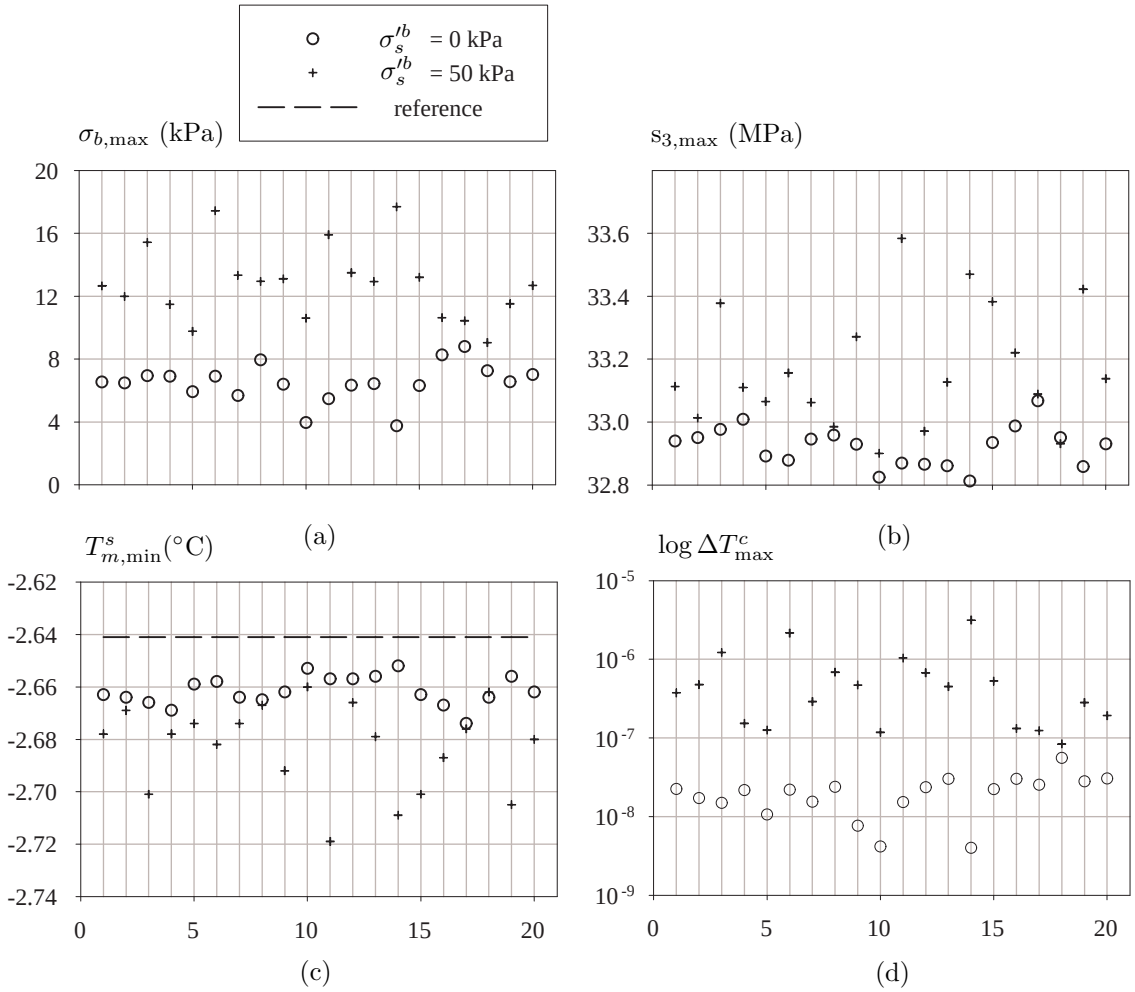

Figure 5.11: Calculated extrema in stresses, melting temperatures and spot temperatures from the ITJ Model simulation of the Vostok accretion ice for macroscopic deviatoric stress $\sigma_s'^b = 0$ and 50 kPa. Abscissae values index the c-axis spherical coordinate set numbers which are not included. The reference melting temperature, based on a hydrostatic stress at depth 3650 m, is indicated by the dashed line in plot (c). $\sigma_{b,\max}$ = maximum shear stress resolved along the basal plane, $s_{3,\max}$ = maximum value of most compressive principal stress, $T^s_{m,\min}$ = minimum melting temperature assuming pressure P_s equals most compressive principal stress, and $\Delta T^c_{\max}$ = maximum temperature increase caused by heat dissipation from creep.

	$\sigma_s'^b = 0$ kPa	$\sigma_s'^b = 50$ kPa
$\overline{s}_{3,\max}$	32.9 MPa	33.2 MPa
$\overline{\sigma}_{b,\max}$	6.5 kPa	12.8 kPa
$\overline{T}^s_{m,\min}$	-2.66°C	-2.68°C

Table 5.3: Average calculated values of $s_{3,\max}$, $\sigma_{b,\max}$ and $T^s_{m,\min}$ from the ITJ Model simulation of Vostok accretion ice, with ($\sigma_s'^b = 50$ kPa) and without ($\sigma_s'^b = 0$ kPa) macroscopic deviatoric stress. $\sigma_s'^b$ = deviatoric component of boundary condition stress, $s_{3,\max}$ = maximum magnitude of most compressive principal stress s_3, $\sigma_{b,\max}$ = maximum resolved shear stress along the basal plane, and $T^s_{m,\min}$ = minimum melting temperature assuming pressure P_s equals magnitude of s_3 in the solid.

were 0.00 to 0.06°C (average 0.02°C) lower than those using a macroscopic hydrostatic stress. This average difference was denoted as $\Delta\overline{T}^{s}_{m,\min}$ and assigned an average value of 0.02°C. The value of $\Delta\overline{T}^{s}_{m,\min}$ was interpreted to be the greatest melting temperature depression calculated from models using a macroscopic deviatoric stress. Based on an assumed temperature gradient in the Vostok accretion ice of 0.014°C m^{-1} (equation 5.2) and a $\Delta\overline{T}^{s}_{m,\min}$-value of 0.02^{o}C, stress-induced melting was predicted near triple junctions in the lower few (i.e., $\gtrsim 1$) meters of accretion ice, where the macroscopic deviatoric stress was assumed to be 50 kPa. This melting appeared negligible in analyses that assumed a macroscopic hydrostatic stress.

The calculated mean strain rate in the y′ direction for models using a macroscopic deviatoric stress was -1.7×10^{-9} s^{-1} near steady state. For pure shear deformation, the x′ strain rate would then be +1.7×10^{-9} s^{-1} in order for dilatational creep to vanish. The corresponding effective strain rate, -1.7×10^{-9} s^{-1}, was within a factor of two of the shear strain rate predicted by the DM map (Figure 4.4) for a 50 kPa shear stress. This indicated that the ITJ Model results were in acceptable agreement with the DM map, which was originally used to predict the significant deformation mechanisms involved. Interestingly, the maximum basal plane shear stresses, $\sigma_{b,\max}$, relaxed to values much lower than 20 kPa. This stress is sometimes taken to be the "yield stress" of single ice crystals. However, the minimum σ_b-value to which single crystals will relax has never been definitively determined. For ice to deform at strain rates as low as 10^{-9} s^{-1}, the average basal plane shear stress would need to relax to values much lower than 20 kPa. Lastly, the temperature changes, ΔT^{c}, associated with heat dissipation were orders of magnitude smaller than the stress-induced melting temperature depressions and were therefore negligible.

Based on results of the ITJ Model, onset of melting was predicted along crystal boundaries, at scales $\approx$ 1% of the crystal size, in the lower few meters of the Vostok accretion ice where the macroscopic deviatoric stress was assumed to be 50 kPa. This stress has been assumed in the accretion ice within several km of the western lake margin. Following the argument on page 98, intergranular melt would have been present *during formation* of the upper several dekameters of the accretion ice. This melting would likely have influenced the incorporation processes of particles, impurities and possibly microbes into the accretion ice from the lake and subglacial sediment. Based on an evaluation of subglacial topography from Studinger et al. (2003), the Vostok drilling station is located at least 10 km southwest of the nearest lake margin. This is interpreted to suggest that the macroscopic deviatoric stress in the accretion ice below Vostok station is much lower than 50 kPa. However, there is no data, other than the distance of the Vostok station from the lake margins, to support this interpretation. If the macroscopic deviatoric stress in the accretion ice below Vostok station is effectively zero, then results from the ITJ Model suggest that intergranular melting associated with mechanical anisotropy in the accretion ice below Vostok station is negligible.

The predicted intergranular melting in the western several km of accretion ice has implications for the entrainment processes of debris and contaminants. Intergranular meltwater would seemingly strengthen the incorporation process of sediment, and possibly microbes, into the accretion ice. This mechanism may act in concert with those previously discussed (Royston-Bishop, in press). Once debris is incorporated, it may be redistributed along grain boundaries by regelation processes associated with stress-induced melting and refreezing. The upper 70 m of accretion ice (accretion ice-1) is sometimes said to be "dirty" due to higher densities of particle inclusions. The mechanism for this could be associated with the argument that intergranular melt, associated with mechanical anisotropy, was present during formation of the upper several dekameters of accretion ice.

The numerical prediction of stress-induced intergranular melting has implications for the permeability of subglacial lake ice. The accretion ice near the margins of subglacial lakes likely contain the highest deviatoric stress. Based on conclusions from the ITJ Model, microscopic stresses along grain boundaries in the lower few meters of the accretion ice would be great enough to induce melting at scales roughly 1% of the crystal size. These findings suggest that drilling further from the lake margins may reduce chances of drilling fluid contamination via the intergranular fluid network in ice.

The rheology of glaciers has usually been described by Glen's flow law. This flow law tends to underestimate strain rates in ice near the melting point because it fails to account for the mechanisms of GBS and grain boundary melting. The predictions of intergranular melting from the ITJ Model suggest that the lower few meters of ice in temperate glaciers would have a relatively high compliance in association with mechanisms of GBS and grain boundary melting.

The Vostok numerical simulation also predicted jumps in strain energy density across grain boundaries when the macroscopic deviatoric stress was 50 kPa. Concentrations in elastic strain energy density were coincident with pressure concentrations near grain boundaries. The elastic strain energies gradually increased as steady state conditions were approached. ANSYS contour plots showing typical steady state (i.e., $t = 5 \times 10^3$ s) elastic strain energy densities (J kg^{-1}) are shown in Figure 5.12. The results of the 16$^{\text{th}}$ and 20$^{\text{th}}$ spherical coordinate sets were represented in these plots because of their intermediate final values in $s_{3,\max}$ (Figure 5.11). Jumps of 1-2% in elastic strain energy density occurred across grain boundaries where pressure concentrations were greatest. These energy discontinuities occurred for a macroscopic deviatoric stress of 50 kPa, which was only 0.15% of the applied hydrostatic stress. It is likely that the regions of relatively high dislocation densities in the Vostok accretion ice (Cullen and Baker, 2002) would coincide with concentrations in strain energy density.

Boundary-migration recrystallization involves the diffusional flow of H_2O molecules across grain boundaries in the direction of decreasing chemical potential. This migration is explained by the Second Law

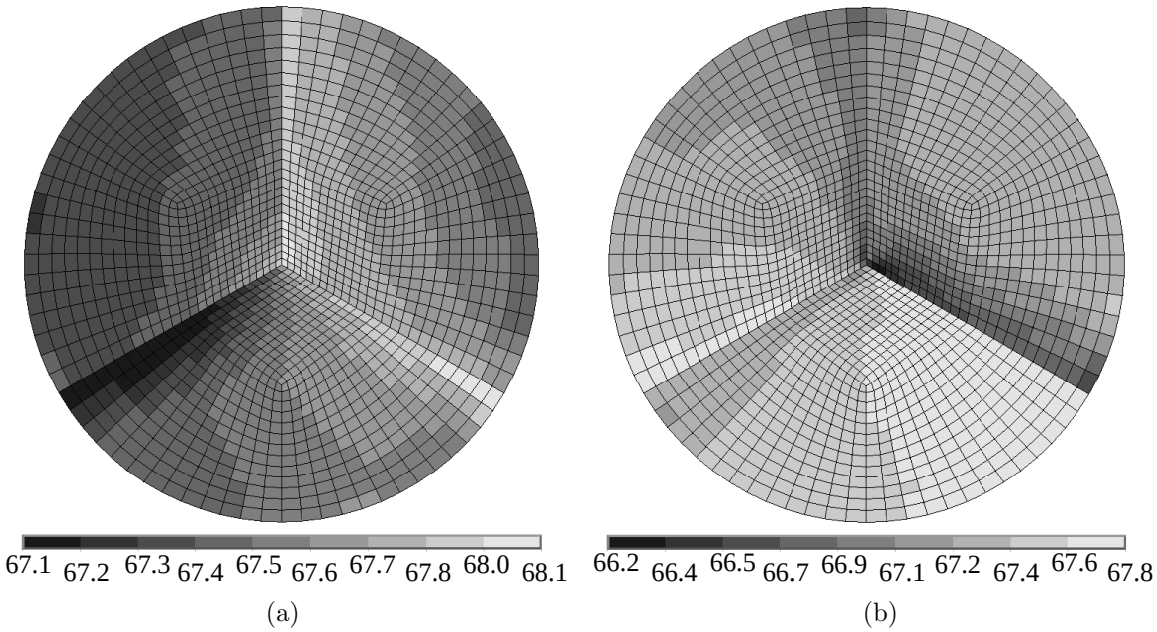

Figure 5.12: ANSYS plot of calculated strain energy density (J kg^{-1}) from ITJ Model simulation of Vostok accretion ice for a macroscopic deviatoric stress of 50 kPa. The results shown are along the z′= 0.25 m plane of the submodel. The crystallographic c-axis orientations follow the (a) 16^{th} and (b) 20^{th} spherical coordinate sets.

of Thermodynamics, which indicates that systems tend to evolve toward lower energy states. Boundary-migration recrystallization is favored by high homologous temperatures and the presence of intergranular fluids, and is hindered by the presence of intergranular impurities (Davis and Reynolds, 1996, p. 189). Two mechanisms driving this type of recrystallization are free surface energies and gradients in strain energy density. Grains containing higher strain energy densities tend to be consumed by those having less energy, causing a boundary to migrate in the direction of the local strain energy gradient. A signature of recrystallization dominated by strain energy gradients is a pervasiveness in irregular and serrated grain boundaries. In contrast, recrystallization driven by free surface energies tends to smooth out grain boundaries and increase grain sizes. The free surface energy contributes a r_m^{-1} term to the phase equilibrium condition (equation 2.25), and is thus more prevalent in aggregates having smaller grain sizes. Montagnat et al. (2001) have attributed the giant crystal sizes of the Vostok accretion ice to an *abnormal grain growth process* driven by a reduction in overall free surface energy.

The following development suggests that strain energy gradients could be a significant mechanism of boundary-migration recrystallization in the Vostok accretion ice. The chemical potential, in units of energy per H_2O molecule, has contributions from free surface energy, μ_r, and strain energy density, μ_n. A rough comparison of the driving forces involving free surface energy and strain energy can be obtained by comparing the jumps in μ_r and μ_n across a grain boundary (Srolovitz, 1989). These jumps are represented

by $\delta\mu_r$ and $\delta\mu_n$ as follows:

$$\begin{aligned} \delta\mu_r &= \frac{2\gamma_{GB}\Omega_v}{r_m} \\ \delta\mu_n &= \delta u_e \Omega_v / \nu_{0s} \end{aligned} \tag{5.5}$$

where γ_{GB}, the solid-solid free surface energy of H_2O, is about $(65 \pm 3) \times 10^{-3}$ J m^{-2} (Ketcham and Hobbs, 1969), Ω_v is the volume per H_2O molecule (Table 4.1), r_m is the mean radius of GB curvature, δu_e is the jump in elastic strain energy density, and ν_{0s} is the specific volume of ice in the stress-free state. Typical results of the ITJ Model indicated maximum δu_e-values of about 1 J kg^{-1} (Figure 5.12). The following inequalities are true if free surface energy drives boundary-migration recrystallization:

$$\begin{aligned} &\delta\mu_r > \delta\mu_n \quad \text{or equivalently,} \\ &r_m < \frac{4\gamma_{GB}\nu_{0s}}{\delta u_e} \end{aligned} \tag{5.6}$$

Based on the above statement, free surface energies would be the driving mechanism of boundary-migration recrystallization when GB curvatures are less than about 140 μm. Many crystals in the Vostok accretion ice clearly have radii of curvature greater than 140 μm. Therefore, boundary-migration recrystallization in the accretion ice would be significantly influenced by strain energy gradients when the macroscopic deviatoric stress is 50 kPa. These rough arguments were supported by observations of grain boundaries in the Vostok ice cores.

Cores of Vostok accretion ice, from depths 3567 to 3591 m, were examined with crossed-polarizers in cold labs at Montana State University, Bozeman, in April 2005. Many grain boundaries were observed to take on irregular shapes, sometimes engulfing certain grains (Figure 5.13). The observations of sharp, irregular crystal boundaries supported the hypothesis that strain energy gradients could be a significant mechanism of boundary-migration recrystallization in the Vostok accretion ice that formed near the lake margins.

The accretion ice in Figure 5.13 formed closer to the lake margin than the deeper ice. The shallower

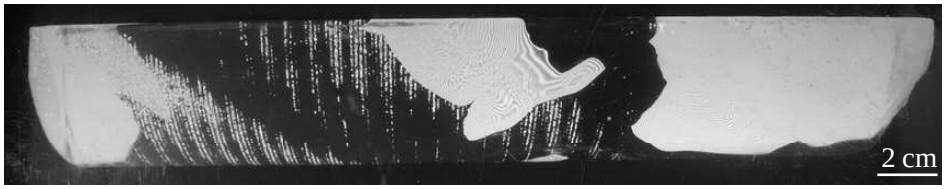

Figure 5.13: Cross-polarized image of ice core from depth 3577.0-3577.3 m of the Vostok accretion ice. Top end to the right. Portions of at least four crystals are shown. Largest crystal in optical extinction encloses smaller crystals along irregular, sharp boundaries.

accretion ice would have contained greater localized concentrations in pressure and strain energy due to both mechanical anisotropy and macroscopic deviatoric stress. This may have resulted in variations of grain boundary morphologies in the accretion ice with depth. Future comparisons of crystal morphologies over the vertical range of the Vostok accretion ice could provide a cursory test of this hypothesis.

CHAPTER 6

MOBILITY OF LIGHT NON-AQUEOUS PHASE LIQUIDS IN SOLID ICE

Purpose of Study

Considerations based on the simple impurity model of Chapter 2 indicated that lattice rejection of sulfate anion to grain boundary (GB) junctions would result in mm-size water veins in the lower several dekameters of the Vostok accretion ice (Figure 2.5). These results were similar to those of an earlier study on water vein chemistries and potential microbial habitats (Price, 2000). The predicted vertical extent of mm-size water veins associated with solute rejection (Chapter 2) far exceeded that attributed to anisotropic elasto-creep (Chapter 5). The next and last focus of this study was the mobility of a Light Non-Aqueous Phase Liquid (LNAPL) hydrocarbon along grain boundaries and the water vein network in unfractured, bubble free ice. The interactions of phase change, vein capillary forces and limited LNAPL solubility offered potentially-intriguing transport phenomena.

LNAPL hydrocarbons generally have a low, but non-vanishing, solubility in water. This non-zero water solubility is largely attributed to the lighter, more soluble aromatic hydrocarbons which contain the benzene ring. LNAPL hydrocarbons include gasoline, oil, jet fuel and other liquid hydrocarbon (LH) fuels. The spillage of these fluids constitute a major form of anthropomorphic pollution in polar regions (Aislabie et al., 2004; Tumeo and Wolk, 1994; Kennicutt II et al., 1990). One useful application of LH fuels is the prevention of drill borehole collapse in deep ice core projects. This utility of LH fuels is made possible by their low freezing temperatures and densities similar to that of ice (Talalay and Gundestrup, 2002; Gerasimoff, 2003). The potential for ice core contamination from drilling fluids complicates biological and climatological studies, clarifying the need for proper decontamination protocols (Christner et al., 2005). Ice core decontamination planning and environmental remediation efforts would benefit from increased knowledge about the effects of structure, chemistry and temperature on the permeability of LH fuels in ice.

Much is unknown about mass transport processes in ice near the melting point. According to the Russian Federation (2001) report on penetration protocols for Lake Vostok, the impermeable state of the ice sheet would prevent large-scale loss of drilling fluids to the lake. The assumption of impermeability was based, at least in part, on X-ray diffraction studies indicating low lattice distortions in crystals from the Vostok accretion ice (Montagnat et al., 2001). To address possible worst-case contamination scenarios, the Russian Federation (2001) considered and discussed infiltration rates of oil products in sea and arctic ice reported from other studies. These infiltration rates ranged from 20 mm day^{-1} in winter

ice, to 490 mm day^{-1} in porous multi-year ice. These rates are lower than those observed in other field assessments (Alexander and Stockton, 2003; Tumeo and Larson, 1994) of fuel spreading rates in sea and lake ice, which indicated average transport rates of nearly 1 m day^{-1}. The fuels in these studies consisted of aviation type JP-5 and JP-8, the latter of which is the main drilling fluid component in the Vostok borehole (Russian Federation, 2001; Victor, 2003). Although the transport mechanisms in these field assessments were not clear, Alexander and Stockton (2003) noted that hydrocarbons had penetrated the ice structure as an emulsion. The roles of fractures, bubbles, brine channels and grain boundaries on LH fuel permeability in ice is not well understood. To increase the fundamental understanding on this topic, three preliminary experiments were carried out in cold labs, at Montana State University-Bozeman, to observe the mobility of JP-8 fuel in ice of different chemistry and temperature. The philosophy was to eliminate the complicating effect of various structures like bubbles and fractures, and instead focus on the permeability of unfractured, bubble free, crystal clear ice grown from both tap and distilled water. This approach seemed particularly relevant to potential mass transport mechanisms deep within ice sheets, where warm, high confining-pressure conditions would tend to inhibit fracture growth and remove bubbles.

Description of Fuel-Ice (FI) Experiments

Between January and March 2005, three preliminary experiments, named the Fuel-Ice (FI) Experiments, were carried out. These were conducted to closely observe, in dark conditions, the mobility of JP-8 fuel in clear, bubble free, unfractured ice grown from both tap and steam distilled water. The ice samples were sliced, using a band saw, from 136-kg blocks of clear sculpturing ice grown at VW Ice in Missoula, Montana. The first two experiments, named Experiment 1 and Experiment 2, used tap water ice from the same block. The last experiment, named Experiment 3, used distilled water ice from a different block.

The ice crystals were very coarse-grained, elongated in the vertical growth direction, and had dimensions of 0.5 to 7 cm (average 3 cm) in the horizontal plane. Crystallographic orientations were examined with a Rigsby stage, an instrument equipped with a 4-axis stage and cross-polarized filters. The c-axis orientations of most crystals were found to be randomly oriented near the horizontal plane, thus bearing similarity to type S2 columnar ice (described on page 84). The ice samples formed blocks measuring 16 cm across and 12 cm in vertical height. Before each experiment, a thin section was cut from the top surface of the ice block and inspected on a Rigsby stage for the locations of grain boundaries and triple junctions. These sections were later melted and sent for chemical analyses using ion chromatography (IC), courtesy of Kathy Welch at Byrd Polar Institute, The Ohio State University. The mass concentrations of major ions in two samples of both the distilled and tap water are listed in Table 6.1. All of the ice was very pure, with ion concentrations several orders of magnitude lower than typical values for tap water. The

Ice	Na^+	K^+	Mg^{2+}	Ca^{2+}	Cl^-	NO_3^-	SO_4^{2-}
Tap (Exper 1)	123.0	19.6	1.4	70.4	68.8	19.7	20.5
Tap (Exper 2)	52.7	27.9	1.8	70.9	58.5	7.0	9.9
Distilled (Exper 3)	8.1	9.9	1.2	64.5	37.0	4.0	7.1
Distilled (additional)	7.0	7.2	0.7	79.8	29.0	1.7	10.4

Table 6.1: Major ion concentrations (ppb mass) in the tap and distilled water of ice used in the Fuel-Ice (FI) Experiments.

concentrations were also below the typical reporting limits of the IC analysis facility. The low ion concentrations have been attributed to an effective rejection process of impurities from the ice lattice during freezing. At the beginning of each experiment, corresponding to a time (t) of 0 hours (h), about 25 ml of JP-8 fuel was carefully poured into the cylindrical pocket at the top of an ice block (Figure 6.1). These pockets had horizontal and vertical dimensions of 5.5 and 2.5 cm, respectively, and were formed prior to the experiments by gradually melting a warm aluminum rod into the ice. This slow melting process prevented the formation of fractures associated with sudden temperature changes. The ice temperatures were measured with Type-T thermocouples, with tolerances of about 0.5°C, placed in 2.5 cm-deep holes drilled near the top and bottom right sides of each ice block (Figure 6.1). Temperature readings were recorded with a Hewlett-Packard Agilent datalogger. All experiments were carried out in a Russell's environmental chamber, designed to laboratory specifications, containing a carbon air filter system. The developments in the ice and fuel were documented with a Canon EOS 300D camera and Sigma 1:1 macro lens on manual focus. The format of Experiment 1 differed slightly from Experiments 2 and 3.

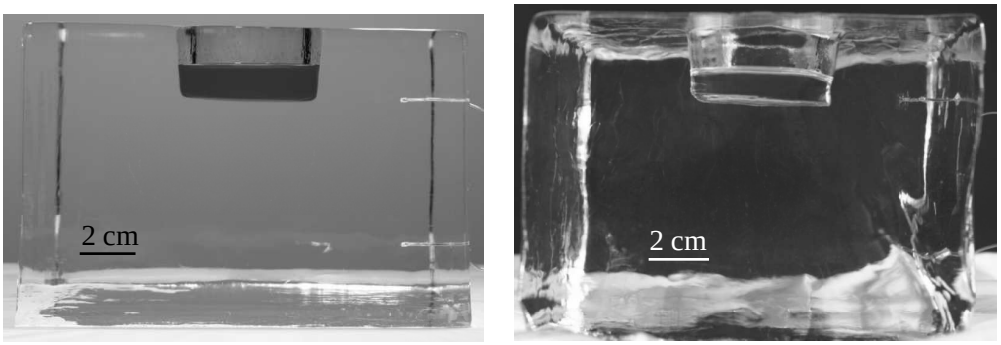

(a) (b)

Figure 6.1: Front views of ice blocks with fuel at the beginning of (a) Experiment 1 and (b) Experiment 2 of the Fuel-Ice Experiments. The JP-8 fuel pockets are shown at the top surfaces of the ice. The fuel in Experiment 1 was dyed red and placed in ice against a white background. No dye nor background was used in Experiments 2 and 3. Thermocouples are visible at the right sides of the blocks.

FI Experiment 1

In Experiment 1, Sudan IV red solvent dye was added to the JP-8 to enhance its visibility. Image sets were manually obtained every 12 h, with twenty minutes transpiring per session, using lighting provided by two 120-W flood lights. These lights were on only during the photo sessions. The ice temperature was gradually increased from -4 to -3°C during the first 72 h of the experiment (Figure 6.2). Somewhat surprisingly, these temperatures were several degrees cooler than the chamber air temperature. This was tentatively attributed to cooling of the ice surface due to heat loss associated with sublimation. Temperature spikes of several degrees occurred during each 20-minute photo session due to heating of the thermocouples. Fuel volatilization noticeably accelerated under the light of each photo session, resulting in undesirable horizontal migration and dripping of fuel over the ice block surfaces. Between times t = 72 and 75 h, the air temperature was incrementally increased from -1 to +2.1°C in an effort to bring the ice

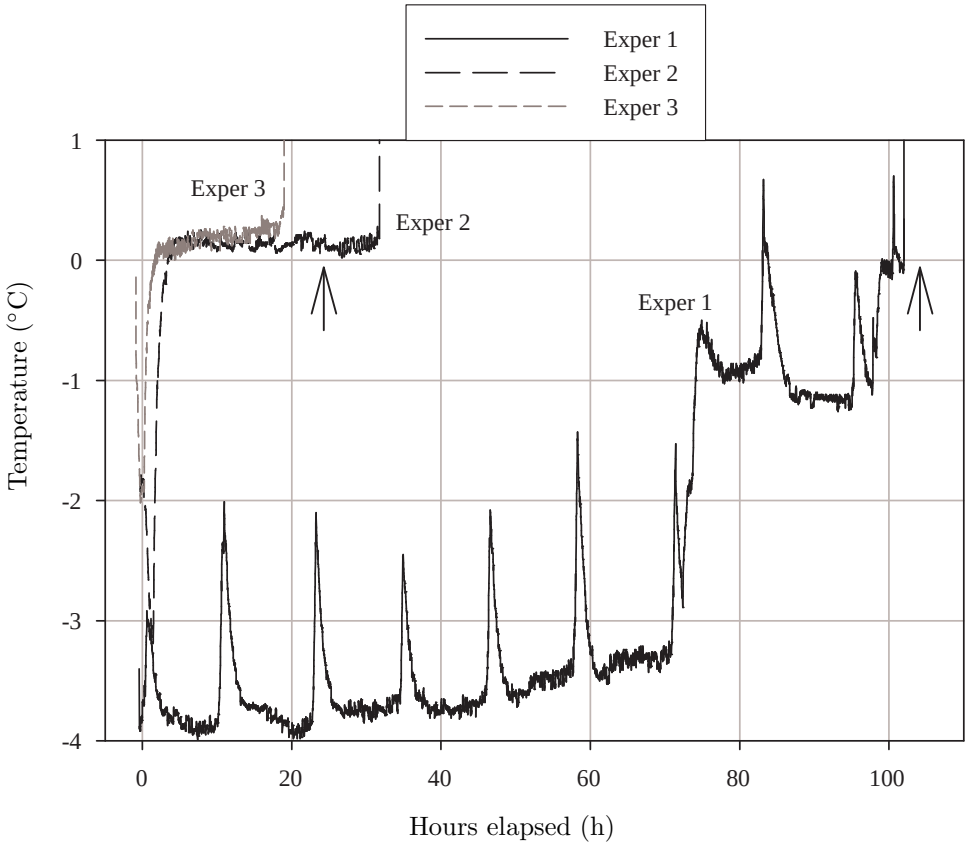

Figure 6.2: Recorded ice temperatures (°C) verses time (h) during the three FI Experiments. The fuel was added to ice at the initial time of 0 h. Original thermocouple readings were reduced by an empirical calibration factor 0.5°C to produce the results shown. Large arrows indicate times when *fuel-tunneling* first occurred. The spikes shown were caused by thermocouple heating under flood lights during the photo sessions of Experiment 1.

temperature to -0.5°C. The last temperature adjustment was made one day later, at time t = 98 h, when the setting was increased to +4.1°C in order to bring the ice to the melting point. Each air temperature setting was found through a trial and error process, whereby thermocouple readings were monitored after each adjustment until values appeared to become stationary. The ice was within thermocouple precision of the melting point by time t = 99 h (Figure 6.2). Based on the results from this experiment, the formats for imaging, optical lighting, and air temperatures were modified in the following two experiments.

FI Experiments 2 and 3

Based on observations in Experiment 1, the solvent dye was not deemed necessary to make detailed observations of the JP-8. Therefore, the solvent dye was not used in Experiments 2 and 3. In these two experiments, computer software was used to automatically capture images every 5 to 30 minutes depending on the speed of visible changes. The flood lights were not used in these experiments; instead, ambient lighting transmitted through a window in the chamber provided illumination sufficient for 30-second exposure times. These dark conditions reduced fuel volatilization, prevented spikes in thermocouple readings (see Figure 6.2), and reduced the extraneous influence of light on experimental conditions. The air temperature in Experiments 2 and 3 was held at +4.1°C, the final setting in Experiment 1 which brought the ice to the melting point with little melting.

Results of FI Experiments

The first visible melting around the JP-8 occurred at temperatures as low as -3°C and was localized along the lower edges of the pockets. The fluid-filled regions took on bulbous and scallop-shaped morphologies (Figure 6.3). The first visible meltwater in Experiment 1 occurred in ice colder than those in the latter two experiments. This has been attributed to the dependence of meltwater volumes on elapsed time. In Experiment 1, the fuel had been in contact with ice for a longer period of time (58 h) than in the following experiments. The meltwater regions at the bottom of the pockets had rather peculiar, bulbous and scalloped-shaped boundaries in all of the experiments. This phenomenon was attributed to the favorable lowering of free surface energy. The gently-curved, concave-inward scalloped boundaries between ice and liquid had lower curvatures, and hence free surface energy densities, than the initial sharp edges of the pockets.

The meltwater regions below the fuel grew in size as the experiments progressed. By 102 h into Experiment 1, and about 12 h into Experiments 2 and 3, the meltwater below the JP-8 had formed pools up to 1 cm in depth (Figure 6.4). The lower boundary of the meltpool in Experiment 1 was considerably more irregular and bulbous than those in the two experiments that followed. Although the

cause for this difference was unclear, it may have been associated with the presence of solvent dye or the slower initial (i.e., t < 99 h) melt rates during Experiment 1. The meltpools likely contained an aqueous solution consisting primarily of water and the relatively soluble aromatic hydrocarbons (e.g., benzene, xylene). These solutes depressed the phase equilibrium temperatures below those occurring in the ice. As a result, the meltpools grew in order to become more dilute and thus evolve towards an equilibrium solute concentration.

In Experiments 1 and 2, the JP-8 traveled vertically along tubes in the ice at elapsed times of 104(±2) and 24 h, respectively (Figure 6.5a-c). The arrows plotted in Figure 6.2 indicate the approximate times of these events, herein referred to as *fuel-tunneling*. The precise timing of fuel-tunneling in Experiment 1 was unknown because it occurred during a 4-h time interval between photo sessions. The fuel tubes in Experiment 1 (Figure 6.5a,b) and Experiment 2 (Figure 6.5c) were named *Tube FIA-1* and *Tube*

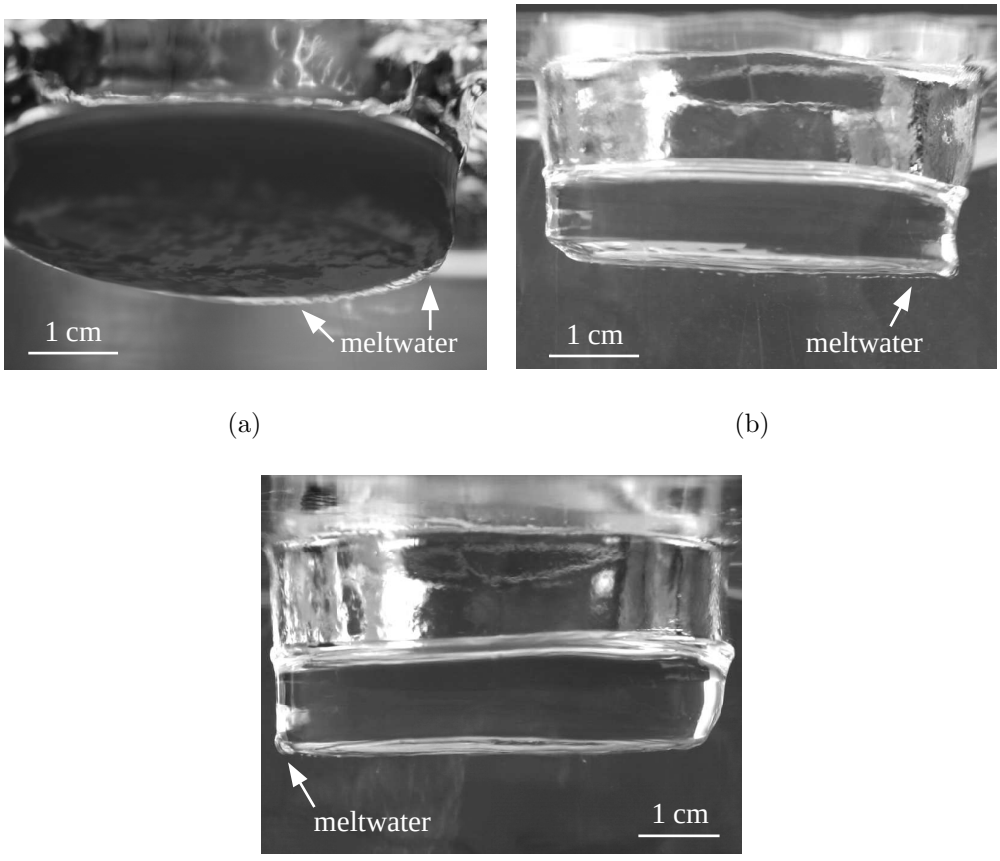

(a) (b)

(c)

Figure 6.3: First visible melting along lower edges of fuel pockets in FI Experiments. (a) Experiment 1, 58 h elapsed, ice temperature -3°C; (b) Experiment 2, 2.5 h elapsed, ice temperature -0.5°C; (c) Experiment 3, 0.9 h elapsed, ice temperature -0.4°C.

.

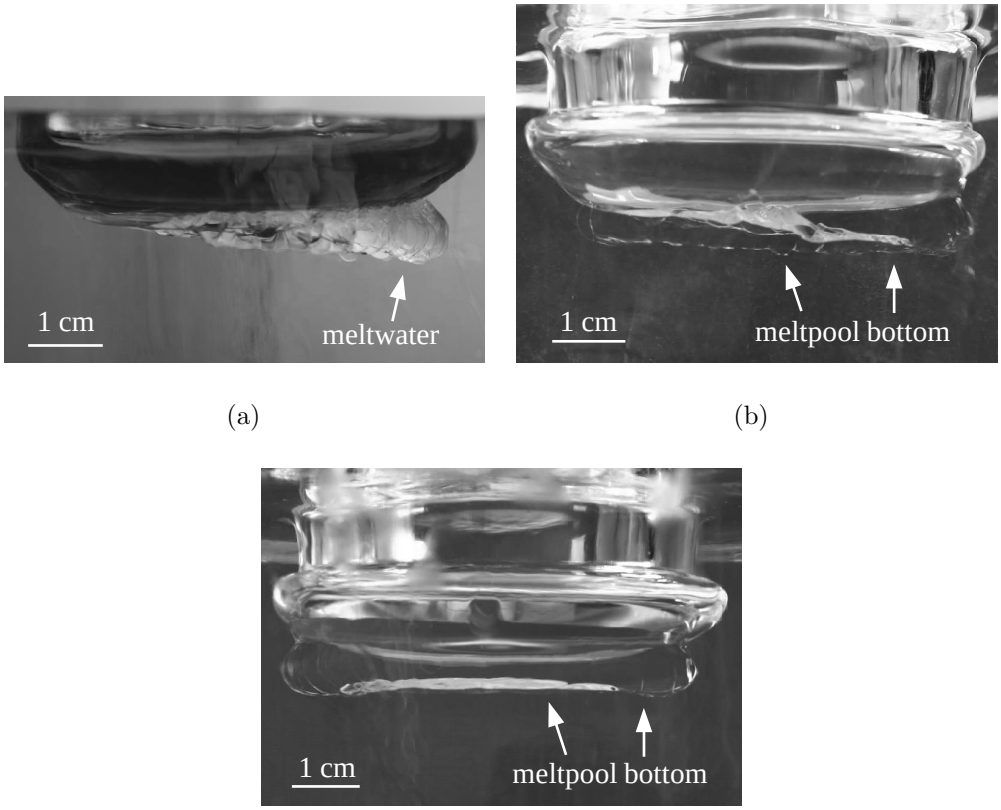

(a) (b)

(c)

Figure 6.4: Meltwater pools below fuel pockets in FI Experiments, ice temperatures within thermocouple tolerance of the melting point. (a) Experiment 1, 102 h elapsed; (b) Experiment 2, 12 h elapsed; (c) Experiment 3, 11 h elapsed.

FIB-1, respectively. The diameters of these tubes ranged from 1 to 2 mm. Tube FIA-1 branched into three segments near the bottom of the ice block. As indicated by images automatically captured every 0.5 h, Tube FIB-1 descended through the 8 cm-high ice block in less than 0.5 h. This corresponded to a minimum average fuel-front velocity of 16 cm h^{-1}. Almost all of the JP-8 had drained through Tube FIB-1 in less than 1.5 h (recorded over 3 successive images). Afterward, Tube FIB-1 sealed closed, completely disappearing from view! The developments were less dynamic in Experiment 3 which used ice grown from distilled water. Throughout the 72 h course of this experiment, the meltpool remained and gradually grew in size (Figure 6.5d).

Later in Experiment 2, at an elapsed time of 32 h, the empty pocket was refilled with 25 ml of cooled, undyed JP-8 fuel. About four minutes later, a new fuel tube formed, named *Tube FIB-2*. This tube had an initial diameter of about 0.5 mm and was located in the upper front side of the pocket (Figure 6.6a). Tube FIB-2 rapidly propagated along a tortuous path through the ice, traversing the entire ice block in less than three minutes. The tube gradually swelled as it channeled an alternating sequence of fuel

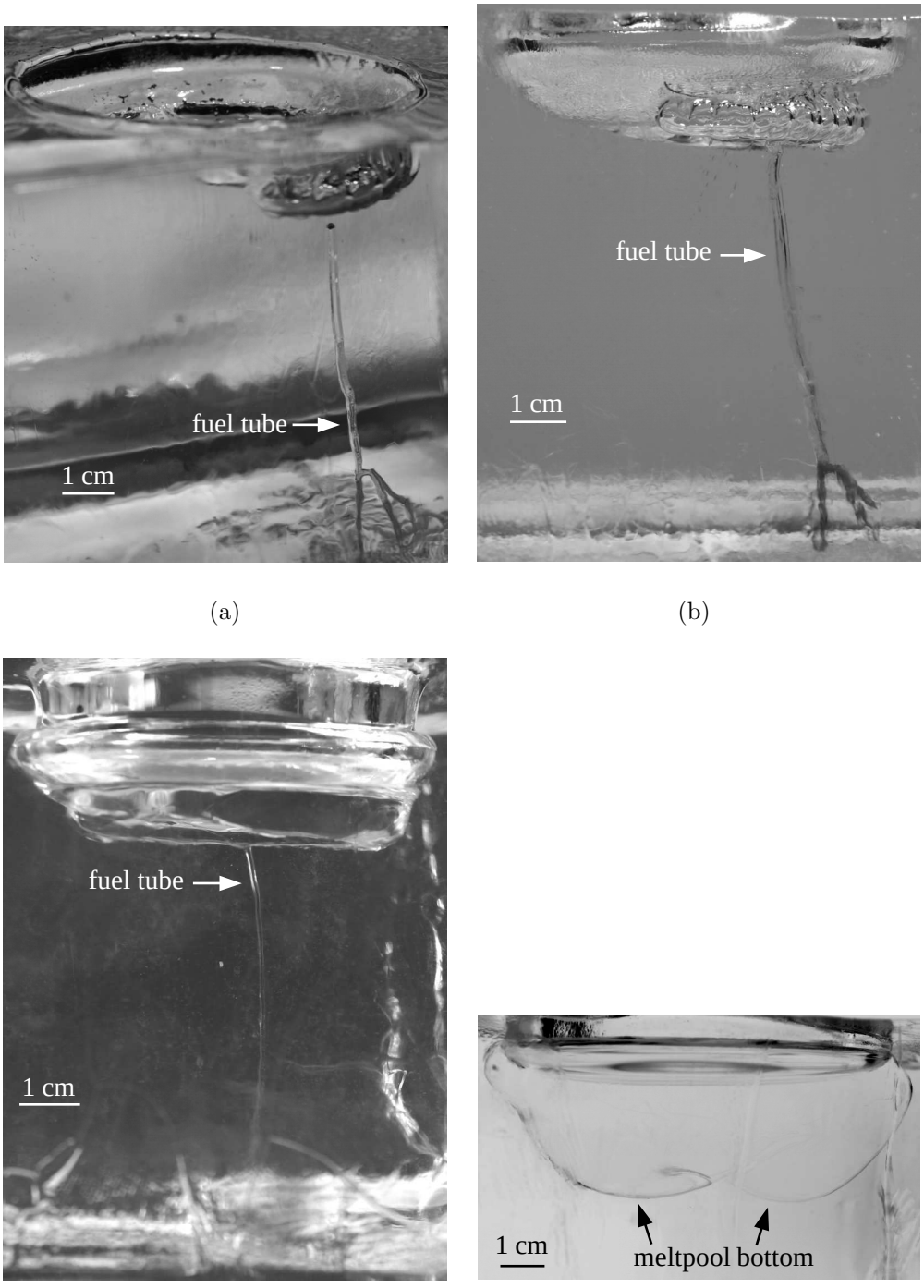

Figure 6.5: Images from series of FI Experiments showing fuel tubes in ice from tap water, and undrained meltpool in ice from distilled water. (a) and (b) Tube *FIA-1* at end of Experiment 1; (c) Tube *FIB-1*, 24 h into Experiment 2; (d) color-inverted image of undrained meltpool, 72 h into Experiment 3. Ice temperatures were all within thermocouple tolerance of the melting point.

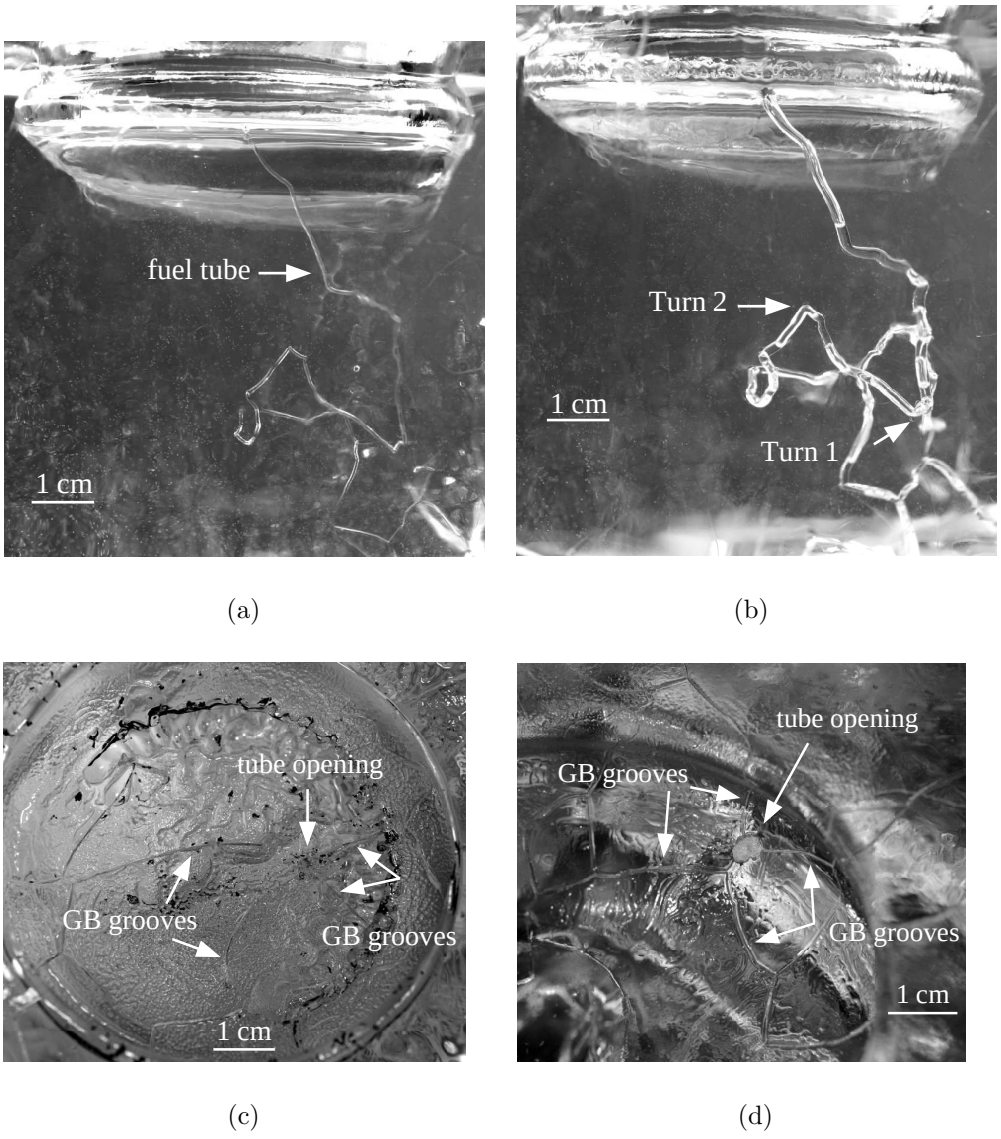

Figure 6.6: Images of Tube FIB-2 in ice from tap water at times (a) t = 32 h and (b) t = 33 h in FI Experiment 2. The tube channeled JP-8 fuel along a tortuous path through the ice. Intersections of grain boundary (GB) grooves were visible at the surface openings of (c) Tube FIA-1 and (d) Tube FIB-2.

and bubbles along its path, reaching a diameter of about 2 mm by a time 1 h after its initial formation (Figure 6.6b). This distinct chain of alternating fuel and bubbles was also observed five months earlier, during a different series of experiments, when a similar fuel tube formed below a pocket of JP-8. However, this earlier experiment included simulated solar radiation at an intensity of 580 W m^{-2}.

The first two turns in Tube FIB-2 have been designated as *Turn 1* and *Turn 2*, respectively (Figure 6.6b). Tube FIB-2 drained the top several millimeters of JP-8 from the pocket between elapsed times of 32 and 33 h into Experiment 2. A short time later, at an elapsed time of approximately 34 h, *Tube*

FIB-1 reactivated and vertically channeled almost all of the remaining JP-8 through the ice in less than 1.5 h. Tube FIB-1 then again sealed closed as it originally had, becoming invisible to the eye, sometime between 36 and 46 h into the experiment.

A close examination of the fuel tubes of Experiments 1 and 2 indicated that they all followed GB junctions, lines where three or more crystals intersect. At the end of Experiment 1, four GB grooves were found to intersect at the Tube FIA-1 opening at the bottom of the fuel pocket (Figure 6.6c). The red dye had collected in these grooves, greatly enhancing their visibility. Upon completion of Experiment 2, the ice block was stored within a bag inside a cold chamber. Two days later, GB grooves in the ice surface had become readily visible as a result of preferential sublimation along grain boundaries. Three of these grooves clearly intersected at the opening of Tube FIB-2 in the top surface of the block (Figure 6.6d). GB junctions in ice have the lowest melting temperatures as a result of free surface energy and concentrated impurities. As a result, they are the first regions in ice to melt. Because both fuel and dissolved solutes in water veins are melting point depressants, and because the observed fuel-tunneling appeared to be driven by a phase transformation process, it seemed natural that the fuel tubes would follow GB junctions through the ice.

A close examination was made on the locations of fuel tubes relative to grain boundaries in the ice of Experiment 2. To do this, eight cm-thick horizontal sections, numbered in increasing order downward, were sliced from the top of the ice block using a band saw (Figure 6.7b). Slices 1 through 4 were taken from ice above Slices 5 through 8, and are not visible in Figure 6.7b. A cross-polarized image of Slice 2 indicated that Tube FIB-2 coincided with a triple junction (Figure 6.7a). Also noted was the close proximity of an adjacent triple junction in Slice 2, almost forming a four-grain junction at the opening of Tube FIB-2.

Slice 4 was taken from further down in the ice, just below the bottom of the fuel pocket. This slice was located just above Slice 5 shown in Figure 6.7b. A triple junction was observed in Slice 4 at a location near the center of the fuel pocket. This junction was located at the boundary of a depression in the bottom of the fuel pocket, formed by melting of ice into the last remaining fuel. In addition, this junction coincided with the approximate location of Tube FIB-1 as observed in the images. These findings suggested that Tube FIB-1 followed the observed triple junction through the ice.

Slice 5 was located just above Turn 2 in Tube FIB-2 (Figure 6.7b). For a sense of reference on the locations of Turns 1 and 2, Figures 6.6b and 6.7b can be compared. Circles were inscribed in Slices 5 and 6 and centered about the vertical line passing Turn 2 (Figure 6.7c,d). The observations of Slices 5 and 6 between cross-polarized films indicated that Turn 2, in Tube FIB-2, followed a triple junction around the apex of a crystal which truncated upward into a grain boundary (Figure 6.7c,d). A similar analysis of Slice 7 and 8, from lower in the ice block, again confirmed that Tube FIB-2 followed a triple junction

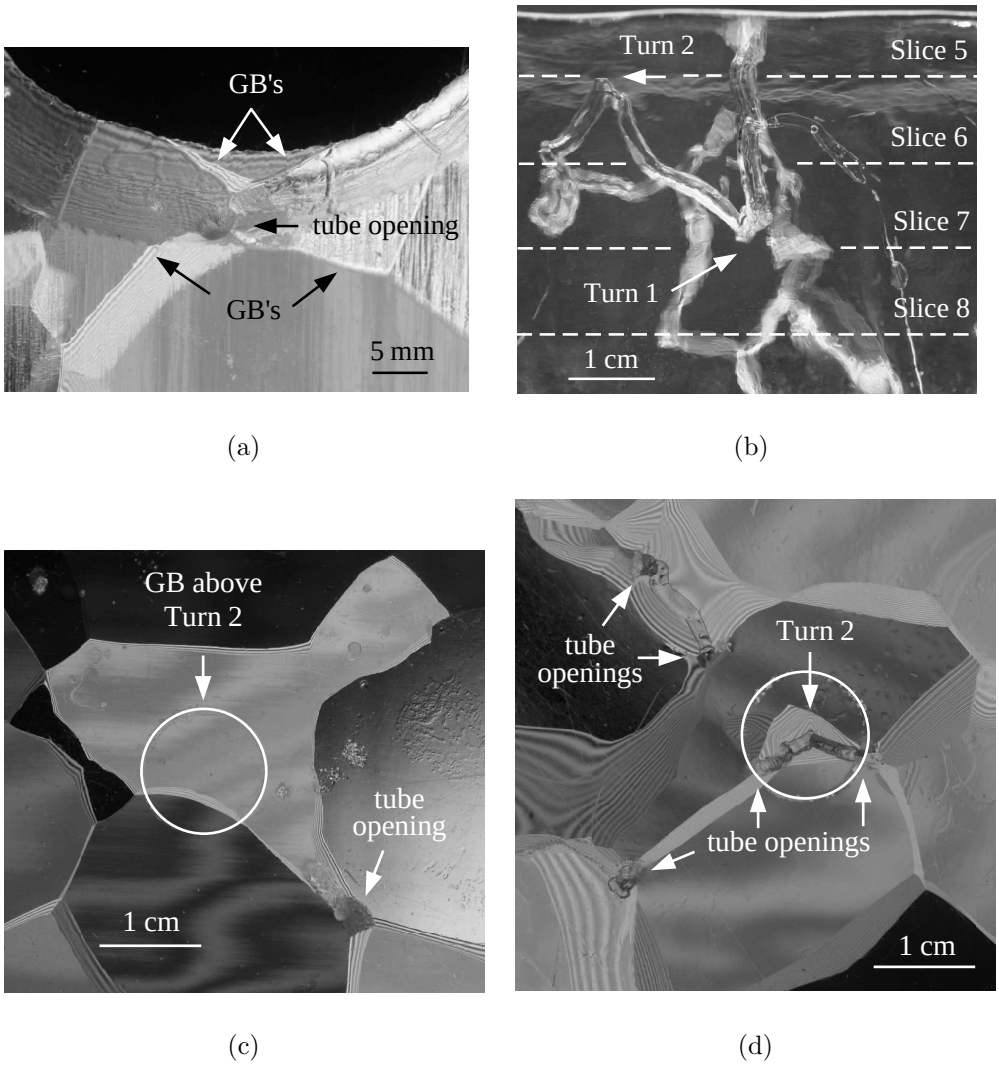

Figure 6.7: Images of fuel tubes, and their locations along grain boundary junctions, in ice of FI Experiment 2. Crossed-polarized filters were used in images (a), (c) and (d). All fuel tubes coincided with triple or four-grain junctions in the ice. (a) Tube FIB-2 opening in fuel pocket, Slice 2 of ice block; (b) location of Slices 5-8 in ice block relative to Turns 1 and 2 in Tube FIB-2; (c) view from top of Slice 5, circled region was just above Turn 2; (d) view of Slice 6 from *below*, circled region contained Turn 2 in Tube FIB-2.

through the ice. However, unlike the case for Turn 2, through-going triple junctions were observed above and below Turn 1. Therefore, Turn 1 did not appear to result from the truncation of a triple junction against a grain boundary, as was the apparent case for Turn 2.

Interpretations and Conceptual Model of Fuel-Tunneling

FI Experiments 1 and 2 demonstrated that JP-8 jet fuel moves rapidly (>16 cm h^{-1}) along GB junctions through solid ice near the melting point. This transport process is referred to as fuel-tunneling.

The single most important conclusion of the study is the following: *solid ice near the melting point is, in general, not impermeable to JP-8 jet fuel*. The finding that all fuel tubes followed GB junctions, and that fuel-tunneling was absent in ice from distilled water, were strong indications that the presence of intergranular impurities played a key role in critical conditions leading up to fuel-tunneling. This phenomenon was not gradual nor predictable, but rather sudden and seemingly triggered by a critical set of environmental conditions.

The two fuel-tunneling events were preceded by a quiescent 24-30 h period. During this period, the ice was within 1°C of the melting point, with overall activity consisting of gradual meltpool growth below a floating layer of immiscible fuel. After this quiescence, rapid (>16 cm h^{-1}) fuel infiltration occurred along GB junctions following both tortuous and vertical paths through the ice. The mechanism of these rapid fuel-tunneling events was certainly not diffusion, the only hydrocarbon transport mechanism that has been addressed for the Lake Vostok accretion ice. Rather, the mechanism appeared to involve a coupling between phase change and pressure gradients in aqueous solutions following GB junctions. The characteristic chains of bubbles in the fuel tubes indicated the development of voids, possibly created by the volumetric reduction accompanying melt. The upward propagation of Tube FIB-2, in FI Experiment 2, suggested that gravity was not the only mechanism driving fuel tube growth, but perhaps also internal pressure gradients associated with the specific volume reduction of melting ice along water vein walls.

At several degrees below the melting point, meltpools formed below the immiscible, floating components of fuel (Figure 6.3). These meltpools likely contained an aqueous solution consisting primarily of the aromatic hydrocarbons, which comprise about 20% of JP-8. Water veins in the ice, ubiquitous and relatively large near the macroscopic melting point, would have intersected the meltpools. The hypothesized mechanism of fuel-tunneling is as follows. During the quiescent 24-30 h period prior to fuel-tunneling, aqueous hydrocarbons diffused from the meltpools down into the ice through water veins. This would have caused water veins to swell in order to evolve toward an equilibrium solute concentration. The melting that accompanied this water vein growth would have caused a localized pressure reduction due to the specific volume decrease in phase change. The low pressure regions would induce an inward diffusion of gases through the water vein. At a critical, diffusion-limited growth rate of water veins, the reduced pressure may have become sufficiently great to suction the fuel-water combination downward. Ongoing phase transformations at the walls of water veins may have sustained this process, thereby advancing the fuel tubes further along their path. This could explain the characteristic chains of bubbles that were observed during the Fuel-Ice Experiments (Figure 6.6b).

A simple model was developed in order to make an "educated guess" about conditions where fuel-tunneling could be expected to occur. The model involves the following three assumptions: (1) the

melting point depression is proportional to solute concentration in water veins (i.e., the ideally dilute solution approximation), (2) all impurities are excluded from the ice lattice and concentrated in triple junctions, and (3) there exists a critical state for fuel-tunneling that depends on water vein size and fuel solubility in water. The third assumption is further developed later.

The hypothesis of the model is that fuel-tunneling occurs at a critical diffusion rate, J_c, of aqueous hydrocarbons through water veins. The diffusion rate, J, is assumed to be a function of water vein radius, r_v, and fuel solubility in water, M_f (mol L^{-1}). The water vein radius is proportional to its diameter (see equation 2.37 and Figure 2.1). The model hypotheses are motivated by the following arguments. If water veins are vanishingly small, *or* if the fuel is completely insoluble in water, then hydrocarbon diffusion into water veins would be negligible. In this case, fuel tunneling is considered very unlikely. Thinner water veins (i.e., smaller r_v-values) are subjected to greater surface tension, which may act as a barrier to hydrocarbon diffusion from the meltpools down into the ice. It is assumed that fuel-tunneling occurs when the hydrocarbon diffusion rate through water veins exceeds a critical value, J_c. Thus, the condition $J(r_v, M_f) > J_c$ is taken to represent an onset of fuel-tunneling. A Taylor series expansion of $J(r_v, M_f)$ to quadratic terms produces the following:

$$J(r_v, M_f) = D_1 + D_2 r_v + D_3 M_f + D_4 r_v^2 + D_5 r_v M_f + D_6 M_f^2 \tag{6.1}$$

It is assumed that $J(r_v, M_f)$ approaches zero when either independent variable r_v *or* M_f vanish. For example, regardless of the size of r_v, the value of $J(r_v, M_f)$ is assumed to vanish if the water solubility of fuel is identically zero. In order for this to hold for all possible cases, all expansion coefficients except D_5 must vanish. After making this simplification, the hydrocarbon diffusion rate becomes simply:

$$J(r_v, M_f) = D_5 r_v M_f \tag{6.2}$$

The criterion for fuel-tunneling is summarized as follows:

$$\begin{aligned} J(r_v, M_f) &> J_c, \qquad \text{fuel-tunneling} \\ J(r_v, M_f) &< J_c, \qquad \text{no fuel-tunneling} \end{aligned} \tag{6.3}$$

where J_c and D_5 are taken to be constants, r_v is the water vein radius and M_f is the solubility (mol L^{-1}) of fuel in water. The diffusion rate, J, has units of kg m^{-2} s^{-1}, therefore D_5 has units of s^{-1}. The FI Experiments essentially present only two data points supporting this model in the following sense. The distilled water ice contained fewer impurities than that from tap water. However, it should be noted that

the ion abundances in both types of ice were below the reporting limits for the IC instrument (Kathy Welch, personal communication), and should therefore be interpreted with some caution. Following the Chapter 2 development of solute colligative effects on water veins, the distilled water ice would have contained smaller water veins, at a given temperature, than the tap water ice. The likelihood of smaller water vein radii in the distilled water ice, together with the observed absence in fuel-tunneling, is consistent with hypothesis of the model (equation 6.3). The vein sizes in the distilled water ice are interpreted as being sufficiently small to have prevented the hydrocarbon diffusion rate from reaching the critical value for fuel-tunneling. The likelihood of larger water veins in the tap water ice, together with the observed formation of fuel tubes, is considered an indication that the hydrocarbon diffusion rate surpassed the critical value for fuel-tunneling.

Next, three supplementary relations are combined with criterion (6.3). It is assumed that during ice growth all impurities are rejected to water veins forming the edges of crystals which all have identical geometry. Therefore, the following mole conservation relation approximates the solute molarity, M_s, (mol L^{-1}) in water veins (recall equation 2.34):

$$M_s = \frac{V_c}{V_v} M_a \tag{6.4}$$

where M_a is the bulk (average) molarity of impurities in the ice, V_c the volume of one crystal and water veins partitioned to it, and V_v the volume of veins partitioned to one crystal. The crystal geometries are approximated as truncated octahedra (Figure 2.2) with flat-to-flat diameter d_g (Frank, 1968). The combination of equations (2.39), (2.42) and (6.4) results in the following expression for water vein molarity, M_s:

$$M_s = \frac{1}{6\alpha_v\sqrt{2}} \left(\frac{d_g}{r_v}\right)^2 M_a \tag{6.5}$$

where the parameter α_v relates the water vein cross sectional area to its radius of curvature (equation 2.36).

The water veins are assumed to be in phase equilibrium with the surrounding ice at a temperature of T. This assumption requires that temperature gradients, pressure gradients and water vein growth rates be sufficiently small that phase equilibrium theory is applicable. The temperature T is then, by definition, the phase equilibrium temperature. This term is synonymous with "melting temperature" and "freezing temperature." The shorter term, "melting temperature," is used in place of the term "phase equilibrium temperature." The melting temperature of water veins is assumed to be proportional to their solute molality, m_s (moles solute per kg solvent), at a fixed atmospheric pressure. This relationship is

stated in the following colligative law for melting point depression, valid for an ideally dilute solution:

$$\Delta T = K_f m_s \tag{6.6}$$

where ΔT is defined as the difference $T - T_r$, with T being the melting temperature and T_r the melting temperature of ice coexisting with pure water (0°C). The parameter K_f is the freezing point constant and m_s the molality of water veins. The free surface energy contribution to ΔT is insignificant for the range in r_v-values encountered in this analysis and has therefore been omitted. For the pressure-temperature conditions in the FI Experiments, one liter of a dilute solution contained approximately 1 kg of H_2O solvent. Therefore, the good approximation is made that $M_s \approx m_s$. Using equations (6.5) and (6.6) to solve for the water vein radius, r_v, the following relation is obtained:

$$r_v = D_7 d_g \sqrt{\frac{M_a}{|\Delta T|}} \tag{6.7}$$

The constant D_7 is defined to be $2^{-1/4}(6\alpha_v/|K_f|)^{-1/2}$, where $|K_f|$ is the absolute value of the freezing point constant, α_v the water vein geometry parameter and $|\Delta T|$ the magnitude of the difference between melting temperature T and the reference melting temperature T_r. Finally, with the use of equations (6.3) and (6.7), onset of fuel-tunneling is predicted to occur when the following condition is satisfied:

$$D_8 M_f d_g \sqrt{\frac{M_a}{|\Delta T|}} > J_c \tag{6.8}$$

where D_8, defined as the product $D_5 D_7$, and J_c are taken to be constants, M_a the bulk molarity of impurities in ice, $|\Delta T|$ the absolute value of the difference $T - T_r$, M_f the solubility of fuel in water (mol L^{-1}) and d_g the grain size. Condition (6.8) illustrates the assumption that fuel-tunneling becomes more likely as grain size, fuel water-solubility, and impurity concentrations increase, and less likely as the temperature T decreases (i.e., $|\Delta T| \uparrow$). Note that d_g is very large for the Vostok accretion ice, so depending on the impurity concentration, fuel-tunneling could occur at temperatures much lower than those in the FI Experiments. The values of parameters D_8 and J_c are unimportant for the application of criterion (6.8) in this study because scaling arguments are made involving ratios in conditions of the FI Experiments and Vostok accretion ice. These scaling arguments lead to the cancellation of parameters D_8 and J_c.

Implications of Fuel-Tunneling for Subglacial Lake Exploration

There has been longstanding debate regarding the permeability of glacial ice via the water vein network following GB junctions (Lliboutry, 1971; Nye and Frank, 1973; Raymond and Harrison, 1975; Colbeck, 1976). The findings of the FI Experiments suggested that tunneling of LNAPL hydrocarbons along GB junctions was closely linked to the presence of intergranular impurities, which in turn affect water vein sizes. The fuel movement observed in the FI Experiments seems to be in contrast with the popular belief that unfractured ice is relatively impermeable to hydrocarbon drilling fluids.

The Russian Antarctic Expedition (RAE) addressed possible hydrocarbon diffusion rates through water veins in the Vostok accretion ice (Victor, 2003). They calculated a diffusion distance of 1 m for a time period of about 10^3 y. In light of the findings from the FI Experiments, these rates seem far too low, especially near the lake ceiling where the ice is at the pressure-dependent melting temperature. The likelihood of fuel-tunneling, observed in this study, should be addressed for a risk assessment of large-scale hydrocarbon contamination of subglacial lakes, Lake Vostok in particular. The critical temperature for fuel-tunneling may be reached as the base of the drill borehole approaches the ceiling of Lake Vostok. This scenario could result in large-scale chemical and biological contamination of the lower accretion ice and lake. To address this issue, an educated guess is made about the vertical range in the Vostok accretion ice where fuel-tunneling may occur. To do this, criterion (6.8) is used along with scaling arguments involving fuel and ice chemistry data, grain sizes, and temperatures in the FI Experiments and Vostok accretion ice.

The condition expressing equal likelihood of fuel-tunneling in the Vostok accretion ice and FI Experiments is obtained by equating criterion (6.8) satisfied in both environments:

$$D_8 M_f^e d_g^e \sqrt{\frac{M_a^e}{|\Delta T^e|}} = D_8 M_f^v d_g^v \sqrt{\frac{M_a^v}{|\Delta T^v|}} = J_c \tag{6.9}$$

The superscripts 'e' and 'v' refer to quantities with respect to the FI Experiments and Lake Vostok accretion ice, respectively. Rearranging equation (6.9), and dropping the absolute value from the temperature ratio, the following scaling relation is obtained:

$$\frac{\Delta T^v}{\Delta T^e} = \left(\frac{M_a^v}{M_a^e}\right)\left(\frac{M_f^v d_g^v}{M_f^e d_g^e}\right)^2 \tag{6.10}$$

The two-component drilling fluid used in the Vostok borehole consists primarily of JP-8 with lesser Freon F-141b (Russian Federation, 2001; Victor, 2003). This composition is very similar to that of pure

JP-8 used in the FI Experiments. Therefore, the approximation is made that $M_f^v \approx M_f^e$. The ice used in the FI Experiments was very pure, with impurity concentrations near the lower detection limits of the IC instrument. Total ion mass fractions in the tap water laboratory ice ranged from about 230 to 320 ppb. These concentrations are much less than some values reported for Vostok accretion ice-1 (i.e., "dirty ice" at depths < 3609 m), and several times greater than values characteristic of the deeper, cleaner accretion ice-2 (Royston-Bishop, unpublished data; De Angelis et al., 2004). Mass fractions of sulfate in the tap water ice (10-21 ppb) were larger than values reported for Vostok accretion ice-1, and quite similar to values reported for Vostok accretion ice-2 (1-24 ppb). The sulfate ion appears to be particularly insoluble in the ice lattice, with a propensity to concentrate along GB junctions (Mulvaney et al., 1988; Fukazawa et al., 1998; Cullen and Baker, 2002) and in solid inclusions (De Angelis et al., 2004). However, the Vostok accretion ice-2 reportedly contains very few solid inclusions. In light of these considerations, the approximation is made that $M_a^v \approx M_a^e$. The upper error in this approximation is probably several hundred percent. Using the aforementioned approximations, the predicted temperature ratio for onset of fuel-tunneling in the Vostok accretion ice and experiments becomes:

$$\frac{\Delta T^v}{\Delta T^e} = \left(\frac{d_g^v}{d_g^e}\right)^2 \tag{6.11}$$

Again, ΔT has been defined as $T - T_r$, where T is the melting temperature of ice in equilibrium with the water vein, and T_r the melting temperature of ice in equilibrium with pure water (i.e., 0°C). The grain size, d_g^v, of the Vostok accretion ice is an order of magnitude greater (i.e., tens of cm's) than that in ice of the FI Experiments (i.e., cm's). With this is mind, the estimation is made that $d_g^v/d_g^e \approx 10$. Based on the assumed ratios in grain size, impurity concentration, and fuel water-solubility, the predicted temperature ratio for onset of fuel-tunneling in the Vostok accretion ice and FI Experiments is:

$$\frac{\Delta T^v}{\Delta T^e} \approx 100 \tag{6.12}$$

The conclusion drawn from the model is that fuel-tunneling may occur in the Vostok accretion ice where depressions in melting temperature, ΔT^v, are two orders of magnitude greater than values, ΔT^e, in the FI Experiments. This ratio results from the giant grain sizes in the Vostok accretion ice, similar bulk ice chemistry in the accretion ice and FI Experiments, and the critical assumption that all impurities in the ice are concentrated in GB junctions. Unfortunately, the ice temperature during fuel-tunneling in the FI Experiments is not precisely known due to thermocouple tolerances of about 0.5°C. Therefore, a reasonable guess in ice temperature is made based on previous thermodynamic studies on the *effective heat capacity*, c_{eff}, of ice (Harrison, 1972; Nye, 1991). The value of c_{eff} consists of two contributions: the heat

capacity of solid ice, c_s, and the latent heat absorbed during the growth of water veins. The latent heat contribution drives c_{eff} to ever-increasing values as the temperature approaches the macroscopic melting point. If all ions in the laboratory ice (Table 6.1) are concentrated in GB junctions between crystals shaped as truncated octahedra, c_{eff} would be twice as large as c_s at a temperature of -0.05°C. Over a temperature range of -0.001 to -0.01°C, c_{eff} would become two to three orders of magnitude greater than c_s. When heat capacities are this great, time scales for temperature fluctuations are large compared to typical laboratory ones (Mader, 1992). Therefore, the ice temperature during fuel-tunneling in the FI Experiments is estimated to be between -0.001 and -0.01°C. Using the reference melting temperature, T_r, value of 0°C, ΔT^e is estimated to range from -0.001 to -0.01°C.

Using the scaling relationship (6.12) and the range in ΔT^e estimated above, fuel-tunneling is predicted to occur in the Vostok accretion ice where the depression in melting temperature, ΔT^v, is as high as -0.1 and as low as -1°C. This corresponds to a temperature between -2.8 and -3.7°C, assuming that the temperature of the lake ceiling is -2.7°C. Assuming a temperature gradient of 0.014°C m^{-1} (equation 5.2), fuel-tunneling is predicted to occur in the lower 6 to 70 m of the accretion ice. If a ΔT^v-value of -0.1°C is assumed, fuel infiltration is predicted in the lower 6 m of ice, and if a ΔT^v-value of -1°C is assumed, fuel infiltration is predicted in the lower 70 m of ice.

The details of the above calculation are as follows. The temperature predicted at onset of fuel-tunneling is set equal to $T_r(h_i) + \Delta T^v$, where $T_r(h_i)$ is the phase equilibrium temperature between pure ice and water at depth h_i, and ΔT^v is the depression in melting temperature (negative value) associated with dissolved solutes in water veins. Let $T(h_i)$ equal the actual temperature in the accretion ice, which is an increasing function of depth, h_i, as a result of overburden pressure. The depth, h_i, in the accretion ice at onset of fuel-tunneling is found from the intersection of curves for $T_r(h_i) + \Delta T^v$ and $T(h_i)$, with ΔT^v taking on values between -0.1 and -1°C. The temperature, $T(h_i)$, in the accretion ice is approximated from equation (5.2), which assumes a linear increase with depth to a value of -2.7°C at the lake ceiling. The values of $T_r(h_i)$ are calculated using phase equilibrium relation (2.46) and the following approximation for glaciostatic pressure, P, as a function of depth, h_i:

$$P = g h_i / \nu_{0s} \tag{6.13}$$

where gravitational constant $g = 9.8$ m s^{-2} and ν_{0s} is the specific volume of ice in the reference state (Table 2.1). For a ΔT^v-value of -0.1°C, fuel-tunneling is predicted in the lower 6 m of accretion ice. For a ΔT^v-value of -1°C, fuel-tunneling is predicted to occur in the lower 70 m of accretion ice.

CHAPTER 7

SUMMARY AND CONCLUSION

This study investigated the relative importance of nonhydrostatic stress and lattice-rejected solutes on the equilibrium of intergranular liquid water in the Vostok accretion ice, Eastern Antarctica. Attention was also focused on the effects of intergranular liquid water on the permeability of ice to a LNAPL hydrocarbon. Many ice properties are controlled by the abundance of internal liquid water, including heat capacity, rheology, permeability via diffusion of gases and solutes, and even the capacity to support microbial life. Liquid water is known to be ubiquitous along GB junctions, at temperatures above the eutectic point of the liquid water solution, as a result of limited ionic substitution in the lattice, solute-trapping between crystals along the freezing front, and nonhydrostatic stress associated with mechanical anisotropy. Previous studies on glacial ice have confirmed that impurities tend to concentrate along grain boundaries (Renaud, 1949; Harrison and Raymond, 1976). Similar studies on Antarctic ice have indicated that sulfate salts and sulfuric acids have a particular tendency to concentrate along triple junctions (Mulvaney et al., 1988; Fukazawa et al., 1998; Cullen and Baker, 2002).

To estimate the influence of lattice-rejected sulfate on water vein sizes in the southern Vostok accretion ice, a simple impurity model was considered that excluded the effects of mechanical anisotropy. Assuming that all sulfate was rejected to solutions in triple junctions, mm-size water veins were predicted in the lower few dekameters of the accretion ice. When it was assumed that only 10% of the bulk sulfate was concentrated in triple junctions, mm-size water veins were predicted in the lower dekameter of the accretion ice. Verification of the model was attempted through simulations of the Mader (1992) experiments. The numerically-predicted vein sizes appeared to be within a factor of three of experimental values when all impurities were assumed to be concentrated in triple junctions. When the assumed fraction of impurities in triple junctions was reduced to 10%, the model predictions seemed very consistent with the experimental observations. Price (2000) had previously followed a similar approach to model water vein chemistry and sizes in the accretion ice, emphasizing implications for potential microbial habitats.

The study also examined the potential effects of intergranular water on the permeability of hydrocarbon drilling fluids in deep glacial ice. The drilling fluid used in the Vostok borehole consists primarily of JP-8, which is also the standard fuel used in commercial and military aircraft. Three preliminary Fuel-Ice (FI) Experiments were conducted, in a cold laboratory at Montana State University-Bozeman, to observe the mobility of JP-8 fuel in clear, unfractured ice in temperate, dark conditions. During experiments using ice grown from tap water, there were initial 24-30 h quiescent periods during which gradual meltpool growth occurred below immiscible fuel. These periods were followed by rapid events of fuel-tube formation along

GB junctions that drained JP-8 from surface reservoirs in the ice. The tubes were 0.5 to 2 mm in diameter, always followed GB junctions along both vertical and winding paths, and had propagation velocities of at least 16 cm hr^{-1}. This fuel-tunneling phenomenon was absent from the experiment that used ice grown from distilled water. These findings suggested that intergranular water along GB junctions, associated with lattice-rejected impurities, played a key role in conditions leading up to fuel-tunneling. A rough model was hypothesized in order to make an educated guess about critical conditions at the onset of fuel-tunneling in the Vostok accretion ice. According to the model, soluble hydrocarbons in the meltpools diffused downward into water veins during the initial quiescent period. As a result, water veins swelled in order to evolve toward equilibrium. Slow melting along vein walls would have been accompanied by localized pressure drops associated with the specific volume decrease of phase change. At a critical diffusion rate, the pressure gradients may have become sufficient to suction the fuel downward. Although not clear, continued tube propagation may have involved a coupling process between phase change and pressure gradients. Scaling arguments of the model involving temperature, crystal geometry and chemistry indicated that fuel-tunneling may occur in the lower 6 m of the accretion ice, and possibly as far up as 70 m from the lake ceiling.

In order to investigate the influence of mechanical anisotropy on intergranular water in the Vostok accretion ice, elastic (ETJ) and elasto-creep (ITJ) models were implemented using ANSYS, a commercial finite element (FE) package. The phase equilibrium condition in this part of the study included nonhydrostatic stress, but omitted the effects of free surface energy and solutes. This simplication was considered to be reasonable since the model predicted onset of melt, rather than simulating the melt process itself. In this sense, the phase equilibrium dependence on anisotropy and solutes were decoupled. When stress boundary conditions were assumed hydrostatic, the calculated values of shear stress, resolved along the basal planes of ice crystals, had magnitudes up to five times greater than values known to cause plastic deformation. Accompanying these numerical results were dislocation densities counted from X-ray topographs (Adams and Brown, unpublished data) of samples from the accretion ice. Additional considerations were given to reports from literature on dislocation densities in the Vostok accretion ice (Cullen and Baker, 2002) and in carefully grown laboratory ice (Oguro, 1988; Cullen and Baker, 2002). It appeared that the accretion ice contained dislocation densities two orders of magnitude greater than non-plastically deformed ice grown in quiescent laboratory conditions. Thus was the conclusion that portions of the Vostok accretion ice had undergone plastic deformation due to the anisotropy of ice crystals, and that an inelastic material model was needed. The ITJ Model was then developed to simulate stress inhomogeneities arising from the anisotropic elastic and creep properties of single ice crystals.

Results from the ITJ Model indicated that, when macroscopic stresses were hydrostatic, initial stress

concentrations associated with elastic anisotropy diminished with time. Numerical simulations were also carried out using a macroscopic deviatoric stress of 50 kPa. This value represented a reasonable estimate for the westernmost Vostok accretion ice, where longitudinal extension has been indicated by radar data (Bell et al., 2002). This deviatoric stress also represents a low value typical for the basal regions of most glaciers. In all of the model simulations, pressure concentrations occurred along grain boundaries, especially triple junctions, that approached steady state values. Assuming a 50 kPa macroscopic deviatoric stress in the western several km of accretion ice, onset of melt was predicted in the lower few meters of ice, at scales ≈1% of the crystal size. This melting became less pronounced as the macroscopic deviatoric stress decreased, appearing to become negligible in models using hydrostatic stress boundary conditions. Such conditions are considered likely to reflect the stress state in the accretion ice over the open part of the lake (Mayer and Siegert, 2000) and under Vostok drilling station. The average strain rates calculated from the ITJ Model were within a factor of two of literature data on the creep of polycrystalline ice (Barnes et al., 1971; Goodman et al., 1981). The calculated onset of internal melting seemed fairly consistent with past experimental observations in polycrystalline ice (Nye and Mae, 1972; Wilson et al., 1996). Results of the ITJ Model also indicated that, for a very small macroscopic deviatoric stress, strain energy jumps across grain boundaries could be an important driving mechanism of boundary-migration recrystallization in the Vostok accretion ice. This finding seemed consistent with the often sharp, irregular-shaped crystal boundaries observed in the Vostok ice cores.

The conclusions drawn from the FI Experiments and a simple impurity model had implications for the permeability of hydrocarbon drilling fluid in subglacial lake accretion ice. The possibility appeared evident for drilling fluid infiltration through ice, along GB junctions, as a drill borehole approaches the ceiling of a subglacial lake. Rough arguments were made that scaled temperature, chemistry and crystal geometry data from the FI Experiments and Vostok accretion ice. These arguments suggested that drilling fluid contamination of Lake Vostok may occur when the drilling borehole, below Vostok station, is within 6 to 70 m of the lake ceiling.

The upper Vostok accretion ice, which formed near the western lake margin (i.e., “accretion ice-1”), contains greater impurity concentrations than the deeper accretion ice, which formed further from the lake margins. The deviatoric stress is likely to also be greater in ice closer to the lake margins, where abrupt transitions occur in the nature of ice flow. Both of these factors would tend to increase the fraction of intergranular water in ice, and in turn may increase the probability of fuel-tunneling observed in this study. The prediction, based on results from the ITJ Model, of melting in the lower few meters of the westernmost accretion ice also had implications for the incorporation processes of debris and microbes into basal ice. The occurrence of stress-induced melting along grain boundaries would seemingly make

intergranular entrainment of debris more effective. Farther from the lake margins, where macroscopic deviatoric stress and intergranular melting are likely less prevalent, the ice structure may become more "closed-off" to debris.

Based on the findings of this study, the accretion ice over subglacial lakes may be permeable to drilling fluids. The permeability of accretion ice may increase near lake margins, where both macroscopic deviatoric stress and impurity concentrations are likely to be greater. The findings of this study also indicate that, when other variables are held fixed, faster drilling and the use of borehole fluids having lower water solubility would lessen chances of forward contamination via the observed fuel-tunneling process. These considerations may assist in future strategies for subglacial lake exploration.

BIBLIOGRAPHY

ANSYS Theory Reference. ANSYS Release 9.0 Documentation.

Adams, E. E. and R. L. Brown. Lake Vostok x-ray dislocation topographs. Unpublished raw data.

Aislabie, J. M., M. R. Balks, J. M. Foght, and E. J. Waterhouse (2004). Hydrocarbon spills on Antarctic soils: effects and management. *Environmental Science & Technology 38*(5), 1265–1274. Electronic version downloaded from http://pubs.acs.org/journals/esthag/index.html.

Alexander, S. P. and W. L. Stockton (2003). Lake Fryxell 79U crash site: initial hydrocarbon monitoring program. Technical report, Raytheon Technical Services Company, Polar Services Company.

Ashby, M. F. (1972). Boundary defects, and atomistic aspects of boundary sliding and diffusional creep. *Surface Science 31*, 498–542.

Baker, I., D. Cullen, and D. Iliescu (2003). The microstructural location of impurities in ice. *Canadian Journal of Physics 81*, 1–9.

Baker, I., F. Liu, K. Jia, X. Hu, D. Cullen, and M. Dudley (2000). Dynamic observations of dislocation/grain-boundary interactions in ice. *Annals of Glaciology 31*, 236–240.

Barnes, P., D. Tabor, and J. C. F. Walker (1971, August). The friction and creep of polycrystalline ice. *Proceedings of the Royal Society of London. Series A, Mathematical and Physical Sciences 324*(1557), 127–155. Electronic version retrieved 03/28/2005 from http://www.jstor.org/journals/00804630.html.

Barrette, P. D. and I. J. Jordaan (2003). 2003. *Cold Regions Science and Technology 36*, 25–36. This would be the note.

Bell, R. E., M. Studinger, A. A. Tikku, G. K. C. Clarke, M. M. Gutner, and C. Meertens (2002, March). Origin and fate of the Lake Vostok water frozen to the base of the East Antarctic ice sheet. *Nature 416*, 307–310.

Burnett, D. S. (1987). *Finite Element Analysis. From Concepts to Applications*. Reading, Massachusetts: Addison-Wesley Publishing Company.

Castelnau, O., G. R. Canova, R. A. Lebensohn, and P. Duval (1997). Modelling viscoplastic behavior of anisotropic polycrystalline ice with a self-consistent approach. *Acta Materialia 45*(11), 4823–4834.

Chandler, D. (1987). *Introduction to modern statistical mechanics*. Oxford University Press.

Christner, B. C., J. A. Mikucki, C. M. Foreman, J. Denson, and J. C. Priscu (2005, April). Glacial ice cores: A model system for developing extraterrestrial decontamination protocols. *Icarus 174*(2), 572–584. Electronic version downloaded 04/24/2005 from http://sciserver.lanl.gov/cgi-bin/sciserv.pl?collection=journals&journal=00191035&volume=collapse.

Clee, T. E., J. C. Savage, and K. G. Neave (1969, February). Internal friction in ice near its melting point. *Journal of Geophysical Research 74*(4), 973–979.

Clifford, J. (1967). Proton magnetic resonance data on ice. *Chemical Communications 17*, 880–881.

Colbeck, S. C. (1976, April). Water flow through veins in ice. Technical Report 76-6, Cold Regions Research and Engineering Laboratory, Corps of Engineers, U.S. Army, Hanover, New Hampshire.

Cullen, D. and I. Baker (2001a). The chemistry of grain boundaries in Greenland ice. *Journal of Glaciology 46*, 703–706.

Cullen, D. and I. Baker (2001b). Observation of impurities in ice. *Microscopy Research and Technique 55*, 198–207.

Cullen, D. and I. Baker (2002). The observation of sulfate crystallites in vostok accretion ice. *Materials Characterization 48*, 263–269.

Davis, G. H. and S. J. Reynolds (1996). *Structural Geology, of Rocks and Regions* (2nd ed.). New York: John Wiley and Sons.

De Angelis, M., J. R. Petit, J. Savarino, R. Souchez, and M. H. Thiemens (2004). Contributions of an ancient evaporitic-type reservoir to subglacial Lake Vostok chemistry. *Earth and Planetary Science Letters 222*, 751–765. Electronic version retrieved from: www.sciencedirect.com.

Defay, R., I. Prigogine, and A. Bellemans (1966). *Surface tension and adsorption*. New York, N.Y.: John Wiley and Sons, Inc.

Dieter, G. E. (1986). *Mechanical Metallurgy* (3rd ed.). New York: McGraw-Hill.

Dowdeswell, J. A. and M. J. Siegert (2003, February). The physiography of modern Antarctic subglacial lakes. *Global and Planetary Change 35*(3-4), 221–236. Electronic version downloaded 04/30/2005 from http://sciserver.lanl.gov/cgi-bin/sciserv.pl?collection=elsevier&journal=09218181.

Dudley, M., F. Liu, and I. Baker (1994). Studies of defect behavior in large-grain, polycrystalline ice using synchrotron x-ray topography. *Molecular crystals and liquid crystals 240*, 73–80.

Duval, P., M. F. Ashby, and I. Anderman (1983). Rate-controlling processes in the creep of polycrystalline ice. *The Journal of Physical Chemistry 87*(21), 4066–4074. Electronic version downloaded 05/25/2005 from http://pubs3.acs.org/acs/journals/toc.page?incoden=jpchax.

Eshelby, J. D. (1961, August). Dislocations in visco-elastic materials. *The Philosophical Magazine. A Journal of Theoretical, Experimental and Applied Physics 6*(68), 953–963.

Frank, F. C. (1968, October). Two-component flow model for convection in the Earth's upper mantle. *Nature 220*(5165), 350–352.

Fukazawa, H., K. Sugiyama, and S. Mae (1998, August). Acid ions at triple junction of antarctic ice observed by raman scattering. *Geophysical Research Letters 25*(15), 2845–2848.

Gagnon, R. E., H. Kiefte, M. J. Clouter, and E. Whalley (1987). Elastic constants of ice Ih, up to 2.8 kbar, by brillouin spectroscopy. *Journal de Physique C1*, 23–28.

Gammon, P. H., J. Kiefte, and M. J. Clouter (1980). Elastic constants of ice by brillouin spectroscopy. *Journal of Glaciology 25*(91), 159–167.

Gerasimoff, M. (2003). Drilling fluid observations and recommendations for U.S. Polar Program, Waiscores Drilling Project. Technical report, Space Science and Engineering Center, University of Wisconsin, Madison.

Ghahremani, F. (1980a). Effect of grain boundary sliding on anelasticity of polycrystals. *International Journal of Solids and Structures 16*, 825–845.

Ghahremani, F. (1980b). Effect of grain boundary sliding on steady creep of polycrystals. *International Journal of Solids and Structures 16*, 847–862.

Gibbs, J. W. (1948). *The Collected Works of J. Willard Gibbs*, Volume I. Thermodynamics. Yale University Press.

Gifkins, R. C. (1976, August). Grain-boundary sliding and its accomodation during creep and superplasticity. *Metallurgical Transactions A 7A*, 1225–1232.

Glen, J. W. and M. F. Perutz (1954). The growth and deformation of ice crystals. *Journal of Glaciology 2*, 397–403.

Gold, L. W. (1963, February). Deformation mechanisms in ice. In W. D. Kingery (Ed.), *Ice and Snow, Properties, Processes, and Applications*, Cambridge, Massachusetts, pp. 8–27. Massachusetts Institute of Technology: The M.I.T. Press.

Goldsby, D. L. and D. L. Kohlstedt (1997). Grain boundary sliding in fine-grained ice i. *Scripta Materialia 37*(9), 1399–1406.

Goldsby, D. L. and D. L. Kohlstedt (2001). Superplastic deformation of ice: experimental observations. *Journal of Geophysical Research 106*(B6), 11017–11030.

Goodman, D. J., H. J. Frost, and M. F. Ashby (1981). The plasticity of polycrystalline ice. *Philosophical Magazine A 43*(3), 665–695.

Griggs, D. T. and N. E. Coles (1954). Creep of single crystals of ice. SIPRE Research Report 11, Snow, ice and permafrost establishment, Core of Engineers, U.S. Army.

Gross, G. W., C. Wu, L. Bryant, and C. McKee (1975, April). Concentration dependent solute redistribution at the ice/water phase boundary. II. Experimental investigation. *The Journal of Chemical Physics 62*(8), 3085–3092.

Ham, R. K. (1961). The determination of dislocation densities in thin films. *Philosophical Magazine 6*, 1183–1184.

Harrison, W. D. (1972). Temperature of a temperate glacier. *Journal of Glaciology 11*(61), 15–29.

Harrison, W. D. and C. F. Raymond (1976). Impurities and their distribution in temperate glacier ice. *Journal of Glaciology 16*(74), 173–181.

Higashi, A. (1967). Mechanisms of plastic deformation in ice single crystals. In *Physics of snow and ice*, Volume 1, pp. 277–289. Proceeding of the International Conference on Low Temperature Science: Institute of Low Temperature Science, Hokkaido University.

Higashi, A., S. Koinuma, and S. Mae (1964, October). Plastic yielding in ice single crystals. *Japanese Journal of Applied Physics 3*(10), 610–616.

Hill, R. (1950). *The Mathematical Theory of Plasticity*. Oxford Engineering Science Series. Oxford: Clarendon Press.

Hirsch, P. B., A. Howie, R. B. Nicholson, D. W. Pashley, and M. J. Whelan (1965). *Electron microscopy of thin crystals*. New York: Plenum Press.

Hobbs, P. V. (1974). *Ice Physics*. London: Oxford University Press.

Hull, D. and D. L. Bacon (1984). *Introduction to Dislocations* (3 ed.), Volume 37 of *International Series on Materials Science and Technology*. Oxford: Pergamon Press.

Hutchinson, J. W. (1976, February). Bounds and self-consistent estimates for creep of polycrystalline materials. *Proceedings of the Royal Society of London. Series A, Mathematical and Physical Sciences 348*(1652), 101–127. Electronic version downloaded 05/01/2005 from http://www.jstor.org.

Hutchinson, J. W. (1977, September). Creep and plasticity of hexagonal polycrystals as related to single crystal slip. *Metallurgical Transactions A 8A*, 1465–1469.

Johnston, W. G. (1962, September). Yield points and delay times in single crystals. *Journal of Applied Physics 33*(9), 2716–2730. Electronic version downloaded 02/2005 from URL: http://scitation.aip.org/journals/doc/JAPIAU-home/top.jsp.

Johnston, W. G. and J. J. Gilman (1959, February). Dislocation velocities, dislocation densities, and plastic flow in lithium flouride crystals. *Journal of Applied Physics 30*(2), 129–144. Electronic version downloaded 05/09/2005 from http://scitation.aip.org/journals/doc/JAPIAU-home/top.jsp.

Jones, D. R. H. (1974). Review: The free energies of solid-liquid interfaces. *Journal of Materials Science 9*, 1–17.

Jouzel, J., J. R. Petit, R. Souchez, N. I. Barkov, V. Y. Lipenkov, D. Raynaud, et al. (1999, December). More than 200 meters of lake ice above subglacial Lake Vostok, Antarctica. *Science 286*(5447), 2138–2141.

Kamb, W. B. (1961a). The glide direction in ice. *Journal of Glaciology 3*, 1097–1106.

Kamb, W. B. (1961b). The thermodynamic theory of nonhydrostatically stressed solids. *Journal of Geophysical Research 66*(1), 259–271.

Kapitsa, A. P., J. K. Ridley, G. de Q. Robin, M. J. Siegert, and I. A. Zotikov (1996, June). A large deep freshwater lake beneath the ice of central East Antarctica. *Nature 381*, 684–686.

Karl, D. M., D. F. Bird, K. Björkman, T. Houlihan, R. Shackelford, and L. Tupas (1999). Microorganisms in the accreted ice of Lake Vostok, Antarctica. *SCIENCE 286*(5447), 2144–2147.

Kennicutt II, M. C., S. T. Sweet, W. Fraser, M. E. Culver, W. L. Stockton, K. Dunton, et al. (1990). Oil spillage in Antarctica. Initial report of the National Science Foundation-sponsored Quick Response Team on the grounding of the Bahia Paraiso. *Environmental Science & Technology 24*(5), 620–624. Electronic version downloaded from http://pubs.acs.org/journals/esthag/index.html.

Ketcham, W. M. and P. V. Hobbs (1969). An experimental determination of the surface energies of ice. *Philosophical Magazine 19*(162), 1161–1173.

Killawee, J. A., I. J. Fairchild, J.-L. Tison, L. Janssens, and R. Lorrain (1998). Segregation of solutes and gases in experimental freezing of dilute solutions: Implications for natural glacial systems. *Geochimica et Cosmochimica Acta 62*(23-24), 3637–3655.

Knight, P. G. (1997). The basal layer of glaciers and ice sheets. *Quaternary Science Reviews 16*(9), 975–993.

Kondaurov, V. I. (2002, April). Thermomechanics of phase transitions of the first order in solids. *Russian Journal of Earth Sciences 4*(2), 85–102. Electronic version downloaded 04/2002 from http://rjes.wdcb.ru/v04/TJE02084/TJE02084.htm.

Kuroiwa, D. (1964). Internal friction of ice. In *Contributions from the Institute of Low Temperature Science*, Number 18 in A, pp. 1–62. Sapporo, Japan: Hokkaido University.

Kwok, R., M. J. Siegert, and F. D. Carsey (2000). Ice motion over Lake Vostok, Antarctica: constraints on inferences regarding the accreted ice. *Journal of Glaciology 46*(155), 689–694.

Levine, B. and I. N. Levine (1988). *Physical Chemistry*. McGraw-Hill College.

Lide, D. R. (Ed.) (2001). *CRC handbook of chemistry and physics* (82 ed.). Boca Raton: CRC Press.

Lide, D. R. (Ed.) (2002). *CRC Handbook of Chemistry and Physics* (83 ed.). Boca Raton: CRC Press.

Liu, F. and I. Baker (1994). Dislocation/grain boundary interactions in ice I_h under creep conditions. Trondheim, Norway, pp. 484–494. IAHR Ice Symposium.

Liu, I.-S. (2002). *Continuum Mechanics*. Berlin: Springer Verlag.

Lliboutry, L. (1993). Internal melting and ice accretion at the bottom of temperate glaciers. *Journal of Glaciology 39*(131), 50–64.

Lliboutry, L. L. (1971). Permeability, brine content and temperature of temperate ice. *Journal of Glaciology 10*(58), 15–29.

Mader, H. M. (1992). Observations of the water-vein system in polycrystalline ice. *Journal of Glaciology 38*(130), 333–347.

Masolov, V. N., V. V. Lukin, A. N. Sheremetiev, and S. V. Popov (2001). Geophysical investigations of the subglacial Lake Vostok in Eastern Antarctica. *Doklady Earth Sciences 379A*(6), 734–738. Translated from from Doklady Akademii Nauk, 379(5), 680-685.

Mayer, C. and M. J. Siegert (2000). Numerical modelling of ice-sheet dynamics across the Vostok subglacial lake, central East Antarctica. *Journal of Glaciology 46*(153), 197–205.

McConnel, J. C. (1891). On the plasticity of an ice crystal. *Proceedings of the Royal Society of London 49*, 323–343.

McKittrick, L. R. and R. L. Brown (1996). On the effect of phase transformations on saline ice compliance. *Journal of Glaciology 42*(142), 519–532.

McLean, D. (1957). *Grain Boundaries in Metals*. Oxford: Clarendon Press.

Mellor, M. and R. Testa (1969). Effect of temperature on the creep of ice. *Journal of Glaciology 8*(52), 131–145.

Michel, B. (1978). *Ice Mechanics*. Québec: L'Université Laval.

Montagnat, M., P. Duval, P. Bastie, B. Hamelin, O. Brissaud, M. de Angelis, et al. (2001). High crystalline quality of large single crystals of subglacial ice above Lake Vostok (Antarctica) revealed by hard X-ray diffraction. *Comptes Rendus de L'Academie des Sciences Series IIA Earth and Planetary Science 333*, 419–425.

Mosher, D. R. and R. Raj (1974, December). Use of the internal friction technique to measure rates of grain boundary sliding. *Acta Metallurgica 22*, 1469–1474.

Mulvaney, R., E. W. Wolff, and K. Oates (1988, January). Sulphuric acid at grain boundaries in antarctic ice. *Nature 331*, 247–249.

Nakamura, T. and S. J. Jones (1970). Softening effect of dissolved hydrogen chloride in ice crystals. *Scripta Metallurgica 4*, 123–126.

Nakaya, U. (1958). Mechanical properties of single crystals of ice. SIPRE Research Report 28, Snow, ice and permafrost establishment, Core of Engineers, U.S. Army.

Nye, J. F. (1957). *Physical properties of crystals, their representation by tensors and matrices*. Oxford: Clarendon Press.

Nye, J. F. (1991). Thermal behavior of glacier and laboratory ice. *Journal of Glaciology 37*(127), 401–413.

Nye, J. F. and F. C. Frank (1973, September). Hydrology of the intergranular veins in a temperate glacier. In *Symposium on the hydrology of glaciers*, Number Publication 95, Cambridge, pp. 157–161.

Nye, J. F. and S. Mae (1972). The effect of non-hydrostatic stress on intergranular water veins and lenses in ice. *Journal of Glaciology 11*(61), 81–101.

Oguro, M. (1988). *Lattice Defects in Ice Crystals*, Chapter III, pp. 29–47. Sapporo, Japan: Hokkaido University Press.

Paterson, M. S. (1973, May). Nonhydrostatic thermodynamics and it geologic applications. *Reviews of Geophysics and Space Physics 11*(2), 355–389.

Petit, J. R., J. Jouzel, D. Raynaud, N. I. Barkov, J. M. Barnola, I. Basile, et al. (1999, June). Climate and atmospheric history of the past 420,000 years from the Vostok ice core, Antarctica. *Nature 399*, 429–436.

Petrenko, V. F. and R. W. Whitworth (1999). *Physics of Ice*. Oxford: Oxford University Press.

Pfann, W. G. (1966). *Zone Melting* (2nd ed.). New York: John Wiley & Sons, Inc.

Picu, C. R. and V. Gupta (1996). Stress singularities at triple junctions with freely sliding grains. *International Journal of Solids and Structures 33*(11), 1535–1541.

Picu, R. C. and V. Gupta (1995a). Crack nucleation in columnar ice due to elastic anisotropy and grain boundary sliding. *Acta Metallurgica et Materialia 43*(10), 3783–3789.

Picu, R. C. and V. Gupta (1995b). Observations of crack nucleation in columnar ice due to grain boundary sliding. *Acta Metallurgica et Materialia 43*(10), 3791–3797.

Price, P. B. (2000). A habitat for psychrophiles in deep antarctic ice. *Proceedings of the National Academy of Sciences of the United States of America 97*(3), 1247–1251.

Priscu, J. C., E. E. Adams, W. B. Lyons, M. A. Voytek, D. W. Mogk, R. L. Brown, et al. (1999). Geomicrobiology of subglacial ice above Lake Vostok, Antarctica. *SCIENCE 286*(5447), 2141–2144.

Raj, R. and M. F. Ashby (1971, April). On grain boundary sliding and diffusional creep. *Metallurgical Transactions 2*, 1113–1127.

Raymond, C. F. and W. D. Harrison (1975). Some observations on the behavior of the liquid and gas phases in temperate glacier ice. *Journal of Glaciology 14*(71), 213–233.

Rempel, A. W., J. S. Wettlaufer, and E. D. Waddington (2002). Anomalous diffusion of multiple impurity species: predicted implications for the ice core climate records. *Journal of Geophysical Research 107*(B12), ECV3–1–ECV3–12.

Renaud, A. (1949, October). A contribution to the study of the glacier grain. *Journal of Glaciology 1*(6), 320–324.

Royston-Bishop, G. Major ion summary for vostok accretion ice. Unpublished data.

Royston-Bishop, G. (In press). Incorporation of particulates into accreted ice above subglacial Lake Vostok, Antarctica. *Annals of Glaciology 40*.

Russian Federation (2001, July). Expert conclusion for the project justification and development clean technology for penetrating the subglacial Lake Vostok (Antarctica). XXIV Conference on the Treaty on the Antarctic, WP-29. St. Petersburg, Russia.

Schoeck, G. (1962, May). Correlation between dislocation length and density. *Journal of Applied Physics 33*(5), 1745–1747.

Schweiger, H. F. and W. Haas (1988, April). Application of the thin-layer interface element to geotechnical problems. In G. Swoboda (Ed.), *Numerical Methods in Geomechanics Innsbruck 1988*, Volume 1 of *Proceedings of the Sixth International Conference on Numerical Methods in Geomechanics*, pp. 907–912. University of Innsbruck: Balkema, Rotterdam.

Schwerdtfeger, P. (1963, October). The thermal properties of sea ice. *Journal of Glaciology 4*(36), 789–807.

Siegert, M. J., R. Kwok, C. Mayer, and B. Hubbard (2000, February). Water exchange between the subglacial Lake Vostok and the overlying ice sheet. *Nature 403*, 643–646.

Siegert, M. J., M. Tranter, J. C. Ellis-Evans, J. C. Priscu, and W. B. Lyons (2003). The hydrochemistry of Lake Vostok and the potential for life in Antarctic subglacial lakes. *Hydrological Processes 17*(4), 795–814.

Skrzypek, J. J. (1993). *Plasticity and Creep. Theory, Examples, and Problems* (English ed.). Boca Raton, Florida: CRC Press.

Smith, C. S. and L. Guttman (1953, January). Measurement of internal boundaries in three-dimensional structures by random sectioning. *Transactions of the American Institute of Mining, Metallurgical, and Petroleum Engineers, Incorporated 197*, 81–87.

Souchez, R., J. R. Petit, J.-L. Tison, J. Jouzel, and V. Verbeke (2000). Ice formation in subglacial Lake Vostok, Central Antarctica. *Earth and Planetary Science Letters 181*, 529–538.

Srolovitz, D. J. (1989). On the stability of surfaces of stressed solids. *Acta Metallurgica 37*(2), 621–625.

Steinemann, S. (1954). Results of preliminary experiments on the plasticity of ice crystals. *Journal of Glaciology 2*, 404–412.

Steinemann, S. (1958, September). Thermodynamics and mechanics of ice at the melting point. In L. J. Tison (Ed.), *Symposium of Chamonix: Physics of the movement of the ice*, Volume 47, pp. 254–265. International Association of Scientific Hydrology.

Studinger, M., R. E. Bell, G. D. Karner, A. A. Tikku, J. W. Holt, D. L. Morse, et al. (2003). Ice cover, landscape setting, and geological framework of Lake Vostok, East Antarctica. *Earth and Planetary Science Letters 205*, 195–210. Downloaded from www.elsevier.com/locate/epsl.

Talalay, P. G. and N. S. Gundestrup (2002, March). Hole fluids for deep ice core drilling. In N. Azuma and Y. Fujii (Eds.), *Memoirs of National Institute of Polar Research*, Number 56, pp. 148–170. Proceedings of Ice Drilling Technology 2000: National Institute of Polar Research.

Taylor, G. I. (1938, May). Plastic strain in metals. *Journal of the Institute of Metals 62*, 307–324. 28th May lecture to the Institute of Metals.

Tiller, W. A. (1964, November). Dendrites. *Science 146*(3646), 871–879. Electronic version downloaded 05/03/2005 from http://www.jstor.org/.

Tumeo, M. A. and M. K. Larson (1994). Movement of fuel spills in the ross ice shelf. *Antarctic Journal of the United States 29*(5), 373–374.

Tumeo, M. A. and A. E. Wolk (1994). Assessment of the presence of oil-degrading microbes at McMurdo Station. *Antarctic Journal of the United States 29*(5), 375–377.

Van Bueren, H. G. (1959, September). Theory of creep of germanium crystals. *Physica 25*(9), 775–791.

Victor, P. (2003). Water sampling of the subglacial Lake Vostok. Technical report, Russian Antarctic Expedition (RAE), Arctic and Antarctic Research Institute (AARI), St-Petersburg, Russia.

Vulliet, L. and K. Hutter (1988, April). Some constitutive laws for creeping soil and for rate-dependent sliding at interfaces. In G. Swoboda (Ed.), *Numerical Methods in Geomechanics Innsbruck 1988*, Volume 1 of *Proceedings of the Sixth International Conference on Numerical Methods in Geomechanics*, pp. 495–502. University of Innsbruck: Balkema, Rotterdam.

Wakahama, G. (1967). On the plastic deformation of single crystal of ice. In *Physics of snow and ice*, Volume 1, pp. 291–311. Proceeding of the International Conference on Low Temperature Science: Institute of Low Temperature Science, Hokkaido University.

Walford, M. E. R. and J. F. Nye (1991). Measuring the dihedral angle of water at a grain boundary in ice by an optical diffraction method. *Journal of Glaciology 37*(125), 107–112.

Wangsness, R. K. (1986). *Electromagnetic Fields* (2nd ed.). New York: John Wiley & Sons.

Weertman, J. (1957, October). Steady-state creep of crystals. *Journal of Applied Physics 28*(10), 1185–1189. Downloaded 02/27/2005 from http://scitation.aip.org/journals/doc/JAPIAU-home/top.jsp.

Weertman, J. (1963, February). The eshelby-schoeck viscous dislocation damping mechanism applied to the steady-state creep of ice. In W. D. Kingery (Ed.), *Ice and Snow, Properties, Processes, and Applications*, Cambridge, Massachusetts, pp. 28–33. Massachusetts Institute of Technology: The M.I.T. Press.

Weertman, J. (1973, August). Creep of ice. In E. Whalley, S. J. Jones, and L. W. Gold (Eds.), *Physics and Chemistry of Ice*, Ottawa, Canada, pp. 320–337. Royal Society of Canada: University of Toronto Press.

Weiss, J. and E. M. Schulson (2000). Grain-boundary sliding and crack nucleation in ice. *Philosophical Magazine A 80*(2), 279–300.

Weisstein, E. W. Truncated octahedron. From Mathworld—A Wolfram Web Resource. Retrieved 04/16/2004 from http://mathworld.wolfram.com/ TruncatedOctahedron.html.

Wilson, C. and Y. Zhang (1994). Comparison between experiment and computer modelling of plane-strain simple-shear ice deformation. *Journal of Glaciology 40*(134), 46–55.

Wilson, C., Y. Zhang, and K. Stüwe (1996). The effects of localized deformation on melting processes in ice. *Cold Regions Science and Technology 24*, 177–189.

Wilson, C. J. L. and B. Marmo (1999). Flow in polycrystalline ice. World Wide Web. The School of Earth Sciences- The University of Melbourne-Australia. Retrieved 04/2004 from URL: http://web.earthsci.unimelb.edu.au/wilson/ice1/.

Zumdahl, S. S. (1993). *Chemistry* (3rd ed.). Lexington, MA: D. C. Heath and Company.

APPENDICES

APPENDIX A

INSTRUCTIONS TO EXECUTE ETB MODEL

The Elastic Two Blocks (ETB) Model is used to simulate stress concentrations between two bonded cubes having anisotropic elastic material properties of ice. Results from this model were presented in Chapter 3 of the dissertation. The input file to run the ETB Model in ANSYS is available in the "AppA-ETB" file collection at Internet URL address http://www.montana.edu/etd/available/sjepsen_1205.html. The file "TwoBlocks.inp" is the input file to be read by ANSYS to execute the model. The file "cmap-grey.cmap" is the ANSYS color map used to create the gray scale contour maps presented in the dissertation. Model parameters can be adjusted by editing the input file TwoBlocks.inp in a text editor.

APPENDIX B

INSTRUCTIONS TO EXECUTE ETJ MODEL

The Elastic Triple Junction (ETJ) Model is used in dissertation Chapter 3 to simulate stresses in a triple junction of three bonded ice crystals that are each assumed to have anisotropic elastic properties. The results of this model are presented in Chapter 3 for 100 randomly-generated c-axis spherical coordinate sets, each of which represent a particular combination of crytallographic c-axis orientations. A "coupled node" and "non-coupled node" analysis is carried out for each c-axis spherical coordinate set. The coupled node analyses couple the z'-displacements of nodes on the z' = 0 and 0.5 m faces of the model. The non-coupled node analyses do not couple any nodal displacements.

The input files to run the ETJ Model in ANSYS are available in the "AppB-ETJ" file collection at Internet URL address http://www.montana.edu/etd/available/sjepsen_1205.html. The instructions for running the ETJ model in ANSYS are as follows. Let N equal the desired number of randomly-generated, c-axis spherical coordinate sets for which to obtain solutions. A coupled node and non-coupled node analysis is carried out for each c-axis spherical coordinate set. Note that the term "generalized plane strain" in any input file comments is to be replaced with the term "coupled node" used in the dissertation. In addition, the term "no plane strain" included in any comments is to be replaced with the term "non-coupled node" used in the dissertation. Noting this terminology change is preferable to reformatting commentary in all of the input files. Locate and open the input file named "Main.inp." This file contains a controlling loop for running the ANSYS input file "ElasticTJ1.inp" a total of 2N times (the first N times for non-coupled node analyses, followed by N times for coupled node analyses). Set N to the desired value, then save Main.inp. The user is encouraged to improve on the efficiency and appearance of the code as is seen fit. Locate and open the macro file named "USERDATA.mac." This file contains the model parameter settings for stress, temperature, material type, mesh density, and geometry. Adjust these values as necessary. Set parameter "mactau" to zero for boundary conditions consisting of purely hydrostatic stress, and adjust parameter "macpres" to the desired magnitude of hydrostatic stress to be applied at the model boundaries.

The ETJ Model is now ready to be implemented. Execute the controlling input file Main.inp in ANSYS. The model should run successfully with different data files being exported to the working directory. These files are described in the following section. The user can by-pass the controlling file Main.inp, and instead execute input file ElasticTJ1.inp for a single (i.e., N = 1) model analysis. To do this, the indicated blocks of code at the beginning of file ElasticTJ1.inp must be judiciously commented out or enabled, as indicated in the commentary. An optional, but recommended, last step is to execute input file "File_Strip.inp" to erase ("clean up") all files except the text data files. The file "cmap-grey.cmap" is the ANSYS color map used to create the gray scale contour maps presented in the dissertation.

Data File Descriptions for Appendix B

mxslocs.txt: Locations (with respect to global frame) of element centroids in the submodel where the maximum hydrostatic pressure and shear stress resolved along the basal plane occurs. Results are for the non-coupled node analyses. Only submodel elements are considered having centroids located in the (central) z' = 0.25 plane, with nodes between x' = .125 and .375 m. Data columns "xmaxhp", "ymaxhp" and "zmaxhp" list the x', y' and z', respectively, element centroid locations where the maximum hydrostatic pressure occurs. Data columns "xmaxtss", "ymaxtss" and "zmaxtss" list the x', y' and z', respectively, element centroid locations where the maximum shear stress, resolved along the basal plane, occurs. Each of the N total data rows correspond to a different c-axis spherical coordinate set. The spherical coordinate values of the N different sets are listed in each row of files "mxsvals.txt" and "mxsvalsPS.txt."

mxslocsPS.txt: Locations (with respect to global frame) of element centroids in the submodel where maximum hydrostatic pressure and shear stress resolved along the basal plane occurs. Results are for the coupled node analyses ("PS" in file name originally indicated "generalized plane strain" analyses). Only submodel elements are considered having centroids located in the (central) z' = 0.25 m plane, with nodes between x' = .125 and .375 m. Data columns "xmaxhp", "ymaxhp" and "zmaxhp" list the x', y' and z', respectively, element centroid locations where the maximum hydrostatic pressure occurs. Data columns "xmaxtss", "ymaxtss" and "zmaxtss" list the x', y' and z', respectively, element centroid locations where the maximum shear stress resolved along the basal plane occurs. Each of the N total data rows correspond to a different c-axis spherical coordinate set.

mxsvals.txt: Maximum element table values of hydrostatic pressure (maxhp) and shear stress resolved along the basal plane (maxtss) in the submodel for the eight randomly calculated c-axis spherical coordinates phi1 (i.e., ϕ_1), theta1 (i.e., θ_1), phi2 (i.e., ϕ_2, etc.), theta2, phi3, theta3, phi4 and theta4. Results are for the non-coupled node analyses. Each maxhp value represents the element solution evaluated at the centroid location "xmaxhp", "ymaxhp" and "zmaxhp" in the corresponding row of file "mxslocs.txt." Each maxtss-value represents the element solution evaluated at the centroid location "xmaxtss", "ymaxtss" and "zmaxtss" in the corresponding row of file "mxslocs.txt."

mxsvalsPS.txt: Maximum element table values of hydrostatic pressure (maxhp) and shear stress resolved along the basal plane (maxtss) in the submodel for the eight randomly calculated c-axis spherical coordinates phi1 (i.e., ϕ_1), theta1 (i.e., θ_1), phi2 (i.e., ϕ_2, etc.), theta2, phi3, theta3, phi4 and theta4. Results are for the coupled node analyses ("PS" in file name originally indicated "generalized plane strain" analyses). Each maxhp value represents the element solution evaluated at the centroid location "xmaxhp", "ymaxhp"

and “zmaxhp” in the corresponding row of file “mxslocsPS.txt.” Each maxtss value represents the element solution evaluated at the centroid location “xmaxtss”, “ymaxtss” and “zmaxtss” in the corresponding row of file “mxslocsPS.txt.”

runtimes.txt: Beginning and ending wall clock times (hours) for the ETJ model run.

subpar.txt: Submodel parameters read by ANSYS during the submodeling routine.

APPENDIX C

INSTRUCTIONS TO EXECUTE MESH CONVERGENCE STUDY FOR ETJ MODEL

A mesh convergence study is carried out in dissertation Chapter 3 to analyze the sensitivity of calculated shear stresses, resolved along the basal plane, to the values of different mesh parameters. The synopsis of this study is as follows. The number of different c-axis spherical coordinate sets to use in the convergence study is given by parameter NUMCOORD. The loop counter i references the c-axis spherical coordinate set and takes on integer values from 1 to NUMCOORD. The number of different meshes for which to compare stress results is given by parameter NUMMESH. The loop counter j references the mesh and takes on integer values from 1 to NUMMESH. The value of NUMMESH is 3 in the convergence study of Chapter 3. For each value of counter i, solutions are obtained for the j = 1, 2 and 3 meshes. These are the intermediate, coarse and fine meshes, respectively. For each c-axis spherical coordinate set, referenced by index i, basal plane shear stresses calculated from the different meshes are interpolated onto the same path. The position of the path, onto which basal plane shear stress results are interpolated from the submodel, is determined from the j = 1 (intermediate) mesh. The same path is then used for the j = 2 and 3 meshes. A different path, referred to as path i, is used for each value of i.

Again, the position of path i is determined from results of the intermediate j = 1 mesh. The path is constrained to lie in the (central) z' = 0.25 m plane and to be parallel to the global x' axis. The y' coordinate of the path is set to coincide with the centroid location of the element having the largest basal plane shear stress in the submodel. The only elements considered for path location and data interpolation are those in the submodel with centroid locations in the (central) z' = 0.25 m plane, with nodes between x' = 0.125 and 0.375 m. Let σ_b denote the magnitude of shear stress resolved along the basal plane. Element solutions for σ_b are interpolated from the element centroids in the submodel onto the different paths.

The input files to run the mesh convergence study of the ETJ Model, in ANSYS, are available in the "AppC-ETJ-MeshConv" file collection at Internet URL address http://www.montana.edu/etd/available/sjepsen_1205.html. The instructions for running the convergence study in ANSYS are as follows. Locate and open the input file named "Main.inp." This file contains a controlling loop for running the ANSYS input file "ElasticTJ2.inp" a total of NUMCOORD × NUMMESH times; that is, NUMMESH times for each c-axis spherical coordinate set. Set the desired values of parameters NUMCOORD and NUMMESH in Main.inp. Also, set the desired number of path interpolation points PTHDVS.

Specify the values of the MESHSET array in Main.inp. This array consists of the following mesh setting parameters: CM1, CM2, FM1 and FM2. Parameters CM1 and CM2 control the mesh density of the coarse model. The value of CM1 is one-half the number of element divisions across the hexagonal prisms in the x'y' plane. The value of CM2 is number of element divisions along the depth (z' direction) of the coarse mesh model. In the convergence study of Chapter 3, CM1 and CM2 are set to 3 and 3,

respectively, for all meshes. Parameters FM1 and FM2 control the mesh density of the submodel. Twice the value of FM1 is equal to the number of element divisions in the submodel along the geometry segment shown in Figure 3.9. All element divisions in the x'y' plane of the submodel scale linearly with the setting of FM1. The value of FM2 is equal to the number of element divisions along the depth (z' direction) of the submodel. MESHSET is the 2D array, of components (j,k), consisting of the values CM1, CM2, FM1 and FM2 for the different meshes. The values in row j are the settings for mesh j, where j runs from 1 to NUMMESH. The MESHSET array consists of four columns (i.e., k = 1 to 4). The data in columns 1, 2, 3, and 4 are the values of mesh parameters CM1, CM2, FM1 and FM2, respectively. Therefore, the values MESHSET(j,1), MESHSET(j,2), MESHSET(j,3), and MESHSET(j,4) are the values of CM1, CM2, FM1 and FM2 for the j^{th} mesh. Fill the MESHSET array with desired values and save Main.inp. The values for all rows (1 to NUMMESH) in the array should be set to the desired values. Make sure to verify that the dimensions of the MESHSET array are consistent with values of NUMCOORD and NUMMESH.

Open the macro file named "USERDATA.mac." Set the values for temperature, TPTR, hydrostatic stress at the model boundary, MACPRES, and deviatoric stress at the model boundary, MACTAU. Specify the material type and make any desired changes in geometry settings. Save the file USERDATA.mac.

The mesh convergence study for the ETJ Model is now ready to be carried out. Execute the controlling input file Main.inp in ANSYS. To execute the file in batch mode, enter the appropriate DOS command at a user prompt; different commands are stored in file "DOSCOMMND." Make sure to update the directory paths specified in the file DOSCOMMND. During the solution stage, ANSYS exports different data files to the current working directory. These files are described in the following section. The file "cmap-grey.cmap" is the ANSYS color map used to create the gray scale contour maps presented in the dissertation.

Data File Descriptions for Appendix C

tssexij.txt: Interpolated path data of shear stress, resolved along basal plane, from submodel elements. The ij post-fix in the file name corresponds to results from mesh j using c-axis spherical coordinate set i. The data in columns 1, 2 and 3 are the x', y' and z' locations, respectively, of the path points. The column 4 data are the interpolated values of shear stress (Pa) resolved along the basal plane.

tssdat$i$.txt: Interpolated path data of shear stress, resolved along basal plane, from submodel elements for all meshes. The i post-fix in the file name corresponds to results from c-axis spherical coordinate set i. The data in columns 1, 2 and 3 are the x', y' and z' locations, respectively, of the different path points.

The data in columns 4, 5, 6,..., 3+NUMMESH are the interpolated values of shear stress (kPa) resolved along the basal plane for meshes 1, 2, 3,..., NUMESH. Each of these files is a compilation of the files named "tssexij.txt" for all values of j.

COORDSETTINGS.txt: Values of all randomly-generated c-axis spherical coordinates. Each row of the file contains, from left to right: theta1 (i.e., θ_1), phi1 (i.e., ϕ_1, etc.), theta2, phi2, theta3, phi3, theta4, phi4. Row i of the data file contains the coordinates for c-axis spherical coordinate set i, where i is an integer ranging from 1 to NUMCOORD.

runtimes.txt: Wall clock times (hours) at beginning of analysis and after each model run. There are a total of NUMMESH×NUMCOORD+1 entries.

subpar.txt: Submodel parameters read by ANSYS during the submodeling routine.

APPENDIX D

INSTRUCTIONS TO EXECUTE MESH SENSITIVITY STUDY FOR ITJ MODEL

The results of a study are presented in Chapter 5 (see page 79) to analyze the sensitivity of calculated hydrostatic stress from the ITJ Model on mesh parameter FM2, the number of elements in the z' direction of the submodel. This appendix provides instructions for running this analysis in ANSYS with use of input files on the accompanying CD. The following summary is similar to that presented in Appendix C. The number of different c-axis spherical coordinate sets to use in the sensitivity study is given by parameter NUMCOORD. The loop counter i references the c-axis coordinate set and takes on integer values from 1 to NUMCOORD. The number of different meshes for which to compare stress results is given by parameter NUMMESH. The loop counter j references the different meshes and takes on integer values from 1 to NUMMESH. The value of NUMMESH was 5 in the analysis for Chapter 5 of the dissertation; this value was one greater than the value of 4 that was actually presented in Chapter 5 of the dissertation. The results from one of the meshes added no real value to the dissertation discussion, were difficult to communicate clearly with four other curves on a grayscale plot, and were therefore removed from the presentation in Chapter 5. For each value of counter i, solutions are obtained for meshes using five different values of FM2 (i.e., $j = 1$ to 5). The mesh with the largest FM2-value corresponds to $j = 1$, and the mesh with the smallest FM2-value corresponds to $j = 5$. For each c-axis spherical coordinate set, referenced by index i, the calculated shear stress resolved along the basal plane from the different meshes are interpolated onto the same path. The position of this path is determined from the $j = 1$ mesh. The same path is then used for the $j = 2$ to 5 meshes. A different path, referred to as path i, is determined and used for each value of i.

Again, the position of path i is determined from results of the $j = 1$ mesh. The path is constrained to lie in the (central) z' = 0.25 m plane, to begin at the central z' axis of the submodel, and to end at the outer edge of the submodel. For a crystal size, d_{g1}, of 0.5 m, the central z' axis of the submodel is located at x' = 0.25 m, y' = 0.25 m. The azimuthal coordinate of the path about the z' direction has yet to be constrained. This coordinate is set to coincide with the centroid location of the element having the largest basal plane shear stress in the submodel. The only elements considered for path location and data interpolation are those in the submodel with centroid locations in the (central) z' = 0.25 m plane. Let σ_h denote the calculated values of hydrostatic stress. Element solutions of σ_h are interpolated from element centroids of different meshes onto the same path and compared. This is done for each c-axis spherical coordinate set (i-value).

The input files to run the mesh sensitivity study of the ITJ Model, in ANSYS, are available in the "AppD-ITJ-MeshSens" file collection at Internet URL address http://www.montana.edu/etd/available/sjepsen_1205.html. The instructions for running the convergence study in ANSYS are as follows. Locate and open the input file named "Main.inp." This file contains a controlling loop for running the ANSYS

input file "CrTJ1.inp" a total of NUMCOORD × NUMMESH times; that is, NUMMESH times for each c-axis spherical coordinate set. Set the desired values of parameters NUMCOORD and NUMMESH in Main.inp. Also, set the desired number of path interpolation points PTHDVS.

Specify the values of components of the MESHSET array in Main.inp. This array consists of the following mesh setting parameters: CM1, CM2, FM1, FM2 and d_{g2}. Parameters CM1 and CM2 control the mesh density of the coarse model. The value of CM1 is one-half the number of element divisions across the hexagonal prisms in the x'y' plane. The value of CM2 is number of element divisions along the depth (z' direction) of the coarse mesh model. In the mesh sensitivity study of Chapter 5, CM1 and CM2 are set to 3 and 3, respectively, for all meshes. Parameters FM1 and FM2 control the mesh density of the fine mesh submodel. The value of FM1 is equal to the number of element divisions along the radius of the fine mesh submodel. The value of FM2 is equal to the number of element divisions along the depth (z' direction) of the fine mesh submodel. The parameter d_{g2} specifies the depth (z' dimension) of the fine mesh submodel. MESHSET is the 2D array, of components (j,k), consisting of the values CM1, CM2, FM1, FM2 and d_{g2} for the different meshes. The values in row j of MESHSET specify the settings for mesh j, with j ranging from 1 to NUMMESH. The MESHSET array consists of five columns (i.e., k = 1 to 5). The data in columns 1, 2, 3, 4 and 5 are the values of mesh parameters CM1, CM2, FM1, FM2 and d_{g2}, respectively. Therefore, the values MESHSET(j,1), MESHSET(j,2), MESHSET(j,3), MESHSET(j,4) and MESHSET(j,5) are the values of CM1, CM2, FM1, FM2 and d_{g2} for the j^{th} mesh. The values of mesh parameters FM2 and d_{g2} are dependent on one another as follows. The element z'-dimensions in the submodel are held fixed at $d_{g1}/13$. Thus, mesh parameter d_{g2} has a value given by FM2×$d_{g1}/13$. The independent variable of the mesh sensitivity study is FM2, and from this follows the value used for d_{g2}. Fill the MESHSET array with desired values and save Main.inp. The values for all rows (1 to NUMMESH) in the array should be specified. Make sure to verify that the dimensions of the MESHSET array are consistent with values of NUMCOORD and NUMMESH.

Open the macro file named "USERDATA.mac." Set the following: TPTR = temperature; macpres = hydrostatic stress applied at model boundary; mactau = deviatoric stress applied at model boundary; MATERIAL = material type; CONTCH = choice of whether or not to use grain boundary sliding (i.e., frictionless "contact"); load step parameters N1, N2 and TFINAL; and geometry parameters a, dc and b. Also, set the option for whether or not to couple the z'-displacements of nodes on the two faces of the coarse model having normals in the z' direction. Enforcing this coupling amounts to carrying out the "coupled node" analyses described in Chapter 3. Not enforcing this coupling amounts to carrying out the "non-coupled node" analyses. For coupled node analyses, set parameters GPLSTCH to 1 and PLSTRCH to 0. For non-coupled node analyses, set both parameters GPLSTCH and PLSTRCH to zero.

The user may also wish to set the z'-displacements to zero of nodes on the two faces of the coarse model having normals in the z' direction (similar to plane strain analysis). This is done by setting parameters GPLSTCH to 0 and PLSTRCH to 1, respectively. Save the file USERDATA.mac.

The mesh sensitivity analysis is now ready to be carried out. Execute the controlling input file Main.inp in ANSYS. To execute the file in batch mode, enter the appropriate DOS command at a user prompt; different commands are stored in file "DOSCOMMND." Make sure to update the directory paths in the DOS commands. During the solution stage, ANSYS exports different data files to the current working directory. These files are described in the following section. The file "cmap-grey.cmap" is the ANSYS color map used to create the gray scale contour maps presented in the dissertation.

Data File Descriptions for Appendix D

pthhprssij.txt: Interpolated path data of hydrostatic stress from submodel elements. The ij post-fix in the file name corresponds to results from mesh j using c-axis spherical coordinate set i. The data in columns 1, 2 and 3 are the x', y' and z' locations (m), respectively, of the path points. The column 4 data are the distances (m) of the path points from the start of the path. The column 5 data are the interpolated values of hydrostatic stress (Pa).

HPRSSDATi.txt: Interpolated path data of hydrostatic stress from submodel elements for all meshes. The i post-fix in the file name corresponds to results from c-axis spherical coordinate set i. Data in columns 1, 2 and 3 are the x', y' and z' locations (m), respectively, of the path points. The column 4 data are the distances (m) of the path points from the start of the path. The data in columns 5, 6, 7,..., 4+NUMMESH are the interpolated values of hydrostatic stress (MPa) for meshes 1, 2, 3,..., NUMESH. Each of these files is a compilation of the files named "pthhprssij.txt" for all values of j.

COORDSETTINGS.txt: Values of all randomly-generated c-axis spherical coordinates. Each row of the file contains, from left to right: theta1 (i.e., θ_1), phi1 (i.e., ϕ_1, etc.), theta2, phi2, theta3, phi3, theta4, phi4. Row i of the data file contains the coordinates of c-axis spherical coordinate set i, where i is an integer ranging from 1 to NUMCOORD.

runtimes.txt: Wall clock times (hours) at beginning of analysis and after each model run. There are a total of NUMMESH×NUMCOORD+1 time entries.

subpar.txt: Submodel parameters read by ANSYS during the submodeling routine.

APPENDIX E

INSTRUCTIONS TO EXECUTE ITJ MODEL

The Inelastic Triple Junction (ITJ) Model is used in Chapter 5 of the dissertation to calculate strain rates and predict onset of internal melting in the Vostok accretion ice. The results of the ITJ Model are also compared to strain rates and internal melting previously observed in polycrystalline ice. This appendix provides instructions for running the ITJ Model in ANSYS with use of the input files on the accompanying CD. The results of this analysis include strain rates, maximum stress concentrations, melting temperatures, and temperature variations associated with heat dissipation from creep—everything except the mesh sensitivity analysis for the ITJ Model. First, a mechanical model is solved using a submodeling routine, followed by a steady state thermal model. A summary of the analysis is as follows.

In the mechanical model, a coarse mesh model is solved, followed by a coarse mesh submodel, and followed lastly by a fine mesh submodel. The coarse mesh submodel, named "CrTJ2Sub1," has a mesh identical to the first coarse mesh model, named "CrTJ2Moth." The submodel CrTJ2Sub1 is solved using displacement boundary conditions interpolated from the model CrTJ2Moth. The coarse mesh submodel is necessary to obtain convergent solutions of the ITJ Model when grain boundary sliding (i.e., frictionless "contact") is included. The reason for this is briefly explained in Chapter 5. The fine mesh submodel, named "CrTJ2Sub2," has a cylindrical geometry and is referred to as just "submodel" in Chapter 5. The fine mesh submodel is solved using displacement boundary conditions interpolated from the coarse submodel CrTJ2Sub1. After the fine mesh submodel CrTJ2Sub2 is solved, data files are written that contain melting temperatures, stress extrema and their locations, heat dissipation rates from creep, and temperature increases from heat dissipation. These data are all from element solutions in the fine mesh submodel, evaluated at centroid locations.

A steady state thermal model is solved after the mechanical models. The heat dissipation data from the mechanical model, in file "ThermData.txt," is read and applied as element heat generation loads (BFE) in the thermal model named "TJthermal.inp." The thermal model has a mesh identical to the fine mesh submodel. In summary, each execution of the ITJ Model consists of solutions of the following sequence of linked models: CrTJ2Moth (mechanical coarse mesh) → CrTJ2Sub1 (mechanical coarse mesh submodel) → CrTJ2Sub2 (mechanical fine mesh submodel) → TJthermal (thermal fine mesh model).

The input files to run the ITJ Model in ANSYS are available in the "AppE-ITJ" file collection at Internet URL address http://www.montana.edu/etd/available/sjepsen_1205.html. The instructions for running this model in ANSYS are as follows. Locate and open the input file named "Main.inp." This file contains a controlling loop for running the ITJ Model a total of NUMCOORD times, once for each c-axis spherical coordinate set. Set the desired integer value of parameter NUMCOORD in Main.inp. This parameter specifies the number of different c-axis spherical coordinate sets for which to obtain solutions. Also, set the desired number of path interpolation points PTHDVS. Do not adjust the parameter

NUMMESH, this is a relict of an earlier model. The user is encouraged to remove unnecessary portions of the model once its structure is well understood. Set the geometry parameters labeled 'a' and "dc." The mesh settings CM1, CM2, FM1 and FM2 are specified in components (1,1), (1,2), (1,3) and (1,4) of the MESHSET array. Specify these values or leave the pre-existing ones. Save the file Main.inp.

Locate and open the macro file named "gencoord.mac." This file exports angles (degrees) of the different c-axis spherical coordinate sets to a file named "COORDSETTINGS.txt." This data file contains NUMCOORD different rows of angles. In the macro file named "gencoord.mac," comment out one of the blocks of code where the values of the COORDSET array are filled, depending on whether user-specified, or randomly-generated, c-axis spherical coordinates are to be used. Commenting out a line of code amounts to pre-appending the line with the character '!.' Usually, when the parameter NUMCOORD > 1, the block of code for user-specified values of the COORDSET array is to be commented out.

Locate and open the macro file named "userdata." Set the following parameter values: TPTR = temperature (K); macpres = hydrostatic stress (Pa) applied at model boundary; mactau = deviatoric stress (Pa) applied at model boundary; MATERIAL = material type; CONTCH = choice of whether or not to use grain boundary sliding (i.e., frictionless "contact"); and the load step parameters N1, N2 and TFINAL. It should be noted that several solutions using creep did not converge when N2 was set to 2, but did converge when N2 was increased to 4. Set the option for whether or not to couple the z'-displacements of nodes on the two faces of the coarse model having normals in the z' direction. Enforcing this coupling amounts to carrying out the "coupled node" analyses described in Chapter 3. Not enforcing this coupling amounts to carrying out the "non-coupled node" analyses. For coupled node analyses, set parameters GPLSTCH to 1 and PLSTRCH to 0. For non-coupled node analyses, set both parameters GPLSTCH and PLSTRCH to zero. The user may also wish to set the z'-displacements to zero of nodes on the two faces of the coarse model having normals in the z' direction (similar to plane strain). This is done by setting parameters GPLSTCH to 0 and PLSTRCH to 1, respectively. All results presented in Chapter 5 used GPLSTCH- and PLSTRCH-values of both zero. Save the file named userdata.mac.

Locate and open the macro file named "matdefn.mac." Set the values of the Hill parameters HPRXX, HPRYY, HPRZZ, HPRXY, HPRYZ and HPRXZ. These are referred to in Chapter 4 of the dissertation as R_{xx}, R_{yy}, R_{zz}, R_{xy}, R_{yz} and R_{xz}, respectively. Comment out *either* the soft crystal *or* hard crystal Norton creep parameters NCC1, NCC2 and NCC3. These are referred to in Chapter 4 as C_1, C_2 and C_3, respectively. Hard crystal parameters are used in the results presented in Chapter 5. Save the file named matdefn.mac.

The ITJ Model is now ready to be implemented. Execute the controlling input file Main.inp in ANSYS. To execute the file in batch mode, enter the appropriate DOS command at a user prompt;

different commands are stored in file "DOSCOMMND." Make sure to update the directory paths in the DOS commands. During the solution stage, ANSYS exports different data files to the current working directory. These files are described in the following section. The file "cmap-grey.cmap" is the ANSYS color map used to create the gray scale contour maps presented in the dissertation.

Data File Descriptions for Appendix E

STRESSVALS.txt: Maximum calculated values of most compressive principal stress, shear stress resolved along the basal plane, hydrostatic stress, and the locations (with respect to global frame) of each stress extremum. The stress extrema are element solutions, evaluated at centroid locations, and selected from elements in the fine mesh submodel having centroids located at z' = 0.25 m (for d_{g1} = 0.5 m). The data are arranged in columns with headers defined as follows: maxhp = maximum hydrostatic stress (Pa), xmaxhp = x' location (m) of maximum hydrostatic stress, ymaxhp = y' location (m) of maximum hydrostatic stress, zmaxhp = z' location (m) of maximum hydrostatic stress, maxtss = maximum shear stress (Pa) resolved along the basal plane, xmaxtss = x' location (m) of maximum shear stress resolved along basal plane, ymaxtss = y' location (m) of maximum shear stress resolved along basal plane, zmaxtss = z' location (m) of maximum shear stress resolved along basal plane, mins3 = greatest magnitude of most compressive principal stress (Pa), xmins3 = x' location (m) of most compressive principal stress of greatest magnitude, ymins3 = y' location (m) of most compressive principal stress of greatest magnitude, zmins3 = z' location (m) of most compressive principal stress of greatest magnitude. Row i of the data corresponds to results from the i^{th} c-axis spherical coordinate set (excluding row of headers).

THERMVALS.txt: Maximum and minimum calculated values of melting temperature (°C) and temperature increase (°C) caused by heat dissipation. These extrema are element solutions, evaluated at centroid locations, and selected from elements in the fine mesh submodel having centroids located at z' = 0.25 m (valid for d_{g1} = 0.5 m). The following variables are defined: TPTR = temperature applied at cylindrical boundary of thermal model, taken to be the "average" temperature in the ice; T = calculated temperature (°C), which equals TPTR plus the increase caused by heat dissipation from creep; ΔT^c = calculated temperature increase (°C) caused by heat dissipation, which equals T - TPTR; T_m = calculated melting temperature (°C); σ_h = calculated hydrostatic stress; s_3 = calculated most compressive principal stress. The data in the file are arranged in columns with headers defined as follows: delT-min = minimum calculated value of ΔT^c; delT-max = maximum calculated value of ΔT^c; Tm-min(HPRES) = minimum calculated melting temperature assuming that the pressure acting normal to the ice-water interface equals σ_h; Tm-max(HPRES) = maximum calculated melting temperature assuming that the pressure acting

normal to the ice-water interface equals σ_h; Tm-min(S3) = minimum calculated melting temperature assuming that the pressure acting normal to the ice-water interface equals s_3; Tm-max(S3) = maximum calculated melting temperature assuming that the pressure acting normal to the ice-water interface equals s_3; Tdiff-min(HPRES) = minimum calculated value of $T_m - \Delta T^c$ assuming that the pressure acting normal to the ice-water interface equals σ_h, this is interpreted to represent the minimum value of TPTR for which to expect onset of melt; Tdiff-max(HPRES) = maximum calculated value of $T_m - \Delta T^c$ assuming that the pressure acting normal to the ice-water interface equals σ_h, this is interpreted to represent the maximum value of TPTR for which to expect onset of melt; Tdiff-min(S3) = minimum calculated value of $T_m - \Delta T^c$ assuming that the pressure acting normal to the ice-water interface equals s_3, this is interpreted to represent the minimum value of TPTR for which to expect onset of melt; Tdiff-max(S3) = maximum calculated value of $T_m - \Delta T^c$ assuming that the pressure acting normal to the ice-water interface equals s_3, this is interpreted to represent the maximum value of TPTR for which to expect onset of melt. Row i of the data corresponds to results from the i^{th} c-axis spherical coordinate set (excluding row of headers).

COORDVALS.txt: The c-axis spherical coordinates (degrees) used in the ITJ Model analysis. Row i of the data corresponds to the values used in the i^{th} c-axis spherical coordinate set (excluding row of headers). The data in the file are arranged in columns with headers defined as follows: theta1 = value of θ for local frame 1 (i.e., θ_1), phi1 = value of ϕ for local frame 2 (i.e., ϕ_1), theta2 = value of θ for local frame 2 (i.e., θ_2), phi2 = value of ϕ for local frame 2 (i.e., ϕ_2, etc.), theta3 = value of θ for local frame 3, phi3 = value of ϕ for local frame 3, theta4 = value of θ for local frame 4, phi4 = value of ϕ for local frame 4.

EPSDY_T.txt: Calculated strain rates (s^{-1}) in the y' direction. The values are element solutions, evaluated at centroid locations, and selected from elements in the fine mesh submodel having centroids located at z' = 0.25 m (for d_{g1} = 0.5 m). The following variables are defined: ϵ'_{yy} = calculated y' component of strain rate, σ_h = calculated hydrostatic stress (Pa); s_3 = calculated most compressive principal stress (Pa). The data in the file are arranged in columns with headers defined as follows: minimum y strain rate = minimum value of ϵ'_{yy}; maximum y strain rate = maximum value of ϵ'_{yy}; mean y strain rate = average of the ϵ'_{yy} values; median y strain rate = median of the ϵ'_{yy} values; min melting temp (HPRES) = minimum calculated melting temperature (°C) assuming that the pressure acting normal to ice-water interface equals σ_h; min melting temperature (S3) = minimum calculated melting temperature (°C) assuming that the pressure acting normal to ice-water interface equals s_3.

ThermData.txt: Calculated heat dissipation rates (J $s^{-1}m^{-3}$), element numbers and melting temperatures (°C) from the mechanical (i.e., not thermal) fine mesh submodel. The data is exported from results of

the fine mesh mechanical model, and is read by the thermal model as element body loads of heat supply. The first eight rows of the file contain model settings. The remaining rows contain data from element solutions of the fine mesh mechanical model, evaluated at element centroids located at z' = 0.25 m (for d_{g1} = 0.5 m). The data in the file are arranged in columns with headers defined as follows: Elem # = element number; Heat Diss = rate of heat dissipation (J $s^{-1}m^{-3}$) from creep; (Equil Temp, P = HPRES) = calculated melting temperature (°C) assuming that the pressure acting normal to ice-water interface equals σ_h; (Equil Temp, P = s3) = calculated melting temperature (°C) assuming that the pressure acting normal to ice-water interface equals s_3.

runtimes.txt: Wall clock times (hours) at beginning of each analysis (entry for each c-axis spherical coordinate set) and at the end of last analysis. There are a total of NUMCOORD+1 time entries.

subpar.txt: Submodel parameters read by ANSYS during the submodeling routine.